

UNCLASSIFIED

SECURITY CLASSIFICATION OF THIS PAGE

(2)

REPORT DOCUMENTATION PAGE

1a. REPORT SECURITY CLASSIFICATION Unclassified		1b. RESTRICTIVE MARKINGS	
2a. SECURITY CLASSIFICATION AUTHORITY Unclassified		3. DISTRIBUTION/AVAILABILITY OF REPORT Approved for public release; distribution unlimited.	
AD-A263 734 		5. MONITORING ORGANIZATION REPORT NUMBER(S) ARO 25349.1-PH	
Duke University FEL Laboratory	b. OFFICE SYMBOL (if applicable)	7a. NAME OF MONITORING ORGANIZATION U.S. Army Research Office	
6c. ADDRESS (City, State, and ZIP Code) FEL Laboratory, P.O. Box 90319 Durham, NC 27708-0319		7b. ADDRESS (City, State, and ZIP Code) P.O. Box 12211 Research Triangle Park, NC 27709-2211	
8a. NAME OF FUNDING/SPONSORING ORGANIZATION		8b. OFFICE SYMBOL (if applicable)	
		9. PROCUREMENT INSTRUMENT IDENTIFICATION NUMBER DAAL03-88-K-0109 DTIC	
8c. ADDRESS (City, State, and ZIP Code)		10. SOURCE OF FUNDING NUMBERS PROGRAM ELEMENT NO. PROJECT NO. S E L E C T E D WORK UNIT NO. ACCESSION NO. MAY 5 1993	
11. TITLE (Include Security Classification) High Resolution Free-Electron Laser Spectroscopy			
12. PERSONAL AUTHOR(S) Madey, John M.J., Szarmes, Eric B.			
13a. TYPE OF REPORT Final Technical	13b. TIME COVERED FROM 88-06-01 TO 91-09-30	14. DATE OF REPORT (Year, Month, Day) 93 March 23	15. PAGE COUNT 140
16. SUPPLEMENTARY NOTATION The views, opinions and/or findings contained in this report are those of the authors and should not be construed as an official position, policy, or decision, unless so designated by other documentation.			
17. COSATI CODES		18. SUBJECT TERMS (Continue on reverse if necessary and identify by block number) Free Electron Laser, Femtosecond pulses, Spectroscopy, Chirped pulses	
19. ABSTRACT (Continue on reverse if necessary and identify by block number) High peak power infrared pulses as short as 350 femtoseconds have been generated using the MK III FEL. Small signal analyses have been developed for operating the FEL with electron pulses whose energy varies linearly with time. Chirped-pulse simulations using modest energy shirps have demonstrated a x15 compression ratio at saturated power levels for 3.4 ps optical pulses at 3.35 um, and coupled pulse simulations have indicated substantial longitudinal mode reduction on microsecond time scales. A Michelson mirror resonator has been operated for the first time on the MK III FEL, along with phase-locked operation using a beamsplitter reflectance of only 1.4%			
93 5 04 06 4		93-09498 	
20. DISTRIBUTION/AVAILABILITY OF ABSTRACT <input type="checkbox"/> UNCLASSIFIED/UNLIMITED <input type="checkbox"/> SAME AS RPT. <input type="checkbox"/> DTIC USERS		21. ABSTRACT SECURITY CLASSIFICATION Unclassified	
22a. NAME OF RESPONSIBLE INDIVIDUAL Dr. Bob D. Guenther		22b. TELEPHONE (Include Area Code) (919) 549-0641	22c. OFFICE SYMBOL

ACCEPTED AS THE FINAL REPORT ON PROPOSAL 25349-PH

contract number DAAL03-88-K-0109

HIGH RESOLUTION FREE-ELECTRON LASER SPECTROSCOPY

A DISSERTATION

SUBMITTED TO THE DEPARTMENT OF APPLIED PHYSICS

AND THE COMMITTEE ON GRADUATE STUDIES

OF STANFORD UNIVERSITY

IN PARTIAL FULFILLMENT OF THE REQUIREMENTS

FOR THE DEGREE OF

DOCTOR OF PHILOSOPHY

DTIC QUALITY INSPECTED 8

By

Eric Brent Szarmes

May 1992

Accession For	
NTIS	CRA&I
DTIC	TAB
Unannounced	
Justification	
By	
Distribution/	
Availability Codes	
Dist	Avail and/or Special
A-1	

© Copyright by Eric Brent Szarmes 1992
All Rights Reserved

I certify that I have read this dissertation and that in my opinion it is fully adequate, in scope and quality, as a dissertation for the degree of Doctor of Philosophy.

John M. J. Madey,
Professor of Physics and Principal Advisor

I certify that I have read this dissertation and that in my opinion it is fully adequate, in scope and quality, as a dissertation for the degree of Doctor of Philosophy.

Steven Chu,
Professor of Physics and co-Advisor

I certify that I have read this dissertation and that in my opinion it is fully adequate, in scope and quality, as a dissertation for the degree of Doctor of Philosophy.

Michael D. Fayer,
Professor of Chemistry

Approved for the University Committee
on Graduate Studies:

Abstract

The broad and continuous tunability of the rf linac-driven free-electron laser (FEL), coupled with its high power picosecond time structure, has greatly enhanced the research capabilities in the field of infrared spectroscopy. However, the duration of the optical pulses is often too long to probe ultrafast processes that occur on time scales of a few tens to a few hundreds of femtoseconds, and the spectral structure of the optical beam, with closely spaced longitudinal modes in a bandwidth determined by the Fourier transform of the short pulses, poses a significant limitation for experiments requiring high spectral resolution.

The temporal resolution can be improved by operating the FEL with electron pulses whose energy varies linearly with time; the resulting optical pulses possess substantial frequency chirps and are susceptible to pulse compression in an external dispersive delay line. The spectral resolution can be enhanced by using an intracavity Michelson interferometer to couple successive optical pulses so that they build up from noise with a definite phase relationship; the longitudinal modes in the output beam are then separated by the rf frequency of the linac and can be individually filtered for applications in high resolution spectroscopy.

In this dissertation, I develop small signal analyses for each of these modes of operation, and report the results of numerical pulse propagation simulations whose parameters were chosen to guide the design of feasible experiments on the Mark III FEL. Chirped-pulse simulations using modest energy chirps have demonstrated a $\times 15$ compression ratio at saturated power levels for 3.4 ps optical pulses at $3.35 \mu\text{m}$, and coupled pulse simulations have indicated substantial longitudinal mode reduction on microsecond time scales. I also develop a simplified derivation of the FEL coupled mode equations using conventional mode locked laser theory, and solve them numerically in the frequency domain to describe the detuning properties of the Michelson resonator FEL. Finally, I report the first operation of a Michelson mirror resonator on the Mark III FEL, and present indirect evidence for phase locked operation using a beamsplitter reflectance of only 1.4 %.

Acknowledgments

Many people contributed directly to the quality of my graduate education. John F. Schultz is gratefully acknowledged for his tutelage during my early years at Stanford, and for teaching me how to handle quality laser optics. Stephen V. Benson generously offered the use of his pulse propagation code, and made several valuable suggestions concerning its modification for the present research. His eternal willingness to patiently answer my many questions on FEL physics is greatly appreciated, and contributed immeasurably to my education in the field. Most of all, I would like to thank John M. J. Madey for his guidance during my graduate career, and for his exemplary professionalism. None of my accomplishments would have been possible without his utterly infinite patience. I greatly appreciated his trust in charging me with the care and development of the Mark III optical system (which was a milestone in my career), and I especially enjoyed working with him personally during the loss modulation experiments.

I wish to acknowledge helpful discussions with Charles Brau and Jim Elliott on the basic aspects of the Michelson mirror resonator, and with Genevieve Barnett on general questions of FEL physics.

This research would not have been possible without the support of several organizations. The Army Research Office provided the funding for this work under contract # DAAL03-88-K-0109. The San Diego Supercomputer Center and the National Center for Supercomputing Applications provided valuable CRAY seedtime for optimizing and debugging the computer code, and the North Carolina Supercomputing Center provided over 100 hours of cpu time on the CRAY Y/MP, on which all of the numerical simulations reported in this dissertation were performed. I am particularly grateful to Bruce Loftis at NCSC for his generosity.

Finally, I would like to formally acknowledge a very early contribution from my brother Victor, who sparked my interest in physics by keeping quiet and letting me think about the answer, and perhaps the greatest contribution from my patient and loving wife Charlotte, who offered tremendous support, especially during times of doubt.

To Charlotte

Table of Contents

Abstract	iv
Acknowledgments	v
Table of Contents	vii
List of Tables	x
List of Figures	xi
Chapter 1 Introduction	1
I. Preamble	1
II. THE MARK III FREE-ELECTRON LASER	2
III. HIGH RESOLUTION ENHANCEMENTS	4
IV. FEL SPECTROSCOPY	7
V. OUTLINE OF THE DISSERTATION	8
VI. REFERENCES	8
Chapter 2 The chirped-pulse free-electron laser	10
I. Preamble	10
II. FEL PULSE PROPAGATION	12
III. GAIN SHIFT AND GAIN REDUCTION IN THE CHIRPED-PULSE FEL	13
IV. NUMERICAL SIMULATIONS OF THE CHIRPED-PULSE FEL	18
V. NUMERICAL BENCH MARKS	21
VI. REFERENCES	25
Chapter 3 Numerical simulations	27
I. Preamble	27
II. GENERAL SIMULATION RESULTS	28
A. <i>General features of chirped optical pulses</i>	28
B. <i>Dependence of frequency chirp on energy chirp</i>	31
C. <i>Dependence of optical power on energy chirp</i>	34
III. ENERGY CHIRPING ON THE MARK III FEL; DESIGN PARAMETERS	38
A. <i>Proposed configuration</i>	38

<i>B. Numerical simulations in the proposed configuration</i>	39
<i>C. Effects of intracavity dispersion</i>	43
<i>D. Simulated cavity detuning curves</i>	45
IV. SUMMARY OF RESULTS	49
V. REFERENCES	50
Chapter 4 The Michelson resonator free-electron laser	52
I. Preamble	52
II. EIGENMODE ANALYSIS OF N COUPLED LASERS	54
<i>A. Formalism</i>	55
<i>B. Biorthogonality</i>	56
<i>C. Equivalent matrix formulation</i>	59
<i>D. Approximate solutions; physical interpretation</i>	59
III. PASSIVE MODE STRUCTURE OF THE MICHELSON RESONATOR	62
<i>A. Frequency response</i>	63
<i>B. Resonant frequencies and losses</i>	64
<i>C. The detuned interferometer</i>	66
IV. NUMERICAL SIMULATIONS	68
V. REFERENCES	76
Chapter 5 Supermode structure and mirror detuning effects	78
I. Preamble	78
II. THE FEL COUPLED MODE EQUATIONS	79
<i>A. Temporal analysis</i>	79
<i>B. Spectral analysis</i>	82
III. THE HARMONICALLY MODE LOCKED FEL	87
IV. SOLUTION OF THE COUPLED MODE EQUATIONS	89
V. NUMERICAL RESULTS; COMPARISON WITH PULSE PROPAGATION SIMULATIONS	92
<i>A. Broadening of cavity detuning curves</i>	93
<i>B. Spectral narrowing of supermodes</i>	95
<i>C. Decrease of the hypermode decay rates</i>	98
VI. REFERENCES	105

Chapter 6 A phase locking experiment on the Mark III free-electron laser	107
I. Preamble	107
II. EXPERIMENTAL DESIGN	108
A. <i>Laser configuration</i>	108
B. <i>Michelson mirror resonator</i>	108
C. <i>Laser diagnostics</i>	110
III. EXPERIMENTAL PROCEDURE AND RESULTS	110
IV. NUMERICAL SIMULATIONS	113
A. <i>Simulation parameters</i>	113
B. <i>Simulation results</i>	115
V. DISCUSSION AND CONCLUSIONS	118
VI. REFERENCES	119
 Chapter 7 Summary and conclusions	 120
 Appendix A Optical diagnostics for chirped-pulse free-electron lasers	 124
I. Preamble	124
II. PULSE PARAMETERS	125
III. MARK III DESIGN PARAMETERS	127
IV. PULSE COMPRESSOR DESIGN	128
V. OPTICAL DIAGNOSTICS	131
VI. EXPERIMENTS AT OTHER WAVELENGTHS	133
VII. REFERENCES	134
 Appendix B Spectral diagnostics for phase locked free-electron lasers	 136
I. Preamble	136
II. RESONATOR DESIGN	136
III. SPECTRAL DIAGNOSTICS	139
IV. REFERENCES	140

List of Tables

	page
Table 2.1 Mark III parameters used in the simulations of the chirped-pulse FEL.	22
Table 4.1 Parameters used in the Michelson resonator simulations on the Mark III FEL.	69
Table 5.1 Definition of FEL parameters, and values used in the coupled mode simulations.	92
Table 6.1 Parameters used in the simulations of the Mark III experiment.	114

List of Figures

	page
Fig. 1.1 An rf linac-driven free-electron laser with Brewster plate output coupling.	3
Fig. 1.2 Temporal structure of the optical beam from the Mark III FEL.	3
Fig. 1.3 Energy chirping in a free-electron laser.	4
Fig. 1.4 Intracavity filtering of laser longitudinal modes: (a) filtering of individual supermodes; (b) filtering of individual hypermodes.	6
Fig. 2.1 The analytical small signal gain (assuming a plane-wave interaction), and the corresponding value of the resonance parameter, for arbitrary values of the energy chirp.	16
Fig. 2.2 The small signal gain as a function of v_0 , for a resonance shift of $\delta = 10\pi$ and a current of $r = 1$.	17
Fig. 2.3 The simulated optical envelope and phase after 100 passes in a chirped-pulse FEL, for a 4 ps tophat electron micropulse with a full width linear energy chirp of +2 %.	23
Fig. 2.4 The value of the resonance parameter yielding the maximum gain in a chirped-pulse FEL, as a function of the full width energy chirp along a 4 ps tophat electron pulse.	24
Fig. 3.1 Optical envelope and phase after 100 passes for electron pulses with a full width energy chirp of: (a) -2 %; (b) 0 %; (c) +2 %.	29
Fig. 3.2 Power spectra for the optical pulses in Fig. 3.1.	29
Fig. 3.3 Optimum quadratic compression of the chirped optical pulses in Fig. 3.1.	30
Fig. 3.4 Simulated frequency chirps, extrapolated to the electron pulse duration, as a function of the pulse width, for energy chirps of +2 % and -2 %.	32
Fig. 3.5 Phase space trajectories on the 100 th pass in a simulation using unchirped electron pulses with a duration of 4 ps.	33
Fig. 3.6 Optical phase after 200 passes, in simulations using unchirped electron pulses with no noise. The optical powers were reset to small signal levels after every 4 passes.	34
Fig. 3.7 Small signal gain, macropulse power prior to saturation, and macropulse power at saturation, as functions of the energy chirp in a 4 ps electron pulse.	35
Fig. 3.8 Energy extraction efficiencies on the 100 th pass for the simulations in Fig. 3.7.	35
Fig. 3.9 Phase space trajectories on the 100 th pass of the optical pulse for electrons near the center of 4 ps electron pulses with various chirps. The cavity is at the <i>synchronous</i> length.	37
Fig. 3.10 Phase space trajectories on the 100 th pass of the optical pulse for electrons near the center of 4 ps electron pulses with various chirps. The cavity is 1.3 μm <i>shorter</i> than the synchronous length.	37
Fig. 3.11 Phase space trajectories on the 100 th pass of the optical pulse for electrons near the center of 4 ps electron pulses with various chirps. The cavity is 1.3 μm <i>longer</i> than the synchronous length.	37
Fig. 3.12 The Mark III chicane path used to bend the electron beam around the cavity mirror. $L_c = 36.7 \text{ cm}$ and $\beta = 11.25^\circ$.	39

Fig. 3.13	Optical envelope and phase after 100 passes for electron pulses with a full width energy chirp of +2 % over 4 ps and various cavity detunings.	40
Fig. 3.14	Power spectra for the optical pulses in Fig. 3.13.	40
Fig. 3.15	Optimum quadratic compression of eight optical pulses for cavities longer and shorter than the synchronous length. The energy chirp is +2 % over 4 ps in each case.	41
Fig. 3.16	Frequency chirp as a function of wavenumber for electron pulses with a +2 % energy chirp over 6 ps.	42
Fig. 3.17	Optical envelope and phase after 100 passes for electron pulses with a full width energy chirp of +2 % over 4 ps, including dispersion in a: (a) CaF ₂ , (b) sapphire, and (c) ZnSe Brewster plate.	45
Fig. 3.18	Cavity power detuning curves for (a) unchirped 4 ps electron pulses, and (b) electron pulses with an energy chirp of +2 % over 4 ps. Positive detunings refer to shorter cavities.	46
Fig. 3.19	Small signal supermode evolution at a cavity detuning of +10 μm for (a) unchirped electron pulses with a duration of 4 ps, and (b) electron pulses with an energy chirp of +2 % over 4 ps.	47
Fig. 3.20	Large signal supermode evolution from spontaneous radiation to full saturation at a cavity detuning of +10 μm.	48
Fig. 4.1	Multiple mirror resonators for coupling successive optical pulses: (a) Michelson mirror resonator with a delay of one rf period, and (b) Fox-Smith interferometer with a round trip time of one rf period in the small resonator.	53
Fig. 4.2	Mutual projections of the non-orthogonal eigenmodes vs. the products of their eigenvalues, for a Michelson mirror resonator with N = 35 pulses and a beamsplitter reflectance of r ² = 50 %.	58
Fig. 4.3	Percent error in calculating the total leakage losses for 35 pulses using the approximate eigenvalues from Section II.D instead of the exact eigenvalues corresponding to the non-orthogonal eigenmodes.	62
Fig. 4.4	Definition of the cavity lengths in a Michelson mirror resonator. The length L of the primary linear cavity is L = L _c + L ₁ .	63
Fig. 4.5	Frequency response of optical resonators under CW excitation.	65
Fig. 4.6	Simulations showing the phase difference between adjacent optical pulses at the end of the macropulse, as a function of the phase offset, in a Michelson resonator FEL with N = 4 and r ² = 50 %.	70
Fig. 4.7	Leakage losses due to interference in the surviving hypermodes at the end of the macropulse for the simulations in Fig. 4.6.	71
Fig. 4.8	Spectra of the simulated macropulses from Fig. 4.6 with phase offsets at the secondary mirror of: (a) φ/2π = 0.1, (b) φ/2π = 0.125, and (c) φ/2π = 0.15.	72
Fig. 4.9	Phase difference between two adjacent optical pulses as a function of pass number, corresponding to the simulation in Fig. 4.8(b). Solid line = simulation; Dashed line = theory.	73
Fig. 4.10	(a), (b): Optical micropulse structure after 160 passes, from simulations of a single pulse in a two-mirror resonator. (c), (d): Same, except for 35 pulses in a perfectly tuned Michelson resonator FEL with r ² = 50 %.	73
Fig. 4.11	(a) Output macropulse power for the single-pulse simulation of Fig. 4.10	74

(dashed), and for the Michelson resonator simulation of Fig. 4.10 (solid).	
(b) Leakage power for the Michelson resonator simulation of Fig. 4.10.	
Fig. 4.12 Macropulse mode structure from the Michelson resonator simulation of Fig. 4.10 after: (a) 50 passes, and (b) 160 passes. The dots in Fig. (a) are the relative mode amplitudes predicted from the growth rate (4.36).	75
Fig. 5.1 Single pass amplification of a CW optical wave due to short electron pulses. The slippage parameter ($N_w\lambda/C\tau_p$) equals 0.525 in each case.	82
Fig. 5.2 Phasor interpretation of the mode locking process in eq. (5.16), showing the superposition of coincident sidebands produced by an active intracavity modulation.	84
Fig. 5.3 Frequency band on the small signal gain curve used in the coupled mode simulations. The region from $\nu = 0$ to $\nu = 6.362$ encloses 675 longitudinal modes separated by the rf frequency.	89
Fig. 5.4 Cavity detuning curves for various fixed values of the secondary Michelson mirror detuning, with $r^2 = 50\%$. The dashed envelope corresponds to $\delta L_{cav} + r^2 \delta L_{Mich} = +10 \mu\text{m}$.	93
Fig. 5.5 Small signal gains (crosses) calculated from the pulse propagation simulations, corresponding to several of the detuning curves from Fig. 5.4.	94
Fig. 5.6 Passive intracavity intensities for various fractional interferometer detunings δN , with $N = 35$ and $\gamma_c = 7.3\%$, from a source of fixed amplitude coupled into the cavity at the resonances of the zeroth order hypermode.	96
Fig. 5.7 Normalized supermode spectra of the lowest order hypermode for various secondary Michelson mirror detunings. The frequency of 0 GHz corresponds to the resonant frequency.	96
Fig. 5.8 Temporal supermodes from the coupled mode (dashed line) and pulse propagation (solid line) simulations for several secondary Michelson mirror detunings.	97
Fig. 5.9 Macropulse spectra from the pulse propagation simulations (after 160 passes) using $N = 10$ pulses, for various Michelson mirror detunings δL_{Mich} . The intensities from the coupled mode simulations are shown as dots.	99
Fig. 5.10 Passive intracavity intensities of the first order hypermode for various fractional interferometer detunings δN , calculated in the same manner as in Fig. 5.6.	101
Fig. 5.11 Criterion for determining the onset of degradation in the hypermode decay rates.	102
Fig. 5.12 Coupled mode simulations of hypermode loss γ_{m_h} for $N = 35$, as a function of secondary Michelson mirror detuning, calculated as the average loss of the $\pm m_h$ hypermodes.	104
Fig. 6.1 Experimental configuration of the Michelson mirror resonator and the optical diagnostics.	109
Fig. 6.2 Oscilloscope traces of the Ge:Au detector response showing the envelopes of 32 macropulses for a Michelson resonator FEL with 1.4 % coupling in which the secondary mirror was (a) detuned, and (b) synchronized.	111
Fig. 6.3 Autocorrelation trace of the optical pulses from the laser in which the secondary mirror was completely detuned. The FWHM pulse duration is 1.2 ps assuming a Gaussian optical pulse profile.	112

Fig. 6.4	Spectrum of the optical beam from the laser in which the secondary mirror was completely detuned, obtained using a 1 m monochromator.	112
Fig. 6.5	Longitudinal mode spectrum of a perfectly tuned Michelson resonator FEL with 35 pulses and a beamsplitter reflectance of 1.4 %.	115
Fig. 6.6	Simulated output macropulse powers for (a) the completely detuned Michelson resonator, and (b) the phase locked Michelson resonator.	116
Fig. 6.7	(a) Simulated output macropulse powers for the Michelson resonator with a slew of 2π radians in the relative phase offset. (b) Macropulse envelopes from Fig. 6.7(a) and Fig. 6.6(b).	116
Fig. 6.8	Coupled mode simulations of the first order hypermode loss in a Michelson resonator with the parameters listed in Table 6.1.	117
Fig. A.1	Optimum quadratic phase compensation factors $K(a,b)$ from eq. (A.6) for various ideal pulse shapes, defined as yielding the maximum compressed peak powers.	126
Fig. A.2	Optimum pulse compression ratios corresponding to the compensation factors in Fig. A.1.	126
Fig. A.3	Typical prism configuration for a single pass dispersive delay line. The prisms are in the minimum deviation geometry to avoid astigmatism in the transmitted beam.	129
Fig. A.4	Double pass, sapphire prism dispersive delay line for the Mark III experiments between 2.5 μm and 4.1 μm .	130
Fig. A.5	Estimated apex-to-apex prism separations for the Mark III experiments between 2.5 and 4.1 μm .	131
Fig. A.6	Layout of the autocorrelator for measuring pulse widths as short as 200 fs.	132
Fig. A.7	Dispersion of several low- or non-hygroscopic infrared materials over their range of transparency; all of these materials also transmit at 633 nm, and may be suitable for delay lines in the near and far infrared.	133
Fig. B.1	The design of the Michelson mirror resonator for the phase locking experiments on the Mark III FEL, showing the position of the beamsplitter, output coupler, and interferometer mirrors.	137
Fig. B.2	Spectral diagnostics for filtering and resolving the individual FEL axial modes in the phase locked optical beam from the Mark III FEL.	139

A NOTE ON SIGN CONVENTIONS

The following sign conventions are observed consistently throughout this dissertation:

1. The carrier phase of the optical electric field is written $\exp[i(kz - \omega t)]$. Consequently, for example, $\omega \equiv -d\theta/dt$.
2. Positive energy (frequency) chirps are defined as energies (frequencies) that *increase* towards the trailing edge of the electron (optical) pulse. The converse is true for negative chirps.
3. Positive cavity detunings refer to cavity lengths that are *shorter* than the synchronous cavity length. The converse is true for negative cavity detunings. (This sign convention is an artifact of the pulse propagation code; it reflects the fact that positive detunings push the optical pulse *forward in time*.)

These sign conventions are noted at appropriate points throughout the dissertation.

Chapter 1

Introduction

The broad and continuous tunability of the rf linac-driven free-electron laser (FEL), coupled with its high power picosecond time structure, has greatly enhanced the research capabilities in the field of infrared (IR) spectroscopy. For example, the access of the Mark III FEL [1]-[3] to the mid-IR band from $2 \mu\text{m}$ to $10 \mu\text{m}$ presently allows the fundamental study on picosecond time scales of the vibrational modes of molecules [4], the dynamics [5] and spectroscopy [6] of advanced and high speed materials for electronics, and the dynamics of important biochemical and photochemical phenomena [7]. However, the duration of the optical pulses is often too long to probe ultrafast processes that occur on time scales of a few tens to a few hundreds of femtoseconds, and the spectral structure of the optical beam, with closely spaced longitudinal modes in a bandwidth determined by the Fourier transform of the short pulses, poses a significant limitation for experiments requiring high spectral resolution. The availability of a mid-IR source with pulse durations on the order of hundreds of femtoseconds and increased peak powers would greatly enhance the study of ultrafast molecular dynamics and nonlinear spectroscopy [8], and a powerful infrared laser with a narrow spectral resolution would fill an important gap in the capabilities of present infrared sources [9].

Fortuitously, the rf linac-driven FEL possesses unique temporal properties that are amenable to improvements in both the temporal and spectral resolution of the optical beam. The temporal resolution can be improved by operating the FEL with electron pulses whose energy varies linearly with time [10]-[12]; the resulting optical pulses possess substantial frequency chirps and are susceptible to pulse compression in an external dispersive delay

line. The spectral resolution can be enhanced by using an intracavity interferometer to couple successive optical pulses so that they build up from noise with a definite phase relationship [13]-[15]; the axial mode spacing is increased from the round trip frequency to the rf frequency, and the modes can be individually filtered for applications in high resolution spectroscopy. The chirped-pulse and phase locked enhancements on the rf linac-driven FEL, and a brief history of their conceptual development, are described below in Section III.

The purpose of this dissertation is to study the implementation of these enhancements in configurations appropriate to high resolution spectroscopy, and to establish a theoretical framework for future applications. In the present work, I develop small signal descriptions for both the chirped-pulse and phase locked FELs, and report the results of extensive numerical simulations which support the theoretical predictions and indicate the feasibility of realizing each of these enhancements on conventional rf linac-driven systems. Simulation parameters are chosen to guide the design of feasible experiments on the Mark III FEL, whose configuration provides a valuable test bed for experimental studies of both energy chirping and phase locking, and practical designs for such experiments are described.

Despite the noted application in recent years to many important experiments in infrared spectroscopy, the infrared free-electron laser is barely if ever mentioned in almost any review of the present status of that field. However, current trends are changing, and the stability and reliability of infrared FELs have been demonstrated at several laboratories offering dedicated user programs in infrared applications [16]. The high resolution enhancements described in this dissertation promise to contribute significantly to further advances in the field.

II. THE MARK III FREE-ELECTRON LASER

A free-electron laser consists of a high brightness source of ultrarelativistic electrons, an electron beam transport system, a spatially periodic magnetic field (the wiggler field), and an optical resonator co-linear with the axis of the wiggler. The configuration of a typical rf linac-driven FEL with Brewster plate output coupling, such as the Mark III FEL, is shown in Fig. 1.1. The laser action is provided by the coupling of the transverse motion of the electrons in the wiggler field to the transverse electric field of the co-propagating optical wave stored in the resonator, and the continuous tunability is provided by continuous changes in either the wiggler magnetic field or the electron energy [17].

The Mark III FEL is driven by a 2.857 GHz pulsed rf linac using electrons from a synchronized microwave gun and a thermionic cathode source. The linac energy can be set continuously from 45 MeV to 25 MeV, for which the 2.3 cm period of the wiggler magnet yields optical wavelengths from 2 μm to 10 μm . At any given energy, the strength of the

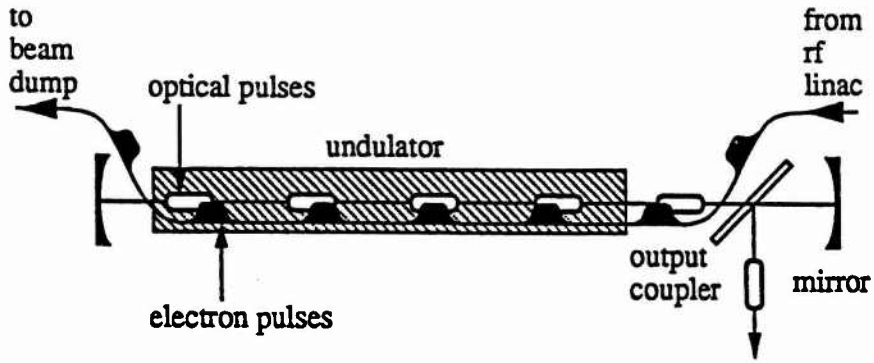


Fig. 1.1 An rf linac-driven free-electron laser with Brewster plate output coupling.

wiggler B-field can also be varied to yield more than an octave of tuning. The 30 MW rf source is pulsed at a repetition rate of 1 Hz to 30 Hz and yields electron *macropulses* with a duration of 1 μ s to 8 μ s. Each macropulse consists of a train of picosecond *micropulses* delivered at the rf frequency of 2.857 GHz, which repetition rate is the result of thermionic emission in the microwave gun which fills every bucket of the rf wave. An important consequence of this driving frequency is that the 1.837 m optical cavity contains 35 circulating optical micropulses that can be successively phase locked to yield spectral modes separated in frequency by 2.857 GHz.

The macropulse and micropulse structures of the optical beam are essentially the same as those of the electron beam and are illustrated in Fig. 1.2. In the absence of any mechanism to couple successive optical pulses, the latter build up independently from noise and the spectral modes are separated by the $\frac{c}{2L}$ round trip frequency. These optical pulses have durations of several picoseconds and peak output powers of several megaWatts, from

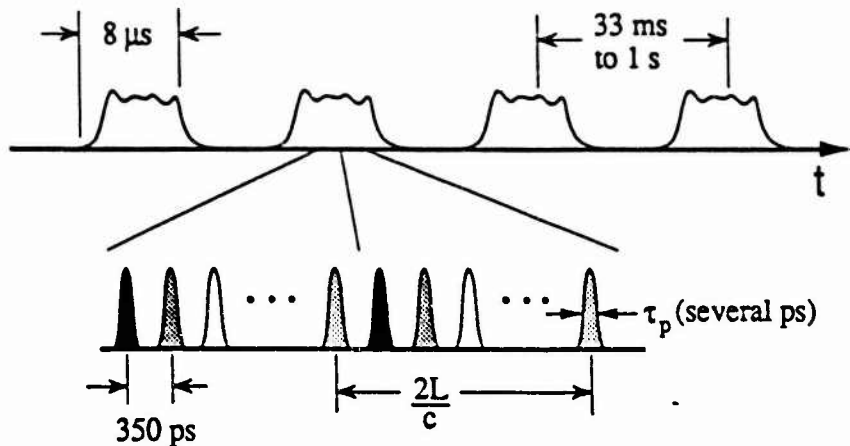


Fig. 1.2 Temporal structure of the optical beam from the Mark III FEL.

which all of the pulse energy (several microJoules) is available for external pulse compression in the chirped-pulse mode. The optical cavity is constructed of metal mirrors, and Brewster plate output coupling appropriate to the horizontally polarized radiation, to exploit the full tuning range of the laser.

III. HIGH RESOLUTION ENHANCEMENTS

The chirped-pulse FEL uses electron pulses with a linear temporal energy dependence to drive the formation of optical pulses with a linear temporal frequency dependence.¹ Electron pulses with such an energy dependence can be produced in an rf linac by accelerating the pulses off the peak of the rf wave at phases where the field gradient is large [10]. Conceptually, the easiest way to visualize the chirped-pulse FEL is to imagine an electron pulse consisting of a continuous succession of much smaller electron pulses, each possessing its own discrete energy. In the description of the FEL interaction as the stimulated scattering of virtual photons from the wiggler field into real photons in the laser field [18], each small section of the electron pulse will scatter photons of different frequencies, because the photon frequency varies as the square of the electron energy [17]. This conceptual picture is illustrated in Fig. 1.3. In principle, the chirped-pulse FEL can operate at any wavelength to which the laser can be tuned.

Moore was the first to propose the concept of energy chirping in an rf linac-driven FEL [10], and suggested that negatively chirped electron pulses (in which the energy decreases towards the trailing edge) would increase the extraction efficiency in an analogous

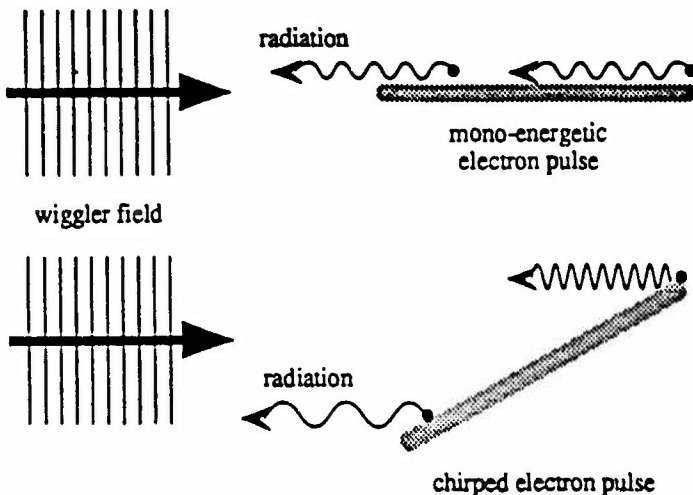


Fig. 1.3 Energy chirping in a free-electron laser.

¹ The laser frequency actually varies as the square of the electron energy. However, a linear temporal approximation is valid for the short pulses considered in the present study.

manner to the tapered wiggler FEL [19]. He developed a theoretical description of such a device in the highly saturated, large signal regime, and derived [10] and applied [11] the appropriate equations of motion in a simulation code to study the behavior of the laser from spontaneous radiation to full saturation. Although enhanced efficiencies were observed in some instances, they were not in accord with the theoretical predictions. At the time of this writing, the operation of a chirped-pulse FEL for the purpose of high energy extraction or external pulse compression has not been reported. Hartemann et al [20] do describe the operation of an FEL amplifier at 10 GHz (30 mm) in which a frequency chirped microwave pulse was actively compressed in the interaction region. However, that scheme was entirely different from the one proposed by Moore; the electron energy was not chirped, and pulse narrowing was achieved only via the amplification of those microwave frequency components that were resonant with the FEL interaction. Therefore, the scheme is more appropriately described as a selective amplification (in which most of the input pulse energy does not appear in the short output pulse), rather than as a true pulse compression (where all of the energy in a chirped output pulse is compressed in an external dispersive delay line).

The phase locked FEL is actually a variation on an old theme. In such an FEL, an intracavity interferometer is used to couple successive optical pulses so that they build up from noise with a definite phase relationship. The most convenient configurations employ multiple mirror resonators such as the Michelson mirror resonator [21] (studied in this dissertation) or the Fox-Smith resonator [22]. However, other schemes have also been proposed, such as multiple intracavity diffraction gratings [13] in which the various diffraction orders undergo different round trip delays with respect to the incoming electron pulses.

The use of an intracavity interferometer for phase locking is most easily understood in the frequency domain. To clarify the picture, we first distinguish between supermodes and hypermodes. *Supermodes* are self-similar sets of longitudinal laser modes that repeat identically from pass to pass, allowing multiplication by a complex constant; the Fourier transform of the dominant supermode yields the shape of the stable circulating optical pulse. *Hypermodes* are sets of longitudinal laser modes that are coupled together by the action of an intracavity loss or gain modulation; if the modulation frequency is some integral multiple N of the round trip frequency (the so-called harmonic mode locking [23]), then every N^{th} mode will be coupled together, and there will be N circulating optical pulses per round trip. For example, $N = 35$ in the Mark III FEL. In the absence of any coupling between the hypermodes, which is the case for the linear, small signal regime of the FEL, each hypermode will evolve independently and will possess its own complete set of supermodes.

Intracavity interferometers can be used to filter individual supermodes and increase the duration of the corresponding optical pulses. This application is illustrated in Fig. 1.4(a)

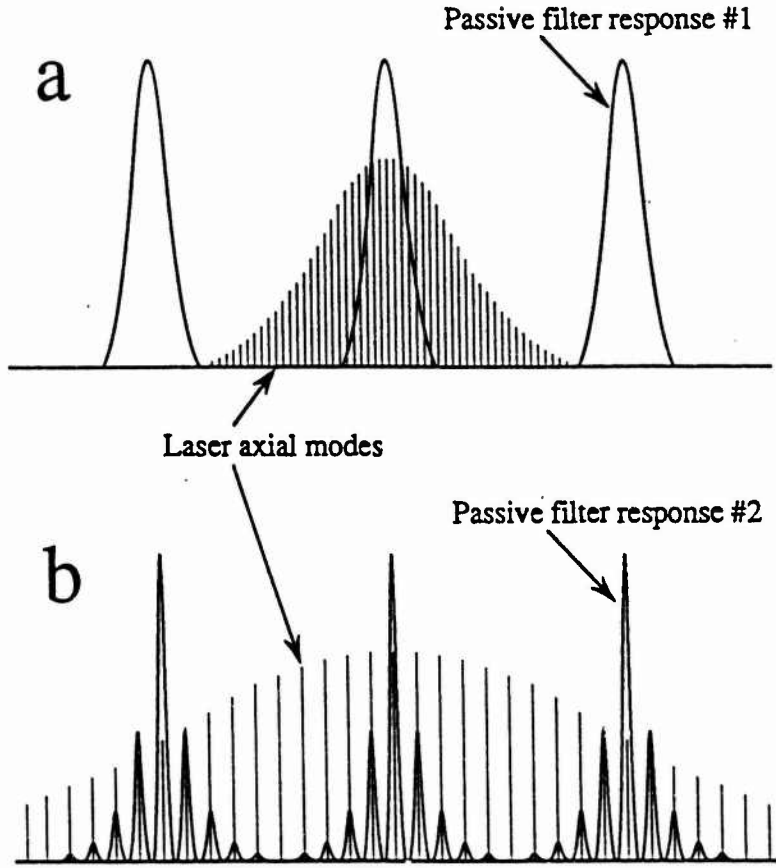


Fig. 1.4 Intracavity filtering of laser longitudinal modes: (a) filtering of individual supermodes; (b) filtering of individual hypermodes.

and has been employed in storage ring FELs [24]. For line selection in cw lasers, the narrow axial modes of a multiple mirror resonator can in some cases be used to select a single laser mode in the gain spectrum and suppress all the others, thereby achieving single mode operation. This application is more conventional and is described in several review articles [25]. In phase locking applications, the narrow axial modes of the multiple mirror resonator do not select a single laser mode, but they do filter a given *hypermode*. The filter can be tuned so that the stable supermode is unaffected by the interferometer, but in the presence of homogeneous laser saturation only a single hypermode will dominate the laser spectrum. This application is illustrated in Fig. 1.4(b), and yields a train of phase locked optical pulses, i.e. pulses possessing identical envelopes and phases, separated by the modulation period.

The history of mode selection and modulation using passive intracavity filters is as old as laser literature. However, the application of multiple mirror resonators for the selection of individual hypermodes in an harmonically mode locked laser appears to be novel, and particular to the rf linac-driven FEL. The reason for this is most likely due to

the fact that, while harmonic mode locking has been demonstrated in conventional lasers using active intracavity modulation [26], harmonic numbers were usually relatively small ($N < 5$). Therefore, no great advantage in terms of mode separation would be obtained from hypermode suppression. On the other hand, rf linacs typically operate at several GHz, and due to engineering constraints most rf linac-driven FELs can only operate with harmonic numbers at least on the order of several tens. Consequently, a considerable advantage in terms of mode separation can be obtained from hypermode suppression. The idea for phase locking appears to have surfaced at several FEL laboratories independently [13]-[15]. However, the present dissertation contains the only complete theoretical description of the operation of such devices known to the author, and also describes the first operation of a phase locked FEL.

IV. FEL SPECTROSCOPY

A summary of potential applications of the chirped-pulse and phase locked FELs would span the entire field of infrared spectroscopy, and the limited space in this Introduction precludes any attempt to present such a summary. However, these devices do possess several unique properties which should be noted.

As previously observed, a stable infrared source with femtosecond time resolution or ultrahigh spectral resolution would greatly extend the research capabilities in infrared spectroscopy. The main advantages of the proposed FEL enhancements over conventional infrared sources are that they do not rely on nonlinear optical processes in crystals (so that they can be very stable), and they can be implemented at any wavelength to which the FEL can be continuously tuned. They are also intrinsically of very high power: compressed optical pulses at $3.35 \mu\text{m}$ with durations of 220 fs and peak powers of 30 MW are feasible, and a single mode from a $4 \mu\text{s}$, 60 mJ mactropulse of phase locked, 3.5 ps optical pulses would yield 150 W of cw power. The spectral resolution of one of these modes is in principle limited only by the duration of the mactropulse; a $4 \mu\text{s}$ macropulse at $3 \mu\text{m}$ would yield a fractional linewidth of $\Delta\lambda/\lambda \sim 10^{-9}$.

An important and unique property of chirped-pulse and phase locked FELs, which evidently has not been previously considered in any other device, is the potential capability to implement both of these enhancements *simultaneously*. This does not violate the Fourier uncertainty principle; each of the fast-time and high spectral resolution components, while present in the same optical beam, would necessarily act on different properties of the physical system under study. In such a configuration, it may be possible to study the competing effects of induced fast dynamical processes, such as collisional energy transfer from selected excited states, on the narrow spectral features of long-lived atomic or molecular states.

For example, it may be possible to use the ultrafast pulses to pump excited vibrational states and to simultaneously use the filtered beam to probe the collisional energy transfer to selected rotational states.

Further applications of high resolution optical beams include experiments in high power, high resolution, Doppler-free, coherent two-photon spectroscopy. If ω is the frequency of the centermost mode coincident with the sample response curve, then that mode plus each pair of surrounding modes all contribute a high resolution two-photon excitation of 2ω . All of the macropulse power could then be utilized to excite the sample response.

V. OUTLINE OF THE DISSERTATION

This dissertation is organized into two Parts. Part I is concerned with the chirped-pulse FEL and is comprised of Chapters 2 and 3 and Appendix A. Chapter 2 describes the small signal theory of the chirped-pulse FEL and the pulse propagation code used in the numerical simulations, and Chapter 3 describes the results of those simulations. Appendix A describes the design of a pulse compression experiment on the Mark III FEL based on the simulation results from Chapter 3.

Part II is concerned with the Michelson resonator FEL and is comprised of Chapters 4 through 6 and Appendix B. Chapter 4 contains a theoretical and numerical description of the passive mode structure and mode decay in a Michelson resonator FEL, and Chapter 5 contains a theoretical and numerical description of the supermode structure and mirror detuning effects. Chapter 6 describes the first operation of a Michelson mirror resonator on the Mark III FEL, and Appendix B presents a more appropriate design of the resonator and diagnostics for applications in high resolution spectroscopy.

Finally, Chapter 7 presents some conclusions and summarizes the important results from this dissertation.

VI. REFERENCES

- [1] S. V. Benson, J. M. J. Madey, J. Schultz, M. Marc, W. Wadensweiler, and G. A. Westenskow, "The Stanford Mark III Infrared Free-Electron Laser," *Nucl. Instr. and Meth.*, vol. A250, p. 39, 1986.
- [2] S. V. Benson, J. Schultz, B. A. Hooper, R. Crane, and J. M. J. Madey, "Status Report on the Stanford Mark III Infrared Free-Electron Laser," *Nucl. Instr. and Meth.*, vol. A272, pp. 22-28, 1987.
- [3] S. V. Benson, W. S. Fann, B. A. Hooper, J. M. J. Madey, E. B. Szarmes, B. Richman, and L. Vintro, "A review of the Stanford Mark III infrared FEL program," *Nucl. Instr. and Meth.*, vol. A296, pp. 110-114, 1990.
- [4] N. J. Tro, D. A. Arthur, and S. M. George, "Infrared free-electron laser as a probe of vibrational dynamics on surfaces," *J. Opt. Soc. Am. B*, vol. 6, pp. 995-1002, 1989.
- [5] J. Ristein, B. Hooper, and P. C. Taylor, "Excitation spectroscopy of thin-film amorphous

- semiconductors using a free-electron laser," *J. Opt. Soc. Am. B*, vol. 6, pp. 1003-1007, 1989.
- [6] W. S. Fann, S. Benson, J. M. J. Madey, S. Etemad, G. L. Baker, and F. Kajzar, "Spectrum of $\chi^{(3)}(-3\omega; \omega, \omega, \omega)$ in Polydiacetylene: An Application of the Free-Electron Laser in Nonlinear Optical Spectroscopy," *Phys. Rev. Lett.*, vol. 62, pp. 1492-1495, 1989.
- [7] W. S. Fann, L. Rothberg, M. Roberson, S. Benson, J. M. J. Madey, S. Etemad, and R. H. Austin, "Dynamical Test of Davydov-like Solitons in Acetanilide Using a Picosecond Free-Electron Laser," *Phys. Rev. Lett.*, vol. 64, p. 607, 1990.
- [8] D. D. Dlott and M. D. Fayer, "Applications of Infrared Free-Electron Lasers: Basic Research on the Dynamics of Molecular Systems," *IEEE J. Quantum Electron.*, vol. 27, pp. 2697-2713, 1991.
- [9] P. F. Bernath, "High resolution infrared spectroscopy of transient molecules," *Annu. Rev. Phys. Chem.*, vol. 41, pp. 91-122, 1990.
- [10] G. T. Moore, "The Chirped-Pulse Free Electron Laser," *Nucl. Instr. and Meth.*, vol. A272, pp. 302-310, 1988; G. T. Moore, "Frequency Chirping of the Free-Electron Laser," *Phys. Rev. Lett.*, vol. 60, pp. 1825-1827, 1988.
- [11] G. T. Moore and J. C. Goldstein, "Chirping for Efficiency Enhancement of the Free Electron Laser," *Nucl. Instr. and Meth.*, vol. A285, pp. 176-185, 1989.
- [12] E. B. Szarmes, S. V. Benson, and J. M. J. Madey, "Pulse compression on the Mark III FEL using energy chirping," *Nucl. Instr. and Meth.*, vol. A296, pp. 755-761, 1990.
- [13] G. R. Edlin, R. W. Jones, and J. F. Perkins, "Phase locked rf linac free electron laser," U. S. Patent No. 4,748,629, May 31, 1988.
- [14] D. Oepts, A. F. G. van der Meer, R. W. B. Best, P. W. van Amersfoot, and W. B. Colson, "Simulations of mode reduction with an intracavity etalon in an rf-linac based FEL," *Nucl. Instr. and Meth.*, vol. A285, pp. 204-210, 1989.
- [15] E. B. Szarmes, S. V. Benson, and J. M. J. Madey, "Mode control on short-pulse FELs using a Michelson-mirror resonator," *Nucl. Instr. and Meth.*, vol. A296, pp. 98-109, 1990.
- [16] See, for example, *Free-Electron Lasers '91: Proceedings of the 13th International FEL Conference*, Santa Fe, NM, to be published in *Nucl. Instr. and Meth.*
- [17] Excellent reviews of FEL theory are given in C. A. Brau, *Free-Electron Lasers*, Boston, MA: Academic Press, 1990; and in W. B. Colson, "Classical free electron laser theory," in *Laser Handbook, Volume 6*. Amsterdam: North-Holland, 1990, ch. 5.
- [18] J. M. J. Madey, "Stimulated Emission of Bremsstrahlung in a Periodic Magnetic Field," *J. Appl. Phys.*, vol. 42, pp. 1906-1913, 1971.
- [19] N. M. Kroll, P. L. Morton, and M. N. Rosenbluth, "Free-Electron Lasers with Variable Parameter Wigglers," *IEEE J. Quantum Electron.*, vol. QE-17, pp. 1436-1468, 1981.
- [20] F. Hartemann, K. Xu, and G. Bekefi, "Pulse compression in a free electron laser amplifier," *Nucl. Instr. and Meth.*, vol. A272, pp. 125-128, 1988.
- [21] K. Kantor, A. Kiss, and T. Salamon, "Michelson interferometer used as a tunable mirror in laser resonators," *Sov. Phys. JETP*, vol. 26, pp. 221-222, 1967.
- [22] P. W. Smith, "Stabilized, Single-Frequency Output from a Long Laser Cavity," *IEEE J. Quantum Electron.*, vol. QE-1, pp. 343-348, 1965.
- [23] A. E. Siegman, *Lasers*, Mill Valley, CA: University Science Books, 1986.
- [24] P. Elleaume, "Microtemporal and spectral structure of storage ring free-electron lasers," *IEEE J. Quantum Electron.*, vol. QE-21, pp. 1012-1022, 1985.
- [25] See, for example, P. W. Smith, "Mode Selection in Lasers," *Proc. IEEE*, vol. 60, pp. 422-440, 1972.
- [26] M. F. Becker, D. J. Kuizenga, and A. E. Siegman, "Harmonic mode locking of the Nd:YAG laser," *IEEE J. Quantum Electron.*, vol. QE-8, pp. 687-693, 1972.

Chapter 2

The chirped-pulse free-electron laser

The generation of optical radiation in a free-electron laser (FEL) can be considered as the stimulated scattering of a spatially periodic, coherent magnetic field (the wiggler field) by a beam of ultra-relativistic electrons [1]. The laser builds up from spontaneous radiation with a wavelength λ determined primarily by the Doppler upshift condition [2]

$$\lambda = \frac{\lambda_w}{2\gamma^2} \left[1 + \left(\frac{e \hat{B} \lambda_w}{2\pi m c^2} \right)^2 \right] \equiv \frac{\lambda_w}{2\gamma^2} [1 + \hat{K}^2] \quad (2.1)$$

where λ_w is the period of the magnetic field, \hat{B} is the rms magnetic field strength, e is the electron charge (cgs units), and $\gamma m c^2$ is the electron energy. To maintain resonance with the electrons, the optical field must slip ahead of the electrons by one optical wavelength as the electrons traverse one period of the wiggler magnet [3]. Therefore, in the stimulated emission process, the interaction of the light with the electrons occurs only within a slippage distance equal to N_w times the optical wavelength, where N_w is the number of wiggler periods. For electron pulses which are much longer than the slippage distance, it is possible to have radiation generated by one section of the electron pulse that never communicates with the electrons far ahead in the pulse; in principle, such electrons can even possess different energies, and generate different optical wavelengths as determined by the Doppler upshift (or resonance) condition (2.1).

The chirped-pulse FEL has been proposed as a means to increase the extraction efficiency of untapered, rf linac-driven FELs via the production of highly chirped, coherent

optical pulses [4], [5]. In such an FEL, the injected electron energy varies linearly with position within the micropulse, and the resulting optical pulses exhibit a linear frequency chirp of the same sign. An enhanced extraction efficiency is predicted for electron micro-pulses in which the energy decreases towards the trailing edge, because electrons trapped in the ponderomotive potential wells are slowed down as they slip behind the optical field and experience a continuous and adiabatic decrease in the optical frequency. Such an energy extraction mechanism is analogous to the operation of a tapered wiggler FEL [6], in which electrons trapped in the ponderomotive potential wells are slowed down by an adiabatic decrease of the wiggler parameter \hat{K} , or alternately the wiggler period λ_w , as they traverse the undulator.

Apart from the predicted capability to increase the extraction efficiency, the chirped-pulse FEL delivers chirped optical pulses which are susceptible to pulse compression in an external dispersive delay line, in contrast to the tapered wiggler FEL. As a means of producing highly chirped output pulses, the FEL does not suffer from the material constraints encountered with fiber techniques, such as optical damage, nonlinear scattering losses, or limited dispersion [7]. The chirped-pulse FEL can operate at almost any wavelength to which the laser can be tuned, and can yield optical chirps of either sign with a magnitude determined by the phase offset of the electron micropulses in the rf linac [4].

A simple calculation shows that substantial compression ratios can be expected even with modest energy chirps. For example, consider a 4 ps electron pulse with a full width energy chirp of $\delta\gamma/\gamma = + 2 \%$, with energies increasing towards the trailing edge. If we assume that the optical pulse at saturation is of the same duration, and that the FEL resonance condition (2.1) determines the lasing frequency at all points along the pulse, then the corresponding linear frequency chirp is $\delta\omega/\omega = 2 \delta\gamma/\gamma = + 4 \%$. This pulse can be compressed by a factor roughly equal to the ratio of the bandwidth of the chirped pulse to the bandwidth of an unchirped pulse of the same duration [8]. If the mean wavelength is 3 μm , then this ratio is approximately $(0.04) \cdot (2\pi c / 3 \mu\text{m}) / (2\pi / 4 \text{ ps}) = 16$, so that the 4 ps pulse should be compressible to roughly 250 fs. At 3 μm , this is only 25 optical cycles. In principle, much larger energy chirps than 2 % should be feasible in some rf linac systems.

In this chapter, I derive some analytical results concerning the FEL interaction in the presence of chirped electron pulses, such as the gain reduction and the shift in the gain curve, and I describe the numerical simulations used to model the optical pulse formation. In the following chapter, I present the results of these numerical simulations with particular emphasis on designing a feasible pulse compression experiment on the Mark III FEL, and in Appendix A, I describe the design of such an experiment using a dispersive delay line consisting of four minimum deviation, Brewster angle sapphire prisms.

II. FEL PULSE PROPAGATION

The interaction between the electrons and optical wave in a planar undulator is described self consistently by the dimensionless Maxwell-Lorentz equations of motion, which for CW electron and optical beams are usually written without regard to microtemporal position as [9]

$$\frac{dv(\tau)}{d\tau} = |a(\tau)| \cos(\xi(\tau) + \vartheta(\tau)) \quad , \quad (2.2)$$

$$\frac{da(\tau)}{d\tau} = -r \langle \exp(-i\xi(\tau)) \rangle_{\xi_0} \quad , \quad (2.3)$$

where $\tau = ct / L$ is the dimensionless time, $\xi(\tau(t)) = (k + k_w)z(t) - \omega t$ is the phase of the electron in the ponderomotive potential, $v(\tau(t)) = d\xi(\tau)/d\tau = L[(k + k_w)\beta_z(t) - k]$ is the phase velocity or energy detuning parameter,

$$a(\tau(t)) = \frac{4\pi N_w^2 e \hat{K} (J_0 - J_1) \lambda_w}{\gamma^2 mc^2} \hat{E}(\tau(t)) e^{i\vartheta(\tau(t))} \quad (2.4)$$

is the dimensionless form of the slowly varying part of the (plane-wave) optical electric field $E(z,t) = \sqrt{2} \hat{E}(\tau(t)) \exp[i(kz - \omega t + \vartheta(\tau(t)))]$ (^ indicating rms values), and

$$r = \frac{8\pi^2 e^2}{mc^2} \left(\frac{L_w}{\gamma} \right)^3 \frac{\hat{K}^2}{\lambda_w} (J_0 - J_1)^2 n_e \quad (2.5)$$

is the dimensionless current density. The parameters appearing in these quantities are defined in Table 2.1 (Section V). Equation (2.2) is the pendulum equation describing the phase space evolution of the electrons in the presence of the optical wave. Equation (2.3) is the reduced wave equation written in the slowly varying envelope approximation, and is driven by transverse electron currents averaged over initial phases $\xi_0 = \xi(0)$; in the present analysis we assume an *instantaneously* mono-energetic electron beam, for which a further average over initial energy detunings $v_0 = v(0)$ is excluded. For a constant value of r characterizing a continuous electron beam, the quantities $\xi(\tau)$, $v(\tau)$, and $a(\tau)$ are functions only of the time τ since the entrance to the undulator.

If the electron beam possesses non-CW properties (for example, if it consists of short pulses or chirped energies), then the above equations, which remain valid on a microscopic scale, must be modified to include the global evolution of the microbunches due to slippage between the electron and optical pulses. This is accomplished by introducing an extra variable dependence on the microtemporal position $\tilde{z} = z - ct$ for each of the quantities $a = a(\tilde{z}, \tau)$, $\xi = \xi(\tilde{z}, \tau)$, $v = v(\tilde{z}, \tau)$, $r = r(\tilde{z})$, and including the slippage s explicitly as follows [9]:

$$\frac{\partial v(\tilde{z}, \tau)}{\partial \tau} = \frac{\partial^2 \xi(\tilde{z}, \tau)}{\partial \tau^2} = |a(\tilde{z} - s\tau, \tau)| \cos(\xi(\tilde{z}, \tau) + \vartheta(\tilde{z} - s\tau, \tau)) , \quad (2.6)$$

$$\frac{\partial a(\tilde{z}, \tau)}{\partial \tau} = -r(\tilde{z} + s\tau) \langle \exp(-i\xi(\tilde{z} + s\tau, \tau)) \rangle_{\xi_0} . \quad (2.7)$$

Here, $s = N_w \lambda$ is the slippage between the optical and electron pulses which obtains as τ varies from 0 to 1 along the undulator. It is important to keep in mind that \tilde{z} and τ are independent variables, and that \tilde{z} refers to a position in the optical pulse at which the optical wave appears stationary for all τ . The same is true of the electron beam quantities.

Equations (2.6,7) may be reduced to a single integral equation for the optical pulse evolution by eliminating the electron beam quantities. Integrating (2.6) twice and expanding to lowest order in the optical field $|a|$ (the small signal regime) yields

$$\xi(\tilde{z}, \tau) = \xi_0 + v_0(\tilde{z})\tau + \int_0^\tau dp \int_0^p dq |a(\tilde{z} - sq, q)| \cos(\xi_0 + v_0(\tilde{z})q + \vartheta(\tilde{z} - sq, q)) + O(|a|^2) . \quad (2.8)$$

Upon evaluating $\xi(\tilde{z}, \tau)$ at $\tilde{z} \rightarrow \tilde{z} + s\tau$, substituting into (2.7), and averaging over initial electron phases $\xi_0 \in [0, 2\pi]$ in the lowest order terms in $|a|$, we obtain after some algebra

$$\frac{\partial a(\tilde{z}, \tau)}{\partial \tau} = \frac{i r(\tilde{z} + s\tau)}{2} \int_0^\tau dp \int_0^p dq a(\tilde{z} + s(\tau-q), q) \exp(-iv_0(\tilde{z} + s\tau)(\tau-q)) . \quad (2.9)$$

A final integration then yields

$$a(\tilde{z}, \tau) = a(\tilde{z}, 0) + \frac{i}{2} \int_0^\tau d\tau' r(\tilde{z} + s\tau') \int_0^{\tau'} dq (\tau' - q) a(\tilde{z} + s(\tau' - q), q) \exp(-iv_0(\tilde{z} + s\tau')(\tau' - q)) \quad (2.10)$$

where one of the integrals has been evaluated explicitly upon changing the order of the innermost integrations. The surviving dependence of v_0 on $\tilde{z} + s\tau'$ allows for the possibility that the electron beam may possess chirped energies, in which case the resonance parameter will change as the optical pulse slips over the electron pulse in one pass through the wiggler.

III. GAIN SHIFT AND GAIN REDUCTION IN THE CHIRPED-PULSE FEL

If the energy chirp is sufficiently small, then the small signal properties of the laser should be similar to those of the unchirped laser, except for the possibility that the spectral width of the resulting optical pulse may be much larger than the transform limit if the pulse

is very long. Specifically, the small signal gain should be unaffected by an energy chirp in which the energy changes by no more than the gain bandwidth along one slippage length. However, energy chirps much greater than this limit should yield appreciable gain reduction, because in that case the lasing electrons cannot maintain resonance with the optical field in one complete pass through the wiggler. In practical applications of the chirped-pulse FEL utilizing highly chirped pulses, it is therefore important to know the gain reduction as a function of the energy chirp.

The small signal gain is obtained by integrating (2.10) for a specific dependence of the energy detuning $v_0(\tilde{z})$ on the microscopic position within the electron beam. However, we should first clarify the difference between the *energy detuning parameter* v_0 , defined in Section II as

$$v_0 \equiv L [(k + k_w)\beta_{z,0} - k], \quad (2.11)$$

and the *resonance parameter*, which has the same form in the absence of energy chirping and assumes a value of $v_0 = 2.606$ in a CW plane-wave FEL. We note that v_0 depends on the frequency ω via $k \equiv \omega/c$, and that, in general, the frequency depends on the time derivative of the slowly varying optical phase ϑ . The difference between the energy detuning parameter and the resonance parameter is that the energy detuning does not include the derivative of the optical phase ϑ in the definition of ω ; the resonance parameter does. This distinction is important because v_0 appearing in (2.10) is the *energy detuning* (2.11), resulting from the fact that the Maxwell-Lorentz equations of motion assume an optical phase of the form $\exp[i(kz - \omega t + \vartheta)]$, in which ω is a constant carrier frequency independent of ϑ . It is this ω that appears in the definition of v_0 , and any temporal dependence of the slowly varying phase ϑ does not enter. Consequently, the \tilde{z} -dependence of v_0 comes only from the \tilde{z} -dependence of $\beta_{z,0}$ (via the chirped energy). We assume a linear energy chirp of the form

$$v_0(\tilde{z}) = v_0 + v_1 \cdot \tilde{z}, \quad (2.12)$$

so that $v_0(\tilde{z} + s\tau') = v_0 + v_1 \cdot (\tilde{z} + s\tau') = v_0(\tilde{z}) + v_1 \cdot s\tau'$, (2.13)

where v_0 is the energy detuning at $\tilde{z} = 0$ in some reference frame fixed with respect to the electron pulse. The connection between the \tilde{z} -dependences of $v_0(\tilde{z})$ and the dimensionless optical field $a(\tilde{z})$ is clarified by imagining a reference frame \tilde{z} attached to each of the electron and optical pulses; these frames are coincident at the beginning of the undulator, but at the end of the undulator the optical reference frame is shifted ahead of the electron reference frame by the slippage distance.

Upon introducing the small gain condition $a(\tilde{z} + s(\tau' - q), q) \rightarrow a(\tilde{z} + s(\tau' - q), 0)$ and substituting (2.13) into (2.10), we obtain after some variable substitutions

$$\Delta a(\tilde{z}) \equiv a(\tilde{z}, 1) - a(\tilde{z}, 0) \quad (2.14)$$

$$= \frac{i}{2s^3} \int_0^s dy \cdot y \cdot a(\tilde{z} + y) e^{-iv_0 y/s} \int_{\tilde{z}+y}^{\tilde{z}+s} dz r(z) e^{-iv_1 zy/s} \quad , \quad (2.15)$$

where v_0 is independent of \tilde{z} . In the absence of energy chirping ($v_1 = 0$), this is the same result obtained from the small gain supermode theory [10], [11]. For a chirped electron beam with constant current, we may set $r(z) = r = \text{constant}$ and integrate (2.15) to obtain

$$\Delta a(\tilde{z}) = -\frac{r}{2s^2 v_1} \int_0^s dy \cdot a(\tilde{z} + y) e^{-iv_0(\tilde{z})y/s} (e^{-iv_1 y} - e^{-iv_1 y^2/s}) \quad (2.16)$$

where we have reinserted $v_0(\tilde{z}) = v_0 + v_1 \cdot \tilde{z}$. To complete the integration, we assume a chirped optical field of the form

$$a(\tilde{z}) = a \cdot e^{i[\phi_0 \tilde{z} + \phi_1 \tilde{z}^2]} \quad , \quad (2.17)$$

in which 'a' is independent of \tilde{z} (reflecting the assumption that the FEL interaction yields the same growth at all points along the optical beam). The connection between ϕ_1 and v_1 is then established from symmetry by requiring that the initial *resonance parameter* be the same at all points along the optical beam, because it is this condition which determines the absolute optical frequency for which the FEL interaction will experience maximum gain. The energy detuning $v_0(\tilde{z})$ and the frequency detuning $\omega(\tilde{z})$ now both enter into the definition of the resonance parameter $\mu(\tilde{z})$, where

$$\omega(\tilde{z}) = -\frac{d\phi}{dt} = -\frac{d\phi}{d\tilde{z}} \frac{d\tilde{z}}{dt} = +c(\phi_0 + 2\phi_1 \tilde{z}) \quad (2.18)$$

(the last equality resulting from the variable substitution $t = -\tilde{z}/c$). For the difference in the resonance parameter between two points \tilde{z}_1 and \tilde{z}_2 ,

$$\Delta \mu \Big|_{\tilde{z}_2 - \tilde{z}_1} \equiv 4\pi N_w \frac{\Delta \gamma}{\gamma} \Big|_{\tilde{z}_2 - \tilde{z}_1} - \frac{N_w \lambda}{c} \Delta \omega \Big|_{\tilde{z}_2 - \tilde{z}_1} \equiv 0 \quad , \quad (2.19)$$

$$\text{or} \quad \Delta v_0 \Big|_{\tilde{z}_2 - \tilde{z}_1} - \frac{\lambda}{c} \Delta \omega \Big|_{\tilde{z}_2 - \tilde{z}_1} \equiv 0 \quad , \quad (2.20)$$

equations (2.18) and (2.12) then immediately yield the result

$$\phi_1 = +\frac{v_1}{2s} \quad . \quad (2.21)$$

Furthermore, we may set $\phi_0 = 0$, which merely incorporates any uniform frequency detuning implicitly into the value of v_0 . Finally, substitution into (2.16) of $a(\tilde{z})$ from (2.17) and $v_0(\tilde{z})$ from (2.12) with the above values of ϕ_0 and ϕ_1 yields the complex small signal gain

$$\frac{\Delta a(z)}{a(z)} = -\frac{i\tau}{v_1 s} \int_0^1 dx e^{-i(v_0 + \frac{v_1 s}{2})x} \sin\left[\frac{v_1 s}{2} x(x-1)\right] . \quad (2.22)$$

The maximum value of the argument of the sine function is $|v_1 s/8|$, so by introducing the small chirp condition

$$\left|\frac{v_1 s}{8}\right| \ll 1 \quad (2.23)$$

we may integrate (2.22) in closed form to yield

$$\frac{\Delta a(z)}{a(z)} = -i \frac{i\left(v_0 + \frac{v_1 s}{2}\right) \left[\exp -i\left(v_0 + \frac{v_1 s}{2}\right) + 1 \right] + 2 \left[\exp -i\left(v_0 + \frac{v_1 s}{2}\right) - 1 \right]}{2 \left(v_0 + \frac{v_1 s}{2}\right)^3} . \quad (2.24)$$

This is exactly the small signal gain for the usual (unchirped) FEL [12], except that the optimum value of the resonance parameter v_0 is shifted to

$$v_0^{\text{opt}} = 2.606 - \frac{v_1 s}{2} , \quad (2.25)$$

which is analogous to the gain shift in the tapered wiggler FEL [9], [13].

The power gain G is related to the real part of the complex gain (2.22):

$$G(\alpha, \delta) = 2 \operatorname{Re} \left\{ \frac{\Delta a(z)}{a(z)} \right\} = -2 \frac{i}{\delta} \int_0^1 dx \cdot \sin[\alpha x] \cdot \sin\left[\frac{\delta}{2} x(x-1)\right] , \quad (2.26)$$

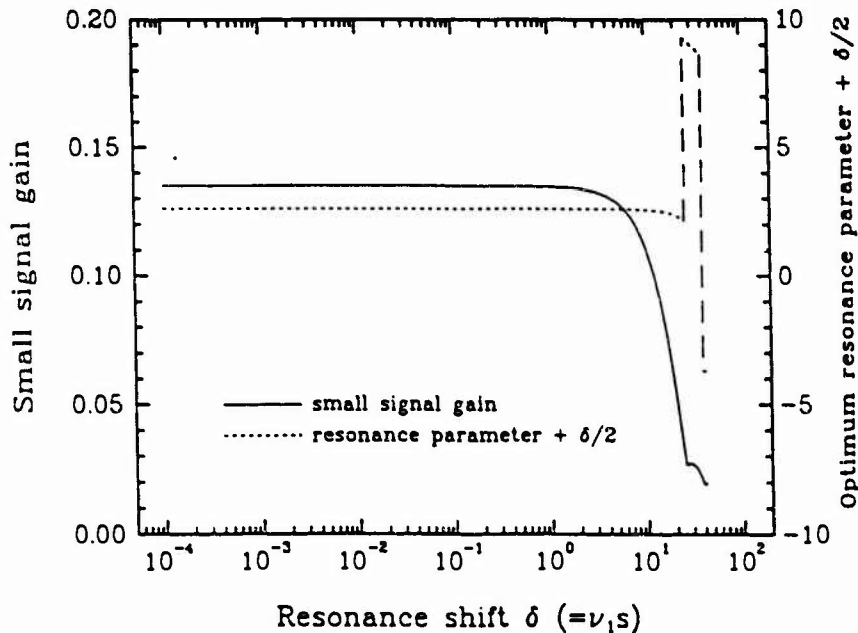


Fig. 2.1 The analytical small signal gain (assuming a plane-wave interaction), and the corresponding value of $\alpha^{\text{opt}} = v_0^{\text{opt}} + \delta/2$, for arbitrary values of the resonance shift $\delta = v_1 s$. Here, v_0^{opt} is the optimum resonance parameter at the beginning of the undulator. The current $\tau = 1$.

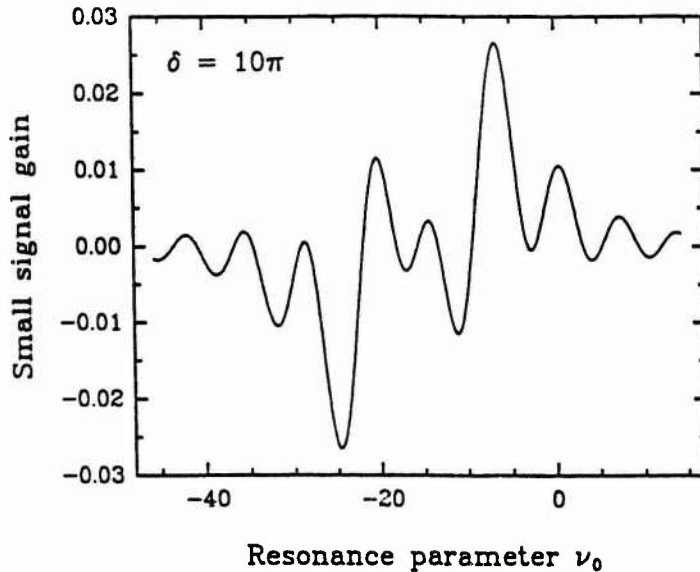


Fig. 2.2 The small signal gain as a function of ν_0 , for a resonance shift of $\delta = 10\pi$ and a current of $r = 1$.

where $\alpha = \nu_0 + \nu_1 s/2$ and $\delta = \nu_1 s$. The maximum value of G and the optimum value of α are plotted in Fig. 2.1 as functions of δ , the resonance shift along the slippage length. We note that the small signal gain drops only slightly for values of δ approaching the gain bandwidth of 2π . However, the gain drops rapidly beyond this point, and the optimum resonance parameter shifts to smaller values corresponding to shorter wavelengths at the entrance to the wiggler. The gain reduction in this regime results from the fact that resonance can be maintained only over a small fraction of the wiggler length, which reduces the effective number of wiggler periods and broadens the spectrum. The spectral distortion is accompanied by fluctuations in the gain function due to the rapid oscillation of the resonance parameter at other positions in the undulator, which fluctuations are illustrated in Fig. 2.2 for the case of $\delta = 10\pi$, and lead to the discontinuities in Fig. 2.1. Similar behavior is observed in tapered wiggler FELs [13], [14], for which the gain function has the same form as (2.26).¹ Nevertheless, in practical applications of the chirped-pulse FEL in pulse compression experiments,

¹ This is most easily seen by solving the Maxwell-Lorentz equations for the case of a tapered wiggler FEL, which take the form [9]

$$\frac{\partial v(\tilde{z}, \tau)}{\partial \tau} = \delta + |a(\tilde{z} - s\tau, \tau)| \cos(\xi(\tilde{z}, \tau) + \phi(\tilde{z} - s\tau, \tau))$$

$$\frac{\partial a(\tilde{z}, \tau)}{\partial \tau} = -r(\tilde{z} + s\tau) \langle \exp(-i\xi(\tilde{z} + s\tau, \tau)) \rangle_{v_0} .$$

The analogous equation to (2.10) is

$$a(\tilde{z}, \tau) = a(\tilde{z}, 0) + \frac{i}{2} \int_0^{\tau} dp r(\tilde{z} + sp) \int_0^p dq (p - q) a(\tilde{z} + s(p - q), q) \exp\left(-iv_0(p - q) + \frac{\delta}{2}(p^2 - q^2)\right) ,$$

which upon setting r , a , and v_0 all independent of \tilde{z} yields precisely the result (2.22) with $\delta \leftrightarrow \nu_1 s$.

it is possible to achieve extremely broad band optical pulses with energy chirps substantially smaller than the gain bandwidth divided by the slippage distance. Therefore, the problems of gain reduction and spectral distortion can be avoided in almost all cases of interest.

In deriving the above results for large energy chirps, it is necessary to justify some approximations. In particular, the dimensionless electric field 'a' and current density 'r' defined in (2.4) and (2.5) are scaled by the electron energy γ , which by assumption is a function of the microscopic position \tilde{z} within the pulse and leads to the \tilde{z} -dependence of v_0 . We have treated γ as a constant in those scaling relations. However, we are really only interested in the interaction of the electrons with the radiation inside a distance no longer than the slippage length (corresponding to a single pass through the undulator), and for the case of $N_w \gg 1$, the relation $\delta = 4\pi N_w \Delta\gamma(\tilde{z})/\gamma$ yields a large variation in the energy detuning parameter δ even for modest changes in γ over the slippage length. For the Mark III FEL with $N_w = 47$, the example of Fig. 2.2 with $\delta = 10\pi$ yields $\Delta\gamma(\tilde{z})/\gamma = 5.3\%$, which is accurately described by the dimensionless equations of motion with constant scaling. An analogous conclusion [9] holds for the tapered wiggler FEL with $N_w \gg 1$, in which case a large δ can be achieved with small variations in $\Delta\lambda_w(t)$ or $\Delta\hat{K}(t)$ along the undulator, so that the dimensionless equations with constant scaling are also appropriate.

IV. NUMERICAL SIMULATIONS OF THE CHIRPED-PULSE FEL

The equations used to model the FEL interaction are based on the Maxwell-Lorentz equations of motion for electrons responding to the multiple transverse modes of an optical resonator [15], and assume the slowly varying envelope approximation for the optical pulse. This approximation will still be valid for the frequency chirps encountered in the present simulations. The radial dependence is factored out of the equations of motion by assuming that the electrons remain on rigid sheets whose spatial and temporal features are independent of the initial phase and velocity of the electrons [16]. With this approximation, a filling factor can be calculated for each of the cavity modes to account for the transverse coupling with the electron beam. We decompose the optical field acting on the electrons as

$$E(\tilde{z}, r, t) e^{i\vartheta(\tilde{z}, r, t)} = \sum_m c_m(\tilde{z}, t) E_m(r, t) e^{i\psi_m(r, t)} \quad (2.27)$$

where $E_m(r, t)$, $\psi_m(r, t)$ are the amplitude and phase of the m^{th} normalized Gauss-Laguerre cavity mode evaluated at the electron position corresponding to radius r and time t since the entrance into the wiggler, and $c_m(\tilde{z}, t) = |c_m(\tilde{z}, t)| \exp[i\phi_m(\tilde{z}, t)]$ is the projection of the field onto the m^{th} mode which depends on both the time t and position \tilde{z} relative to the center of the optical pulse.

In terms of the dimensionless current density r and electric field a_m , defined as

$$r(\tilde{z}) = \frac{8\pi^2 e^2}{mc^2} \left(\frac{L_w}{\gamma} \right)^3 \frac{\hat{K}^2}{\lambda_w} (J_0 - J_1)^2 n_e(\tilde{z}) \quad (2.28)$$

and $a_m(\tilde{z}, t) = \frac{4\pi N_w^2 e \hat{K} (J_0 - J_1) \lambda_w}{\gamma^2 mc^2} c_m(\tilde{z}, t)$, $\quad (2.29)$

where the dimensionless time $\tau = (c/L)t$, the equations used to model the interaction can then be written as follows [17]:

$$\frac{\partial v(\tilde{z}, \tau)}{\partial \tau} = \sum_m |a_m(\tilde{z}, \tau)| R_A |f_m^*(\tau)| \cos[\xi(\tilde{z}, \tau) + \phi_m(\tilde{z}, \tau) - \arg(f_m(\tau))] \quad (2.30)$$

$$\frac{\partial \xi(\tilde{z}, \tau)}{\partial \tau} = v(\tilde{z}, \tau) \quad (2.31)$$

$$\frac{\partial a_m(\tilde{z}, \tau)}{\partial \tau} = -r(\tilde{z}) f_m(\tau) \langle \rho_{\text{micr}}(\xi_0, v_0) \exp[-i\xi(\xi_0, v_0)] \rangle_{\xi_0, v_0} \quad . \quad (2.32)$$

Equations (2.30) and (2.31) comprise the pendulum equation for the phase ξ and velocity v of the electrons. Equation (2.32) is the modified wave equation written in the slowly varying envelope approximation. The quantity $f_m(\tau)$ is a complex filling factor calculated for the m^{th} transverse mode evaluated at the electron position corresponding to time τ , and R_A is the ratio of the area of the optical mode to that of the electron beam; these filling factors are calculated from the weighted averages of the phase and amplitude of the optical modes over the radial electron distribution assuming paraboloidal charge sheets. The longitudinal charge distribution $n_e(\tilde{z})$ is taken to be a tophat pulse, but a density fluctuation ρ_{micr} is included in the wave equation to incorporate the effects of shot noise.

To integrate the equations of motion, the longitudinal electron pulse distribution is divided into several hundred bins in the \tilde{z} coordinate, each bin containing ten samples of the local electron density for which the position ξ and velocity v are allowed to evolve. For each time step $\delta\tau$ along the wiggler, the pendulum equations are integrated for each sample via a second order Runge-Kutta using the optical fields coincident with the corresponding bins at time τ , and the resulting contributions to the fields at each bin are then calculated from the wave equation. Optical pulse slippage is included in each time step by linear interpolation between the bins, and the integration continues in this fashion from pass to pass to a point usually just short of full saturation (to prevent distortion of the optical amplitude and phase by the sideband instability.) Cavity length detuning is also included on each pass by linear interpolation of the magnitude and phase between the optical bins, where the phase is

first smoothed by adding or subtracting multiples of 2π at each bin. Only the lowest order TEM₀₀ mode is included in the present simulations, consistent with the measured Strehl ratio (> 0.8) for the optical beam delivered by the Mark III FEL.² Conclusions regarding the formation of chirped optical pulses should remain generally valid, since chirping primarily affects only the longitudinal mode structure, not the transverse structure.

The number of bins in \tilde{z} is determined by the sampling rate required to accommodate the large spectral widths of the chirped optical pulses. The most sensitive diagnostic for this criterion is evidently a numerical check on the conservation of energy, which is performed by comparing the total energy gained by the optical pulse to the energy lost by all of the electron samples in the electron pulse. For simulations using the energy chirps reported in Chapter 3, it was usually necessary to at least quadruple the number of bins that were used in simulations of the unchirped laser. (In contrast, the resulting optical pulse formation, as well as any deviations from energy conservation, were insensitive to the number of electron samples *per bin* in the range of ten to forty samples.) Energy conservation was then usually satisfied to within deviations smaller than 1 or 2 %, which was typical in simulations of the unchirped laser.

To simulate the injected electron pulses, the samples within any given bin are initialized with a constant velocity v_0 and are distributed uniformly over 2π radians of optical phase ξ_0 . A constant v_0 is appropriate for the instantaneous energy spreads which occur in the Mark III FEL, for which an inhomogeneous gain reduction factor [18] is used to scale the current. Classical shot noise is included by random modulations of the sampled electron beam density according to a thermal distribution [19]. The chirped electron energies are prepared by assigning a velocity $v_0 = v_0(\tilde{z})$ which depends linearly on the position within the micropulse, and the optical pulse is then allowed to evolve under the effects of the FEL interaction, optical pulse slippage, and cavity detuning in the manner described above. No assumption is made regarding the time dependence of the optical phase; it evolves naturally from the FEL interaction as the laser turns on from noise.

Parameters which otherwise depend on the energy and wavelength are held constant along the micropulses. In particular, the scaling relations which define the current density $r(\tilde{z})$ and electric field $a_m(\tilde{z}, \tau)$ use the mean γ , and the complex filling factor $f_m(\tau)$ uses the mean λ . For full width energy chirps of $\delta\gamma/\gamma < 5\%$, the application of these approximations along the entire pulse length is consistent with the previous justification of constant scaling along one slippage length. Finally, the duration of the chirped electron pulses is assumed to remain constant along the wiggler, which approximation is accurate in the present

² Experimentally, mode selection is enforced in the Mark III FEL by the long and slender vacuum chamber which must fit in the 7 mm gap between the jaws of the wiggler magnet.

simulations to within, for example, 0.5 % for a 4 ps electron pulse with a 2 % energy chirp.³ The simulation parameters are appropriate to the Mark III FEL and are listed in Table 2.1.

V. NUMERICAL BENCH MARKS

For unchirped electron pulses, the FEL pulse propagation code has been accurately bench marked both analytically [17] and experimentally [20], [21] with respect to the longitudinal structure of the resulting optical pulses. However, the chirped-pulse code predicts novel phenomena, and it is therefore prudent to check the numerical simulations with readily calculated quantities particular to the chirped-pulse FEL. One possible candidate is the gain reduction predicted in Section III to occur for large energy chirps. Unfortunately, the finite spectral width of the numerical window in the present code limits the chirped-pulse bandwidth of the simulated optical pulses, and in order to observe any gain reduction for energy chirps much larger than the gain bandwidth divided by the slippage distance, it is necessary to limit the pulse length to the order of the slippage length. This introduces appreciable lethargy and other short-pulse supermode effects which were not included in the quasi-CW analysis of Section III, but which can also be expected to affect the small signal gain [22]. On the other hand, the gain shift predicted from (2.25) is linear in the energy chirp for *any* magnitude of chirp, and this gain shift is therefore suitable as a second candidate for bench marking the code. In contrast to the gain reduction, the gain shift should

³ It is interesting to consider more closely the description of the FEL interaction in the presence of energy chirping. As noted, a chirped electron pulse with higher energies at the trailing edge will be compressed in one transit through the wiggler; an electron pulse with lower energies at the trailing edge will be broadened. Does this mean, for example, that we have to track changes in the peak current along the wiggler? Well, consider a section of the electron pulse which is one optical wavelength long. The difference in velocity between the leading and trailing edges is

$$dv_{\parallel} = \beta_{\parallel} c d\gamma / \gamma^3 ,$$

where $d\gamma = \gamma_{\parallel}^{\text{front}} - \gamma_{\parallel}^{\text{back}}$. In one transit through the wiggler, the change in length of this small section is

$$(d\lambda)_{\text{wiggler}} = \Delta t_w \cdot dv_{\parallel} = \frac{N_w \lambda_w}{\beta_{\parallel} c} d\gamma / \gamma ,$$

where we have substituted the resonance condition $\lambda = \lambda_w / (2 \gamma_{\parallel}^2)$. Now, if the pulse has higher energies at the trailing edge, then *decreasing* wavelengths will be overtaking it as it becomes compressed; if the pulse has lower energies at the trailing edge, then *increasing* wavelengths will be overtaking it as it broadens. Indeed, it turns out that the total change in optical wavelength that slips over the pulse in one pass through the wiggler is

$$(d\lambda/\lambda)_{\text{slippage}} = 2 (d\gamma/\gamma)_{\text{per wavelength}} \cdot (N_w \text{ wavelengths}) ,$$

or $(d\lambda)_{\text{slippage}} = 2 N_w \lambda d\gamma / \gamma$, so that $(d\lambda)_{\text{slippage}} = (d\lambda)_{\text{wiggler}}$. Consequently, electrons which are distributed within one optical period at the beginning of the wiggler remain distributed within exactly one period at the end of the wiggler, and the gain can be calculated as the total energy lost by these electrons to the coincident optical wave. In our chirped-pulse simulations, we assume that the electron bins remain fixed in one pass through the wiggler, but we also assume that the optical frequency ω is fixed. Chirping is then described only by changes in the phase θ , and so the simulations remain consistent with the above picture.

Parameter	Definition	Simulation value
<i>Optical beam parameters</i>		
λ	Resonant optical wavelength	3.35 μm
γ_c	Extraneous cavity losses	7.3 %
z_R	Rayleigh range	53.23 cm
L_c	Cavity length	1.837 m
<i>Electron beam parameters</i>		
γ	Electron beam energy / mc^2	83.19
$\delta\gamma/\gamma$	Full width linear energy chirp	2 %
τ_p	Duration of tophat electron pulse	4 ps
I	Peak electron current (including gain reduction)	18.8 A
v_{rf}	RF frequency	2.857 GHz
ϵ_x	Normalized horizontal emittance ($1/e$)	$8\pi \text{ mm}\cdot\text{mrad}$
ϵ_y	Normalized vertical emittance ($1/e$)	$4\pi \text{ mm}\cdot\text{mrad}$
β_x	Horizontal focussing parameter	45 cm
<i>Wiggler parameters</i>		
N_w	Number of wiggler periods	47
L_w	Wiggler length	108.1 cm
λ_w	Wiggler period	2.3 cm
\hat{B}	RMS wiggler field	4.7 kGauss
$(J_0-J_1)^2$	Bessel function factor	0.738

Table 2.1 Mark III parameters used in the simulations of the chirped-pulse FEL.

be manifest even for long electron pulses with small energy chirps, and so it can be accurately checked with the present code.

Figure 2.3 shows the simulated optical pulse formation after 100 passes in a laser driven by electron pulses with a full width energy chirp of + 2 % over a duration of 4 ps (positive chirps indicating energies which increase towards the trailing edge.) The slippage parameter has the value $N_w\lambda/c\tau_p = 0.131$ for the parameters listed in Table 2.1. We see that the optical phase indeed exhibits the quadratic time dependence indicative of a linear frequency chirp with higher frequencies towards the trailing edge (recall that $\omega = -d\vartheta/dt$ in the present formalism.) This time dependence is quantified by fitting a least-squares polynomial of third degree to the optical phase within the FWHM region of the optical pulse, and is written

$$\vartheta_{opt}(t) = \vartheta_0 - \omega_0(t - t_0) - b(t - t_0)^2 - \sigma(t - t_0)^3 \quad (2.33)$$

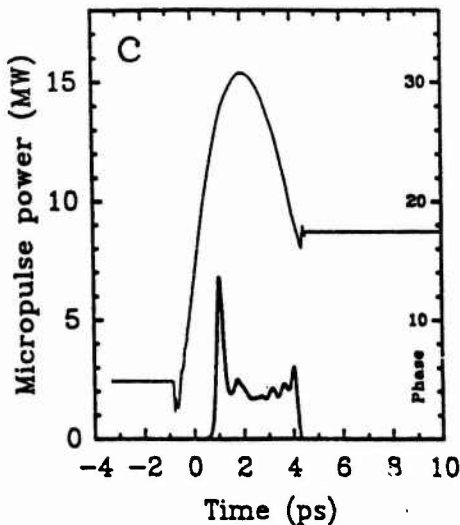


Fig. 2.3 The simulated optical envelope and phase after 100 passes in a chirped-pulse FEL, for a 4 ps tophat electron micropulse with a full width linear energy chirp of +2 %. Other simulation parameters are listed in Table 2.1.

so that

$$\omega_{\text{opt}}(t) = -\frac{d\vartheta_{\text{opt}}(t)}{dt} = \omega_0 + 2b(t - t_0) + 3\sigma(t - t_0)^2 \quad , \quad (2.34)$$

where ω_0 is the frequency at the center of the optical pulse, b is the optical chirp parameter [8], and σ is the third order fitting constant.

To benchmark the pulse propagation code, the optical pulse formation is simulated in an oscillator configuration using electron pulses with various energy chirps. The optimum value of the resonance parameter then evolves naturally from the gain interaction as the laser turns on from noise, and is determined by the temporal dependence of the optical phase after the final pass through the oscillator. These simulations are performed at the synchronous cavity length, as required by the implicit assumption in Section III that the \tilde{z} reference frames attached to each of the electron and optical pulses are coincident at the beginning of the undulator. The synchronous length is the only choice of cavity detuning that maintains this relationship between the electron and optical pulses from pass to pass. The resonance parameter μ at the beginning of the undulator is then calculated as an average along the electron pulse from the midpoint to the trailing edge (which region avoids the erosion due to lethargy at the front end of the optical pulse) according to the definition

$$\mu \equiv \left\langle v_0(\tilde{z}) \cdot \frac{N_w \lambda}{c} \omega(\tilde{z}) \right\rangle_{\tilde{z}} \quad , \quad (2.35)$$

where $v_0(\tilde{z})$ is the injected electron energy detuning and $\omega(\tilde{z})$ is calculated from (2.34) as a function of $\tilde{z}(t)$. Figure 2.4 shows the simulated resonance parameter as a function of the

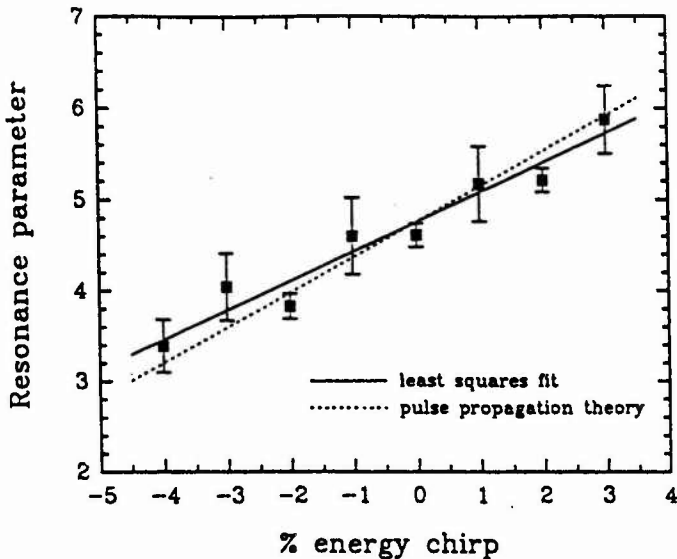


Fig. 2.4 The value of the resonance parameter yielding the maximum gain in a chirped-pulse FEL, as a function of the full width energy chirp along a 4 ps tophat electron pulse. The squares are the values calculated from the simulations, and the solid line is the corresponding least squares fit. Simulation parameters are listed in Table 2.1. The dotted line is the predicted shift from (2.25).

energy chirp, in which the dotted line is the predicted shift from eq. (2.25).⁴ The error bars at each value of the energy detuning represent the standard deviations for eight simulations in which only the numerical seed for the electron shot noise was varied. The agreement between the slopes of the numerical and theoretical curves is seen to be well within error. The resonance parameter at zero energy chirp is approximately 4.6 instead of 2.6, because the Guoy phase shift of the lowest order Gauss-Laguerre resonator mode manifests itself as an additional frequency shift to the relativistic electrons; the magnitude of the corresponding shift in the resonance parameter is roughly given by [23]

$$\Delta\mu^{\text{Guoy}} \approx + \frac{L_w}{z_R} , \quad (2.36)$$

which has a value of + 2.03 for the parameters listed in Table 2.1.

In Chapter 3, I report the results of extensive simulations of the chirped-pulse FEL using the pulse propagation code described above. Particular emphasis is placed on studying the bandwidth and stability of chirped optical pulses for the purposes of pulse compression. However, we will also find, even in moderately saturated interactions, that an enhanced extraction efficiency can be achieved with either sign of the energy chirp (in which case the

⁴ In this chapter and the next, we define positively chirped pulses to have energies which increase towards the trailing edge. Therefore, we see from (2.12) that the corresponding v_1 is negative. Conversely, v_1 is positive for negatively chirped pulses.

energy extraction mechanism is *not* related to the adiabatic deceleration of trapped electrons.) The design of a feasible pulse compression experiment on the Mark III FEL is described in Appendix A.

VI. REFERENCES

- [1] J. M. J. Madey, "Stimulated Emission of Bremsstrahlung in a Periodic Magnetic Field," *J. Appl. Phys.*, vol. 42, pp. 1906-1913, 1971.
- [2] A. Hofmann, *Theory of Synchrotron Radiation*, Stanford, CA: Stanford Synchrotron Radiation Laboratory, 1986.
- [3] W. B. Colson, *Free Electron Laser Theory*, Ph.D. Dissertation, Stanford, CA: Department of Physics, Stanford University, 1977.
- [4] G. T. Moore, "The Chirped-Pulse Free Electron Laser," *Nucl. Instr. and Meth.*, vol. A272, pp. 302-310, 1988.
- [5] G. T. Moore, "Frequency Chirping of the Free-Electron Laser," *Phys. Rev. Lett.*, vol. 60, pp. 1825-1827, 1988.
- [6] N. M. Kroll, P. L. Morton, and M. N. Rosenbluth, "Free-Electron Lasers with Variable Parameter Wigglers," *IEEE J. Quantum Electron.*, vol. QE-17, pp. 1436-1468, 1981.
- [7] See, for example, B. Wilhelmi, W. Rudolph, E. Dopel, and W. Dietel, "Advantages and limits of light pulse compression inside and outside the laser cavity," *Optica Acta*, vol. 32, pp. 1175-1189, 1985.
- [8] A. E. Siegman, *Lasers*, Mill Valley, CA: University Science Books, 1986. Chapter 9.
- [9] W. B. Colson, "Classical free electron laser theory," in *Laser Handbook, Volume 6*. Amsterdam: North-Holland, 1990, ch. 5, pp. 115-194.
- [10] G. Dattoli, A. Marino, and A. Renieri, "A multimode small signal analysis of the single pass free electron laser," *Opt. Commun.*, vol. 35, pp. 407-412, 1980.
- [11] F. T. Arecchi, J. Gea, and F. Romanelli, "A heuristic derivation of the time dependent properties of a free electron laser," *Opt. Commun.*, vol. 36, pp. 144-148, 1981.
- [12] C. A. Brau, *Free-Electron Lasers*, Boston, MA: Academic Press, 1990.
- [13] C. A. Brau, "Small signal gain of free electron lasers with nonuniform wigglers," *IEEE J. Quantum Electron.*, vol. QE-16, pp. 335-339, 1980.
- [14] P. Bosco and W. B. Colson, "Spontaneous radiation from relativistic electrons in a tapered undulator," *Phys. Rev. A*, vol. 28, pp. 319-327, 1983.
- [15] P. Elleaume and D. A. G. Deacon, "Transverse mode dynamics in a free-electron laser," *Appl. Phys. B*, vol. 33, pp. 9-16, 1984.
- [16] S. V. Benson, *Diffractive effects and noise in short pulse free-electron lasers*, Ph.D. Dissertation, Stanford, CA: Department of Physics, Stanford University, 1985.
- [17] S. V. Benson and J. M. J. Madey, "Transverse mode frequency pulling in free electron lasers," *Opt. Commun.*, vol. 56, pp. 212-218, 1985.
- [18] D. A. G. Deacon, "Inhomogeneous broadening calculation with a single integral," *HEPL Note TN-84-2*, Stanford, CA: High Energy Physics Laboratory, Stanford University, 1984.
- [19] S. V. Benson and J. M. J. Madey, "Shot and quantum noise in free electron lasers" *Nucl. Instr. and Meth.*, vol. A235, pp. 55-60, 1985.
- [20] J. F. Schultz, *Optical materials and intracavity optical devices for tunable IR free electron lasers*, Ph.D. Dissertation, Stanford, CA: Department of Physics, Stanford University, 1987.
- [21] B. A. Richman, J. M. J. Madey, and E. Szarmes, "First Observation of Spiking in the Time Domain in a Free-Electron Laser," *Phys. Rev. Lett.*, vol. 63, pp. 1682-1684, 1989.

- [22] G. Dattoli, T. Hermann, L. Mezi, and A. Torre, "A review of the theory of pulse propagation in the long bunch low gain regime," *Nucl. Instr. and Meth.*, vol. A272, pp. 351-363, 1988.
- [23] W. B. Colson and P. Elleaume, "Electron dynamics in free electron laser resonator modes," *Appl. Phys. B.*, vol. 29, pp. 101-109, 1982.

Chapter 3

Numerical simulations

The numerical simulations presented here were performed using the PIC code EPOCH [13], which is a three-dimensional, time-dependent, electromagnetic simulation code. The code uses a finite-difference spatial grid and a leap-frog time-stepping scheme. The electron motion is solved using a semi-Lagrangian method, while the optical field is solved using a finite-difference time-domain (FDTD) method. The code includes a variety of physical models, such as the Lorentz force, self-consistent electric and magnetic fields, and particle-particle interactions.

The concept of energy chirping, as an alternative to wiggler tapering, was originally proposed by Moore [1], [2] as a means of increasing the extraction efficiency of rf linac-driven FELs. In the chirped-pulse FEL, the injected electron energy varies linearly with position within the micropulse, and the resulting optical pulses exhibit a linear frequency chirp of the same sign. The theory predicts an enhanced extraction efficiency for electron micropulses in which the energy decreases towards the trailing edge, because electrons trapped in the ponderomotive potential wells are slowed down as they slip behind the optical field and experience a continuous and adiabatic decrease in the optical frequency. Of particular importance for the generation of high peak powers, it was noted by Moore that all of the extracted energy would appear in a frequency chirped optical pulse, so that even higher peak powers than determined by the saturation mechanism could be achieved by means of external pulse compression.

However, extensive simulations of the chirped-pulse FEL by Moore and Goldstein [3] showed no evidence for the predicted trapping behavior, although they did observe an enhanced extraction efficiency for some modes of operation. The authors attributed the absence of electron trapping to the cogeneration of optical sidebands within the broad spectrum of the chirped optical pulses, which sidebands tend to depopulate the ponderomotive traps. Such detrapping was previously predicted to occur in the tapered wiggler FEL [4], and an extensive literature has developed on the characterization and control of these instabilities [5]-[12]. Unfortunately, the broad band nature of the chirped-pulse FEL precludes the use of spectral filtering in that laser to control the formation of sidebands.

In this chapter, I report the results of numerical simulations on the optical pulse formation in chirped-pulse FELs using the pulse propagation code described in Chapter 2. In contrast to the goal of demonstrating enhanced extraction efficiencies, particular emphasis will be placed on studying the bandwidth and stability of chirped optical pulses, and the effects of intracavity dispersion, for the purposes of pulse compression. Nevertheless, we will find even in moderately saturated interactions that an enhanced extraction efficiency can be achieved with either sign of the energy chirp (in which case the energy extraction mechanism is not related to the adiabatic deceleration of trapped electrons.) Furthermore, we will demonstrate the presence of an intrinsic frequency chirp which occurs even in simulations of the unchirped FEL and can significantly affect the bandwidth of the optical pulses from the chirped-pulse FEL. The simulations reported in this chapter are the extension of previous investigations [13] and were chosen in part to guide the design of feasible pulse compression experiments on the Mark III FEL; the appropriate simulation parameters are listed in Chapter 2, Table 2.1. The design of the pulse compressor and optical diagnostics for an experiment using positively chirped electron and optical pulses is described in Appendix A.

II. GENERAL SIMULATION RESULTS

In this section, I present general simulation results for FELs operating with modest energy chirps, i.e. $\delta\gamma/\gamma < 5\%$ over the duration of the electron micropulses. As noted in the previous chapter, the dimensionless Maxwell-Lorentz equations of motion are appropriate for describing energy chirps of this magnitude. To properly simulate larger energy chirps, and especially large changes in the electron energy at saturation, the more general set of equations developed by Moore [2], [3] is required in which the electron energy is tracked via $\gamma(\tau)$ instead of the dimensionless energy detuning $v(\tau)$. In contrast, the present simulations are allowed to evolve only into the early stages of saturation in order to mimic actual pulse compression experiments in an FEL. Although several reasons for this restriction will be noted below, the foremost is to prevent the formation of the sideband instability from distorting the optical envelope and phase prior to compression in a dispersive delay line.

A. General features of chirped optical pulses

Figure 3.1 shows typical results for the optical pulse formation at $3.35 \mu\text{m}$ in a chirped-pulse FEL with a cavity length detuning of $+1.3 \mu\text{m}$ (shorter than synchronous) after 100 passes through the oscillator. Graphs (a), (b), and (c) display the optical envelope and phase for energy chirps of -2% (energies decreasing towards the trailing edge), 0% , and $+2\%$ respectively across a tophat electron pulse situated between 0 ps and 4 ps on the abscissa. The corresponding power spectra are shown in Fig. 3.2.

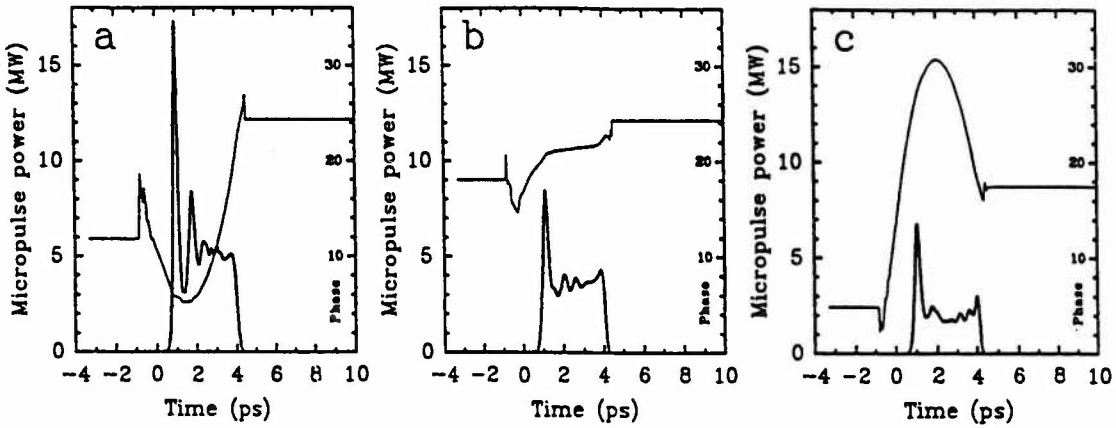


Fig. 3.1 Optical envelope and phase after 100 passes for electron pulses with a full width energy chirp of: (a) - 2 % (the corresponding optical chirp is - 3.45 % over 4 ps; the FWHM pulse width is 3.27 ps); (b) 0 % (the corresponding optical chirp is +0.10 % over 4 ps; the FWHM pulse width is 3.22 ps); (c) + 2 % (the corresponding optical chirp is + 4.60 % over 4 ps; the FWHM pulse width is 3.38 ps.) The cavity detuning is +1.3 μ m (shorter than synchronous.)

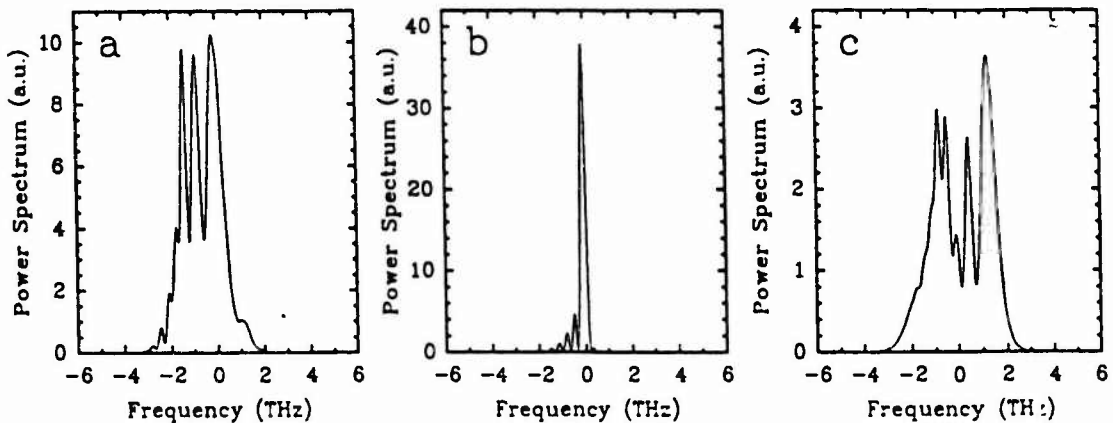


Fig. 3.2 (a) Power spectrum for the negatively chirped optical pulse in Fig. 3.1(a); (b) power spectrum for the unchirped optical pulse in Fig. 3.1(b); (c) power spectrum for the positively chirped optical pulse in Fig. 3.1(c).

We see from Fig. 3.1 that the phase of each of the chirped optical pulses exhibits the quadratic time dependence indicative of a linear frequency chirp, and that the chirped-pulse spectra from Fig. 3.2 show substantial broadening over the unchirped spectrum by more than a factor of ten. For ideal phase compensation, this ratio roughly gives the order by which the chirped optical pulses can be compressed [14]. Several other features are also immediately evident from these figures.

First, the average optical power appears to increase roughly linearly from positive chirps to negative chirps, with all other simulation parameters remaining the same; the larger power in the negatively chirped pulse has led to the onset of the sideband instability, producing spikes in the optical envelope and a slight distortion in the optical phase at the front end of the pulse. The dependence of the power on the energy chirp will be shown below to be present only for finite cavity length detunings.

Second, the optical pulses are slightly shorter than the electron pulses, even though the cavity length detuning is finite. This is due to the effect of laser lethargy [15], which for cavity detunings near the synchronous length yields a group velocity for the optical pulses which is less than that of the electron pulses, and leads to an erosion at the front end of the optical pulses. This effect has practical consequences for pulse compression experiments on the chirped-pulse FEL, because the reduced optical pulse widths yield slightly reduced bandwidths, thereby limiting the ultimate optical pulse compression ratios.

Third, we see from Fig. 3.2 that the spectrum of the positively chirped pulse is broader than that of the negatively chirped pulse, even though the energy chirps have the same magnitude (2 % over 4 ps). This discrepancy in the spectral widths is not due to differences in the pulse duration (3.27 ps vs. 3.38 ps for the negatively vs. positively chirped pulses), but is instead due to differences in the frequency chirp (-3.45 % vs. +4.60 % over 4 ps for the negatively vs. positively chirped pulses). This difference in the magnitude of the frequency chirps is manifest in *all* simulations of negatively vs. positively chirped pulses, and substantially affects the pulse compression ratio. Figure 3.3 compares the optimally

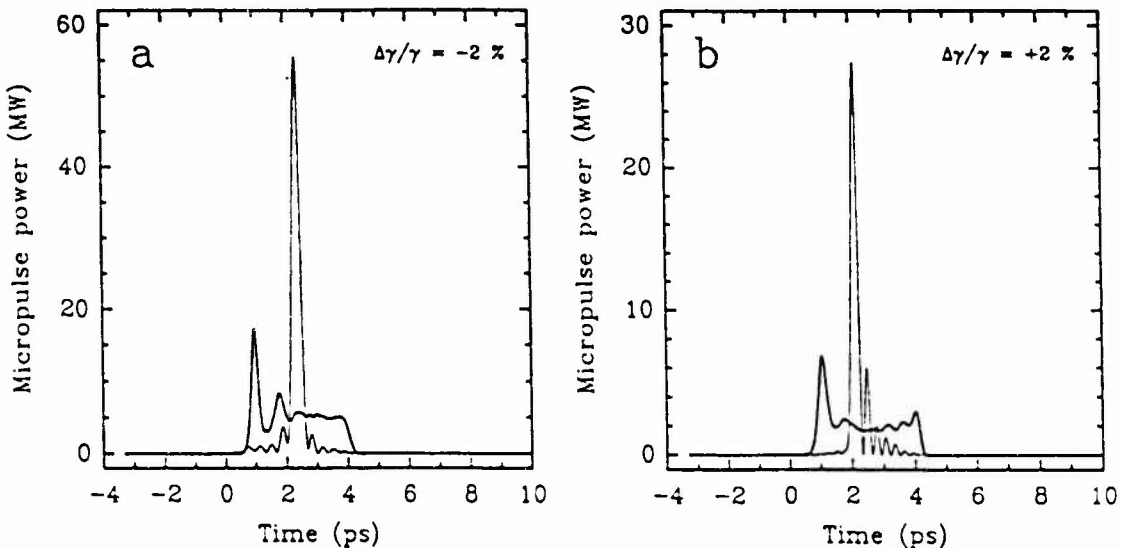


Fig. 3.3 (a) Optimum quadratic compression of the optical pulse in Fig. 3.1(a). The compressed pulse has a FWHM duration of 300 fs and a peak power of 56 MW. (b) Optimum quadratic compression of the optical pulse in Fig. 3.1(c). The compressed pulse has a FWHM duration of 230 fs and a peak power of 27 MW.

compressed pulses for each of the two cases assuming only quadratic phase compensation.¹ The positively chirped pulse can be compressed to 230 fs, compared to only 300 fs for the negatively chirped pulse (the greater peak power in the latter case is due to the larger energy content of the original optical pulse.) In the following two paragraphs, we will examine more closely the discrepancies in both the optical frequency chirps and the average optical powers for negatively and positively chirped pulses.

B. Dependence of frequency chirp on energy chirp

If one assumes that the FEL resonance condition determines the lasing wavelength at all points along the optical pulse, then for small chirps the time dependent frequency can be written in terms of the time dependent energy as

$$\frac{1}{\omega} \frac{d\omega}{dt} = \frac{2}{\gamma} \frac{d\gamma}{dt} . \quad (3.1)$$

The chirp parameter 'b' from eq. (2.34) of Chapter 2 can be written as

$$b(\lambda) = \frac{2\pi c}{\lambda} \frac{1}{\gamma} \frac{d\gamma}{dt} \quad (3.2)$$

where λ is the optical wavelength.

Figure 3.4 shows the frequency chirp $\Delta\omega/\omega$ at 3.35 μm (extrapolated to the duration of the electron pulses), as function of the electron pulse width, for full width energy chirps of +2 % and -2 %. The error bars represent the standard deviations for eight simulations in which only the numerical seed for the electron shot noise was varied. The dashed lines are the frequency chirps predicted from the resonance condition (3.1). We see that for pulse widths $\tau_p \gtrsim 2$ ps ($N_w \lambda / c \tau_p \gtrsim 0.3$), the frequency chirps exhibit a definite, positive offset which is larger in most cases than the statistical errors and range in magnitude from $\Delta\omega/\omega|_{\text{offset}} \sim 0.3\%$ to $\Delta\omega/\omega|_{\text{offset}} \sim 0.9\%$. This apparently intrinsic frequency chirp occurs even in simulations of the unchirped laser, for which the extrapolated frequency chirp

¹ Propagation through a dispersive delay line is accomplished by taking the Fourier transform of the optical electric field,

$$\tilde{E}(\omega) = \int_{-\infty}^{\infty} E(t) e^{+i\omega t} dt .$$

multiplying by a frequency dependent quadratic phase factor,

$$\exp \left[-i \frac{1}{b \cdot K} (\omega - \omega_0)^2 \right] .$$

and taking the inverse Fourier transform to obtain the compressed optical pulse. Here, b is the chirp parameter from eq. (2.34) of Chapter 2, and the parameter K is varied in order to obtain the optimum compression ratio (defined in all cases as yielding the maximum compressed peak power, not the minimum FWHM pulse duration.) The optimum value of K was usually found to be in the range of 4.3 to 4.4, and would have been almost exactly 4 for linearly chirped Gaussian pulses [14].

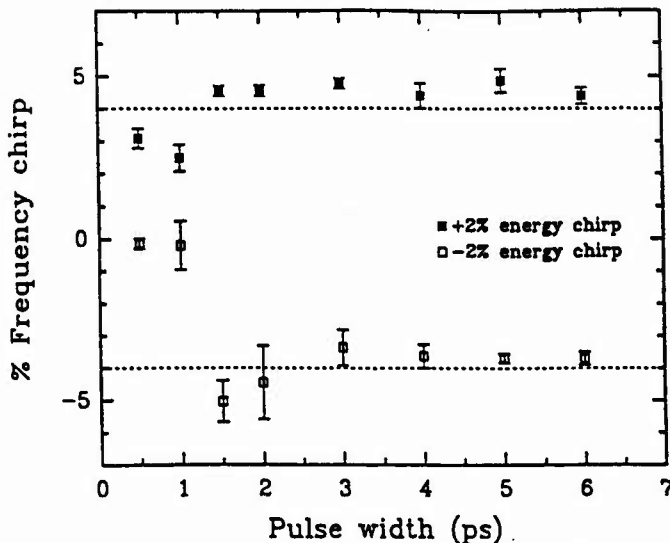


Fig. 3.4 Simulated frequency chirps, extrapolated to the electron pulse duration, as a function of the pulse width, for energy chirps of +2 % and -2 %. The error bars are the standard deviations after 100 passes for eight simulations in which only the electron shot noise was varied. The dashed lines are the chirps predicted from the resonance condition (3.1). The cavity detuning is +1 μm .

was found to be $\Delta\omega/\omega = (0.5 \pm 0.4) \%$ in a series of thirty simulations using unchirped electron pulses with a duration of 4 ps. This offset is substantial compared to the energy chirps being considered for pulse compression.

From symmetry, one can argue that for very long electron pulses (or small slippage parameters), the resonance conditions (3.1) and (3.2) would have to determine the frequency chirp at all points along the pulse. Therefore, the most likely sources of the discrepancy are the end effects accompanying pulses of finite duration. There are two such end effects that can contribute to the intrinsic frequency chirp with the observed sign.

The first contribution results from the effects of saturation and slippage, and originates from the fact that electrons at the trailing edge of the electron pulse interact with a lower average intensity in one pass through the wiggler due to optical slippage in the forward direction. The gain curve for these electrons is not shifted as far towards long wavelengths as for the electrons on the leading edge [16], yielding an optical pulse chirped towards increasing frequencies. A related effect also occurs at the leading edge of the optical pulse, which usually exhibits some erosion due to lethargy. For electrons located within one slippage distance in front of the leading edge, the effective number of wiggler periods in the laser interaction is reduced because the optical pulse does not overtake them until some distance along the undulator. This leads to an increased extraction efficiency for those electrons and the formation of a superradiant spike [17]; the corresponding enhanced degree of saturation forces the optical frequency to longer wavelengths at the leading edge. Figure 3.5 compares the simulated phase space trajectories of electrons at the leading edge, the center, and at the

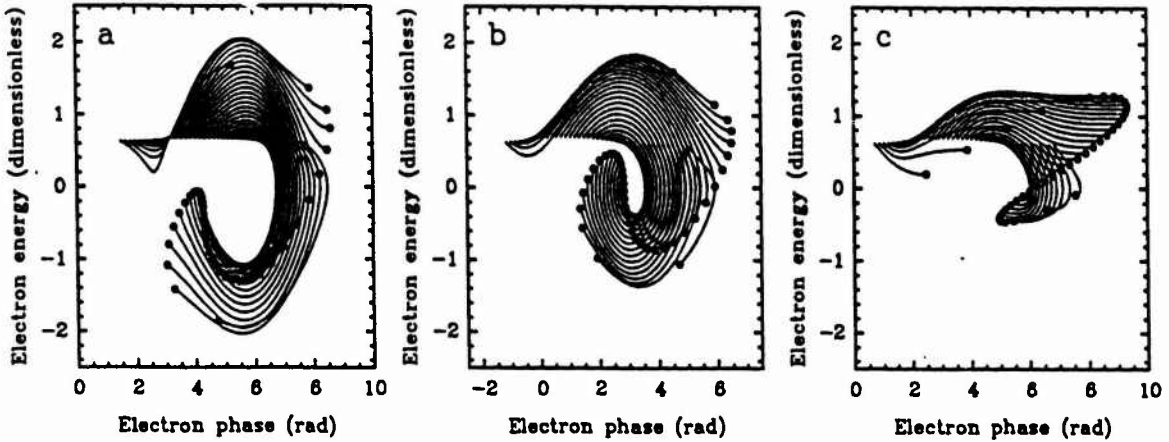


Fig. 3.5 Phase space trajectories on the 100th pass in a simulation using unchirped electron pulses with a duration of 4 ps. (a) electrons located within one half of the slippage distance in front of the optical pulse at the beginning of the undulator; (b) electrons at the center of the electron pulse; (c) electrons at the end of the electron pulse.

trailing edge of an unchirped electron pulse on the 100th pass of the optical pulse. We see that the center electrons execute more than one half of one revolution in the phase space buckets, but that the electrons at the trailing edge do not evolve as deeply into saturation. Conversely, the electrons at the leading edge execute much deeper orbits. Note that the superradiant spike is manifest in each of Figs. 3.1(a),(b),(c), and that the optical phase in the unchirped pulse exhibits a slight, overall, positive frequency chirp, especially near the ends of the optical pulse.

The second contribution to the intrinsic frequency chirp results from the Guoy phase shift of the TEM₀₀ transverse resonator mode. This phase shift is manifest as an additional frequency shift to the relativistic electrons as they traverse the undulator [18]. However, since it is also nonlinear (being related to the arctangent of the displacement along the undulator), it can lead to nonlinear frequency effects in the optical wave as the latter slips over the electrons. Figure 3.6 shows the optical phase in simulations (without noise) using unchirped electron pulses and different Rayleigh ranges in resonators set to the synchronous length. In order to eliminate any saturation effects, the optical powers were renormalized to small signal levels after every four passes. We see that the optical phase again exhibits a positive frequency chirp, and that the chirp parameter *increases* with decreasing Rayleigh range. The corresponding frequency chirps, extrapolated to a 4 ps duration, are 0.31 %, 0.36 %, and 0.44 %. These chirps are reduced for cavity lengths shorter than the synchronous length, suggesting that the nonlinear effects responsible for chirping become smeared out as the optical pulse is pushed forward from pass to pass.

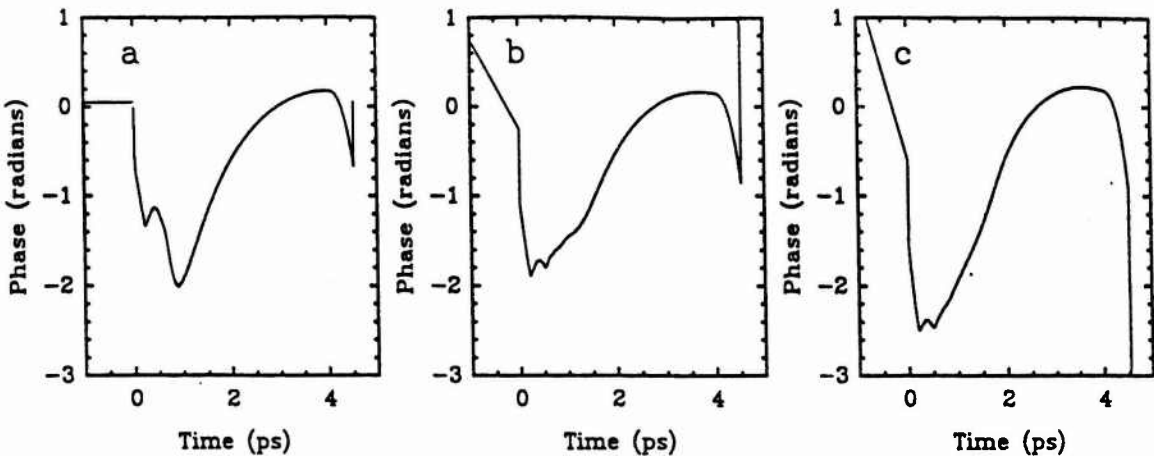


Fig. 3.6 Optical phase after 200 passes, in simulations using unchirped electron pulses with no noise. The optical powers were reset to small signal levels after every 4 passes. (a) Rayleigh range $z_R = 103.5$ cm, chirp parameter $b = 0.22(10^{24}) \text{ s}^{-2}$; (b) Rayleigh range $z_R = 73.1$ cm, chirp parameter $b = 0.25(10^{24}) \text{ s}^{-2}$; (c) Rayleigh range $z_R = 53.2$ cm, chirp parameter $b = 0.31(10^{24}) \text{ s}^{-2}$.

Finally, we should note from Fig. 3.4 that there is apparently no correlation between the frequency chirp and energy chirp for pulse widths $\tau_p \gtrsim 2$ ps. This result may be due to the onset of the superradiant interaction [17] for electron pulse lengths on the order of the slippage length, which would dominate the effects of energy chirping, or it may be due to the random effects of noise on the optical pulse formation for short pulses oscillating near the synchronous cavity length.

C. Dependence of optical power on energy chirp

In order to check the prediction by Moore of enhanced extraction efficiencies for negatively chirped pulses, I performed several series of simulations with the present code by varying the energy chirps over the 4 ps duration of the electron pulses. For each value of the energy chirp, eight simulations were performed in which only the numerical seed for the electron shot noise was varied. The results for cavity detunings of $0 \mu\text{m}$ and $+1 \mu\text{m}$ (shorter than synchronous) are summarized in Fig. 3.7.

We see that for oscillation at the synchronous length, there is no statistically significant dependence on the energy chirp in any of the small signal gain, the macropulse power prior to the onset of saturation (pass 30), or the macropulse power at saturation (pass 100). These results are not surprising; the theoretical efficiency enhancement for small chirps is simply the slippage parameter times the full width energy chirp of the pulse [1],

$$\eta = \frac{N_w \lambda}{c \tau_p} \left(\frac{\Delta \gamma}{\gamma} \right)_{\tau_p}, \quad (3.3)$$

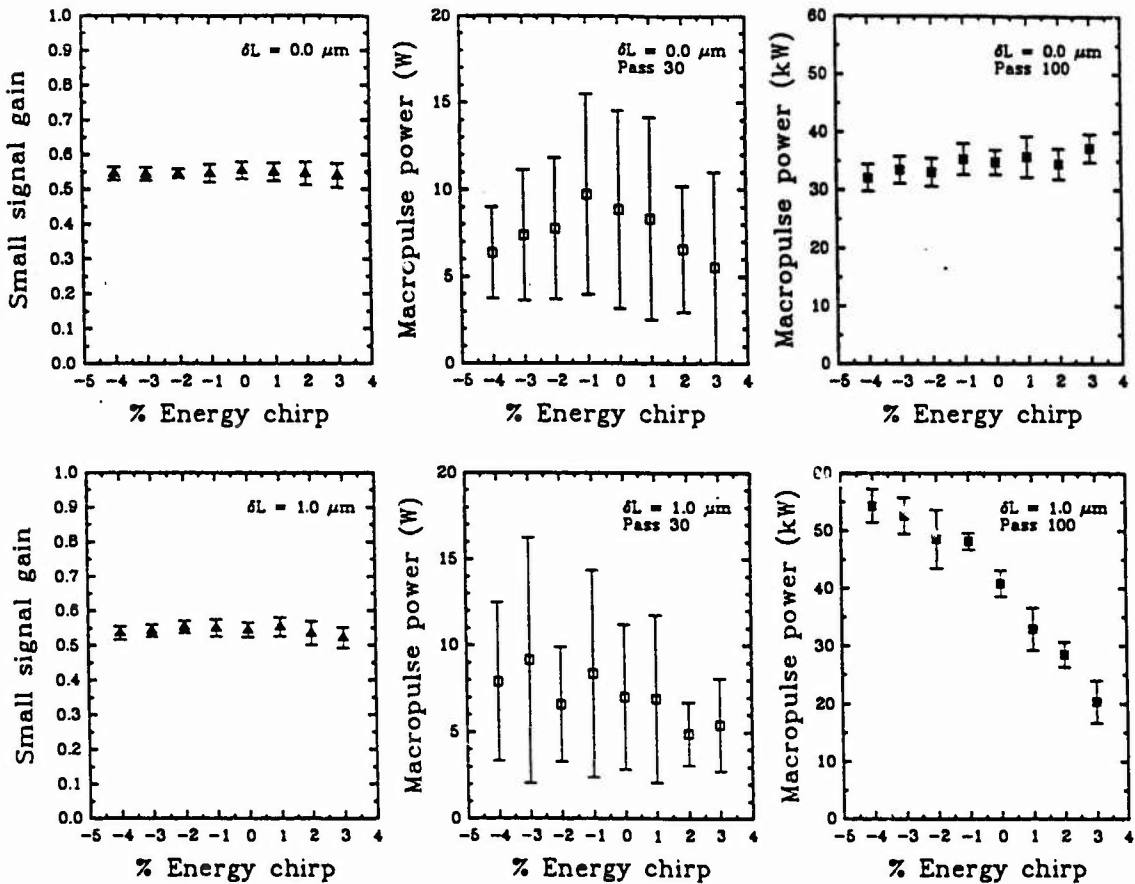


Fig. 3.7 Small signal gain, macropulse power prior to saturation, and macropulse power at saturation, as functions of the energy chirp in a 4 ps electron pulse. The upper graphs are for oscillation at the synchronous cavity length, and the lower graphs are for oscillation at a cavity detuning 1 μm shorter than synchronous. Error bars represent the standard deviations for eight simulations in which only the numerical seed for the electron shot noise was varied.

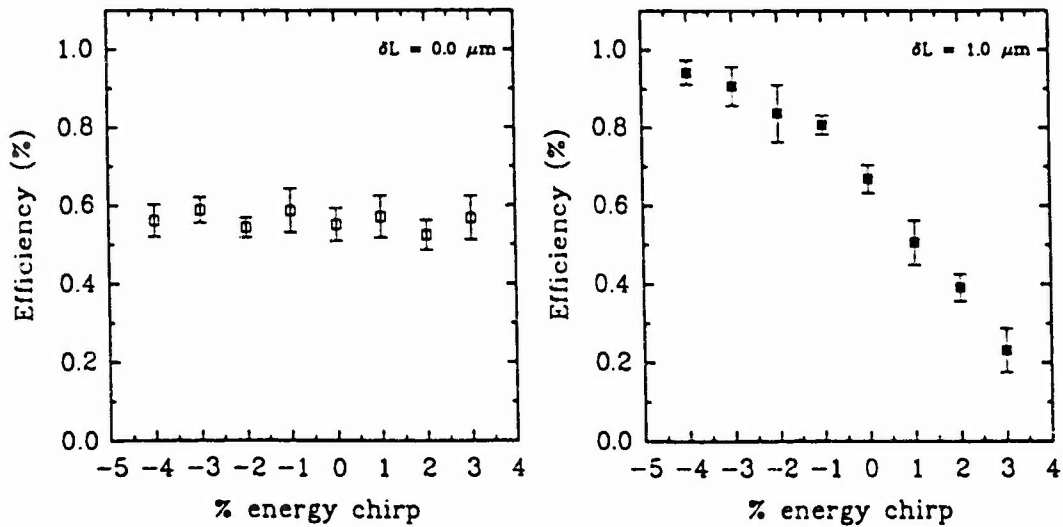


Fig. 3.8 Energy extraction efficiencies on the 100th pass for the simulations in Fig. 3.7.

and even for an energy chirp of - 4 % over 4 ps the enhancement is only 0.53 %. This is substantially smaller than the $1/2N_w$ efficiency of the Mark III FEL, so that no significant advantage is to be expected from energy chirps of this magnitude. Furthermore, eq. (3.3) assumes that all of the electrons become trapped at the beginning of the undulator, whereas the present simulations are only weakly saturated at pass 100.

For oscillation at a cavity detuning 1 μm shorter than synchronous, there is again no statistically significant dependence on the energy chirp in either the small signal gain or the macropulse power prior to the onset of saturation.² However, the saturated macropulse powers show a large and unexpected dependence on the energy chirp. Figure 3.8 displays similar results in terms of the electron energy extraction efficiency. This enhanced energy extraction can be understood by recalling that, as the laser saturates, the optical wavelength continually increases as the peak of the gain curve shifts to larger values of the resonance parameter [16]. In an unchirped FEL, this shift in wavelength occurs adiabatically under the influence of pumping and cavity losses, because the old radiation takes time to decay away. However, in an FEL operating with a negative energy chirp, the effect of finite cavity detunings is to *discretely* shift the resonance parameter to larger values *on each pass*, so that optimum resonance can be maintained throughout saturation. The electrons continually undergo expanding orbits in the phase space buckets, which deepen in response to the accelerated growth in laser power (this is illustrated in Fig. 3.10(c).)³ A similar argument by Moore [3] also suggested that finite detunings would enhance the extraction efficiency of negatively chirped pulses: the optical pulse would be pushed below resonance on each pass, so that the injected electrons would fall a greater distance in the ponderomotive buckets.

Finally, if this argument is valid, then precisely the same reasoning should predict an enhanced extraction efficiency for electron pulses with a *positive* energy chirp operating with cavity detunings *longer* than the synchronous length. Figures 3.9, 3.10, and 3.11 display the phase space trajectories on pass 100 for cavity detunings of 0 μm , +1.3 μm (shorter than synchronous), and -1.3 μm (longer than synchronous), respectively. Each figure plots the trajectories for energy chirps of (a) +2 %, (b) 0 %, and (c) - 2 %. The assertion of an enhanced efficiency for positive chirps is illustrated dramatically in Fig. 3.11.

² The independence of the small signal gain on the energy chirp for a detuning of 1 μm can be explained by noting that, for a 4 % energy chirp over 4 ps, the shift in the resonance parameter on each pass is only 0.63 % of the gain bandwidth, and after 14 passes (corresponding to the cavity decay time for a round trip loss of 7.3 %), the resonance shift is still only 8.8 % of the gain bandwidth.

³ Crudely, for a 4 % energy chirp over 4 ps, a detuning of 1 μm yields a shift in the resonance parameter of $\Delta\mu = 0.039$; the corresponding energy shift is $\Delta\gamma/\gamma = 0.007 \%$. If this energy is released to the optical field on each pass during saturation beyond roughly pass number 60 (as indicated by the simulations), then at pass 100 the energy yield (assuming optimum bucket growth) is $(\Delta\gamma/\gamma)_{\text{sat}} \sim 40 (0.007 \%) = 0.3 \%$. This is roughly the order of the enhanced efficiency observed in Fig. 3.8 for an energy chirp of - 4 %.

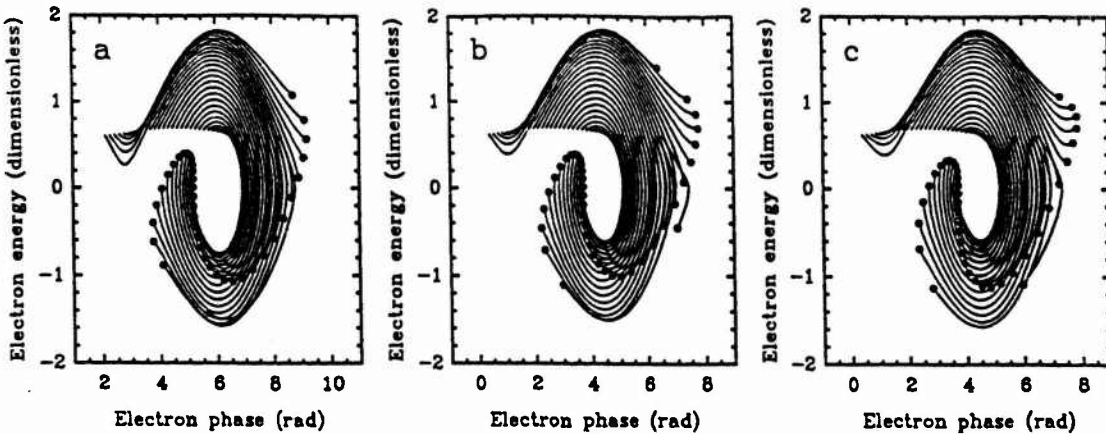


Fig. 3.9 Phase space trajectories on the 100th pass of the optical pulse for electrons near the center of a 4 ps electron pulse. The cavity length is at the *synchronous* length. The figures depict the trajectories for full width energy chirps of: (a) +2 %; (b) 0 %; (c) -2 %. There is little qualitative difference among the extraction efficiencies.

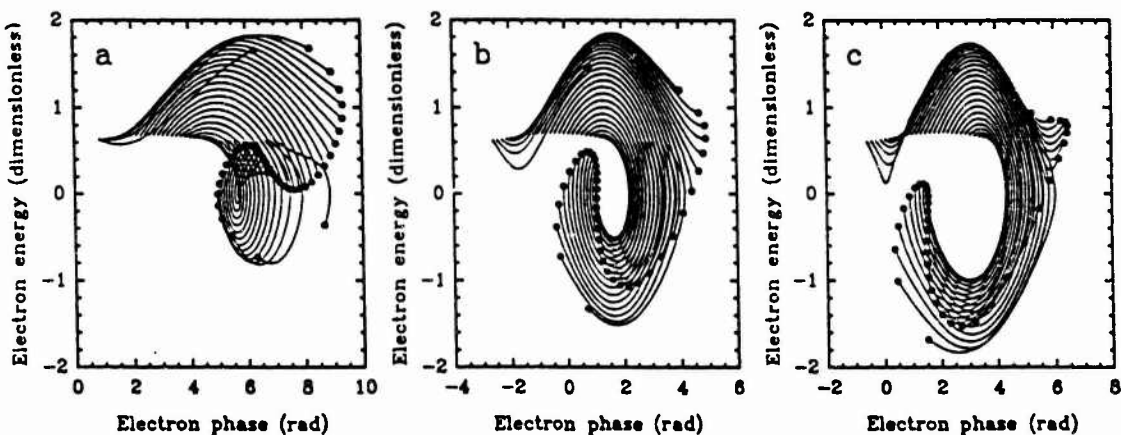


Fig. 3.10 Same as in Fig. 3.9, except that the cavity length is 1.3 μm *shorter* than synchronous. The figures depict the trajectories for full width energy chirps of: (a) +2 %; (b) 0 %; (c) -2 %. The -2 % chirp shows substantially greater energy extraction than the +2 % chirp.

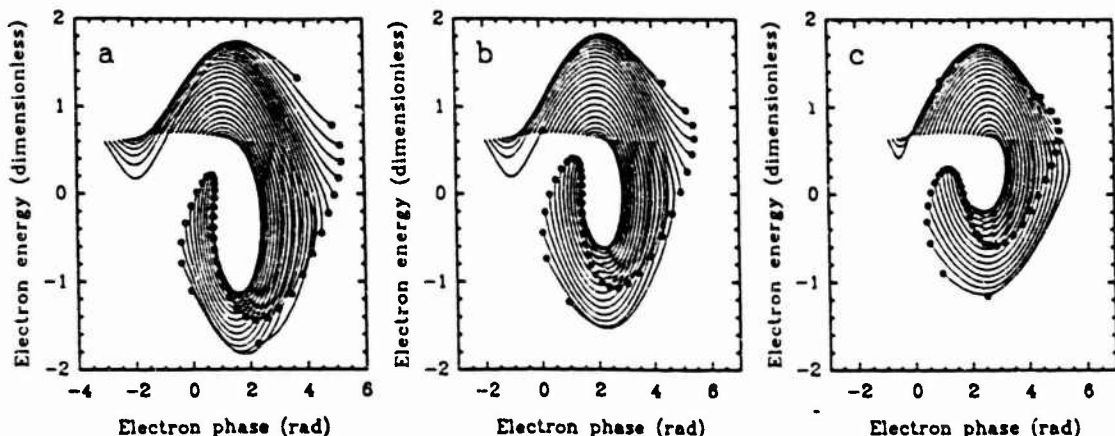


Fig. 3.11 Same as in Fig. 3.9, except that the cavity length is 1.3 μm *longer* than synchronous. The figures depict the trajectories for full width energy chirps of: (a) +2 %; (b) 0 %; (c) -2 %. Here, the +2 % chirp shows substantially greater energy extraction than the -2 % chirp.

III. ENERGY CHIRPING ON THE MARK III FEL; DESIGN PARAMETERS

In this section, I suggest a feasible configuration for operating the Mark III FEL in the chirped-pulse mode, and present the appropriate simulation results for designing a pulse compression experiment near $3 \mu\text{m}$. Practical operating parameters such as the shape of the cavity detuning curve and the stability of the compressed optical pulses will be addressed. The simulations assume that chirped electron pulses with the desired properties can be delivered to the laser. Energy chirping can be accomplished in an rf linac simply by dephasing the electrons from the gun with respect to the peak rf voltage of the traveling wave in the linac [1], and simple relations are invoked to determine the appropriate phase offset and the resulting energy spread. The chosen parameters are somewhat modest for the Mark III linac, and the confidence for achieving them is based partly on the early operation of the Mark III FEL.⁴ At any rate, a complete and rigorous investigation of the generation and transport of chirped electron pulses from the gun and linac would require extensive particle simulations which are beyond the scope of the present study.

A. Proposed configuration

As noted above, electron micropulses with a linear energy dependence on time can be produced at the rf linac by accelerating the pulses off the peak voltage of the traveling wave at phases where the field gradient is large. In principle, energy chirps of either sign are possible. However, the electron micropulses must be compatible with the downstream transport, which is a primary constraint on any chirped-pulse system. Moore has suggested a magnetic compression system for negatively chirped pulses that is appropriate for use on the Los Alamos FEL [1]. In the case of the Mark III FEL, dispersion in the chicane path preceding the wiggler complicates the use of negatively chirped pulses by increasing the pulse width and lowering the current, and therefore the available gain. Accordingly, the present experiments are designed for positively chirped pulses. The Mark III chicane path is shown in Fig. 3.12.

The energy chirp induced in the linac, and the subsequent dispersion in the chicane path preceding the wiggler, are given by simple expressions if the electron pulses are much shorter than the rf period and the energy chirps are on the order of a few percent [20]. The full width energy chirp induced in the linac at a phase offset of ψ is given by

⁴ The original momentum filter for the alpha magnet in the Mark III gun was not optimally designed, and the electrons were not properly bunched at the entrance to the linac. The gun current was also limited, and in order to generate the peak currents required to achieve lasing, the gun had to be dephased relative to the linac so that the resulting chirped electron pulses could be compressed in the chicane path preceding the wiggler. Based on these experiences, it has been suggested that phase offsets as large as 15° can be achieved with the present design [19].

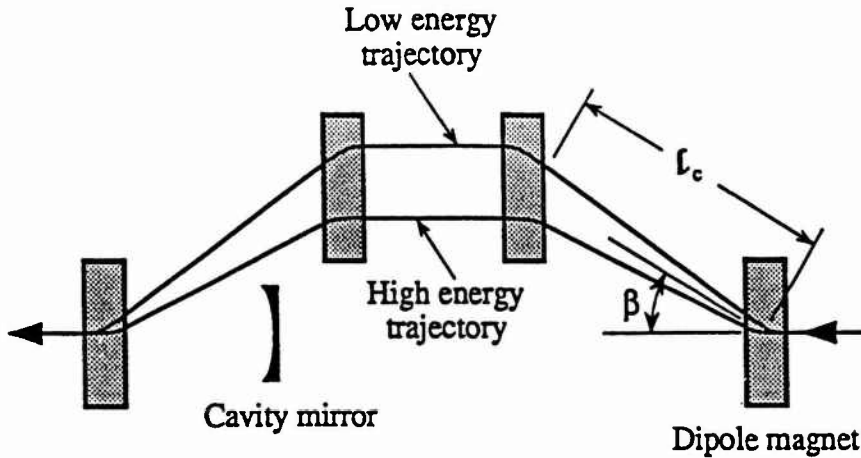


Fig. 3.12 The Mark III chicane path used to bend the electron beam around the cavity mirror. $l_c = 36.7 \text{ cm}$ and $\beta = 11.25^\circ$.

$$\left(\frac{\Delta\gamma}{\gamma} \right)_{\tau_p} = \tau_p \omega_{rf} \tan \psi , \quad (3.4)$$

where τ_p is the pulse duration in the linac and $\omega_{rf} = 2\pi v_{rf}$ is the angular rf frequency ($v_{rf} = 2.857 \text{ GHz}$). The temporal dispersion in the chicane path is given by

$$\Delta\tau_p = -\frac{2l_c}{c} \left(\frac{\Delta\gamma}{\gamma} \right)_{\tau_p} \beta \tan \beta , \quad (3.5)$$

where l_c and β are shown in Fig. 3.12 for the Mark III FEL.

As suggested by the simulations in Section II, substantial optical pulse compression ratios can be achieved by driving the laser with electron pulses having a +2 % energy chirp over 4 ps, and this is chosen to be the nominal operating configuration for the Mark III FEL experiments. From (3.4), a 6 ps electron pulse in the linac, which is a feasible pulse width from the gun, will exhibit an energy chirp of +2 % at a phase offset of $\psi = 10.5^\circ$, which is a modest phase offset for the Mark III linac. From (3.5), the resulting dispersion in the chicane path will then be $\Delta\tau_p = -1.92 \text{ ps}$, so that the 6 ps electron pulse should be compressed to just over 4 ps prior to injection into the laser. Note that the 6 ps electron pulse in the linac spans phase angles between $\psi = 7.4^\circ$ and $\psi = 13.6^\circ$, so that the energy chirp is not exactly linear. However, simulations using the corresponding nonlinear energy distribution yielded no observable effect on either the formation or compression of the resulting optical pulses.

B. Numerical simulations in the proposed configuration

Figure 3.13 shows typical results for the optical pulse formation at $3.35 \mu\text{m}$ in a chirped-pulse FEL after 100 passes through the oscillator and various cavity length detunings. The corresponding power spectra are shown in Fig. 3.14. Several important features are evident from these figures. First, the average powers during the optical micropulses

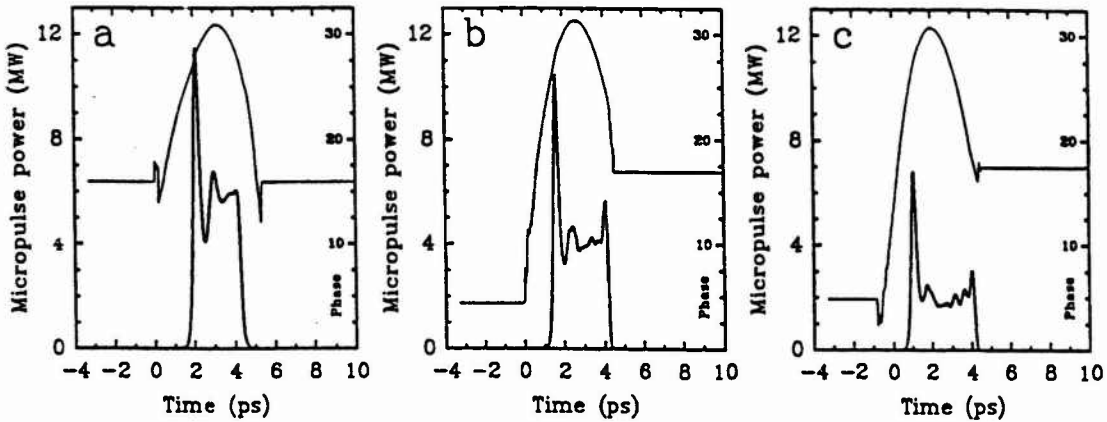


Fig. 3.13 Optical envelope and phase after 100 passes for electron pulses with a full width energy chirp of +2 % over 4 ps and various cavity detunings. (a) Detuning = 1.3 μm *longer* than synchronous (the corresponding optical chirp is +3.99 % over 4 ps; the FWHM pulse width is 2.42 ps); (b) Detuning = 0 μm (the corresponding optical chirp is +4.56 % over 4 ps; the FWHM pulse width is 2.84 ps); (c) Detuning = 1.3 μm *shorter* than synchronous (the corresponding optical chirp is +4.60 % over 4 ps; the FWHM pulse width is 3.38 ps).

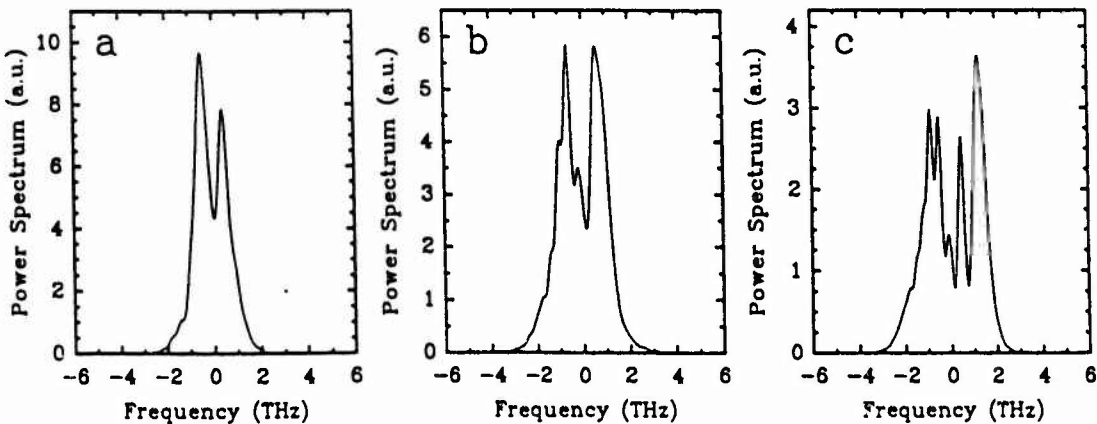


Fig. 3.14 (a) Power spectrum for the optical pulse in Fig. 3.13(a); (b) power spectrum for the optical pulse in Fig. 3.13(b); (c) power spectrum for the optical pulse in Fig. 3.13(c).

decrease dramatically as the cavity detuning is changed from longer-than-synchronous to shorter-than-synchronous values. This change in optical power is due to the dependence of the extraction efficiency on cavity detuning which was previously predicted to occur for positively chirped pulses. Second, laser lethargy more greatly erodes the front end of the optical pulses at longer cavity lengths. As a result, the total energy content does not change as greatly as the optical powers would indicate. Third, the spectral widths displayed in Fig.

3.14 are narrower for optical pulses oscillating at longer cavity lengths, but the frequency chirps are roughly independent of cavity detuning. This variation in spectral width is due directly to the effect of lethargy on the final pulse widths; pulses experiencing a greater erosion will be shorter and will yield reduced bandwidths for a given frequency chirp. (Note that this variation in the spectral width occurs in contrast to Figs. 3.1 and 3.2, in which the pulse widths were roughly the same but the *frequency chirps* were different.)

An important consequence of the reduced bandwidth is that the pulse compression ratio will be limited for longer cavity lengths. Figure 3.15 displays the compressed optical pulses for cavity detunings 1.3 μm longer and 1.3 μm shorter than the synchronous length. In figure (a), eight simulations were performed using different numerical seeds for the electron shot noise, and the resulting optical pulses were compressed in the *same* optimum dispersive delay line. The same is true of figure (b), except that the corresponding delay line was optimized for that case. We see that the pulses from the longer cavity can only be compressed to 301 ± 10 fs, compared to 222 ± 3 fs for the pulses from the shorter cavity. The large fluctuations in pulse width in the former case are due to the fact that the laser is largely driven by noise at cavity lengths longer than the synchronous length [21], resulting in unstable frequency chirps across the short pulses. The presence of noise also yields a much greater intrinsic timing jitter (± 90 fs for the longer cavity, compared to only ± 22 fs for the shorter cavity), because the *average* laser frequency also exhibits greater fluctuations, and different frequencies will yield different absolute group delays in a given dispersive delay

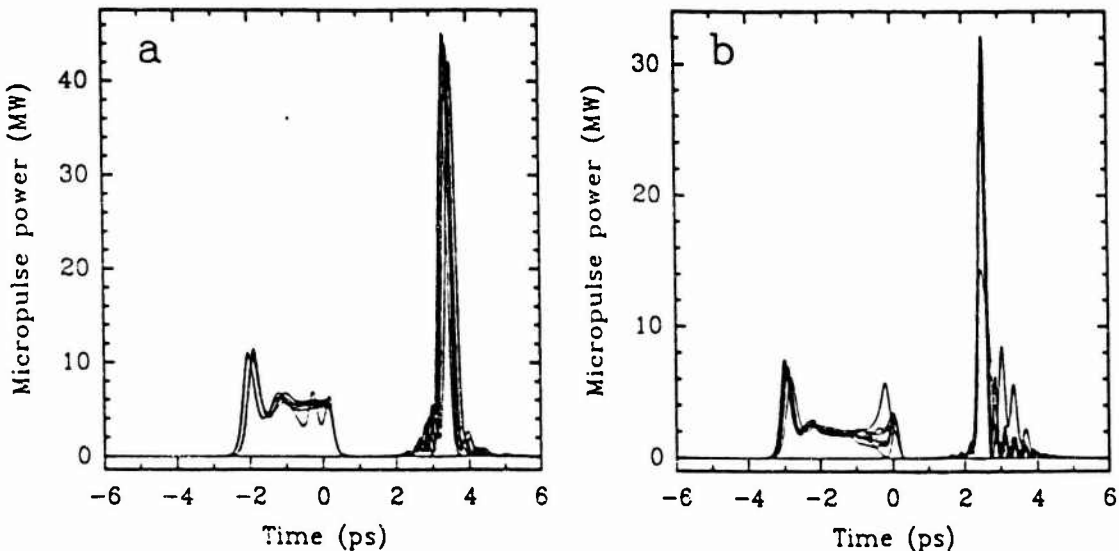


Fig. 3.15 Optimum quadratic compression of eight optical pulses in which only the numerical seed for the electron shot noise was varied. (a) cavity detuning = $-1.3 \mu\text{m}$ (longer than synchronous); the compressed pulse widths are 301 ± 10 fs and the intrinsic timing jitter is ± 90 fs. (b) cavity detuning = $+1.3 \mu\text{m}$ (shorter than synchronous); the compressed pulse widths are 222 ± 3 fs and the intrinsic timing jitter is ± 22 fs. The energy chirp is $+2\%$ over 4 ps in each case.

line [14]. Since the compressed optical power is only slightly higher for the longer cavity than for the shorter cavity, any benefits to nonlinear spectroscopy would be effectively eliminated by the increased pulse widths and large temporal fluctuations. On the contrary, pulse widths of 222 ± 3 fs would be appropriate for most studies of ultrafast processes in the infrared, and a 10 % timing jitter would be sufficiently small to allow accurate cross-correlation experiments using different pulses in the pulse train. Not least, a compressed peak power of 30 MW would be appropriate for studying many nonlinear interactions, for which the diffraction-limited optical beam at $3.35 \mu\text{m}$ could easily be focused to intensities greater than $2(10^{13}) \text{ W/cm}^2$.

For the purpose of designing an appropriate dispersive delay line for the compressed pulses in Fig. 3.15(b), we note that the average chirp parameter of the uncompressed pulses is $\langle b \rangle = +3.3(10^{24}) \text{ s}^{-2}$, and the optimum compensation factor K (see Footnote 1) is found to be $K = 4.3$. Accordingly, the optimum delay line uses a *fixed* second order dispersion constant of $1/\langle b \rangle K = +7.0(10^{-26}) \text{ s}^2$. These pulses can be compressed from $\tau_p = 3.4$ ps to $\tau_p = 220$ fs. For extending the design to other wavelengths, it is useful to assume that the frequency chirp is determined by the resonance condition, so that the chirp parameter 'b' is inversely proportional to the wavelength for a given pulse width, as indicated by (3.2). Figure 3.16 displays this result for various wavelengths using electron pulses with a +2 % energy chirp over 6 ps. The linearity is very good, and the slope of the graph differs only slightly from the theoretical slope due to the intrinsic frequency chirps indicated in Fig. 3.4. The design of a dispersive delay line using sapphire prisms is described in Appendix A.

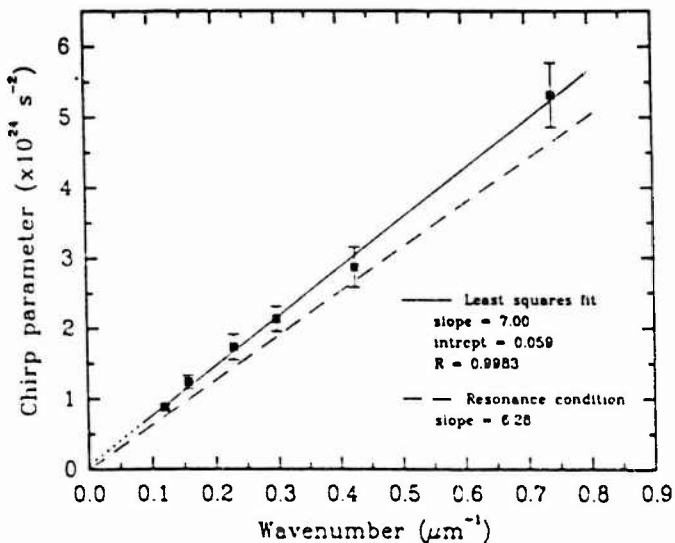


Fig. 3.16 Frequency chirp as a function of wavenumber for electron pulses with a +2 % energy chirp over 6 ps, indicating that the frequency chirp is inversely proportional to the wavelength. The slope of the simulated points differs slightly from the theoretical slope because of the intrinsic frequency chirp indicated in Fig. 3.4.

C. Effects of intracavity dispersion

The Mark III FEL uses metal cavity mirrors and Brewster plate output coupling to exploit the wide tunability of the device. Apart from a slight inconvenience in the geometry of the outcoupled beams, the insertion of an intracavity Brewster plate poses no problems to the operation of the unchirped laser (of course, the potential for optical damage [22] is absent in methods such as hole coupling [23].) Indeed, the dependence of the dispersion on wavelength has proven to be extremely useful for the operation of the laser on higher harmonics [24]. However, in the chirped-pulse FEL, a significant amount of intracavity dispersion can be expected to have detrimental effects on the optical pulse structure.

The most important complication of dispersion arises from the potential to distort the chirped optical pulses as the laser builds up to saturation. The effect of group velocity dispersion is to impose a wavelength dependent group delay on the different spectral components in the pulse, and since these components are localized temporally via the frequency chirp, the pulse will be temporally distorted. This is essentially how a pulse compressor works [14], except that the compression (or broadening) now occurs inside the cavity. In the chirped-pulse FEL, a severe temporal distortion of the spectral components from pass to pass can eventually preclude the optical pulse from maintaining resonance with the incoming electron pulses over the entire pulse duration.

The effect of dispersion can be estimated by assuming that the optical pulses have a Gaussian profile and a linear chirp, which pulses are characterized by Siegman [14] in terms of a chirp parameter 'b' and a pulse width parameter 'a' via the definitions

$$\omega(t) = \omega_0 + (2b)t \quad \text{and} \quad a = \frac{2 \log_e 2}{\tau_p^2} . \quad (3.6)$$

Here, $\omega(t)$ is the time-dependent optical frequency and τ_p is the FWHM pulse duration. If a Gaussian optical pulse with initial parameters a_0 and b_0 propagates through a dispersive medium over a distance z , Siegman has shown that the resulting pulse parameters are then

$$b(z) = \frac{b_0(1 + 2\beta''z b_0) + 2\beta''za_0^2}{(1 + 2\beta''z b_0)^2 + (2\beta''za_0)^2} \quad \text{and} \quad a(z) = \frac{a_0}{(1 + 2\beta''z b_0)^2 + (2\beta''za_0)^2} , \quad (3.7)$$

where $\beta'' = (\partial^2/\partial\omega^2)\left[\frac{\omega n(\omega)}{c}\right]$ is the second order dispersion of the medium and $n(\omega)$ is the refractive index. In the chirped-pulse FEL, an appropriate distance z is roughly twice the thickness of the Brewster plate times the number of passes corresponding to the decay time of the resonator. For a 2 mm thick Brewster plate with a total round trip loss of 7.3 %, the radiation decay time is roughly 15 passes, and $z \sim 60$ mm. For calcium fluoride or sapphire

Brewster plates, the second order dispersions at $3.35 \mu\text{m}$ can be found from the published Sellmeier data [25] to be $\beta''_{\text{CaF}_2} = -1.6(10^{-25}) \text{ s}^2/\text{m}$ and $\beta''_{\text{sapphire}} = -8.2(10^{-25}) \text{ s}^2/\text{m}$.

We may now estimate the effects of the dispersion on the circulating optical pulses. For the uncompressed optical pulses from paragraph B, we take $b_0 = +3.3(10^{24}) \text{ s}^{-2}$ and $a_0 = +1.20(10^{23}) \text{ s}^{-2}$ (corresponding to $\tau_p = 3.4 \text{ ps}$.) For the calcium fluoride Brewster plate, eqs. (3.7) then yield $b(60 \text{ mm}) = +3.5(10^{24}) \text{ s}^{-2}$ and $a(60 \text{ mm}) = +1.37(10^{23}) \text{ s}^{-2}$ (corresponding to $\tau_p = 3.2 \text{ ps}$.) The pulse is compressed by only 6 % over the repeated round trips, and the chirp parameter is only slightly altered by the dispersion. However, the situation is different for the sapphire plate, for which eqs. (3.7) yield $b(60 \text{ mm}) = +4.9(10^{24}) \text{ s}^{-2}$ and $a(60 \text{ mm}) = +2.63(10^{23}) \text{ s}^{-2}$ (corresponding to $\tau_p = 2.3 \text{ ps}$.) The chirp parameter is significantly increased by the dispersion, and the optical pulse shows substantial compression by more than 32 %. Even in the absence of any other distortions, this compression will significantly reduce the optical bandwidth and, consequently, the external pulse compression ratio.

I have performed simulations of the chirped-pulse FEL to investigate the effects of dispersion in the Brewster plate. The FEL pulse propagation code is the same as in previous simulations, except that the optical pulse is transmitted through the Brewster plate on each pass by taking the Fourier transform of the optical field, multiplying by a frequency dependent phase factor of the form

$$\exp\left[+i\frac{\beta'' 2t}{2}(\omega - \omega_0)^2\right] , \quad (3.8)$$

where $2t$ is twice the thickness of the Brewster plate, and taking the inverse Fourier transform to obtain the transmitted optical pulse. Figures 3.17(a,b) compare the simulated optical envelope and phase after 100 passes in a chirped-pulse FEL using calcium fluoride and sapphire Brewster plates. The energy chirp is +2 % over 4 ps and the cavity detuning is $+1.3 \mu\text{m}$; these figures can be compared with Fig. 3.13(c) in which no Brewster plate was present.

We see that the dispersion from the calcium fluoride plate has little effect on either the optical envelope or phase. The chirp parameter is $b = +3.4(10^{24}) \text{ s}^{-2}$, and the pulse width is 2.90 ps, which is 14 % shorter than the width of the optical pulse from Fig. 3.13(c). Evidently, the pulse shortening due to dispersion is slightly underestimated in the previous analysis. However, that analysis is still instructive given the crude assumptions and the neglect of the FEL interaction. This optical pulse can be compressed to 255 fs.

On the other hand, dispersion in the sapphire Brewster plate yields a considerable distortion in both the envelope and phase of the circulating optical pulse. The final pulse width is only 1.95 ps, which is 42 % shorter than the optical pulse width from Fig. 3.13(c).

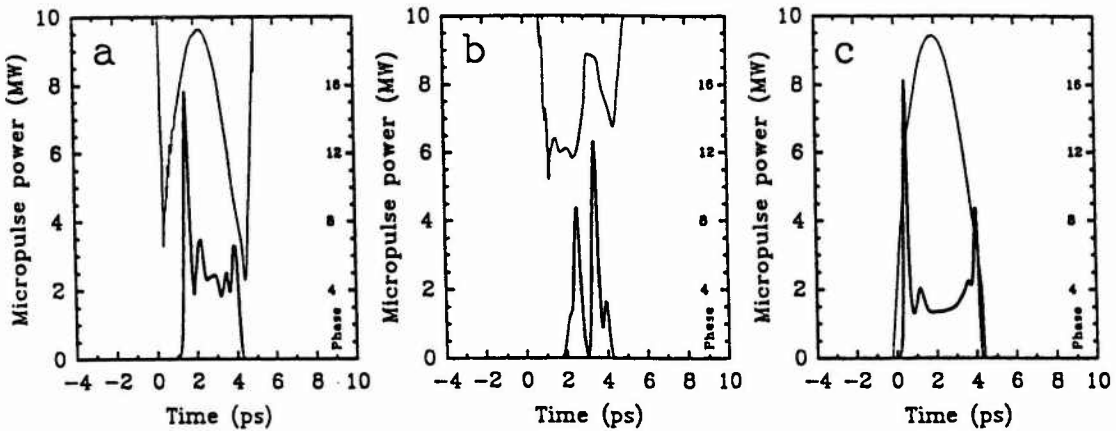


Fig. 3.17 Optical envelope and phase after 100 passes at $3.35 \mu\text{m}$ for electron pulses with a full width energy chirp of $+2\%$ over 4 ps including dispersion in: (a) a 2 mm calcium fluoride Brewster plate, (b) a 2 mm sapphire Brewster plate, and (c) a 2 mm zinc selenide Brewster plate.

The reduced optical bandwidth and pulse energy are too small to yield a useful compressed optical pulse. Consequently, in the chirped-pulse operation of the Mark III FEL near $3 \mu\text{m}$, sapphire Brewster plates cannot be used. However, the effects of dispersion even in the calcium fluoride Brewster plate can be reduced considerably by using a 1 mm thickness instead of a 2 mm thickness. Alternately, one can employ a different material. For example, zinc selenide has a dispersion at $3.35 \mu\text{m}$ of $\beta''_{\text{ZnSe}} = +1.3(10^{-25}) \text{s}^2/\text{m}$. A ZnSe Brewster plate will therefore *broaden* the circulating optical pulse, thereby increasing the total optical bandwidth and yielding a larger external pulse compression ratio. This is illustrated for a 2 mm ZnSe Brewster plate by the optical pulse in Fig. 3.17(c), which has a duration of 3.90 ps and can be compressed to 211 fs. Finally, one can insert an extraneous Brewster plate into the cavity which has a dispersion opposite to that of the output coupler. The appropriate thickness can then be chosen to yield a zero net round trip dispersion.

D. Simulated cavity detuning curves

One of the most important and basic diagnostics of laser performance is the shape and width of the cavity detuning curve. Accordingly, I have performed a series of simulations to study the effects of energy chirping on the detuning properties of the FEL. Several effects of cavity length detuning have already been established in previous paragraphs, such as the enhanced energy extraction efficiency for energy chirps of either sign, and the effect of lethargy on the erosion of the leading edge of the optical pulse which decreases the optical bandwidth.

Figure 3.18 compares the cavity power detuning curves for unchirped 4 ps electron

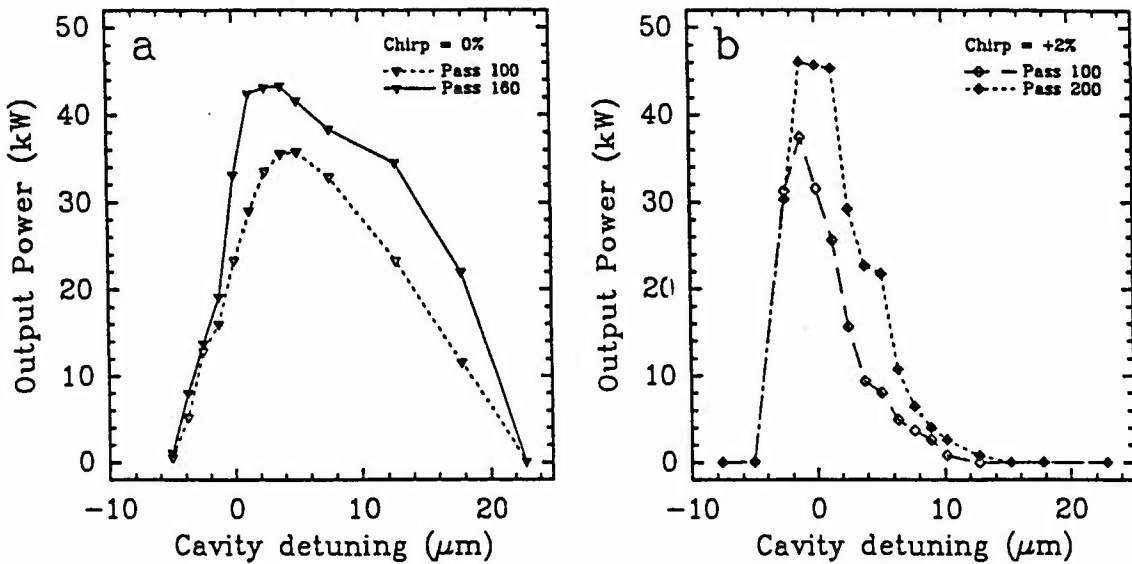


Fig. 3.18 Cavity power detuning curves for (a) unchirped 4 ps electron pulses, and (b) electron pulses with an energy chirp of +2 % over 4 ps. Positive detunings refer to *shorter* cavities.

pulses, and electron pulses with an energy chirp of +2 % over 4 ps. We see that the detuning curve for the chirped laser shows significant erosion on the short-cavity side compared to the unchirped laser, and that the former shows an increased power at a detuning of $\delta L \sim -1 \mu\text{m}$ on the long-cavity side. Otherwise, the optical power on the long-cavity side is extinguished at a detuning of $\delta L \sim -5 \mu\text{m}$ in both cases. The erosion on the short-cavity side can be explained by noting that, for large detunings, the chirped optical pulse is pushed ahead of the incoming electrons too quickly for resonance to be maintained over a sufficiently large number of passes. This effect was first noted by Moore [2]. The origin of the erosion of the detuning curve is illustrated in Fig. 3.19, which shows the small signal supermode evolution for both the unchirped and chirped lasers at a cavity detuning of +10 μm. These simulations were performed with no noise starting from a tophat seed pulse, and the optical powers were renormalized to small signal levels after every four passes (the onset of saturation would have occurred at roughly pass number sixty if the optical powers were not renormalized.) We see that the unchirped supermode evolves monotonically towards a stable pulse located roughly near the center of the electron pulse. However, the chirped laser decays markedly during the early passes as the optical pulse walks off the front of the electron pulse. Surprisingly, even the chirped laser exhibits a stable supermode which develops into two sub-pulses at the leading and trailing edges of the electron pulse (the trailing pulse is much more dominant in the small signal regime.)

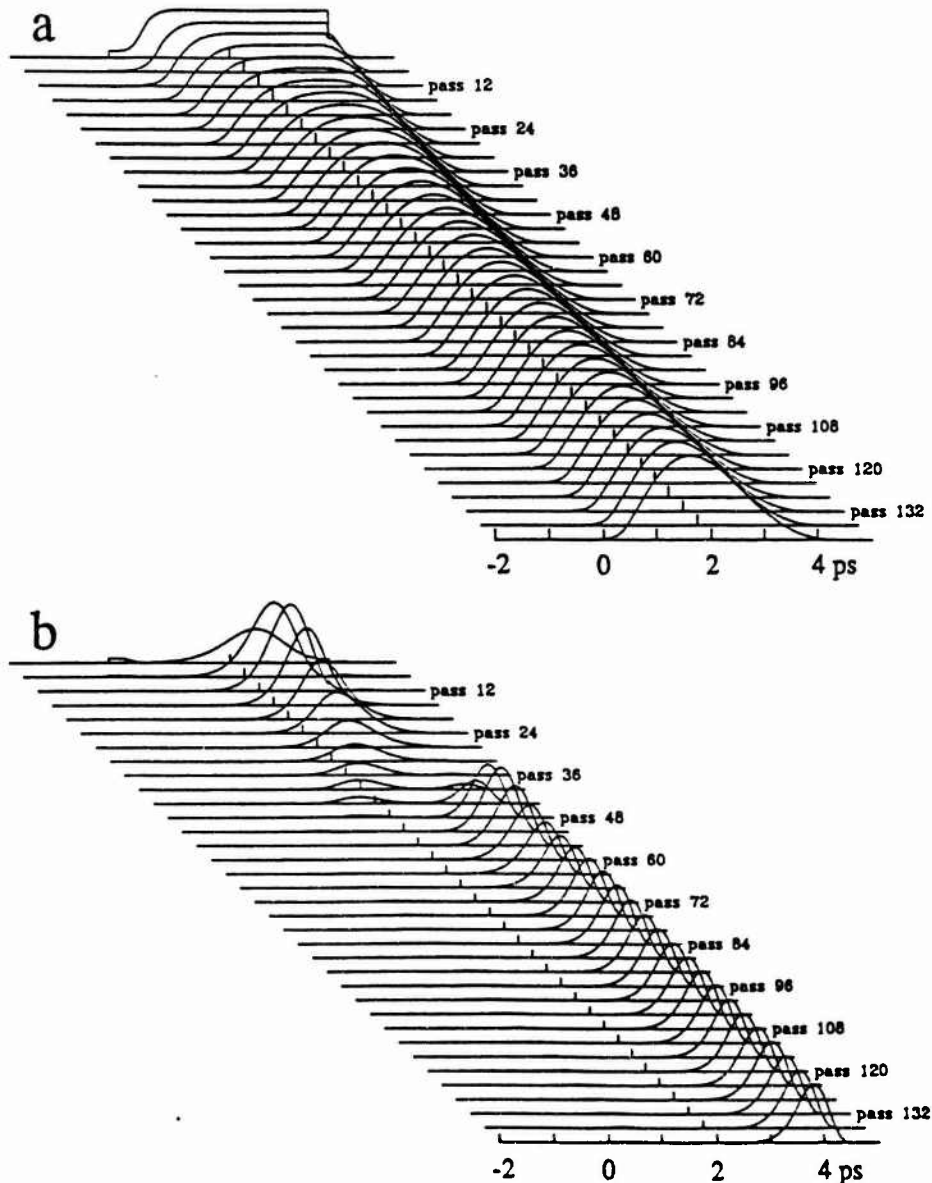


Fig. 3.19 Small signal supermode evolution at a cavity detuning of $+10 \mu\text{m}$ (shorter than synchronous), for (a) unchirped electron pulses with a duration of 4 ps, and (b) electron pulses with an energy chirp of $+2\%$ over 4 ps. The optical powers were renormalized after every 4 passes. The electron pulses are located between 0 ps and $+4$ ps at the beginning of the undulator.

The large signal supermode of the chirped laser is similar to the small signal supermode, and was obtained from simulations which were driven by noise from spontaneous radiation to full saturation over 200 passes. The large signal evolution is illustrated in Fig. 3.20. We see that the sub-pulses at the beginning and end of the optical pulse are roughly the same size and roughly coincide with the beginning and end of the electron pulse. The optical phase at each of these points is linear, which corresponds to lasing at two distinct frequencies. This effect was also first reported by Moore [3]. Although the peak powers

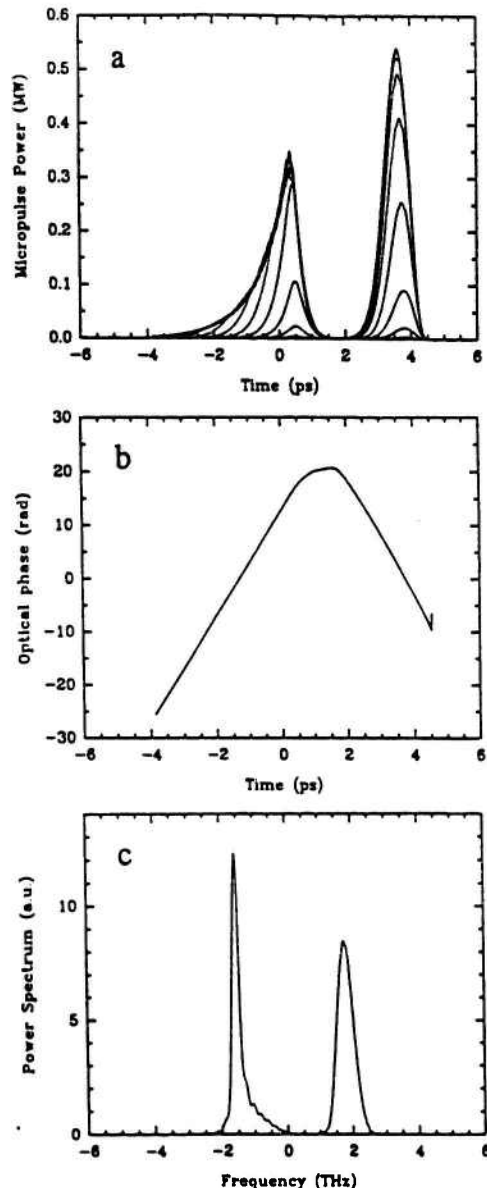


Fig. 3.20 Large signal supermode evolution at a cavity detuning of $+10 \mu\text{m}$ (shorter than synchronous) from spontaneous radiation to full saturation. (a) Evolution of the optical envelope over 200 passes, each curve representing 10 passes. The electron pulse is located between 0 ps and 4 ps. (b) Optical phase at pass 200, showing a linear time dependence at the beginning and end of the electron pulse. (c) Optical spectrum at pass 200, showing two distinct frequencies corresponding to the linear phase variations at the ends of the optical pulse.

are fairly high (just under one megaWatt), the total pulse energy is relatively small because the central region of the pulse does not lase at all.⁵ Nevertheless, operating the chirped-pulse FEL at such large detunings would provide extremely useful diagnostics on the laser

⁵ We should note that corresponding optical spectrum can be confused in some experiments with the sideband instability which, of course, it is not: the sideband instability is extinguished for large detunings, in contrast to the lobes of the chirped-pulse spectrum, and the temporal sideband modulations are also inconsistent with the substructure of the chirped optical pulses.

performance. In particular, optical autocorrelation would provide direct information on the duration of the electron pulses, and the corresponding optical spectrum would then provide an estimate of the energy chirp. Such diagnostics would greatly expedite the reconfiguration of the dispersive delay line for optimum pulse compression.

IV. SUMMARY OF RESULTS

From the simulations reported in this chapter, the following conclusions appear to be justified.

1. Substantial frequency chirps can be obtained with relatively short electron pulses and modest energy chirps. Simulations of the optical pulse formation at 3.35 μm using electron pulses with a +2 % energy chirp over 4 ps yielded optical pulses with a duration of 3.4 ps which could be compressed by more than a factor of 15 to 220 fs.
2. Due to an intrinsic, positive frequency chirping in the FEL (even for un-chirped electron pulses), electron pulses with a positive energy chirp yield larger frequency chirps than electron pulses with a negative energy chirp of the same magnitude. Consequently, positive chirps yield larger pulse compression ratios than negative chirps.
3. Cavity lengths shorter than the synchronous length yield slightly longer optical pulses than longer cavities, because the erosion due to laser lethargy is reduced. Therefore, shorter cavities yield optical pulses with a greater total energy content, as well as a greater optical bandwidth and pulse compression ratio for a given frequency chirp. The optical pulse formation is also intrinsically more stable due to the reduced effects of noise.
4. For cavity lengths shorter than the synchronous length, negatively chirped electron pulses exhibit a substantially greater energy extraction than positively chirped pulses; the converse is true for cavity lengths longer than the synchronous length. Since shorter cavities are generally preferred over longer cavities for the reasons noted in 3, negative chirps would be more appropriate in applications requiring high peak powers (even though the compressed pulses are longer.)
5. Intracavity dispersion, such as from a Brewster plate output coupler, can distort the envelope and phase of the optical pulse as the laser builds up to saturation. However, the effect of dispersion can generally be neglected if

$$|2\beta'' z b_0| \ll 1 , \quad (3.9)$$

where β'' is the second order dispersion defined in (3.7), z is roughly twice the thickness of the Brewster plate times the number of passes corresponding to the decay time of the resonator, and b_0 is the optical chirp parameter in the absence of dispersion.

6. When operating the chirped-pulse FEL with cavity lengths shorter than the synchronous length, the optical pulses will eventually be pushed out of resonance with the incoming electron pulses. Therefore, the macropulse duration should not extend too far into saturation. A limited macropulse would also preclude the formation of the sideband instability and the corresponding distortion of the optical envelope and phase prior to pulse compression.

The simulations reported in this chapter have indicated the feasibility of obtaining broad band, frequency-chirped optical pulses by imposing a modest degree of energy chirping in an FEL. Simulations of the formation and compression of chirped optical pulses on the Mark III FEL have yielded pulses with durations of just over 200 fs and peak powers of several tens of megaWatts. Although such pulses would be appropriate for many fast-time resolved and nonlinear studies in the infrared, the broad spectral width associated with such optical beams would appear to preclude the possibility of concurrently achieving high spectral resolution. However, in Part Two of this dissertation, I study a method to increase the spectral resolution of the optical beam by using an intracavity interferometer to phase lock successive optical pulses, and thereby separate the longitudinal modes of the laser. Such an enhancement, which is intrinsically important for high resolution infrared spectroscopy, can in principle be implemented simultaneously with energy chirping to yield a train of ultrashort, phase locked optical pulses. Consequently, in some applications, the improved temporal resolution need not occur at the expense of spectral resolution.

V. REFERENCES

- [1] G. T. Moore, "The Chirped-Pulse Free Electron Laser," *Nucl. Instr. and Meth.*, vol. A272, pp. 302-310, 1988.
- [2] G. T. Moore, "Frequency Chirping of the Free-Electron Laser," *Phys. Rev. Lett.*, vol. 60, pp. 1825-1827, 1988.
- [3] G. T. Moore and J. C. Goldstein, "Chirping for Efficiency Enhancement of the Free Electron Laser," *Nucl. Instr. and Meth.*, vol. A285, pp. 176-185, 1989.
- [4] N. M. Kroll, P. L. Morton, and M. N. Rosenbluth, "Free-Electron Lasers with Variable Parameter Wigglers," *IEEE J. Quantum Electron.*, vol. QE-17, pp. 1436-1468, 1981.
- [5] N. M. Kroll and M. N. Rosenbluth, *Physics of Quantum Electronics, Volume 7*, Reading, MA: Addison-Wesley, 1980. p. 147.

- [6] W. B. Colson and R. A. Freedman, "Synchrotron Instability for Long Pulses in Free-Electron Laser Oscillators," *Opt. Commun.*, vol. 46, pp. 37-42, 1983.
- [7] R. A. Freedman and W. B. Colson, "The Sideband Instability in Free-Electron Laser Oscillators: Effects of Tapering and Electron Energy Spread," *Opt. Commun.*, vol. 52, pp. 409-414, 1985.
- [8] D. C. Quimby, J. M. Slater, and J. P. Wilcoxon, "Sideband Suppression in Free-Electron Lasers with Multiple Synchrotron Periods," *IEEE J. Quantum Electron.*, vol. QE-21, p. 979, 1985.
- [9] W. B. Colson, "The Trapped-Particle Instability in Free-Electron Laser Oscillators and Amplifiers," *Nucl. Instr. and Meth.*, vol. A250, pp. 168-175, 1986.
- [10] J. C. Goldstein, B. E. Newnam, and R. W. Warren, "Sideband suppression by an intracavity optical filter in the Los Alamos free-electron laser oscillator," *Nucl. Instr. and Meth.*, vol. A272, pp. 150-154, 1988.
- [11] J. E. Sollid, D. W. Feldman, R. W. Warren, H. Takeda, S. J. Gitomer, W. J. Johnson, and W. E. Stein, "Sideband suppression in the Los Alamos free-electron laser using a Littrow grating," *Nucl. Instr. and Meth.*, vol. A285, pp. 147-152, 1989; J. E. Sollid, D. W. Feldman, and R. W. Warren, "Sideband suppression for free-electron lasers," *ibid*, pp. 153-157, 1989.
- [12] B. A. Richman, J. M. J. Madey, and E. Szarmes, "First Observation of Spiking Behavior in the Time Domain in a Free-Electron Laser," *Phys. Rev. Lett.*, vol. 63, pp. 1682-1684, 1989.
- [13] E. B. Szarmes, S. V. Benson, and J. M. J. Madey, "Pulse compression on the Mark III FEL using energy chirping," *Nucl. Instr. and Meth.*, vol. A296, pp. 755-761, 1990.
- [14] A. E. Siegman, *Lasers*, Mill Valley, CA: University Science Books, 1986. Chapter 9.
- [15] H. Aj-Abawi, J. K. McIver, G. T. Moore, and M. O. Scully, *Physics of Quantum Electronics, Volume 9*, Reading, MA: Addison-Wesley, 1982. p. 415.
- [16] W. B. Colson and S. K. Ride, "The free-electron laser: Maxwell's equations driven by single-particle currents," in *Physics of Quantum Electronics, Volume 7*, Reading, MA: Addison-Wesley, 1980. p. 377.
- [17] G. T. Moore and N. Piovella, "Superradiant Short-Pulse Propagation in the Free-Electron Laser Oscillator," *IEEE J. Quantum Electron.*, vol. 27, pp. 2522-2528, 1991.
- [18] W. B. Colson and P. Elleaume, "Electron dynamics in free electron laser resonator modes," *Appl. Phys. B.*, vol. 29, pp. 101-109, 1982.
- [19] S. V. Benson, private communication.
- [20] See, for example, B. A. Richman, *Three-Dimensional Guiding Effects in a Free-Electron Laser*, Ph.D. dissertation, Stanford, CA: Stanford University, 1991. Appendix A.
- [21] S. V. Benson and J. M. J. Madey, "Shot and quantum noise in free electron lasers" *Nucl. Instr. and Meth.*, vol. A235, pp. 55-60, 1985.
- [22] S. V. Benson, E. B. Szarmes, B. A. Hooper, E. L. Dottery, and J. M. J. Madey, "Laser Damage on Zinc Selenide and Cadmium Telluride using the Stanford Mark III Infrared Free-Electron Laser," *Laser Induced Damage in Optical Materials: 1987*, NIST Special Publication 756, pp. 41-49, 1988.
- [23] A. F. G. van der Meer *et al*, "The FELIX Project - Status Report October 1990," *FOM-Instituut voor Plasmaphysica Rijnhuizen Report 90-199*, 1990.
- [24] S. V. Benson and J. M. J. Madey, "Demonstration of harmonic lasing in a free-electron laser," *Phys. Rev. A*, vol. 39, pp. 1579-1581, 1989.
- [25] W. G. Driscoll, ed., *Handbook of Optics*, New York, NY: McGraw-Hill, 1978.

Chapter 4

The Michelson resonator free-electron laser

Due to engineering constraints, most rf linac-driven free-electron lasers (FELs) operate with a large number of optical pulses circulating within the cavity at any time. An example is the Mark III FEL [1] which drives 35 independent optical pulses. The spectral energy distribution of the output beam is comprised of the Fourier transform of the individual optical pulses enveloping a fringe pattern imposed by the axial mode structure of the optical resonator. However, the axial mode spacing is independent of the number of pulses contained in the cavity for devices in which the optical pulses build up independently from noise, and in this respect, the spectral properties are the same as if the cavity contained only a single pulse. Conventional two-mirror resonators with lengths of several meters, typical for rf linac-driven systems, have axial mode spacings of less than 100 MHz, and it is therefore difficult to isolate these modes for applications in high resolution spectroscopy.

One can take advantage of the large number of pulses by using an intracavity interferometer to couple successive optical pulses at the beamsplitter [2], [3]. In such a configuration, the circulating optical pulses will evolve from pass to pass with a definite phase relationship as they build up from noise. The axial mode spacing (or free spectral range) is thereby increased by a factor equal to the number of pulses in the cavity up to a frequency interval equal to the driving frequency of the rf linac. For S-band linacs this is usually several gigaHertz, resulting in spectral modes which can be more easily isolated in applications to high resolution spectroscopy.

In a previous publication [3], the phase locking properties of a Michelson mirror

resonator on short-pulse FELs were examined. The configuration of the Michelson resonator is shown in Fig. 4.1(a) in which the coupling is provided by an extra delay of one rf period in the secondary arm of the interferometer. Numerical simulations of the Michelson resonator FEL were reported which confirmed the corresponding increase in the axial mode spacing of the output beam on time scales appropriate to microsecond macropulse lengths, and a preliminary eigenmode analysis was developed which accurately predicted the mode decay rates. Apart from demonstrating the expected increase in the free spectral range, the simulations also indicated that the phase locked optical beam grows to the same saturated power level as the randomly phased beam. This latter property is particularly important for applications in nonlinear spectroscopy. Since the spectral width of the output beam is determined primarily by the duration of the short electron pulses, a decrease by a factor of

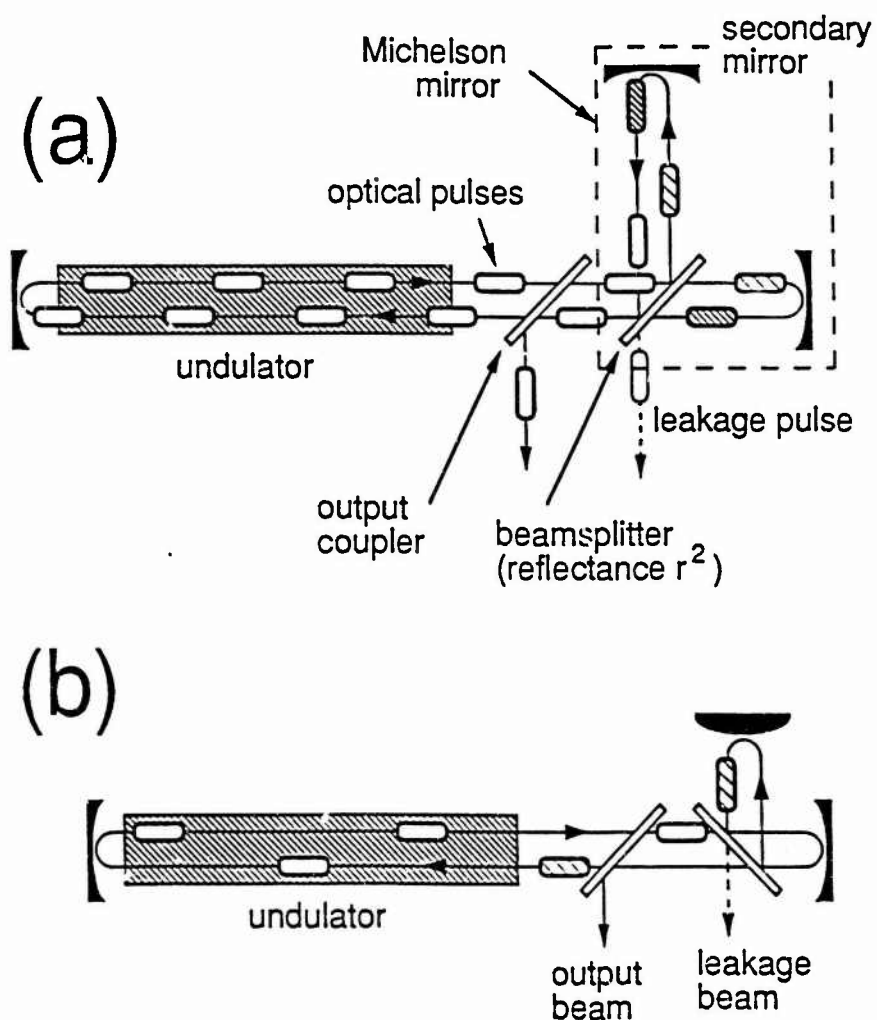


Fig. 4.1 Multiple mirror resonators for coupling successive optical pulses in the macropulse: (a) a Michelson mirror resonator with a delay of one rf period in the secondary arm, and (b) a Fox-Smith interferometer with a round trip time of one rf period in the small resonator.

N in the number of modes yields an increase by the same factor in the power per mode, where N is the number of pulses in the cavity. This can be well over an order of magnitude increase in the spectral brightness.

In the present chapter, I fully develop the eigenmode analysis of the Michelson mirror resonator, and more importantly, I demonstrate its equivalence to an independent frequency domain analysis based on the passive mode structure of that resonator. The advantage of the former is that it yields a rigorous solution to the initial value problem in terms of biorthogonal eigenvectors, and provides a convenient interpretation of the phase locking process in the time domain. However, within the context developed below, it is valid only for the perfectly tuned interferometer. The frequency domain analysis can be applied to an arbitrarily detuned interferometer, and is crucial to describing the detuning properties of the actively mode coupled laser in terms of the FEL interaction (which theory is developed in the following chapter [4].) The latter analysis can also be readily adapted to other resonator configurations such as the Fox-Smith interferometer shown in Fig. 4.1(b). In Section II, I develop the eigenmode analysis of the perfectly tuned Michelson resonator FEL, and in Section III, I derive the passive frequency response of the three-mirror resonator from which the stable longitudinal mode structure is extracted. Finally, in Section IV, I present numerical simulations which illustrate the analytical results.

II. EIGENMODE ANALYSIS OF N COUPLED LASERS

Conventional rf linac-driven FELs, as noted above, usually operate with a large number N of optical pulses circulating in the cavity at any time, and pulses which build up independently from noise can be considered as N separate lasers driven independently by fresh electron pulses on every pass. However, if an interferometer is used to couple a fraction of each pulse to its successors, then the resulting operation can be viewed as a kind of injection locking or injection seeding of one laser by the others as the lasers turn on from noise. The coupled pulse formalism derives from this viewpoint, the eigenmode analysis motivated by the search for stable configurations which can support the injection locking process in a cyclical fashion. The performance of the system depends on the beamsplitter reflectance, the phase offset of the secondary mirror on the scale of an optical wavelength, and the detunings of the two coupled resonators relative to their respective synchronous lengths (as determined by the arrival times of the incoming electron micropulses). In the following analysis, we assume that these relative detunings are identical and yield an optimized gain interaction with the electron beam. In particular, we assume that the delay in the secondary arm of the interferometer is an exact integral multiple of the rf period, so that successive pulses are perfectly overlapped at the beamsplitter.

A. Formalism

For simplicity, we first consider the coupling of $N = 4$ optical pulses circulating within the short cavity of a Michelson mirror resonator (the primary linear cavity), with $N+1 = 5$ pulses in the long cavity, so that the primary pulses are *delayed* by one rf period in the secondary arm of the interferometer. The analysis can be easily extended to any number of pulses. We assume a net round trip energy gain of 2α , a beamsplitter of reflectance r^2 and transmittance $t^2 = 1 - r^2$, and a relative phase offset of φ at the secondary mirror. Let the complex amplitudes of these pulses be represented by $E_q(n)$, where q labels the pulses within the primary cavity ($q = 1, \dots, N$) and n labels the pass number. Then the following set of equations describes the pass to pass evolution of the coupled pulses which arrive in the order $E_1(n), E_2(n), E_3(n), E_4(n), E_1(n+1), E_2(n+1)$, etc.

$$E_1(n+1) = e^\alpha [E_1(n) t^2 + E_4(n-1) r^2 e^{i\varphi}] , \quad (4.1)$$

$$E_2(n+1) = e^\alpha [E_2(n) t^2 + E_1(n) r^2 e^{i\varphi}] , \quad (4.2)$$

$$E_3(n+1) = e^\alpha [E_3(n) t^2 + E_2(n) r^2 e^{i\varphi}] , \quad (4.3)$$

$$E_4(n+1) = e^\alpha [E_4(n) t^2 + E_3(n) r^2 e^{i\varphi}] . \quad (4.4)$$

Defining the column vector of pulses on pass n as

$$|E(n)\rangle = \begin{bmatrix} E_4(n-1) \\ E_1(n) \\ E_2(n) \\ E_3(n) \\ E_4(n) \end{bmatrix} , \quad (4.5)$$

we may recast equations (4.1-4.4) into the matrix format

$$|E(n+1)\rangle = \mathbf{M} |E(n)\rangle , \quad (4.6)$$

where the coupling matrix \mathbf{M} has elements

$$\mathbf{M} = \begin{bmatrix} 0 & 0 & 0 & 0 & 1 \\ e^{\alpha r^2} e^{i\varphi} & e^{\alpha t^2} & 0 & 0 & 0 \\ 0 & e^{\alpha r^2} e^{i\varphi} & e^{\alpha t^2} & 0 & 0 \\ 0 & 0 & e^{\alpha r^2} e^{i\varphi} & e^{\alpha t^2} & 0 \\ 0 & 0 & 0 & e^{\alpha r^2} e^{i\varphi} & e^{\alpha t^2} \end{bmatrix} . \quad (4.7)$$

We now search for solutions of (4.6) of the form

$$E_q(n+1) = \gamma E_q(n) = \gamma^{n+1} E_q(0) \quad (4.8)$$

where γ is independent of n and is by definition the same for all N pulses (this is required by the symmetry of the system with respect to time displacement). The equivalent eigenvalue problem can be written

$$\gamma |V_i\rangle = M |V_i\rangle \quad (4.9)$$

where the eigenvalues γ_i are the $N+1$ distinct solutions of the characteristic equation

$$\gamma(\gamma - e^{\alpha t^2})^N = (e^{\alpha t^2} e^{i\phi})^N, \quad (4.10)$$

which may also be written as

$$\gamma = e^{\alpha} \left[t^2 + r^2 \frac{\exp i(\phi - \frac{2\pi m}{N})}{\gamma^{1/N}} \right], \quad m = 0, \dots, N-1. \quad (4.11)$$

The corresponding $N+1$ eigenvectors $|V_i\rangle$ form a complete set for the solution of the initial value problem, defined by the requirement of specifying a unique superposition of the eigenvectors $|V_i\rangle$ for any initial pulse distribution. This assertion can be justified physically by noting that there are a total of $N+1$ degrees of freedom which must be specified as part of the initial value problem, corresponding to the N pulses in the primary cavity plus the pulse in the secondary arm which couples to the first pulse in the primary cavity. Therefore, the $N+1$ eigenvectors are sufficient to form any initial superposition, which we write as

$$|E(0)\rangle = \sum_{i=1}^{N+1} c_i |V_i\rangle. \quad (4.12)$$

$$\text{Furthermore, } |E(n)\rangle = M^n |E(0)\rangle = \sum_{i=1}^{N+1} c_i M^n |V_i\rangle = \sum_{i=1}^{N+1} c_i \gamma_i^n |V_i\rangle. \quad (4.13)$$

It is evident that as the pulses evolve from pass to pass, the eigenvector(s) with the largest eigenvalue(s) will dominate the structure of the pulse train.

B. Biorthogonality

It can readily be shown that M does not commute with its adjoint M^\dagger (i.e. it is not a *normal* matrix). Therefore, eigenvectors corresponding to distinct eigenvalues are generally non-orthogonal, and the coefficients c_i in (4.12) cannot be calculated directly from the projections of the initial column vector $|E(0)\rangle$ onto the eigenvectors $|V_i\rangle$. Nevertheless, if one considers the adjoint eigenvalue problem

$$\xi_i | \underline{U}_i \rangle = \mathcal{M}^\dagger | \underline{U}_i \rangle , \quad (4.14)$$

then it is possible to show [5] that the eigenvalues ξ_i of the adjoint equation are related to the eigenvalues γ_i by

$$\xi_i = \gamma_i^* \quad (4.15)$$

and that the corresponding (appropriately normalized) eigenvectors satisfy the orthonormality relation:

$$\langle \underline{U}_i | \underline{V}_j \rangle = \delta_{ij} . \quad (4.16)$$

This property of the vectors $| \underline{U}_i \rangle$ and $| \underline{V}_i \rangle$ is known as *biorthogonality*, and is of theoretical interest because it allows a rigorous solution of the initial value problem in a completely analogous manner to the usual orthogonal projection. In particular, we obtain the following solution for the coefficients c_i in (4.12):

$$c_i = \langle \underline{U}_i | \underline{E}(0) \rangle . \quad (4.17)$$

Explicitly, the biorthogonal eigenvectors $| \underline{U}_i \rangle$ can be constructed from the elements of the $| \underline{V}_i \rangle$ as follows:

$$| \underline{V}_i \rangle = \begin{bmatrix} e_4(-1) \\ e_1(0) \\ e_2(0) \\ e_3(0) \\ e_4(0) \end{bmatrix}_i \quad \text{and} \quad | \underline{U}_i \rangle = \begin{bmatrix} [e^{\alpha r^2} e^{-i\phi}] e_4^*(-1) \\ e_4^*(0) \\ e_3^*(0) \\ e_2^*(0) \\ e_1^*(0) \end{bmatrix}_i . \quad (4.18)$$

The biorthogonality property is completely equivalent to the non-orthogonality of the $| \underline{V}_i \rangle$ in describing the evolution of the pulse train. For example, consider the total energy $P(n)$ on a given pass n , which we define as

$$P(n) = \langle \underline{E}(n) | \underline{E}(n) \rangle , \quad (4.19)$$

where $| \underline{E}(n) \rangle$ is given by (4.13). This quantity is of considerable practical interest for calculating the leakage losses due to destructive interference of the pulses at the beamsplitter. Explicit calculation yields

$$P(n) = \sum_i c_i^* \langle \underline{V}_i | \mathcal{M}^{\dagger n} \sum_j c_j \mathcal{M}^n | \underline{V}_j \rangle \quad (4.20)$$

$$= \sum_i \sum_j c_i^* c_j \sum_k \langle \underline{V}_i | \mathcal{M}^{\dagger n} | \underline{U}_k \rangle \langle \underline{U}_k | \mathcal{M}^n | \underline{V}_j \rangle \quad (4.21)$$

where we have inserted the closure relation

$$\hat{I} = \sum_k |\underline{U}_k\rangle\langle\underline{V}_k| \quad (4.22)$$

for the complete bases of biorthogonal eigenmodes $|\underline{V}_k\rangle$, $|\underline{U}_k\rangle$; this relation is analogous to the one for orthonormal bases that is familiar from quantum mechanics [6]. Using the eigenvalue equations (4.9) and (4.14), and the biorthogonality relations (4.15) and (4.16), we then obtain

$$P(n) = \sum_i \sum_j c_i^* c_j \sum_k \langle \underline{V}_i | \gamma_k^{*n} | \underline{U}_k \rangle \langle \underline{V}_k | \gamma_j^n | \underline{V}_j \rangle \quad (4.23)$$

$$= \sum_i \sum_j c_i^* c_j \gamma_j^n \sum_k \gamma_k^{*n} \delta_{ik} \langle \underline{V}_k | \underline{V}_j \rangle \quad (4.24)$$

$$= \sum_i |c_i|^2 |\gamma_i|^{2n} + \sum_i \sum_{j \neq i} c_i^* c_j \gamma_i^{*n} \gamma_j^n \langle \underline{V}_i | \underline{V}_j \rangle \quad (4.25)$$

where the $|\underline{V}_i\rangle$ are assumed to be normalized to unit length.

We note that the result (4.25) would obtain by directly squaring the absolute value of the last equality in (4.13), and that the second term would be absent if the eigenvectors were orthogonal. It is therefore interesting to examine the degree of non-orthogonality of the $|\underline{V}_i\rangle$ to determine under which conditions, if any, the second term in (4.25) may be neglected. To this end, I have plotted in Fig. 4.2 the magnitudes of the mutual projections $|\langle \underline{V}_i | \underline{V}_j \rangle|$ versus the products of the corresponding eigenvalues $|\gamma_i^* \gamma_j|$ for the case of $N = 35$ pulses and a beamsplitter reflectance of $r^2 = 50\%$. The qualitative nature of the graph

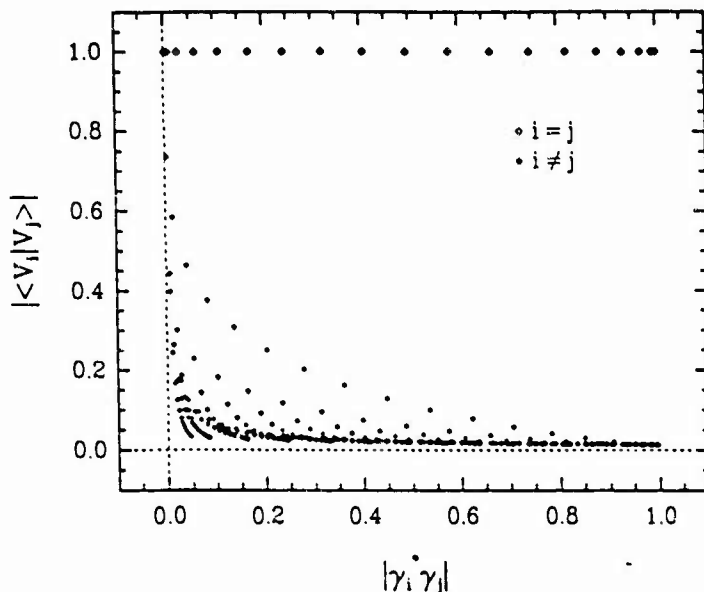


Fig. 4.2 Mutual projections of the non-orthogonal eigenmodes vs. the products of their eigenvalues, for a Michelson mirror resonator with $N = 35$ pulses and a beamsplitter reflectance of $r^2 = 50\%$.

is independent of both r^2 and N . We see that for $i \neq j$, the non-orthogonality can be quite large (as high as $|\langle \underline{V}_i | \underline{V}_j \rangle| = 0.74$), but that these extremes only occur for small products of the eigenvalues; *eigenvectors corresponding to larger products of the eigenvalues have a greater degree of mutual orthogonality.* As a result, the eigenvectors with the greatest non-orthogonality will decay away after relatively few passes, leaving only the eigenvectors with the largest eigenvalues and the greatest degree of mutual orthogonality to support the evolution of the pulse train. In paragraph D, we will derive an approximate solution using orthogonal vectors, and in Section III, we will discuss the physical origin of the non-orthogonality.

C. Equivalent matrix formulation

The coupled pulse problem with $N = 4$ pulses in the primary cavity assumed that a fraction r^2 of each pulse is delayed by one rf period before coupling to the succeeding pulse. An equivalent formulation can be made with $N+1 = 5$ pulses in the primary cavity in which a fraction $t^2 = 1 - r^2$ of each pulse is *advanced* by one rf period before coupling to the preceding pulse. The coupled pulse equations in this case can then be written

$$E_1(n+1) = e^\alpha [E_1(n) r^2 e^{i\varphi} + E_2(n) t^2] , \quad (4.26)$$

$$E_2(n+1) = e^\alpha [E_2(n) r^2 e^{i\varphi} + E_3(n) t^2] , \quad (4.27)$$

$$E_3(n+1) = e^\alpha [E_3(n) r^2 e^{i\varphi} + E_4(n) t^2] , \quad (4.28)$$

$$E_4(n+1) = e^\alpha [E_4(n) r^2 e^{i\varphi} + E_5(n) t^2] , \quad (4.29)$$

$$E_5(n+1) = e^\alpha [E_5(n) r^2 e^{i\varphi} + E_1(n+1) t^2] \quad (4.30)$$

$$\cdot = e^\alpha [E_5(n) r^2 e^{i\varphi} + e^\alpha E_1(n) r^2 t^2 e^{i\varphi} + e^\alpha E_2(n) t^4] . \quad (4.31)$$

The eigenmodes $|\underline{Y}_i\rangle$ of the corresponding matrix equation are identical to the $|\underline{V}_i\rangle$ of the original formulation with $N = 4$ pulses, but the eigenvalues η_i are different. The equality of the eigenmodes follows from the fact that the two formulations are physically equivalent, but the eigenvalues are different because the original problem describes the evolution of every fourth pulse, the latter problem the evolution of every fifth pulse. Indeed, one finds that $|\gamma_i|^5 = |\eta_i|^4$.

D. Approximate solutions; physical interpretation

A useful approximation to the above analysis is obtained for cases in which N is very large (good results are obtained for $N \gtrsim 10$). In particular, we see from (4.11) that as $N \rightarrow \infty$, the denominator of the second term ($\gamma^{1/N}$) approaches unity for any value of γ .

The number of eigenvalues is then essentially reduced to N, corresponding to the N solutions

$$\gamma_m' = e^{\alpha} \left[t^2 + r^2 \exp i\left(\phi - \frac{2\pi m}{N}\right) \right], \quad m = 0, \dots, N-1. \quad (4.32)$$

The number of eigenvectors is still rigorously N+1, but the eigenvector corresponding to the smallest eigenvalue will decay to a negligible magnitude after only a few passes. Therefore, neglecting it altogether will not appreciably affect the evolution of the pulse train as the number of passes increases. In fact, the N eigenvalues (4.32) are exact solutions of the modified eigenvalue problem

$$\gamma_m' |\underline{V}_m' \rangle = \mathbf{M}' |\underline{V}_m' \rangle, \quad (4.33)$$

for which the modified N x N coupling matrix \mathbf{M}' has elements

$$\mathbf{M}' = \begin{bmatrix} e^{\alpha} t^2 & 0 & 0 & e^{\alpha} r^2 e^{i\phi} \\ e^{\alpha} r^2 e^{i\phi} & e^{\alpha} t^2 & 0 & 0 \\ 0 & e^{\alpha} r^2 e^{i\phi} & e^{\alpha} t^2 & 0 \\ 0 & 0 & e^{\alpha} r^2 e^{i\phi} & e^{\alpha} t^2 \end{bmatrix}. \quad (4.34)$$

The corresponding eigenvectors are mutually orthogonal, which results from the fact that \mathbf{M}' is a normal matrix (i.e. $\mathbf{M}' \mathbf{M}'^\dagger = \mathbf{M}'^\dagger \mathbf{M}'$).

The approximation consists of replacing the N+1 non-orthogonal eigenvectors of (4.9) with the N orthogonal eigenvectors of (4.33) in the superposition describing the evolution of the pulse train; these N orthogonal eigenvectors have elements

$$|\underline{V}_m' \rangle = \frac{1}{\sqrt{N}} \begin{bmatrix} 1 \\ \exp(i\frac{2\pi m}{N}) \\ \exp(i\frac{4\pi m}{N}) \\ \exp(i\frac{6\pi m}{N}) \\ \vdots \\ N \text{ elements} \end{bmatrix}. \quad (4.35)$$

To justify this approximation physically, we note that the non-orthogonality of the N+1 eigenvectors $|\underline{V}_i \rangle$ results from the formal asymmetry of (4.1) with respect to the remaining coupled pulse equations, in which the first pulse on pass n+1 couples the pulses from two previous passes instead of only the preceding pass n. However, if the number of pulses N

is large, then after many passes they will begin to evolve more slowly from pass to pass, and on this basis we may replace pulse $E_N(n-1)$ with pulse $E_N(n)$ in the formulation of the coupled pulse equation (4.1). This single substitution leads to the modified eigenvalue problem (4.33).

The orthogonal eigenvectors $|V_m\rangle$ can be given a straightforward physical interpretation. In the frequency domain, they correspond to distinct spectral modes displaced from one another by one primary cavity axial mode spacing (as can be demonstrated by computing the Fourier series for each eigenvector), and therefore fill the entire free spectral range of the multiple mirror resonator. In the time domain, they represent configurations in which each pulse differs in phase from its successor by $2\pi m/N$. This ensures that as the phase information propagates along the pulse train, a given pulse in the primary cavity will remain in phase with itself from pass to pass. For any arbitrary value of ϕ , one of the eigenvectors will have the largest eigenvalue and will dominate the spectrum as the macropulse evolves. Therefore, each mode can be selected in turn by varying the value of ϕ at the secondary mirror. This property of the resonator is important for applications to spectroscopy.

The squares of the absolute values of the eigenvalues (with the gain e^α omitted) correspond to the relative growth rates and are found from (4.32) to be

$$|\gamma_m|^2 = 1 - 2r^2 t^2 \left[1 - \cos\left(\phi - \frac{2\pi m}{N}\right) \right] . \quad (4.36)$$

The corresponding mode losses are

$$\delta_m \equiv 1 - |\gamma_m|^2 = 2r^2 t^2 \left[1 - \cos\left(\phi - \frac{2\pi m}{N}\right) \right] , \quad (4.37)$$

and result from destructive interference of the eigenmodes at the beamsplitter. As a numerical example, consider a Michelson mirror resonator with $N = 35$ circulating pulses in the primary cavity and a beamsplitter reflectance of $r^2 = 50\%$. In this case the relative single pass power growth for the dominant mode and its two nearest neighbors ($\phi = 0; m = 0, 1, 2$) is $1 : 0.9920 : 0.9681$. The relative power after 300 passes is therefore $1 : 0.09 : 6(10^{-5})$. This number of passes corresponds to a time of $4 \mu s$ for the Mark III FEL, showing that appreciable mode decay can result in feasible macropulse durations.

Finally, we may estimate the total leakage losses due to destructive interference of the randomly phased pulses at the beamsplitter. The total pulse energy $P(n)$ in the resonator on pass n was given in (4.25), and the total losses are

$$\delta_{TOT}(n) = \frac{P(n-1) - P(n)}{P(n-1)} = 1 - \frac{P(n)}{P(n-1)} . \quad (4.38)$$

If the N pulses in the laser start up independently from electron shot noise, then we may

assume that the initial pulses are randomly phased and that all of the coefficients c_i in (4.25) are equal. If we also assume that the second term in (4.25) is absent, then the losses at the beam splitter become

$$\delta_{\text{TOT}}(n) = 1 - \frac{\sum_{m=0}^{N-1} \left\{ 1 - 2r^2 t^2 \left[1 - \cos\left(\phi - \frac{2\pi m}{N}\right) \right] \right\}^n}{\sum_{m=0}^{N-1} \left\{ 1 - 2r^2 t^2 \left[1 - \cos\left(\phi - \frac{2\pi m}{N}\right) \right] \right\}^{n-1}}. \quad (4.39)$$

Although this expression cannot be simplified, it is readily evaluated on a small computer. Figure 4.3 shows the error in the estimated leakage losses incurred by using (4.39), instead of the result (4.38) in which $P(n)$ is given by (4.25). As suggested by the discussion at the end of paragraph B, the approximation significantly improves with the number of passes.

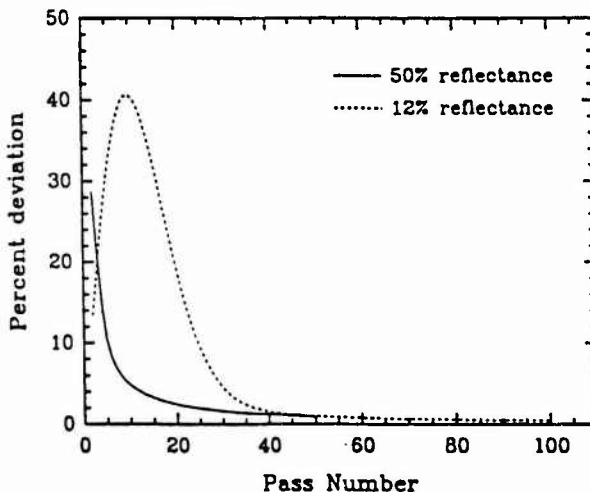


Fig. 4.3 Percent error in calculating the total leakage losses for $N = 35$ pulses using the approximate eigenvalues from Section II.D instead of the exact eigenvalues corresponding to the non-orthogonal eigenmodes, for two values of the beam splitter reflectance.

III. PASSIVE MODE STRUCTURE OF THE MICHELSON RESONATOR

The spectral energy distribution of the circulating optical field inside a laser cavity consists, in general, of a superposition of discrete longitudinal cavity modes oscillating with frequencies ω_n . For a plane-wave optical field with a slowly varying amplitude $E(t)$ and phase $\psi(t)$, this superposition can be written as the modal expansion [7]

$$E(t) e^{i\psi(t)} e^{-i\omega t} = \sum_n E_n(t) e^{-i\omega_n t}, \quad (4.40)$$

in which the $E_n(t)$ are complex valued spectral components which have a slowly varying time dependence only over many passes in the cavity, and essentially describe the long term spectral evolution of the laser field. The Michelson mirror resonator actually consists of

two coupled linear resonators, each possessing its own complete set of longitudinal modes appropriate for the superposition of optical fields in the respective uncoupled resonators. However, it is clear that neither of these sets of modes can completely describe the field in the Michelson mirror resonator, because the mode spacings are incommensurate with one another due to the difference in the cavity lengths. To obtain an appropriate set of longitudinal modes, one must consider the frequency response of the linear resonators when coupled in the Michelson configuration.

A. Frequency response

The frequency response of an arbitrary resonator is calculated by coupling a tunable CW source of fixed amplitude into the cavity through the output coupler. The discrete resonances of the resulting circulating field comprise the only frequencies which can be supported by the resonator, and therefore yield a complete set of longitudinal modes. The generalized frequency response of a two-mirror cavity with length L_c and complex mirror reflectivities r_1 and r_2 , obtained in this manner, is [8]

$$\left| \frac{E_{\text{circ}}}{E_{\text{inc}}} \right|^2 = \left| \frac{1 - (\delta_c/2)}{1 - e^{-\delta_c/2} e^{\alpha} r_1 r_2 \exp[i\omega \frac{2L_c}{c}]} \right|^2 \quad (4.41)$$

where E_{inc} and E_{circ} are the incident and circulating field amplitudes, δ_c is the round trip power loss due to diffraction and output coupling, and 2α is the round trip power gain.

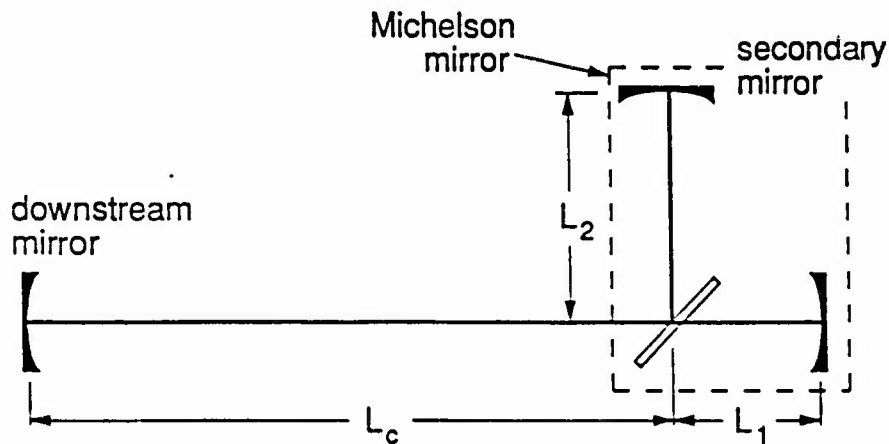


Fig. 4.4 Definition of the cavity lengths in a Michelson mirror resonator. The length L of the primary linear cavity is $L = L_c + L_1$.

We take the two cavity mirrors to be a perfect reflector ($r_1 = 1$) and the Michelson mirror shown in Fig. 4.4, for which the reflectance r_2 , assuming perfectly reflecting mirrors, is

$$r_2 = r^2 \exp\left[i\omega \frac{2L_2}{c}\right] + t^2 \exp\left[i\omega \frac{2L_1}{c}\right] \quad (4.42)$$

Here, r^2 is reflectance of the beamsplitter and $t^2 = 1 - r^2$ is the transmittance. If we define the length L of the primary cavity to be

$$L = L_c + L_1 , \quad (4.43)$$

and let the round trip time equal an integral number N of rf periods, then by introducing a delay of one rf period in the secondary arm of the interferometer we may write

$$\frac{\omega}{c} 2(L_2 - L_1) = \frac{\omega}{c} \frac{2L}{N} - \varphi , \quad (4.44)$$

where φ is a residual phase offset on the scale of an optical wavelength. Substituting (4.42), (4.43), and (4.44) into the frequency response (4.41) yields the final result

$$\left| \frac{E_{\text{circ}}}{E_{\text{inc}}} \right|^2 = \left| \frac{1 - (\delta_c/2)}{1 - e^{-\delta_c/2} e^{i\alpha} e^{i2\pi\Delta f_m} \left[1 - \exp i \left[\frac{2\pi\Delta f_m}{N} - \varphi \right] \right]} \right|^2 \quad (4.45)$$

where Δf_m is the frequency in units of the axial mode spacing of the primary cavity:

$$\Delta f_m = \Delta f \cdot \frac{2L}{c} . \quad (4.46)$$

Figure 4.5 shows the normalized frequency response of a Michelson mirror resonator with 7 % net round trip power losses, a beamsplitter reflectance of $r^2 = 50$ %, and a phase offset of $\varphi = 0$ at the secondary mirror. Figures (a), (b), and (c) are for $N = 10, 20$, and 30 rf periods respectively, with the abscissa in units of the $c/2L$ round trip frequency of the primary linear cavity.

B. Resonant frequencies and losses

We see from Fig. 4.5 that the dominant modes are separated by the rf frequency, and that the satellite modes oscillate with reduced amplitudes resulting from increased interference losses at the beamsplitter. The resonances are roughly separated in frequency by the axial mode spacing of the primary cavity, yielding a total of N modes per rf interval. This is the same result obtained from the approximate eigenmode solution in Section II. Furthermore, we may identify the outer bracket in the denominator of (4.45) as a complex 'loss factor' γ , in analogy with the identification of $e^{-\delta_c/2} \approx 1 - \delta_c/2$ as the loss factor due to the loss $\delta_c/2$. Setting $\Delta f_m \approx m$ in (4.45), where m is an integer, we then obtain

$$|\gamma|^2 = 1 - 2r^2t^2 \left[1 - \cos \left(\frac{2\pi m}{N} - \varphi \right) \right] , \quad (4.47)$$

which is identical to the result obtained from the eigenmode analysis for the coupled pulse problem. This result, together with the mode structure noted above, demonstrates the equivalence of the time domain and frequency domain analyses. The dominant modes, separated by the rf frequency, ultimately support the oscillation of the optical pulses under the

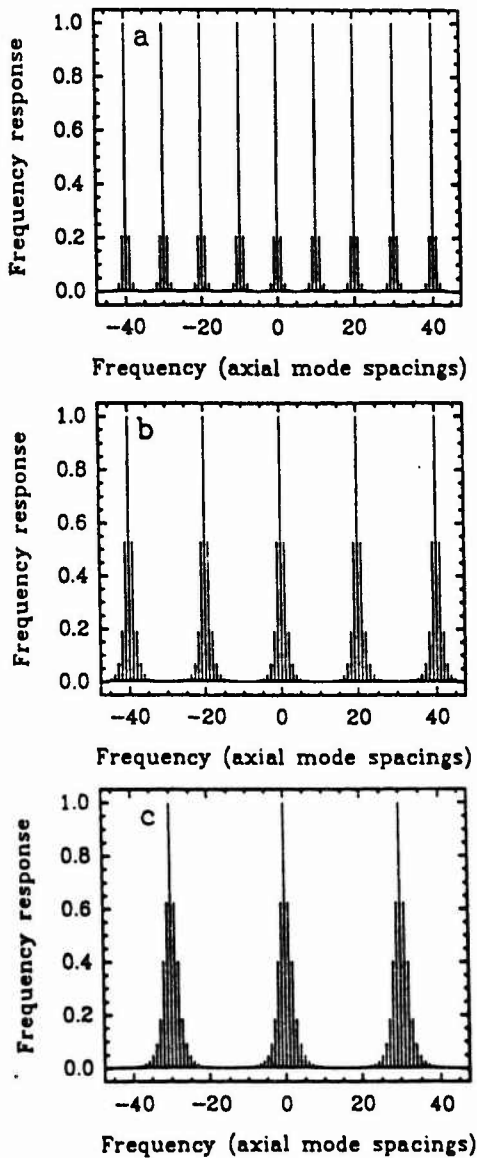


Fig. 4.5 Passive frequency response of optical resonators under CW excitation, showing the axial mode structure for a Michelson mirror resonator with a 50 % beamsplitter reflectance, a delay of 1 rf period in the secondary arm of the interferometer, and a round trip time in the primary linear cavity of: (a) $N = 10$ rf periods, (b) $N = 20$ rf periods, and (c) $N = 30$ rf periods.

influence of active mode coupling by the short electron pulses, after the remaining modes have decayed away. However, one other point should be noted concerning the process of mode decay.

The motivation for studying the passive mode structure was to determine which frequencies can be supported by the multiple mirror resonator under pulsed excitation by an electron beam. In the case of a CW excitation, the mode amplitudes derived in paragraph A do not vary with time. However, some of the 'modes' have very high losses, even on

the order of unity, and in the case of pulsed excitation these modes will decay away with rates determined by those losses. What does it mean to say that we have a 'mode' which lasts for only one or a few round trips? Clearly, such modes are not appropriate for the modal expansion indicated in (4.40), because the mode coefficients $E_n(t)$ are no longer slowly varying with time and cannot be identified by a single frequency ω_n . In fact, modes with lifetimes on the order of one round trip will have spectral widths on the order of the round trip frequency, and will therefore overlap adjacent modes. This overlap is equivalent to 'an expansion of one mode in terms of the others', and comprises the physical origin of the non-orthogonality of the modes which we discovered in Section II. As noted in Fig. 4.2, the degree of overlap is more extreme for modes with smaller eigenvalues. It is interesting that the eigenmode analysis allows us to compute these mutual projections exactly.

C. The detuned interferometer

We now extend the analysis in paragraph A to the case in which the interferometer is not perfectly tuned to the overlap of successive pulses. For simplicity, we set $\phi = 0$ and write

$$\frac{\omega}{c} 2(L_2 - L_1) = \frac{\omega}{c} \frac{2L}{N} (1 + \delta N) , \quad (4.48)$$

where δN represents the small fraction of an rf period by which the round trip time in the secondary arm is detuned. The complex loss factor γ in the denominator of (4.45) can then be rewritten

$$\gamma = \sqrt{1 - 2r^2 t^2 \left[1 - \cos \left(2\pi \Delta f_m \frac{1+\delta N}{N} \right) \right]} \exp \left[i \tan^{-1} \left(\frac{r^2 \sin \left(2\pi \Delta f_m \frac{1+\delta N}{N} \right)}{t^2 + r^2 \cos \left(2\pi \Delta f_m \frac{1+\delta N}{N} \right)} \right) \right] \quad (4.49)$$

where Δf_m is not restricted to integral values. If we let D equal an integer which represents the approximate number of rf frequency intervals by which Δf_m is detuned from some reference mode, we may then introduce the small quantity

$$2\pi \left(\Delta f_m \frac{1+\delta N}{N} - D \right) \quad (4.50)$$

and expand (4.49) in small arguments of the trigonometric terms to obtain

$$\gamma \approx \exp \left[-2r^2 t^2 \pi^2 \left(\Delta f_m \frac{1+\delta N}{N} - D \right)^2 \right] \exp \left[i 2\pi r^2 \left(\Delta f_m \frac{1+\delta N}{N} - D \right) \right] . \quad (4.51)$$

In this approximation the frequency response (4.45) of the resonator becomes

$$\left| \frac{E_{\text{circ}}}{E_{\text{inc}}} \right|^2 = \left| \frac{1 - (\delta_c/2)}{1 - \exp \left[\alpha - \frac{\delta_c}{2} - 2r^2 t^2 \pi^2 \left(\Delta f_m \frac{1+\delta N}{N} - D \right)^2 \right] \exp \left[i 2\pi \Delta f_m + i 2\pi r^2 \left(\Delta f_m \frac{1+\delta N}{N} - D \right) \right]} \right|^2 \quad (4.52)$$

in which the loss and resonance terms have been grouped into the exponentials. Resonances

occur when

$$2\pi\Delta f_m + 2\pi r^2 \left(\Delta f_m \frac{1+\delta N}{N} - D \right) = 2\pi(ND + m) \quad (4.53)$$

where $m \ll N$ is a second integer. The corresponding resonant frequencies are

$$\Delta f_m = ND + \frac{m - r^2 D \delta N}{1 + r^2/N}, \quad (4.54)$$

and the *power* losses at the resonant frequencies are

$$\delta_D = \delta_c + 4\pi^2 r^2 t^2 \left(\frac{m}{N} + D \delta N \right)^2 \quad (4.55)$$

in which all terms of order $(\delta N/N)$ or $(1/N^2)$ have been neglected relative to the remaining terms. Note that for $\delta N = 0$, this is the same loss derived from (4.47) or (4.36) for modes separated by the axial mode spacing of the primary linear cavity. However, it is important to note that the preceding method of extracting the resonant frequencies and mode losses can be applied to the frequency response of any resonator configuration with arbitrary mirror detunings.

Hypermodes are identified by a given m , and correspond to sets of longitudinal modes that are separated by the rf frequency. If the interferometer is perfectly tuned ($\delta N = 0$), then all of the longitudinal modes in a given hypermode will have the same loss, but different hypermodes will have different losses depending on m . If $\delta N \neq 0$, then the longitudinal modes *within* a given hypermode will have different losses depending on D , and the spacing between the modes in a given hypermode will deviate from the exact rf frequency, depending on δN . This last point is of particular importance for the analysis of the actively mode coupled laser in the presence of a pulsed electron beam, the theory for which is developed in the following chapter. For that analysis, we provide the following computation for the frequency spacing between the axial modes of a given detuned hypermode. By approximating the denominator in the second term of (4.54) to unity, we have from (4.46)

$$\Delta f^{(D+1)} - \Delta f^{(D)} \equiv \frac{c}{2L} [\Delta f_m^{(D+1)} - \Delta f_m^{(D)}] = \frac{c}{2L} (N - r^2 \delta N). \quad (4.56)$$

Note that $N \equiv v_{rf} \frac{2L_0}{c}$ for some ideal cavity length L_0 , where v_{rf} is the rf frequency, but that L appearing in (4.56) can deviate from this ideal length by δL . This quantity represents the cavity detuning of the primary linear cavity relative to the incoming electron pulses. Expanding (4.56) to the lowest order in δL and δN , and defining $\delta L \equiv c \delta T_c / 2$ and $\delta N \equiv \delta T_M v_{rf}$, yields

$$\Delta f^{(D+1)} - \Delta f^{(D)} = v_{rf} - v_{rf} \frac{c}{2L_0} (\delta T_c + r^2 \delta T_M) \quad (4.57)$$

where δT_c and δT_M represent the round trip temporal detunings of the linear cavity and the interferometer respectively ($\delta T_{c,M} > 0$ for cavities *longer* than the synchronous length). With the definitions $\omega_{ax} \equiv 2\pi[\Delta f^{(D+1)} - \Delta f^{(D)}]$, $\omega_{rf} \equiv 2\pi\nu_{rf}$, and $T_c \equiv 2L/c$, this last result can be written

$$T_c(\omega_{rf} - \omega_{ax}) = \omega_{rf}(\delta T_c + r^2 \delta T_M) \quad . \quad (4.58)$$

The interpretation of this result is straightforward: if the beamsplitter reflectance $r^2 = 0$, then the only contribution to the cavity detuning comes from the downstream mirror of the primary cavity. If $r^2 = 1$, then we have a two-mirror cavity consisting of the downstream mirror and the second reflection mirror, and both mirrors contribute equally to the desynchronization of the optical pulses with respect to the incoming electron pulses. For $0 < r^2 < 1$, the result is interpolated.

IV. NUMERICAL SIMULATIONS

I have performed numerical simulations on the operation of Michelson mirror resonators in which the optical pulses build up from spontaneous radiation to full saturation. The computer code is described in Chapter 2, and essentially performs a one-dimensional integration of the coupled Maxwell-Lorentz equations for each pulse, in which the transverse coupling between the electron and optical beams is included by means of a complex filling factor appropriate to the Gaussian modes of the resonator. Shot noise is included by random modulations of the electron beam density at fixed positions within an optical wavelength and generally dominates the effect of quantum noise [9]; the latter is included in the present application to ensure that the initial optical phase of each optical pulse is completely randomized.

The Michelson mirror resonator is simulated in the following fashion. On a given pass n , each pulse $E_q(n)$ [$= E_{q,n}(t) e^{i\vartheta_{q,n}(t)}$] interacts with a fresh electron micropulse, undergoes cavity losses and cavity detuning in relation to the electron micropulses, and is then coupled to its predecessor $E_{q-1}(n)$ by means of the relations

$$E_q(n+1) = r^2 E_q(n) + r^2 E_{q-1}^d(n) e^{i\varphi} \quad (4.59)$$

for $q = 2, \dots, N$, or

$$E_1(n+1) = r^2 E_1(n) + r^2 E_N^d(n-1) e^{i\varphi} \quad (4.60)$$

for $q = 1$. The total leakage power is also calculated on each pass n according to the summation

$$P_{\text{leak}}(n) = \sum_{q=1}^N P_q(n) \quad , \quad (4.61)$$

Parameter	Definition	Simulation value
<i>Optical beam parameters</i>		
λ	Resonant optical wavelength	3.35 μm
N	Number of circulating optical pulses	35
δ_c	Cavity losses	7.3 %
δ_{out}	Output coupling	5.5 %
z_R	Rayleigh range	73.08 cm
<i>Electron beam parameters</i>		
γ	Electron beam energy / mc^2	83.19
τ_p	Electron pulse duration	4 ps
I	Peak electron current	18.8 A
v_{rf}	RF frequency	2.857 GHz
ϵ_x	Normalized horizontal emittance ($1/e$)	$8\pi \text{ mm}\cdot\text{mrad}$
ϵ_y	Normalized vertical emittance ($1/e$)	$4\pi \text{ mm}\cdot\text{mrad}$
β_x	Horizontal 'Rayleigh range'	45 cm
<i>Wiggler parameters</i>		
N_w	Number of wiggler periods	47
L_w	Wiggler length	108.1 cm
λ_w	Wiggler period	2.3 cm

Table 4.1 Parameters used in the Michelson resonator simulations on the Mark III FEL.

where

$$P_q(n) = \left| \pi E_q(n) - \pi E_{q-1}^d(n) e^{i\phi} \right|^2 \quad (4.62)$$

for $q = 2, \dots, N$, or

$$P_1(n) = \left| \pi E_1(n) - \pi E_N^d(n-1) e^{i\phi} \right|^2 \quad (4.63)$$

for $q = 1$. The superscript d indicates relative cavity length detuning at the secondary mirror prior to coupling, and is performed by shifting the entire slowly varying optical envelope and phase in the numerical window with linear interpolation between the sample points (the effects of changing the relative cavity detunings between the two coupled resonators were only qualitatively studied in the present work; more extensive quantitative studies are reported in the following chapter.) The phase offset $e^{i\phi}$ is performed by direct multiplication independently of the cavity detuning, and the above steps are then repeated for pass

$n+1$ using the pulses $E_q(n+1)$. The parameters for these simulations are appropriate to those of the Mark III FEL and are listed in Table 4.1.

Figure 4.6 illustrates the previous assertion that the surviving spectral mode can be selected by varying the phase offset φ at the secondary mirror. In these simulations the primary linear cavity contains $N = 4$ circulating pulses, the beamsplitter reflectance is $r^2 = 50\%$, and the relative cavity length detuning in the interferometer is zero. We see that the relative phase difference between successive optical pulses at the end of the macropulse exhibits a discrete jump of $\Delta\vartheta = \pi/2$ when the relative phase offset at the secondary mirror crosses $\varphi = \pi/4$; similar jumps would also occur at phase offsets of $\varphi = 3\pi/4, 5\pi/4$, and $7\pi/4$. This optical phase difference is calculated as an RMS average across the temporal profile of each pair of adjacent pulses ($q, q+1$) with a weighting factor equal to the geometric mean of the powers at each sample point. The differences for each of the $N = 4$ pairs of adjacent pulses are then averaged.

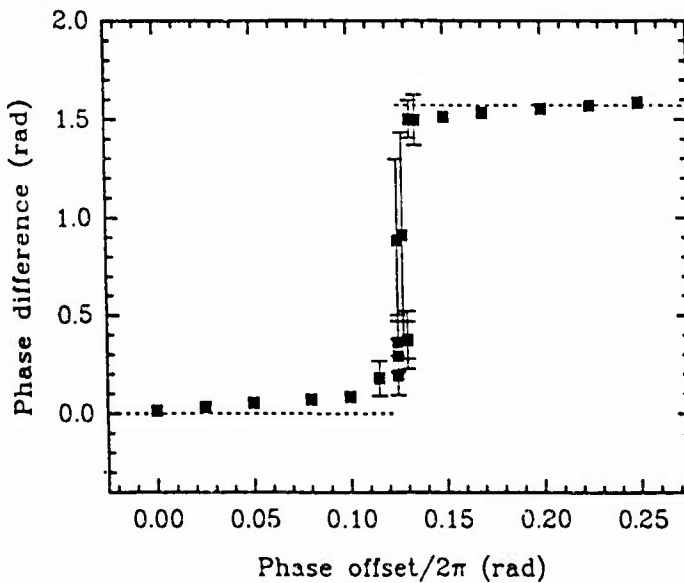


Fig. 4.6 Simulations showing the phase difference between adjacent optical pulses at the end of the macropulse (100 passes), as a function of the phase offset at the secondary mirror, in a Michelson resonator FEL with $N = 4$ circulating pulses in the primary linear cavity and a beamsplitter reflectance of 50 %.

The discrete phase difference between the pulses is a manifestation of a single hypermode in the axial mode spectrum. However, the optical macropulses exhibit increased losses for phase offsets near the discontinuities. These losses are illustrated in Fig. 4.7 and result from destructive interference between successive pulses at the beamsplitter, even though the pulses are perfectly phase locked. The magnitude of these losses is given roughly by (4.37), but they can never be greater than

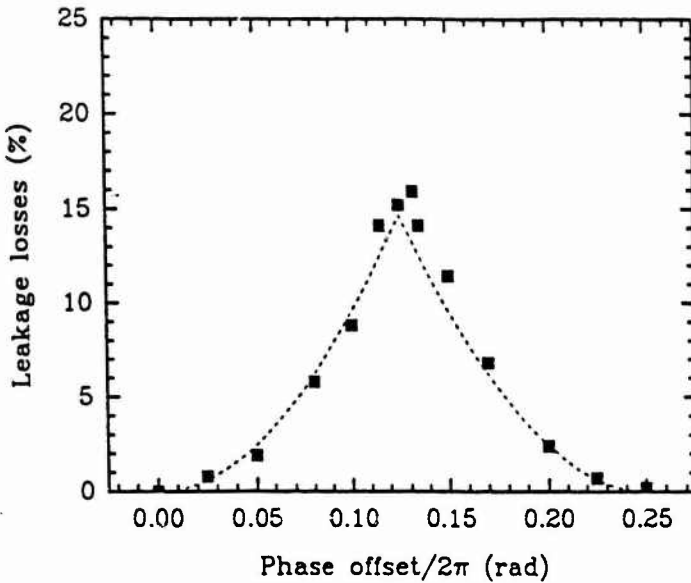


Fig. 4.7 Leakage losses due to interference in the surviving hypermodes at the end of the macropulse for the simulations in Fig. 4.6. The dashed line is the prediction of (4.37) with $N = 4$.

$$\delta_{\max} = 2 r^2 t^2 \left[1 - \cos\left(\frac{\pi}{N}\right) \right] \quad (4.64)$$

which decreases for increasing N . The dashed line in Fig. 4.7 is the analytical loss as a function of ϕ predicted from (4.37) for $N = 4$, where the hypermode number is $m = 0$ for $\phi < \pi/4$ and $m = 1$ for $\phi > \pi/4$. The agreement between the analytical and simulated losses is surprisingly good, in light of the fact that (4.37) was derived from the approximate eigenmode analysis assuming large N .

The surviving spectral modes for phase offsets of $\phi/2\pi = 0.1, 0.125$, and 0.15 are shown in Fig. 4.8. These macropulse power spectra $S(\omega)$ are calculated from the temporal averages of the amplitude E and phase ϑ along each optical pulse¹ according to

$$S(\omega) = \frac{1}{N} \left| \sum_{k=1}^N \bar{E}_k e^{i\bar{\vartheta}_k} e^{-ikT\omega} \right|^2 \quad (4.65)$$

where T is the rf period, ω the frequency, overbars denote power-weighted temporal averages, and the sum is over all N pulses in the output macropulse. The spectra for $\phi < \pi/4$ and $\phi > \pi/4$ show single hypermodes shifted by one quarter of the free spectral range of the Michelson mirror resonator, but the spectrum for $\phi = \pi/4$ shows two competing

¹ This approximation is based on the fact that temporal variations of the amplitude and phase within the pulses contribute to a broad spectral envelope, whereas the absolute fluctuations of these quantities among the pulses determine the mode structure of the pulse train.

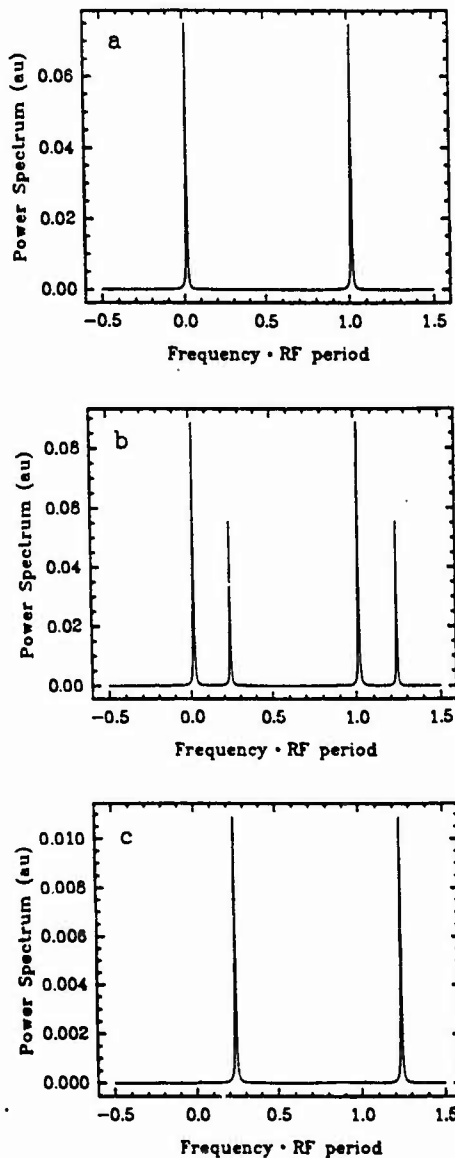


Fig. 4.8 Spectra of the simulated macropulses from Fig. 4.6 with phase offsets at the secondary mirror of: (a) $\phi/2\pi = 0.1$, (b) $\phi/2\pi = 0.125$, and (c) $\phi/2\pi = 0.15$.

hypermodes (the bias of the relative amplitudes is due to start up from noise.) An explicit calculation in the eigenmode analysis of the two surviving non-orthogonal modes for the case of $N = 4$ and $\phi = \pi/4$ can be used to reconstruct the pulse train according to the relative mode amplitudes measured from Fig. 4.8(b). Figure 4.9 displays the beating of the phase difference between adjacent pulses ($q, q+1$) in the resulting pulse train, and is seen to agree very well with the simulation in both the amplitude and period of the oscillations.

To evaluate the theory for large N , I performed simulations of the Michelson resonator FEL with $N = 35$ pulses, $r^2 = 50\%$ coupling, $\phi = 0$ phase offset at the secondary

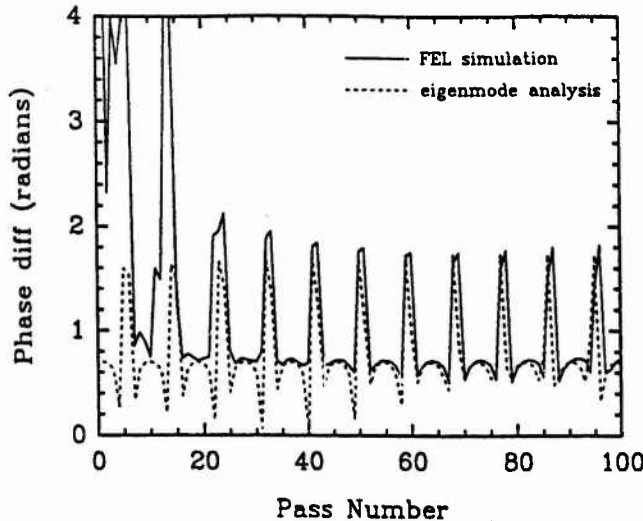


Fig. 4.9 Phase difference between two adjacent optical pulses as a function of pass number, corresponding to the simulation in Fig. 4.8(b). The solid line is the simulated phase difference, and the dashed line is the result of an explicit calculation in the eigenmode analysis using the amplitudes of the two surviving non-orthogonal modes measured from Fig. 4.8(b).

mirror, and zero relative detuning in the interferometer. Figure 4.10 compares the saturated optical pulse power and spectrum after 160 passes with a simulation using only a single pulse in the corresponding two-mirror cavity. We see that the overall spectral properties

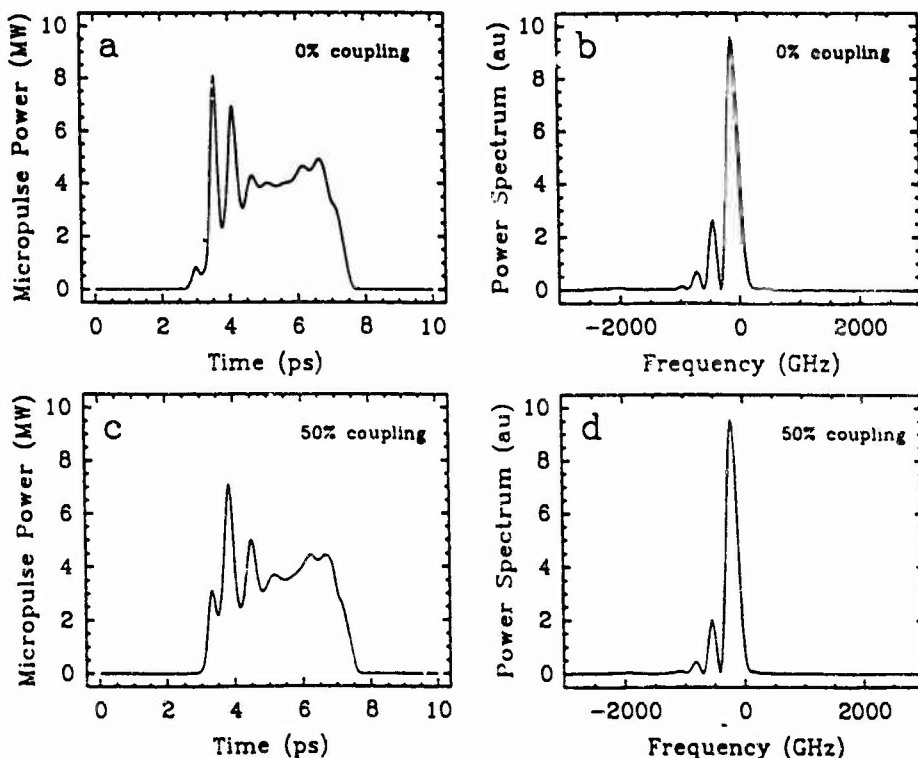


Fig. 4.10 (a), (b): Temporal and spectral structure of the optical micropulses after 160 passes, from FEL simulations of a single pulse in a two-mirror resonator. (c), (d): Same as in (a), (b), except for $N = 35$ pulses in a perfectly tuned Michelson resonator FEL with a beamsplitter reflectance of 50%

are essentially unaffected by the presence of the perfectly tuned interferometer. Both simulations show the slight formation of sidebands at a frequency of -2000 GHz, corresponding to the spikes at the front end of the optical pulses, and both simulations yield pulses of roughly the same duration and average optical power. Other properties of the laser, such as the shape of the cavity detuning curve, also turn out to be unaffected by the presence of the perfectly tuned interferometer. These results can be understood using simple arguments: in the time domain, the tuned interferometer couples phase locked optical pulses that are perfectly overlapped in time, and in the absence of leakage losses the properties of the saturated laser are then determined only by the separate interaction of the electron pulses with each optical pulse. In the frequency domain, the pulsed electron beam produces coupling only among the modes of a *given* hypermode, and the surviving hypermode of the perfectly tuned interferometer is identical to the hypermodes of the corresponding two-mirror cavity.

The solid curve in Fig. 4.11(a) shows the output power in the resulting macropulse as the laser turns on from noise, compared with the output power using the same simulation parameters for only the single pulse in the cavity (dashed curve). We see that the Michelson resonator FEL exhibits a slight delay in the turn on time due to the presence of leakage losses at the beamsplitter, but that the macropulse power otherwise grows to essentially the same level at saturation as the hypermodes and leakage losses decay from pass to pass. The corresponding leakage power is plotted as the solid curve in Fig. 4.11(b), and the theoretical leakage power is plotted as the dashed curve; this theoretical result is obtained by

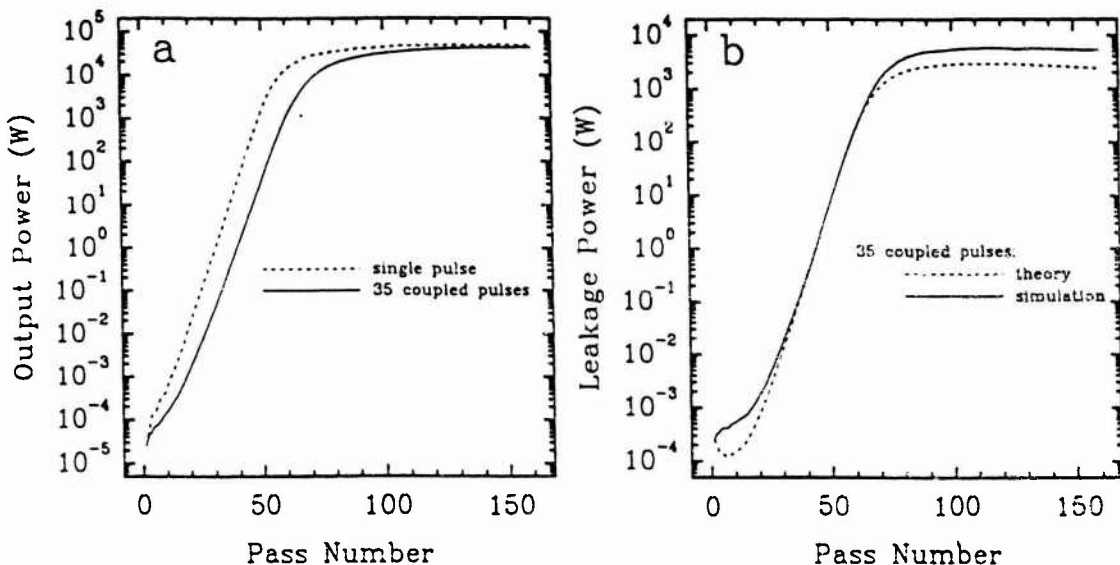


Fig. 4.11 (a): Output macropulse power for the single-pulse simulation of Fig. 4.10 (dashed line), and for the Michelson resonator simulation of Fig. 4.10 (solid line). (b): Leakage power for the Michelson resonator simulation of Fig. 4.10, showing the theoretical curve (dashed line) calculated from (4.39), and the simulated curve (solid line).

multiplying the leakage losses from (4.39) by the simulated intracavity power assuming 5.5 % output coupling. The simulated leakage power initially exceeds the theoretical prediction at the start of the macropulse (pass one to pass twenty), because the presence of spontaneous radiation in the simulations uniformly repopulates all of the modes as they decay at the beamsplitter. However, as the intracavity power grows to the onset of saturation (pass twenty to pass sixty), the relative magnitude of the spontaneous radiation is reduced and the theoretical leakage power begins to show excellent agreement with the simulated leakage power.

In the saturated regime beyond pass sixty, the simulated and theoretical leakage powers in Fig. 4.11(b) again begin to show a significant difference which is maintained to the end of the macropulse. The origin of this discrepancy lies in the theoretical calculation of the leakage losses, where we assumed in (4.39) that the surviving hypermode was the lowest order mode with $m = 0$. Figure 4.12(a) indicates that this assumption is accurate up to at least pass fifty, but Fig. 4.12(b) shows that the surviving mode at saturation is $m = 1$. Therefore, instead of resulting from hypermode *decay* (for which (4.39) yields a theoretical leakage power of 2400 W), the losses at saturation result primarily from destructive *interference* of the $m = 1$ hypermode at the beamsplitter. If we compute the leakage losses at saturation from (4.37) using $\phi = 0$ and $m = 1$, we obtain an average theoretical leakage power of 5900 W, which compares more favorably with the simulated leakage power of 5600 W. The reason for the shift in the dominant hypermode from $m = 0$ before saturation

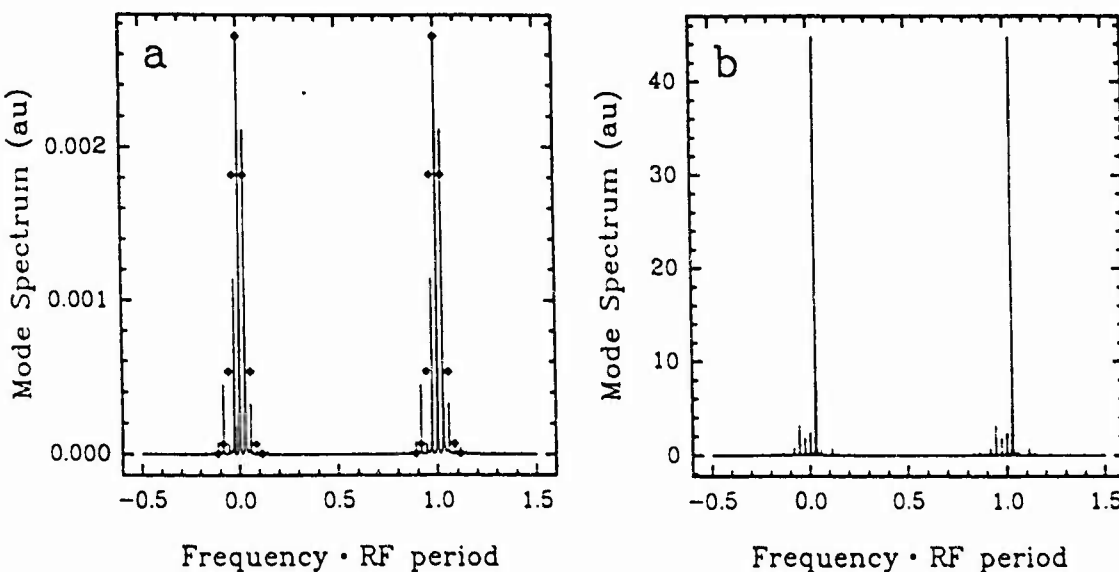


Fig. 4.12 Macropulse mode structure from the Michelson resonator simulation of Fig. 4.10 after: (a) 50 passes, and (b) 160 passes. The dots in Fig. (a) are the relative mode amplitudes predicted from the growth rate (4.36).

to $m = 1$ after saturation is presently unknown. However, it may result from nonlinear mode competition [10], coupled with the presence of a small amount of spontaneous radiation at saturation. In most simulations, the surviving hypermode was indeed $m = 0$, but in these cases the theoretical leakage power at saturation usually exceeded the simulated leakage power, and a greater degree of mode reduction was observed in the corresponding spectra than would be predicted from the mode analysis. These results are also consistent with an extraneous mode reduction mechanism. It may be possible to confirm this conjecture in the time domain by changing the depth of saturation via the total resonator losses [11], and observing any changes in the mode structure and leakage losses. To perform such simulations in the absence of noise, the initial mode populations can be biased by preparing the initial pulses with (4.12), in which the $| \underline{V}_i \rangle$ are given by (4.35) and the c_i are given unit length and random phase.

In the following chapter, I further develop the theory of the Michelson resonator FEL to properly include the FEL interaction of short electron pulses with the longitudinal modes of the Michelson mirror resonator. The theory is based on a conventional mode locked laser analysis using the passive mode structure derived in Section III of the present chapter, and accordingly, provides a means of accounting for finite interferometer detunings. The primary motivation for extending the theory is the following (presently unanswered) question: What range of interferometer detunings yields hypermode decay rates that are appropriate for applications in spectroscopy? The range should lie somewhere between the perfect overlap of successive pulses (which yields optimum hypermode decay), and the complete detuning of successive pulses (which merely yields the axial mode spectrum of a two-mirror resonator with increased losses.) Apart from answering this question, the extended theory will also be shown to provide a novel and general method for numerically studying the evolution of FEL supermodes in arbitrary resonator configurations.

V. REFERENCES

- [1] S. V. Benson, W. S. Fann, B. A. Hooper, J. M. J. Madey, E. B. Szarmes, B. Richman, and L. Vintro, "A review of the Stanford Mark III infrared FEL program," *Nucl. Instr. and Meth.*, vol. A296, pp. 110-114, 1990.
- [2] D. Oeps and W. B. Colson, "Phase Locking in an Infrared Short-Pulse Free-Electron Laser," *IEEE J. Quantum Electron.*, vol. 26, pp. 723-730, 1990.
- [3] E. B. Szarmes, S. V. Benson, and J. M. J. Madey, "Mode control on short-pulse FELs using a Michelson mirror resonator," *Nucl. Instr. and Meth.*, vol. A296, pp. 98-109, 1990.
- [4] E. B. Szarmes and J. M. J. Madey, "The Michelson resonator free-electron laser - Part II: Supermode structure and mirror detuning effects," *IEEE J. Quantum Electron.*, to be published.

- [5] R. Bellman, *Introduction to Matrix Analysis*, New York, NY: McGraw Hill, 1960.
- [6] C. Cohen-Tannoudji, B. Diu, and F. Laloë, *Quantum Mechanics*, vol. 1, New York, NY: Wiley-Interscience, 1977. Chapter II.
- [7] A. E. Siegman, *Lasers*, Mill Valley, CA: University Science Books, 1986.
- [8] A. E. Siegman, *ibid*, Chapter 11.
- [9] S. V. Benson and J. M. J. Madey, "Shot and quantum noise in free electron lasers" *Nucl. Instr. and Meth.*, vol. A235, pp. 55-60, 1985.
- [10] I. Kimel and L. R. Elias, "Narrow-band radiation from long-pulse free-electron lasers," *Phys. Rev. A*, vol. 35, pp. 3818-3824, 1987; I. Kimel and L. R. Elias, "Analytical study of multimode competition," *Nucl. Instr. and Meth.*, vol. A296, pp. 528-531, 1990.
- [11] R. Hajima, H. Ohashi, and S. Kondo, "Numerical studies on mode competition in long-pulse FELs," *Nucl. Instr. and Meth.*, vol. A296, pp. 383-387, 1990.

Chapter 5

Supermode structure and mirror detuning effects

Multiple mirror resonators have been suggested as a means to separate and isolate the longitudinal cavity modes of rf linac-driven free-electron lasers (FELs) for applications in high resolution spectroscopy. Proposed configurations have included the diffraction grating resonator [1], the intracavity etalon or Fox-Smith interferometer [2], and the Michelson mirror resonator [3], [5], which are all designed to couple successive optical pulses so that they build up from pass to pass with a definite phase relationship. These resonators differ in operation from thin intracavity etalons, which have also been proposed as a means to alter the gross spectral and temporal properties of FELs by filtering individual pulses [4].

In the previous chapter, the passive properties of the Michelson mirror resonator (see Fig. 4.1) were shown to provide a good quantitative description of the performance of such resonators on short pulse FELs if the interferometer mirrors were perfectly tuned. The passive theory was sufficient to account for mode decay, beamsplitter leakage, and mode selectivity via the phase offset of the secondary interferometer mirror. Furthermore, gross laser properties such as the spectral and temporal profiles of the pulses, as well as the cavity detuning curve, were unaffected by the presence of the perfectly tuned interferometer. However, as I report in this chapter, finite detunings of the interferometer can severely alter the cavity detuning curve, the laser spectrum and pulse structure, and the rate of mode decay, and cannot be described by the passive theory. These effects can have important implications for the practical application of such resonators.

Analytical descriptions of the detuning properties of FEL resonators have been

successfully applied to conventional two-mirror systems, as well as to thin intracavity etalons, in the regimes of small slippage parameters and small cavity detunings [4], [6], [7]. However, these techniques are difficult to apply to the Michelson resonator FEL, because the latter can operate at saturation with mirror detunings even greater than half of the optical pulse width. Nevertheless, the longitudinal mode structure of such resonators is always well defined even for arbitrary mirror detunings. Therefore, a self-consistent description of the FEL interaction in terms of longitudinal cavity modes should provide a general analysis of the performance of such resonators.

In the present chapter, I develop such a description by applying conventional mode locked laser theory [8] to the rf linac-driven Michelson resonator FEL. This analysis actually reproduces the small signal, small gain coupled mode equations obtained from early descriptions of the short pulse FEL [9], [10], but the application of the conventional theory represents a significant simplification in the derivation of those equations, while simultaneously providing a clear and intuitive picture of the mode locking mechanism due to short pulse effects in the absence of noise. The coupled mode equations can be applied to the mode structure of any resonator configuration, and are valid for arbitrary slippage parameters, cavity detunings, and electron pulse shapes; they are applied in the present study to resonator configurations which include mode dependent cavity losses. I derive the coupled mode equations in Section II, indicate in Section III how harmonic mode locking can simplify the numerical solutions described in Section IV, and compare those solutions in Section V with simulations of the Michelson resonator FEL using a pulse propagation code based on the Maxwell-Lorentz equations of motion.

II. THE FEL COUPLED MODE EQUATIONS

In this section, I derive the longitudinal coupled mode equations for FELs driven by short electron pulses using the injection locking analysis of conventional mode locked laser theory. The analysis starts from the Maxwell-Lorentz formulation of the FEL interaction [11], and yields in a straightforward manner the coupled mode equations derived previously from a rigorous Hamiltonian formalism for the interaction of short electron pulses with multiple resonator modes [9]. In Section IV, I will apply these equations to the mode evolution in a Michelson mirror resonator with mode dependent cavity losses arising from the detuning of the second reflection mirror.

A. *Temporal analysis*

The starting point for the analysis of the longitudinal effects in an FEL is the pair of generalized Maxwell-Lorentz equations of motion, which were recorded in Chapter 2 as

$$\frac{\partial v(\tilde{z}, \tau)}{\partial \tau} = \frac{\partial^2 \xi(\tilde{z}, \tau)}{\partial \tau^2} = |a(\tilde{z} - s\tau, \tau)| \cos(\xi(\tilde{z}, \tau) + \vartheta(\tilde{z} - s\tau, \tau)) , \quad (5.1)$$

$$\frac{\partial a(\tilde{z}, \tau)}{\partial \tau} = -\tau(\tilde{z} + s\tau) \langle \exp(-i\xi(\tilde{z} + s\tau, \tau)) \rangle_{\xi_0} . \quad (5.2)$$

Here, $\tau = ct/L$ is the dimensionless time, $\xi(\tau(t)) = (k + k_w)z(t) - \omega t$ is the phase of the electron in the ponderomotive potential, $v(\tau(t)) = d\xi(\tau)/d\tau = L [(k + k_w)\beta_z(t) - k]$ is the phase velocity or resonance parameter, and $s = N_w \lambda$ is the slippage between the optical and electron pulses which obtains as τ varies from 0 to 1 along the undulator. The quantity

$$a(\tau(t)) = \frac{4\pi N_w^2 e \hat{K}(J_0 - J_1) \lambda_w}{\gamma^2 mc^2} \hat{E}(\tau(t)) e^{i\vartheta(\tau(t))} \quad (5.3)$$

is the dimensionless form of the slowly varying part of the (plane-wave) optical electric field $E(z, t) = \sqrt{2} \hat{E}(\tau(t)) \exp[i(kz - \omega t + \vartheta(\tau(t)))]$ (^ indicating rms values), and

$$r = \frac{8\pi^2 e^2}{mc^2} \left(\frac{L_w}{\gamma} \right)^3 \frac{\hat{K}^2}{\lambda_w} (J_0 - J_1)^2 n_e \quad (5.4)$$

is the dimensionless current density. The parameters appearing in these quantities are defined in Table 5.1 (Section V). Equations (5.1) and (5.2) were combined in Chapter 2 to yield the small signal pulse propagation equation

$$a(\tilde{z}, \tau) = a(\tilde{z}, 0) + \frac{i}{2} \int_0^\tau dt' r(\tilde{z} + s\tau') \int_0^{\tau'} dq (\tau' - q) a(\tilde{z} + s(\tau' - q), q) \exp(-iv_0(\tilde{z} + s\tau') \cdot (\tau' - q)) , \quad (5.5)$$

which was derived for a long (essentially CW) electron beam with energy chirping. In this section, we assume that the pulses possess no energy chirp, and focus instead on the mode locking effects of short electron pulses of arbitrary shape and duration. For this analysis, a slightly more convenient form of (5.5) is obtained by expressing the microtemporal position in terms of the time $t = -\tilde{z}/c$ (not related to τ) instead of the position \tilde{z} . For the set of independent variables (t, τ) we may rewrite (5.5), with an implicit change in the form of the functions $\tilde{r} \rightarrow r$ and $\tilde{a} \rightarrow a$, as

$$a(t, \tau) = a(t, 0) + \frac{i}{2} \int_0^\tau dt' r(t - \frac{s\tau'}{c}) \int_0^{\tau'} dq (\tau' - q) a\left(t - \frac{s(\tau' - q)}{c}, q\right) \exp(-iv_0(\tau' - q)) , \quad (5.6)$$

where we have eliminated the \tilde{z} -dependence of the phase velocity v_0 . The minus sign in the

argument for t results from a reversal of the leading and trailing edges of the pulses when the independent variable is changed from \tilde{z} to t .

Equation (5.6) is the primary result of the temporal analysis in the small signal regime, and is valid for both small and large gains and for any degree of optical slippage. We proceed to illustrate its application to an important example, namely, the small gain amplification of a weak CW optical wave due to a short electron pulse.

We first identify the small gain regime by setting $a(t - \frac{s(\tau' - q)}{c}, q) \rightarrow a(t - \frac{s(\tau' - q)}{c}, 0)$, so that for a CW input field $a(t, 0) = a_0$ we may then eliminate any reference to the micro-temporal position t in the optical field appearing in the integrand of (5.6). Extracting the optical field from the integral and carrying the pulse evolution to $\tau = 1$ then yields

$$\begin{aligned} \Delta a(t) &\equiv a(t, 1) - a(t, 0) \\ &= a_0 \frac{i}{2} \int_0^1 d\tau' r(t - \frac{s\tau'}{c}) \int_0^{\tau'} dq (\tau' - q) \exp(-iv_0(\tau' - q)) \end{aligned} \quad (5.7)$$

$$= a_0 \frac{i}{2} \int_0^{\frac{N_w \lambda}{c}} \left(\frac{c}{N_w \lambda} \right) dt' r(t - t') \frac{1}{v_0^2} \left[\left(iv_0 \frac{ct'}{N_w \lambda} + 1 \right) \exp(-iv_0 \frac{ct'}{N_w \lambda}) - 1 \right] \quad (5.8)$$

$$= a_0 \int_{-\infty}^{\infty} dt' r(t - t') g_{v_0}(t') \quad , \quad (5.9)$$

where the time dependence of the dimensionless current density is given by

$$r(t) = \frac{8\pi^2 e^2}{mc^2} \left(\frac{L_w}{\gamma} \right)^3 \frac{\hat{K}^2}{\lambda_w} (J_0 - J_1)^2 n_e(t) \quad , \quad (5.10)$$

and the gain function

$$g_{v_0}(t) \left\{ \begin{array}{l} = \frac{i}{2v_0^2} \left(\frac{c}{N_w \lambda} \right) \left[\left(iv_0 \frac{ct}{N_w \lambda} + 1 \right) \exp(-iv_0 \frac{ct}{N_w \lambda}) - 1 \right] \text{ for } 0 < t < \frac{N_w \lambda}{c} \\ = 0 \text{ otherwise.} \end{array} \right. \quad (5.11)$$

By normalizing the electron density $n_e(t) \equiv \frac{N_e}{c \langle A \rangle} f(t)$ to a total charge of eN_e in the electron pulse, where $\langle A \rangle$ is the optical mode area, we may finally write the integral in (5.9) as

$$\frac{\Delta a(t)}{a_0} = K \int_{-\infty}^{\infty} dt' f(t - t') g_{v_0}(t') \quad , \quad (5.12)$$

$$\text{where } \int_{-\infty}^{\infty} f(t) dt = 1 , \text{ and } \mathcal{K} = \frac{8\pi^2 e^2}{mc^2} \left(\frac{L_w}{\gamma} \right)^3 \frac{\hat{K}^2}{\lambda_w} (J_0 - J_1)^2 \frac{N_e}{c(A)} , \quad (5.13)$$

and $g_{v_0}(t)$ is given by (5.11). The amplified field of a CW input wave is proportional to the convolution of the electron pulse shape with the gain function $g_{v_0}(t)$. This result is illustrated in Fig. 5.1 in which we display, for two electron pulse shapes, the single pass amplification of a CW optical field at the peak of the small signal gain curve using a one dimensional pulse propagation code [12], and the same interactions using a numerical convolution of (5.12). In the following paragraph we will apply (5.12) to the derivation of the coupled mode equations.

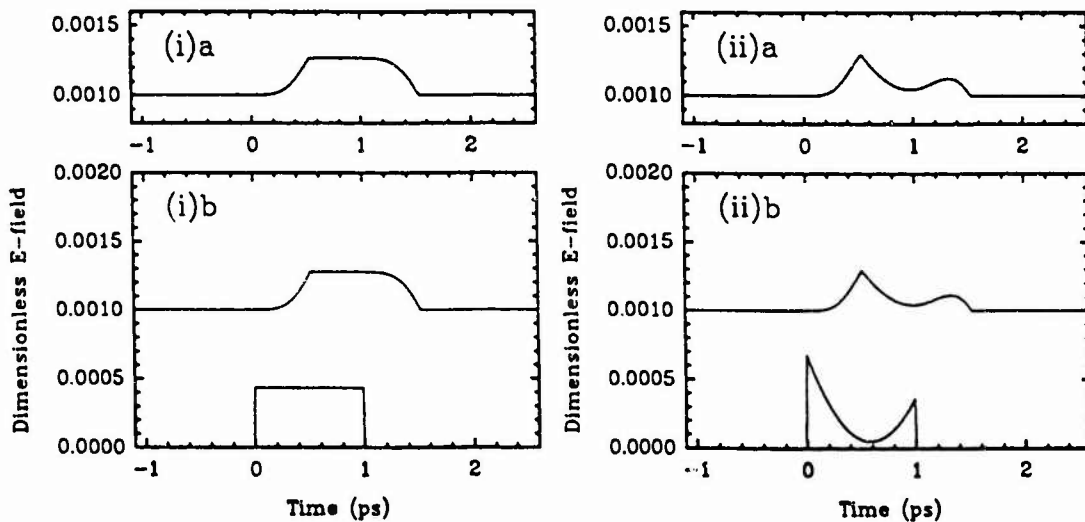


Fig. 5.1 Single pass amplification of a CW optical wave due to short electron pulses. (i)a, simulation using a pulse propagation code; (i)b, numerical convolution of eq. (5.12), both using the tophat pulse shown at bottom. (ii)a;b, same as in (i) except using the inverse parabolic pulse shown at bottom. The slippage parameter ($N_w \lambda / c \tau_p$) equals 0.525 in each case.

B. Spectral analysis

The spectral energy distribution of the circulating optical field inside a laser cavity consists, in general, of a superposition of longitudinal cavity modes oscillating within the gain spectrum. For a slowly varying optical field whose plane-wave components are given by (5.3), this superposition can be written as the modal expansion [13]

$$E(t) e^{i\vartheta(t)} e^{-i\omega t} = \sum_n E_n(t) e^{-i\omega_n t} = \sum_n E_n(t) e^{-i2\pi f_n t} \quad (5.14)$$

in which the $E_n(t)$ are complex valued spectral components which have a slowly varying time dependence only over many passes in the cavity, and essentially describe the long term

spectral evolution of the laser field. In the case of a free running laser oscillation the longitudinal modes can be identified as the axial normal modes of the cavity and are separated in frequency by the passive axial mode spacings (plus any frequency pulling effects). However, in the presence of forcing due to active intracavity loss or gain modulation, the longitudinal modes will be separated by the driving frequency of the forced modulation, and the laser will reach a sustained oscillation only if this driving frequency is sufficiently close to the axial normal mode spacing. In this time-perturbative description of the laser field, the active modulation produces sideband components on each of the (essentially CW) resonant normal modes, and these sidebands then injection lock those neighboring normal modes with which they are in resonance. The successive sideband growth and injection locking process continues until all of the modes, separated by the driving frequency, are phase locked to one or more of their neighbors.

The frequency domain analysis of mode locking which describes this injection locking process is applied by Siegman to the active loss and phase modulation of a conventional laser oscillator [14]; our derivation of the FEL coupled mode equations for the case of gain modulation by a pulsed electron beam essentially follows those analyses. We start with the slowly varying evolution equation for the n^{th} mode of a laser oscillator, derived by Siegman and written for the case of intracavity modulation (with the sign of ω indicated in (5.14)) as

$$\frac{dE_n}{dt} + \left[\frac{\tilde{\gamma}_n}{2} - i(\omega_n - \omega_c) \right] E_n = \frac{\Delta E_n^{\text{mod}}}{T_c} \quad (5.15)$$

or as $\Delta E_n + \left[\frac{\gamma_n}{2} - i T_c (\omega_n - \omega_c) \right] E_n = \Delta E_n^{\text{mod}} , \quad (5.16)$

where E_n is the complex amplitude of the n^{th} laser mode, T_c is the cavity round trip time, $\tilde{\gamma}_n$ is the rate of fractional energy loss, γ_n is the fractional energy loss in one round trip, and ΔE_n^{mod} is the change in amplitude ΔE_n induced on E_n by the modulator after one round trip. The driving frequency ω_n must lie sufficiently close to one of the axial normal mode frequencies ω_c in order for the injection locking to succeed, and indeed $T_c(\omega_n - \omega_c) \equiv (\phi_n - \phi_c)$ must be much smaller than 2π . The phasor interpretation of (5.16) is then straightforward: the only contributions to the mode E_n arise from the small phase shift $\exp[i(\phi_n - \phi_c)]$, the cavity losses $(\gamma_n/2)E_n$, and the modulator ΔE_n^{mod} . This phasor interpretation is illustrated in Fig. 5.2.

We now consider a CW input field of frequency ω_k , and calculate the sideband modulation after a single pass through the undulator due to a train of electron pulses separated in time by T_e . For the input waveform we write

$$E_{in}(t) = E_k \exp(-i2\pi f_k t) , \quad (5.17)$$

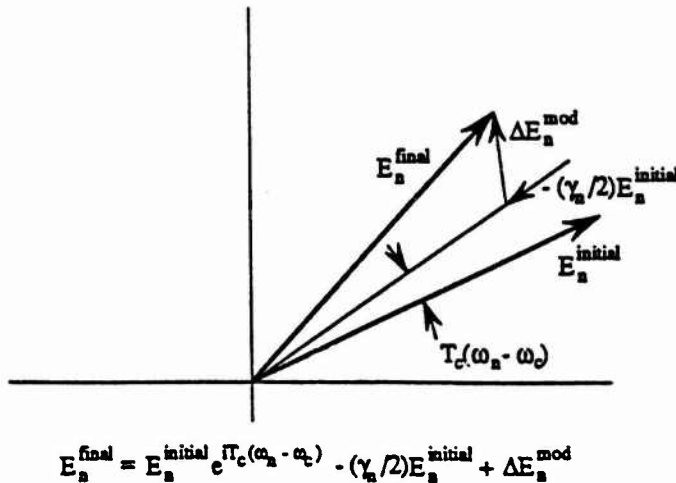


Fig. 5.2 Phasor interpretation of the mode locking process in eq. (5.16), showing the superposition of coincident sidebands produced by an active intracavity modulation.

and the input spectrum is just

$$\tilde{E}_{in}(f) = E_k \delta(f - f_k) \quad (5.18)$$

where $\delta(f)$ is the delta function and the tilde refers to the Fourier domain. Note that the sign of ω in the expansion (5.14) implies the Fourier transform pair

$$h(t) = \int_{-\infty}^{\infty} \tilde{h}(f) e^{-i2\pi ft} df \quad , \quad (5.19)$$

$$\tilde{h}(f) = \int_{-\infty}^{\infty} h(t) e^{+i2\pi ft} dt \quad . \quad (5.20)$$

To compute the output waveform, we recall from (5.12) that the amplified field of a CW input wave is proportional to the convolution of the electron pulse shape $f(t)$ with the gain function $g_{v_k}(t)$ given in (5.11); in this case the resonance parameter v_k corresponds to the input frequency ω_k . Note that the small gain restriction on this result is consistent with a general time-perturbative analysis. If instead of a single electron pulse we then have a train of pulses separated by T_e , we obtain for the output field

$$E_{out}(t) = E_k \exp(-i2\pi f_k t) \cdot \left\{ 1 + [\mathcal{K} f(t) * g_{v_k}(t)] * \sum_n \delta(t - nT_e) \right\} \quad (5.21)$$

where \mathcal{K} is given in (5.13) and $*$ indicates convolution. Note that only the complex envelope of the added field is modulated by the comb function $\sum_n \delta(t - nT_e)$. By successively applying the Fourier convolution theorem and the sifting property of the delta function, we compute the output spectrum to be:

$$\tilde{E}_{\text{out}}(f) = E_k \delta(f - f_k) + K E_k \delta(f - f_k) * \left[(\tilde{f}(f) \cdot \tilde{g}(f; v_k)) \cdot \frac{1}{T_e} \sum_n \delta(f - \frac{n}{T_e}) \right] \quad (5.22)$$

$$= E_k \delta(f - f_k) + \frac{K}{T_e} E_k \left[(\tilde{f}(f - f_k) \cdot \tilde{g}(f - f_k; v_k)) \cdot \sum_n \delta(f - f_k - \frac{n}{T_e}) \right] \quad (5.23)$$

$$= E_k \delta(f - f_k) + \frac{K}{T_e} \sum_n E_k \tilde{f}(f_n - f_k) \tilde{g}(f_n - f_k; v_k) \cdot \delta(f - f_n) \quad (5.24)$$

where we have defined $f_n = f_k + \frac{n}{T_e}$. The terms in the summation with $n \neq 0$ represent the sideband components $\delta(f - f_n)$ induced on the input wave E_k by the pulsed electron beam. If many such modes E_k are present, then the total contribution to the mode amplitude E_n for a given f_n is then simply the sum over k (including $f_k = f_n$) of all other sidebands coincident with that mode E_n . The modulator term in (5.16) for a pulsed electron beam therefore becomes

$$\Delta E_n^{\text{mod}} = \frac{K}{T_e} \sum_k E_k \tilde{f}(f_n - f_k) \cdot \tilde{g}(f_n - f_k; v_k) \quad . \quad (5.25)$$

Explicit calculations yield

$$\tilde{f}(f_n - f_k) = \int_{-\infty}^{\infty} dt f(t) \exp [+i2\pi (f_n - f_k) t] \quad (5.26)$$

$$= \int_{-\infty}^{\infty} dz \hat{f}(\bar{z}) \exp [-i (k_n - k_k) \bar{z}] \quad (5.27)$$

where each of $f(t)$ and $\hat{f}(\bar{z})$ is normalized, and

$$\tilde{g}(f_n - f_k; v_k) = \int_{-\infty}^{\infty} dt g_{v_k}(t) \exp [+i2\pi (f_n - f_k) t] \quad (5.28)$$

$$= -\frac{1}{2} \left[\left(\frac{\sin v_n}{v_n v_k} + \frac{\cos v_n - 1}{v_n v_k} \left(\frac{1}{v_n} + \frac{1}{v_k} \right) - \frac{\cos (v_n - v_k) - 1}{v_k^2 (v_n - v_k)} \right) + i \left(\frac{\cos v_n}{v_n v_k} - \frac{\sin v_n}{v_n v_k} \left(\frac{1}{v_n} + \frac{1}{v_k} \right) + \frac{\sin (v_n - v_k)}{v_k^2 (v_n - v_k)} \right) \right] \quad (5.29)$$

$$= -\frac{1}{2} [C(v_n, v_k) + i S(v_n, v_k)] \quad (5.30)$$

where $C(v_n, v_k)$ and $S(v_n, v_k)$ are also defined in ref. [9], and we have substituted from $(\omega_n - \omega_k)$ to $(v_n - v_k)$ via the definition of the resonance parameter:

$$v_n - v_k = -\frac{N_w \lambda}{c} (\omega_n - \omega_k) \quad . \quad (5.31)$$

The function $C(v_n, v_k) + i S(v_n, v_k)$ may also be written as

$$E(v_n, v_k) \equiv C(v_n, v_k) + i S(v_n, v_k) = e^{-iv_n} \left[\frac{1}{(v_n - v_k)} \left(\frac{1 - e^{iv_k}}{v_k^2} - \frac{1 - e^{iv_n}}{v_n^2} \right) + \frac{i}{v_n v_k} \right] . \quad (5.32)$$

Note that this function, and the integral in (5.27), are complex conjugates of the corresponding functions defined by Dattoli *et al* [10], because those authors chose a phase $\exp[i(\omega t - kz + \vartheta)]$ which differs from our choice $\exp[i(kz - \omega t + \vartheta)]$. The complete coupled mode equations (5.16) can now be written

$$\Delta E_n = \left[-\frac{\gamma_n}{2} + i T_c (\omega_n - \omega_c) \right] E_n - \frac{\kappa}{2T_e} \sum_k E_k \tilde{f}(f_n - f_k) \cdot E(v_n, v_k) , \quad (5.33)$$

where κ is given by (5.13), $\tilde{f}(f_n - f_k)$ is given by (5.26) or (5.27), and $E(v_n, v_k)$ is given by (5.32). Equation (5.33) is the form of the coupled mode equations which we will apply to the analysis of the Michelson mirror resonator in Section IV. However, it may also be cast as separate equations for the mode energy $W_n \equiv |E_n|^2$ and phase $\phi_n \equiv \arg(E_n)$ as:

$$\Delta W_n = -\gamma_n W_n - \frac{\kappa}{T_e} \sum_k (W_n W_k)^{1/2} \cdot [B_{n,k}^c \cos(\phi_n - \phi_k) + B_{n,k}^s \sin(\phi_n - \phi_k)] \quad (5.34)$$

$$\Delta \phi_n = T_c (\omega_n - \omega_c) - \frac{\kappa}{2T_e} \sum_k \left(\frac{W_k}{W_n} \right)^{1/2} \cdot [B_{n,k}^s \cos(\phi_n - \phi_k) - B_{n,k}^c \sin(\phi_n - \phi_k)] \quad (5.35)$$

$$\text{where we have defined}^1 \quad B_{n,k} \equiv B_{n,k}^c + i B_{n,k}^s \equiv \tilde{f}(f_n - f_k) \cdot E(v_n, v_k) . \quad (5.36)$$

Finally, we note that the term $T_c (\omega_n - \omega_c)$ on the RHS of (5.35) can be written in terms of the temporal detuning between the electron and optical pulses. Defining the modulation frequency of the electron beam as $\omega_m \equiv 2\pi/T_e$ and the passive axial mode spacing (for a two-mirror resonator) as $\omega_{ax} \equiv 2\pi/\Gamma_c$, we may label the oscillating longitudinal modes ω_n and the corresponding normal modes ω_c (with which the former are in resonance) in terms of the mode number n as follows:

$$\omega_n = \omega_0 + n\omega_m \quad (5.37)$$

$$\text{and} \quad \omega_c = \omega_0 + n\omega_{ax} , \quad (5.38)$$

where ω_0 is a reference frequency and n is necessarily the same for each set. The detuning term $T_c (\omega_n - \omega_c)$ on the RHS of (5.35) can then be written

¹ The functions $B_{n,k}^c, B_{n,k}^s$ are identical to those defined by Dattoli *et al* [10] for a mono-energetic electron beam of zero emittance. Therefore, the coupled mode equations reported by those authors can be recovered in form by setting $\phi_{n,k} \rightarrow -\phi_{n,k}$ and $\Delta \phi_n \rightarrow -\Delta \phi_n$, as required by the opposite choice of phase.

$$\begin{aligned}
 T_c(\omega_n - \omega_c) &= T_c [(\omega_0 + n\omega_m) - (\omega_0 + n\omega_{ax})] \\
 &= \frac{2\pi}{\omega_{ax}} n (\omega_m - \omega_{ax})
 \end{aligned} \quad , \quad (5.39)$$

and since this term contributes only to the phase ϕ_n of the mode E_n , the addition of another term *independent* of n merely results in a common shift of the reference phase of the modes. We may therefore write, using (5.39) and the definitions of ω_n , ω_m , and ω_{ax} :

$$\begin{aligned}
 T_c(\omega_n - \omega_c) &\rightarrow T_c(\omega_n - \omega_c) + \frac{\omega_0 2\pi (\omega_m - \omega_{ax})}{\omega_m \omega_{ax}} \\
 &= \omega_n (T_c - T_e) \\
 &\equiv \omega_n \delta T_{cav} \quad ,
 \end{aligned} \quad (5.40)$$

where we have defined $\delta T_{cav} = T_c - T_e$. This completes the derivation of the coupled mode equations. It is interesting to note that the time dependent evolution equation of the small gain supermode theory [10], which arises from a transformation of the coupled mode equations into the time domain, can be obtained directly from the evolution equation (5.5) (in the absence of chirping) simply by introducing a few variable substitutions and interchanging the order of integration; in this case, the cavity loss and detuning terms must be added explicitly. In Section IV, we will apply the coupled mode equations (5.33) to the evolution of the longitudinal modes in a Michelson mirror resonator with mode dependent losses γ_n arising from the detuning of the second reflection mirror, and in Section V, we will compare the numerical solutions with one dimensional simulations of the FEL interaction using the Maxwell-Lorentz equations of motion.

III. THE HARMONICALLY MODE LOCKED FEL

Harmonic mode locking is defined as the forced modulation of a laser cavity at a frequency which is some multiple N of the round trip frequency, producing N mode locked laser pulses per round trip. Becker *et al* [15] describe the harmonically mode locked Nd:YAG laser for $N = 2$ up to $N = 5$. The primary difference between mode locking with $N = 1$ and $N > 1$ is that, in the spectral description of the mode locking process, harmonic modulation produces sideband components on any given mode which are $N > 1$ axial mode spacings away. As a result, the modulator couples together only every N^{th} longitudinal mode, and as many as N such sets of coupled modes, or *hypermodes*, may oscillate at any instant. The number of hypermodes which do oscillate depends in part on the spatial distribution of the gain medium. In the above experiments described by Becker *et al*, mode locking with $N = 2$ either produced laser oscillation in both hypermodes simultaneously, or

in one or the other hypermode randomly, depending respectively on whether the laser rod was located near the center or near the end of the laser cavity. They never did observe the continuous oscillation of a single hypermode.

Due to engineering constraints, most rf linac-driven FELs operate with large harmonic numbers, such as the Mark III FEL [16] which contains $N = 35$ circulating optical pulses. Such FELs, if constructed with conventional two-mirror resonators, will oscillate simultaneously in all N hypermodes, because the optical pulses build up independently from noise and are driven independently by fresh electron pulses on every pass. The resulting optical pulse train therefore reproduces itself only after every round trip and yields a spectrum of longitudinal modes separated by the round trip frequency.

However, if an rf linac is used to drive a multiple mirror resonator such as a Michelson interferometer, successive optical pulses can be coupled by means of the beam splitter and will build up from pass to pass only if they interfere constructively in the direction of the undulator. The operation of such resonators is described in the previous chapter. The stable cavity eigenmode consists of N phase locked optical pulses separated by the rf period of the linac, yielding a single hypermode in the output spectrum with longitudinal modes separated by the rf frequency. One can also describe the spectral evolution towards a single hypermode in terms of the decay of all other hypermodes due to interference at the beam splitter, relative to that hypermode with the lowest such losses. Homogeneous laser saturation then ensures that only a single or at most a few hypermodes dominate the laser spectrum, even in the deeply saturated large signal regime.

From the above discussion, it is clear that the evolution of each hypermode in the small signal regime is described independently by its own set of coupled mode equations, with mode losses appropriate to each hypermode. Therefore, when we solve the coupled mode equations in Section IV to describe the detuning effects in a Michelson mirror resonator, we assume that only the dominant hypermode and its nearest neighbors comprise the laser spectrum. Harmonic mode locking then allows us to reduce by a factor of N the number of modes coupled together within the gain bandwidth; in the simulations to be reported, the reduction is from $\sim 24,000$ modes to ~ 680 modes for each hypermode, yielding tractable computation times even on a small workstation. Figure 5.3 shows the spectral range in which we solve the coupled mode equations.

Finally, it may be important to note that the coupled mode equations can be solved in the above manner even for harmonically driven two-mirror resonators, with a similar reduction in the number of modes, in order to investigate the supermode evolution for arbitrary electron pulse shapes. The supermode theory can then be parameterized directly in the spectral domain for any electron pulse shape and any degree of optical slippage. The

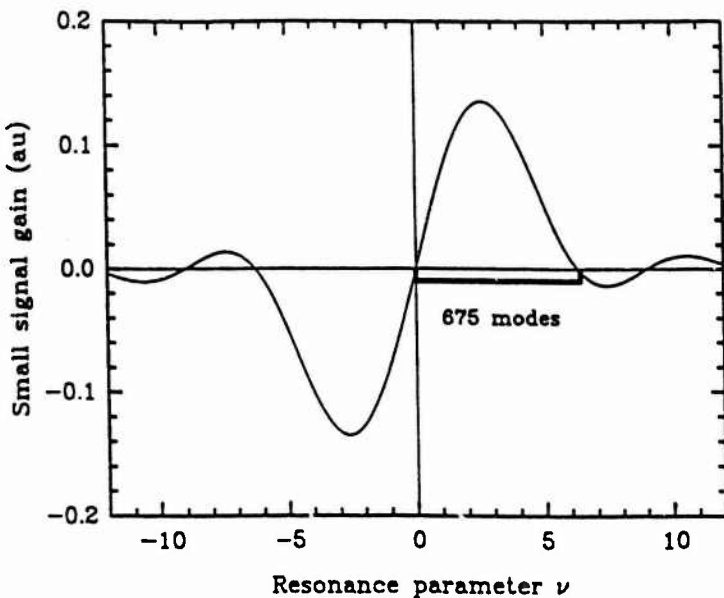


Fig. 5.3 Frequency band on the small signal gain curve used in the coupled mode simulations. The region from $\nu = 0$ to $\nu = 6.362$ encloses 675 longitudinal modes separated by the rf frequency.

main disadvantage is that the iterative procedure used to solve the coupled mode equations yields only the lowest order supermode, in contrast to the usual analytical treatment of supermodes in the long bunch regime [4], [6], [7].

IV. SOLUTION OF THE COUPLED MODE EQUATIONS

The coupled mode equations (5.33) are most conveniently solved by iteration on an initial configuration of longitudinal modes. This method, known as the *power method* [17], is appropriate for extracting the dominant eigenvector and associated eigenvalue of a matrix. Its application in the present case is suggested formally (as well as physically) by (5.33), in which successive multiplications by a coupling matrix correspond to the physical mode locking mechanism on successive passes in the resonator. From (5.33), the corresponding matrix equation may be written

$$\bar{\bar{M}} \cdot \bar{E}^P = \bar{E}^{P+1} , \quad (5.41)$$

where \bar{E}^P is a vector containing the complex mode amplitudes on pass P , and the matrix $\bar{\bar{M}}$ has components

$$M_{nk} = \left[1 - \frac{\gamma_n}{2} + i T_c (\omega_n - \omega_c) \right] \delta_{nk} - \frac{\kappa}{2T_c} \tilde{f}(f_n - f_k) \cdot E(v_n, v_k) . \quad (5.42)$$

The FEL supermodes are defined as the eigenvectors of this coupling matrix, which form a complete basis due to the fact that $\bar{\bar{M}}$ is normal (i.e. $\bar{\bar{M}} \bar{\bar{M}}^\dagger = \bar{\bar{M}}^\dagger \bar{\bar{M}}$). For the finite subspace

of vectors spanned by the possible configurations of modes in Fig. 5.3, we assume that the initial configuration has a non-zero projection onto the lowest order supermode, and that subsequent matrix iterations correspond to the spectral evolution of the FEL supermodes in the regime for which spontaneous radiation is negligible.

To solve the coupled mode equations, the longitudinal modes E_n in Fig. 5.3 are initially populated with equal amplitudes and zero phase. The matrix multiplication indicated by (5.41) is then performed and the modes renormalized so that $\sum_n |E_n|^2$ remains constant on each pass. This matrix multiplication and renormalization are then repeated until the modes converge on the lowest order supermode, as indicated by the convergence of the gain $G_c(p)$ of the centermost mode E_c with the gain $G_T(p)$ of the entire spectrum, which we calculate on each pass p (prior to normalization) according to

$$G_c(p) = \frac{|E_c^p|^2}{|E_c^{p-1}|^2} - 1 \quad (5.43)$$

$$\text{and} \quad G_T(p) = \frac{\sum_n |E_n^p|^2}{\sum_n |E_n^{p-1}|^2} - 1 \quad . \quad (5.44)$$

(For the numerical results reported in Section V, the solution of the coupled mode equations usually consisted of 75 iterations, and in most cases the 'eigenvalues'² [i.e. $1 + G_{c,T}(p)$] settled to within 1% of one another after approximately 20 iterations.)

The mode dependent cavity loss and detuning terms which uniquely characterize the Michelson mirror resonator were derived in the previous chapter. If the interferometer contains one rf period of delay in the secondary arm, then the mode loss of the n^{th} mode is given by

$$\gamma_n = \gamma_c + 4\pi^2 r^2 t^2 \left[\frac{m_h}{N} + n \delta N \right]^2 \quad , \quad (5.45)$$

where γ_c is the cavity loss due to mirror reflection and output coupling, r^2 is the power reflectance of the beamsplitter, $t^2 = 1 - r^2$ is the transmittance, m_h is the hypermode number ($m_h = 0$ defining the lowest order hypermode), N is the number of circulating optical pulses in the resonator, and δN is the small fraction of an rf period representing the detuning of the Michelson interferometer. For finite detunings δN , the mode loss can become greater than unity for large $|n|$, in which case the mode loss γ_n is set equal to unity. The resonator detuning term for the n^{th} mode (compare with (5.40)) is given by

² The unconventional use in this chapter of the term 'eigenvalue' refers to $|\lambda|^2$, where λ is the complex eigenvalue of the coupling matrix and whose corresponding eigenvector is the lowest order supermode.

$$T_c(\omega_n - \omega_c) = \omega_n (\delta T_{cav} + r^2 \delta T_{Mich}) , \quad (5.46)$$

where $\omega_n = n \omega_{rf}$ is the longitudinal mode frequency, $\delta T_{cav} = T_c - NT_e$ is the temporal desynchronism of the optical and electron pulses in the corresponding two-mirror resonator, and δT_{Mich} is the temporal desynchronism of the Michelson interferometer (proportional to δN).

The numbering of the modes is unambiguous. For a given set of simulation parameters, the centermost mode is obtained by solving the coupled mode equations for the lowest order hypermode with zero detuning in the interferometer, and labelling as $n = 0$ that mode which is coincident with the maximum amplitude of the laser spectrum. This mode is then labelled as $n = 0$ for all other interferometer detunings and hypermode numbers for the given set of simulation parameters. This prescription is physically motivated by the fact that the laser wavelength is not affected by the presence of an intracavity interferometer under *any* degree of pulse coupling (a fact which is confirmed by FEL simulations of the Michelson mirror resonator using the Maxwell-Lorentz equations of motion). Given the quadratic dependence of γ_n on n , we accordingly choose a numbering scheme which precludes any wavelength shift for finite detunings δN .

Finally, we note that the coupled mode equations are strictly valid only for plane-wave interactions in the small signal, small gain regime. However, they can be used to describe the one dimensional interaction with realistic transverse cavity modes if one defines an appropriate filling factor for the coefficient \mathcal{K} in (5.13). Alternately, for the comparison in Section V with the pulse propagation simulations in which only the lowest order Gauss-Laguerre mode is assumed, we calculate the coefficient \mathcal{K} directly from the gain of that mode by assuming *continuous* electron and optical beams, and integrating the Maxwell-Lorentz equations directly in terms of the interaction with transverse cavity modes [18]. If we define the gain $g_0(v_p)$ at the peak of the small signal gain curve as

$$g_0(v_p) \equiv \frac{a(1) - a(0)}{a(0)} , \quad (5.47)$$

where $a(0)$, $a(1)$ are the complex fields at the beginning and end of the undulator, then from (5.33) the corresponding gain for a single longitudinal mode in the laser spectrum is

$$g_0(v_p) \equiv \frac{\Delta E}{E} = -\frac{\mathcal{K}}{2T_e} E(v_p, v_p) , \quad (5.48)$$

where $v_p = 2.606$ is the resonance parameter for maximum small signal gain³. In the case

³ The corresponding resonance parameter in the pulse propagation code is actually $v_p \sim 4.1$ due to the phase shift of the TEM00 mode.

of a tophat electron pulse of full width τ_p (used in the present study) and the same value of the peak current, we then obtain

$$\mathcal{K} = 2 \tau_p \frac{|g_0(v_p)|}{|E(v_p, v_p)|} . \quad (5.49)$$

\mathcal{K} can be obtained in a similar manner for other electron pulse shapes by appropriately scaling the number of electrons N_e in the pulse.

V. NUMERICAL RESULTS; COMPARISON WITH PULSE PROPAGATION SIMULATIONS

As noted in the Introduction, increasing the interferometer detuning of a Michelson mirror resonator can severely alter the spectral and temporal properties of the laser. The most important effects are a broadening and shifting of the cavity detuning curve, a narrowing of the overall laser spectrum, and a decrease in the rate of hypermode decay, all of

Parameter	Definition	Simulation value
<i>Optical beam parameters</i>		
λ	Resonant optical wavelength	$3.35 \mu\text{m}$
N	Number of circulating optical pulses	35
r^2	Beamsplitter reflectance	50 %
γ_c	Extraneous cavity losses	7.3 %
z_R	Rayleigh range	73.08 cm
(A)	Average optical mode area = $\frac{\lambda z_R}{2} \left[1 + \frac{1}{3} \left(\frac{L_w}{2 z_R} \right)^2 \right]$	0.01447 cm^2
<i>Electron beam parameters</i>		
γ	Electron beam energy / mc^2	83.19
τ_p	Duration of tophat electron pulse	4 ps
I	Peak electron current	18.8 A
T_e	RF period	350.1 ps
<i>Wiggler parameters</i>		
N_w	Number of wiggler periods	47
L_w	Wiggler length	108.1 cm
λ_w	Wiggler period	2.3 cm
\hat{K}	RMS wiggler parameter	1.008
$(J_0 - J_1)^2$	Bessel function factor	0.738

Table 5.1 Definition of FEL parameters, and values used in the coupled mode simulations.

which can have practical consequences for the operation of such resonators or their application to spectroscopy. In the following paragraphs, we present numerical solutions of the coupled mode equations for Michelson resonator FELs with finite detunings in the interferometer, and compare the results with those from an FEL pulse propagation code using the Maxwell-Lorentz equations of motion and realistic transverse cavity modes; the latter simulations are described in Chapter 4 and include both electron shot noise and quantum noise. The simulation parameters are appropriate to the operation of the Mark III FEL and are listed in Table 5.1. It is interesting to note that the coupled mode simulations run as fast on a SUN04 workstation as the corresponding pulse propagation simulations run on a CRAY Y/MP supercomputer.

A. Broadening of cavity detuning curves

The fact that finite interferometer detunings can affect the cavity detuning curve is seen immediately from (5.46), in which the frequency detuning term affects the FEL supermodes only via the net combination of δT_{cav} and δT_{Mich} . Therefore, any finite value of the latter should alter the detunings δT_{cav} for which the FEL supermodes experience maximum gain. Of course, finite detunings δT_{Mich} also introduce mode dependent losses for each hypermode, and the actual supermode structure depends on this parameter in a manner described below in paragraph B.

Figure 5.4 displays the cavity detuning curves for several values of the detuning δL_{Mich} , calculated from the coupled mode simulations for the lowest order hypermode. The

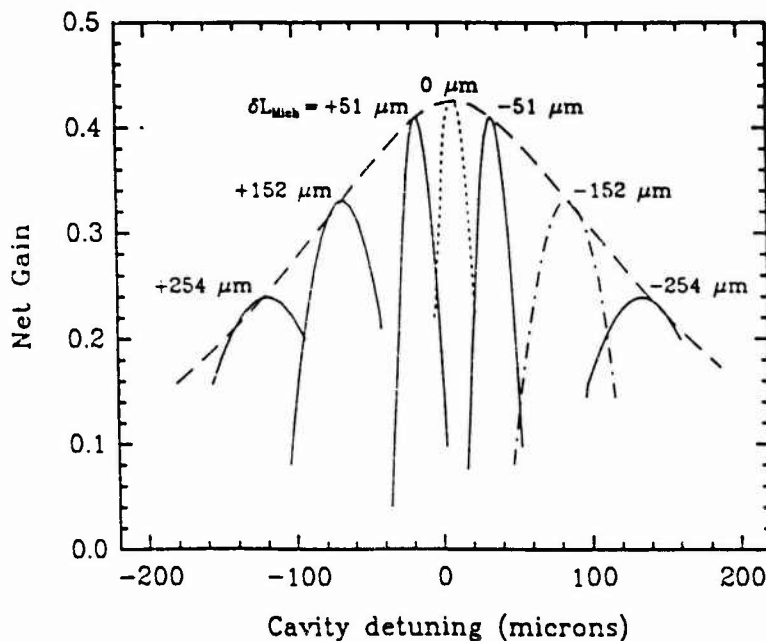


Fig. 5.4 Cavity detuning curves for various fixed values of the secondary Michelson mirror detuning, with $r^2 = 50\%$. The dashed envelope corresponds to $\delta L_{cav} + r^2 \delta L_{Mich} = +10 \mu\text{m}$. Note that, in this chapter, $\delta L > 0$ refers to cavity detunings shorter than the synchronous length.

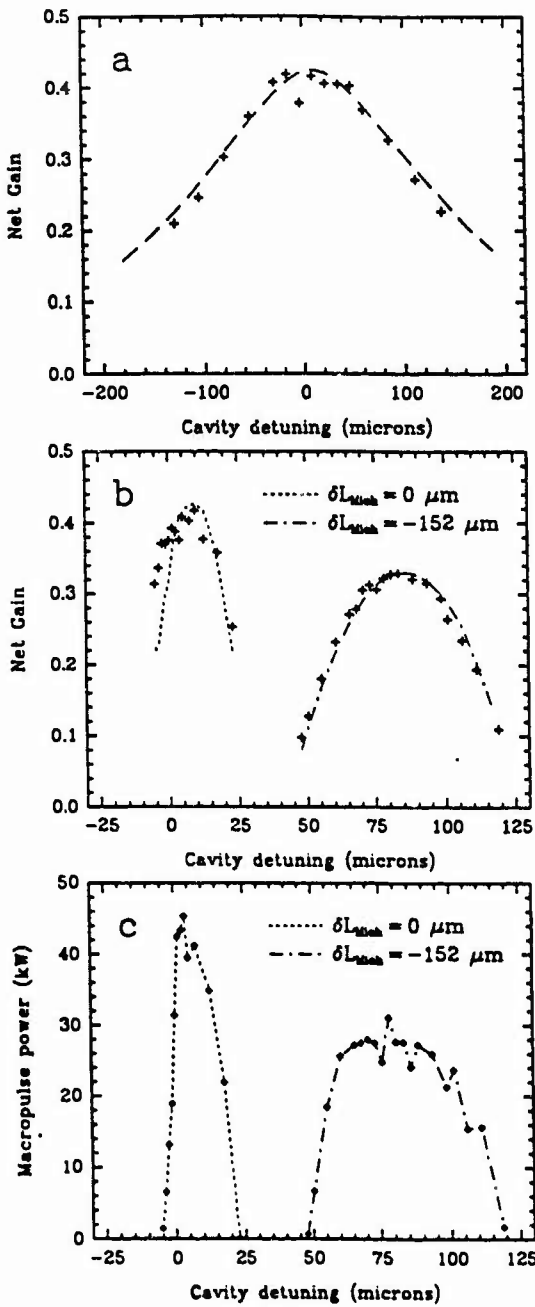


Fig. 5.5 Small signal gains (hash marks) calculated from the pulse propagation simulations, and corresponding to: (a) the dashed envelope in Fig. 5.4; and (b) the cavity detuning curves for $\delta L_{\text{Mich}} = 0 \mu\text{m}$ and $\delta L_{\text{Mich}} = -152 \mu\text{m}$ in Fig. 5.4. Figure 6(c) shows the output power detuning curves at saturation for the simulations in (b) after 160 passes.

dashed envelope corresponds to combinations of δT_{cav} and δT_{Mich} for which the effective cavity detuning in (5.46) is 10 μm shorter than synchronous; this detuning is predicted by the supermode theory [7] to yield the maximum gain for the parameters listed in Table 5.1. The broadening of the detuning curves is a manifestation of the general effect of an intra-cavity etalon [4], and is produced to a greater degree in a highly reflecting etalon because of

the multiple reflections. These broadened and shifted detuning curves may yield a practical advantage in the initial search for the synchronous mirror positions of the Michelson resonator, especially if several beamsplitters are switched during operation. They are also related to pulse shaping effects described below in paragraph B.

The small signal gains from the corresponding pulse propagation simulations are indicated in Fig. 5.5, and were obtained by averaging over passes for which the optical power was well above the noise level but beneath the onset of saturation. These values were adjusted to account for the finite leakage losses resulting from the decay of the higher order hypermodes. Figures 5.5a and 5.5b reproduce the detuning envelope and two of the cavity detuning curves from Fig. 5.4. The slight enhancement in the gains near the synchronous cavity length in Fig. 5.5b is due to the build up from noise in the pulse propagation simulations, as observed in previous studies [19]. The power detuning curves in Fig. 5.5c were obtained from the above simulations for the same parameters as in Fig. 5.5b, and indicate that essentially the same degree of broadening is maintained at saturation. Finally, we note that the reduced gains on the wings of the detuning envelope result from leakage losses in the lowest order hypermode. These losses are always present for finite interferometer detunings, even in the perfectly phase locked case, because successive circulating pulses are always displaced relative to one another by the Michelson mirror. It may be possible to exploit these leakage losses for outcoupling the intracavity power in an inherently uni-directional output beam. However, there is a trade off between increasing the output coupling with this scheme and maintaining a phase locked optical beam; the latter problem is studied below in paragraph C.

B. Spectral narrowing of supermodes

In this paragraph we show how the mode dependent cavity losses (5.45) in the lowest order hypermode alter the form of the surviving FEL supermodes. This result is not unexpected; these cavity losses result from the detuning of the Michelson interferometer, and the finite displacement between successive pulses effectively lengthens the spatial supermodes at the beamsplitter. The corresponding decrease in the width of the overall spectrum is consistent with mode suppression at the extremes of the gain band where the losses are higher. These mode losses are indicated in Fig. 5.6 by the passive mode intensities of the lowest order hypermode for various Michelson detunings δN , which curves were calculated from the passive frequency response of the detuned Michelson resonator [5] at the resonant frequencies of that hypermode (assuming $\gamma_c = 7.3\%$ extraneous cavity losses). We see that the losses are independent of mode number only for a zero detuning δN ; finite detunings increase the losses symmetrically about the center mode.

Supermode spectra from the coupled mode simulations are illustrated in Fig. 5.7 for

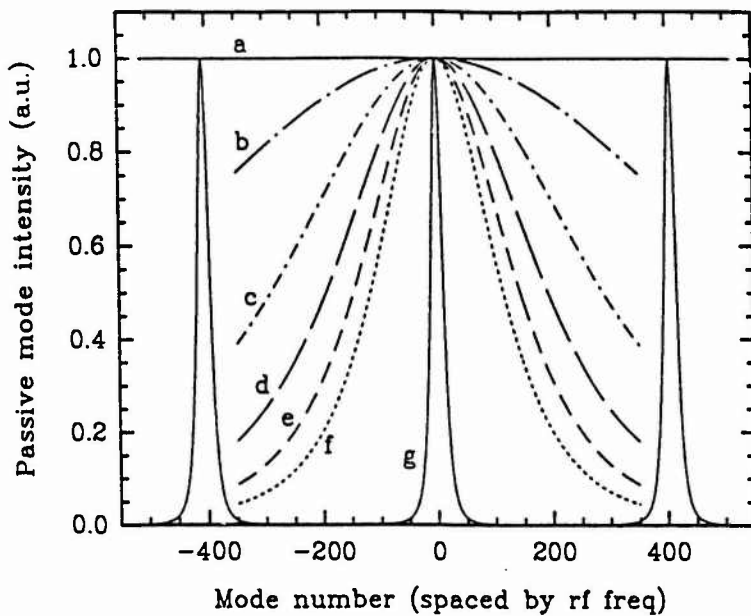


Fig. 5.6 Passive intracavity intensities for various fractional interferometer detunings δN , with $N = 35$ and $\gamma_c = 7.3\%$, from a source of fixed amplitude coupled into the cavity at the resonances of the zeroth order hypermode. (a) $\delta N = 0$; (b) $\delta N = 0.0001$; (c) $\delta N = 0.0002$; (d) $\delta N = 0.0003$; (e) $\delta N = 0.0004$; (f) $\delta N = 0.0005$; (g) $\delta N = 0.005$.

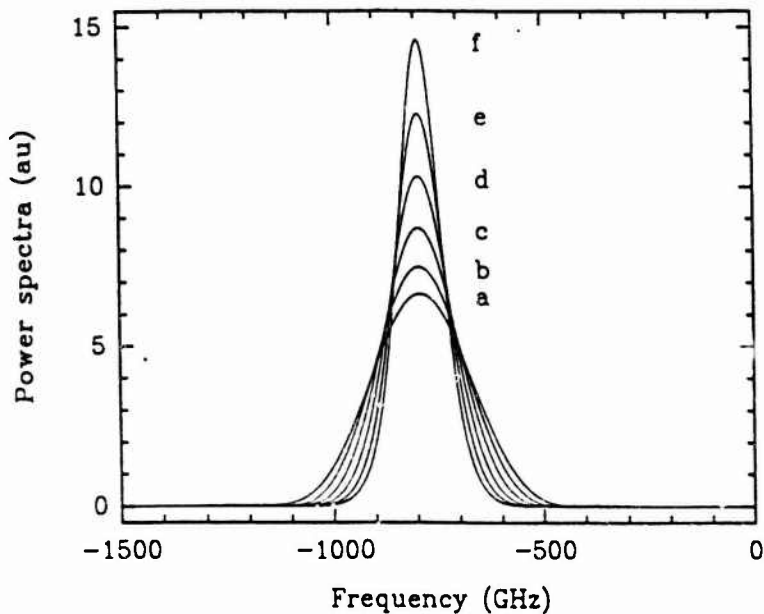


Fig. 5.7 Normalized supermode spectra of the lowest order hypermode for various secondary Michelson mirror detunings. (a) $\delta L_{\text{Mich}} = 0 \mu\text{m}$; (b) $\delta L_{\text{Mich}} = -51 \mu\text{m}$; (c) $\delta L_{\text{Mich}} = -102 \mu\text{m}$; (d) $\delta L_{\text{Mich}} = -152 \mu\text{m}$; (e) $\delta L_{\text{Mich}} = -203 \mu\text{m}$; (f) $\delta L_{\text{Mich}} = -254 \mu\text{m}$. The frequency of 0 GHz corresponds to the resonant frequency.

secondary mirror detunings ranging from $\delta L_{\text{Mich}} = 0 \mu\text{m}$ to $-254 \mu\text{m}$ ($\delta T_{\text{Mich}} > 0$). The cavity detunings δT_{cav} were adjusted to yield an effective detuning in (5.46) of $10 \mu\text{m}$. The overall spectrum is indeed narrowed by increased interferometer detunings. Furthermore, a

detuning of $\delta L_{\text{Mich}} = -254 \mu\text{m}$, corresponding to $\delta N = 0.005$, is seen to yield a spectral width of 120 GHz (40 modes), which compares with a width of ~ 20 modes from the passive mode structure for the same δN and γ_c in Fig. 5.6. This broadening of the passive spectrum, even in the presence of gain, is due to mode coupling by the short electron pulses.

A comparison between the coupled mode and pulse propagation simulations is illustrated in Fig. 5.8, which displays the surviving temporal supermodes for secondary mirror

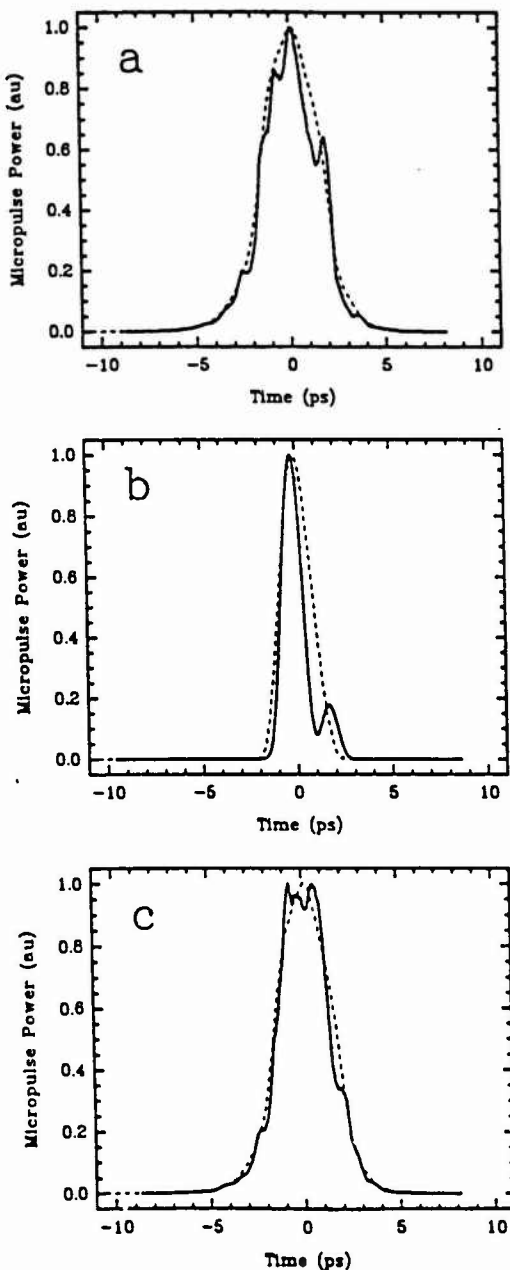


Fig. 5.8 Temporal supermodes from the coupled mode (dashed line) and pulse propagation (solid line) simulations for secondary Michelson mirror detunings of: (a) $\delta L_{\text{Mich}} = +279 \mu\text{m}$; (b) $\delta L_{\text{Mich}} = 0 \mu\text{m}$; (c) $\delta L_{\text{Mich}} = -254 \mu\text{m}$.

detunings of $\delta L_{\text{Mich}} = +279 \mu\text{m}$, $\delta L_{\text{Mich}} = 0 \mu\text{m}$, and $\delta L_{\text{Mich}} = -254 \mu\text{m}$ at the peaks of the cavity detuning curves. The temporal supermodes from the coupled mode simulations were obtained simply by Fourier transforming the spectra and normalizing the maximum powers to unity; the pulse propagation supermodes were obtained by averaging the N pulses in the cavity just prior to the onset of saturation, and again normalizing the powers to unity. The time of 0 ps corresponds to the centroid of each curve. Aside from power fluctuations in the pulse propagation simulations due to the build up from noise in the presence of the higher order hypermodes, the agreement with the coupled mode simulations is excellent. The anomaly in the pulse propagation curve for $\delta L_{\text{Mich}} = 0 \mu\text{m}$ may be due to an incomplete decay of the higher order supermodes prior to the onset of saturation.

Finally, as suggested by the broad power detuning curve in Fig. 5.5c, the optical pulses should remain broad at saturation. This is in fact confirmed from the pulse propagation simulations, and suggests that the Michelson resonator can be used for pulse shaping in applications requiring variable pulse widths. Such manipulations would be much easier than altering the linac configuration to yield variable electron pulse widths. On the other hand, the resulting pulses would generally not be appropriate for high resolution spectroscopy, because large detunings of the secondary mirror decrease the decay rates of the higher order hypermodes. This is shown in the following paragraph.

C. Decrease of the hypermode decay rates

Applications of the Michelson resonator FEL in high resolution spectroscopy depend upon the suppression of the higher order hypermodes in a time much shorter than the duration of the macropulse. Optimum hypermode decay is obtained by perfectly overlapping the pulses in the interferometer, whereas completely detuning the pulses merely yields the axial mode spectrum of a two-mirror resonator with increased losses. Therefore, the problem of determining the range of interferometer detunings which yield tolerable decay rates has immediate practical consequences. In this paragraph we report the results of both coupled mode and pulse propagation simulations for the case of finite interferometer detunings.

The incomplete decay of the higher order hypermodes is illustrated in Fig. 5.9, which shows the macropulse spectra after 160 passes obtained from pulse propagation simulations of a Michelson resonator FEL with $N = 10$ circulating pulses and an optimum beamsplitter reflectance of $\beta^2 = 50\%$. The cavity detunings were adjusted in (5.46) to yield an effective desynchronization of $10 \mu\text{m}$. The dots in Fig. 5.9 are the relative mode intensities after 160 passes calculated from the corresponding coupled mode simulations with $N = 10$, which were obtained from the eigenvalues Λ_{m_h} of the surviving supermodes for each of the $m_h = 0, \pm 1, \pm 2$ hypermodes according to

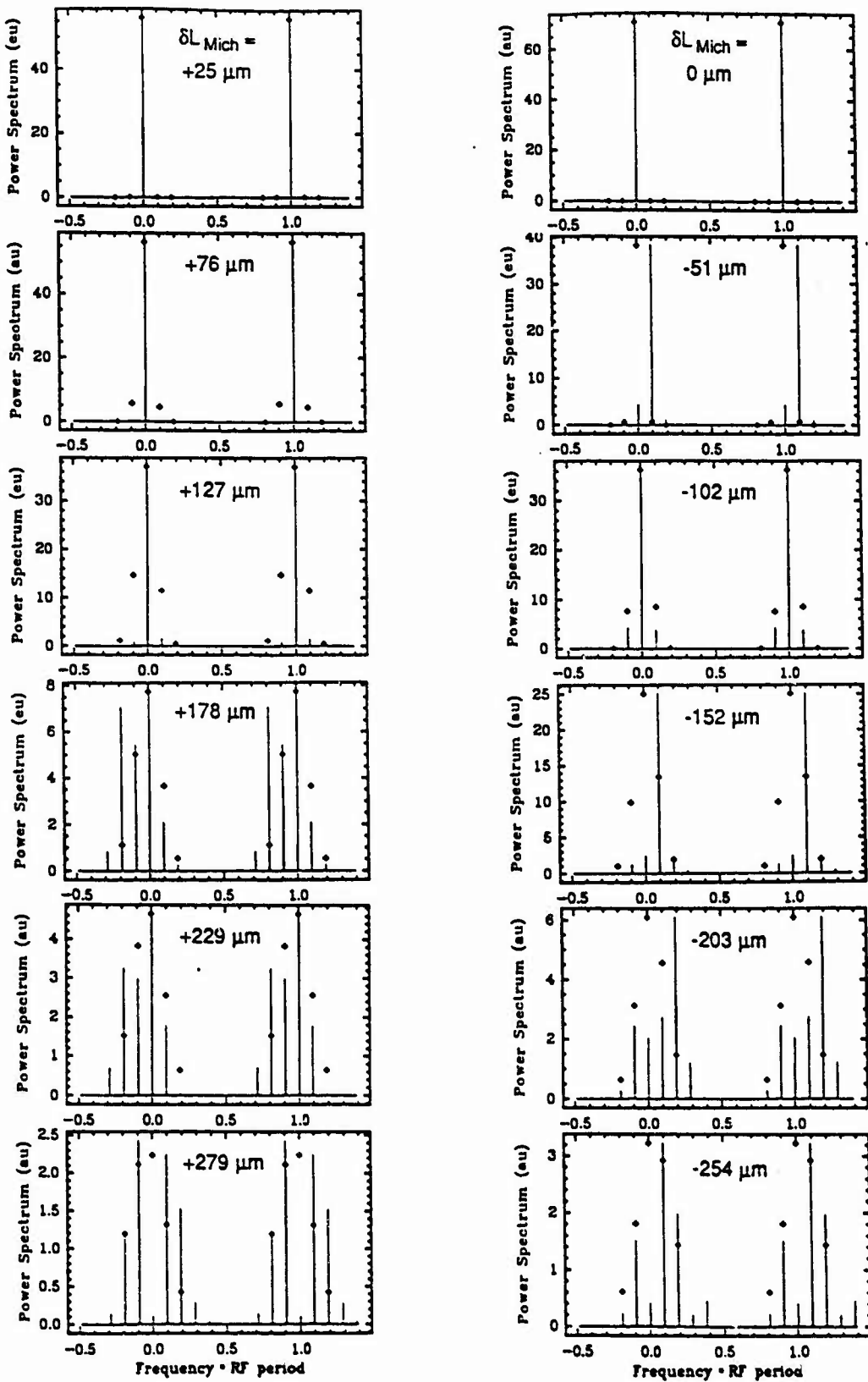


Fig. 5.9 Macropulse spectra from the pulse propagation simulations (after 160 passes) using $N = 10$ pulses. The secondary Michelson mirror detunings δL_{Mich} are indicated on each graph, and the relative intensities from the corresponding coupled mode simulations are shown as dots.

$$I_{mb}(160) = \frac{\sum_{p=1}^{160} P_{macr}(p) (\Lambda_{mb}^{rel})^p}{\sum_{p=1}^{160} P_{macr}(p)} ; \quad \Lambda_{mb}^{rel} \equiv \frac{\Lambda_{mb}}{\Lambda_0} , \quad (5.50)$$

where $P_{macr}(p)$ is the macropulse power at pass p from the pulse propagation simulations, and $(\Lambda_{mb}^{rel})^p$ is the relative spectral hypermode intensity 'at pass p '.

Discrepancies between the simulations can be attributed to several factors, such as the build up from shot noise in the pulse propagation simulations, which initially biases and continuously populates the mode intensities, and the onset of saturation in these simulations, which flattens and shifts the gain curve. Both of these effects are omitted from the classical small signal analysis from which the coupled mode equations are derived in Section II. The relative mode intensities from the coupled mode simulations are also seen to vary more continuously with interferometer detuning than the spectra from the pulse propagation simulations, which may be evidence for mode competition effects in the latter simulations during the onset of saturation.

Aside from these discrepancies, we see that the coupled mode simulations reproduce the widths of the surviving groups of hypermodes fairly accurately (at least to the extent that applications to spectroscopy can be practically assessed), and that the asymmetry of the intensities with respect to the lowest order hypermode is clearly manifest in each set of simulations. The tolerable detuning range of the interferometer is fairly large, yielding essentially complete hypermode decay for detunings $|\delta L_{Mich}| \gtrsim 70 \mu m$; the corresponding shift in the overlap of successive pulses is $\sim 140 \mu m$, which compares to a slippage length of $160 \mu m$ or an electron pulse length (4 ps) of $1200 \mu m$. Larger detunings yield mode spectra that are not appropriate for high resolution spectroscopy. This detuning range is substantially less than the pulse length, but much larger than the fractional wavelength stability of the mirrors which must be maintained in order to select and tune the hypermodes. We can provide a simplified understanding of these results by examining the passive mode structure of the detuned Michelson mirror resonator.

From the expression for hypermode loss given in (5.45), we see that for finite detunings δN there exists a mode

$$n_0 = - \frac{m_h}{N \delta N} \quad (5.51)$$

which exhibits essentially zero interferometer loss, even for the higher order hypermodes; this result is illustrated in Fig. 5.10, which shows the mode structure of the first order hypermode for various detunings δN . If the detuning is small, the mode n_0 is positioned well

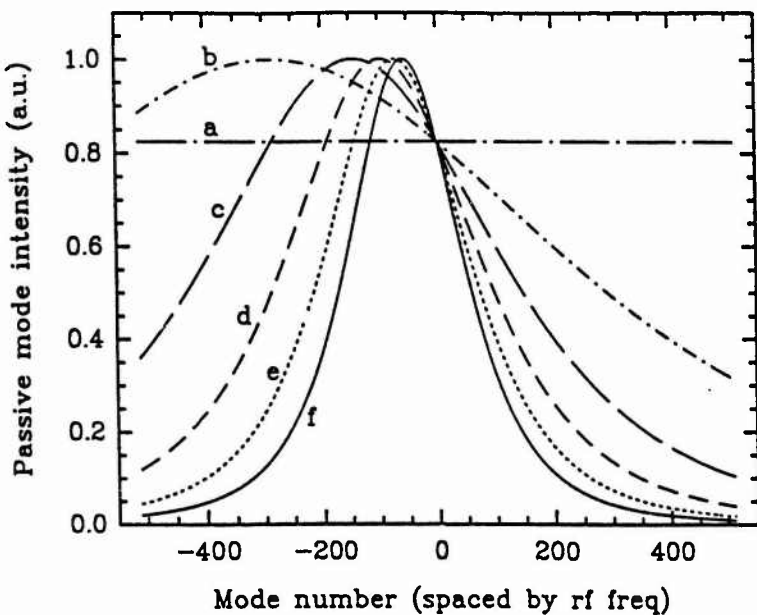


Fig. 5.10 Passive intracavity intensities of the first order hypermode for various fractional interferometer detunings δN , calculated in the same manner as Fig. 5.6. (a) $\delta N = 0$; (b) $\delta N = 0.0001$; (c) $\delta N = 0.0002$; (d) $\delta N = 0.0003$; (e) $\delta N = 0.0004$; (f) $\delta N = 0.0005$.

outside of the gain curve, and the mode losses within the gain curve exhibit only a linear dependence on frequency with little net change in absolute value. However, increasing the interferometer detuning shifts the mode n_0 towards the peak of the lowest order hypermode located (by definition) near the center of the gain curve. Eventually the peaks of, say, the zeroth and first order hypermodes will both be centered on the gain curve. Since the hypermode curvature (i.e. the second derivative of mode loss with respect to mode number) is independent of the hypermode number m_h , these hypermodes will yield FEL supermodes with essentially the same total leakage losses, and, consequently, the same relative decay rates.

From the above observations, we suspect that a decrease in the hypermode decay rates should occur somewhere between small detunings, for which there is essentially no change in the relative loss of the zeroth and higher order hypermodes, and large detunings, for which several of the lowest order hypermodes are peaked near the center of the gain curve and yield essentially identical net gains. The crossover point can be quantified by considering the shift in the peak of the first order hypermode due to a finite detuning δN_c (the analysis does not distinguish between $m_h = \pm 1$), for which the following criterion is chosen: *The hypermode decay rates start to decrease when the first order hypermode is peaked at a frequency f_c for which the small signal gain is equal to the net gain of that hypermode in the case of zero detuning.* This criterion is illustrated schematically in Fig. 5.11 and is motivated by the paraphrase that, for zero detuning, the difference in the relative

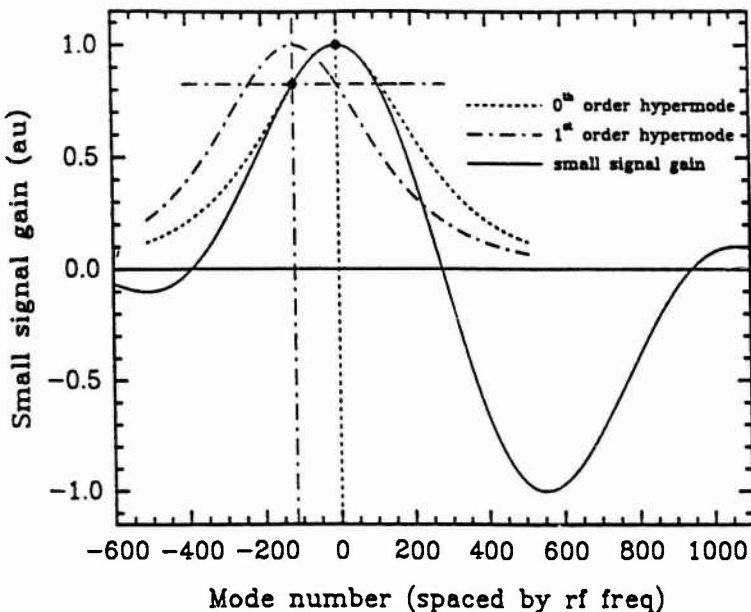


Fig. 5.11 Criterion for determining the onset of degradation in the hypermode decay rates. The onset of degradation occurs when the first order hypermode is peaked at a frequency for which the small signal gain is equal to the net gain of that hypermode in the case of zero detuning. The mode shift and hypermode losses are only schematic and are greatly exaggerated.

decay of the zeroth and first order hypermodes is due to different *losses*, whereas for finite detunings, the difference in the relative decay is due to different *gains* (the mode structures being equal, but peaked at different positions on the gain curve). The transition should actually be somewhat gradual, because the FEL supermodes of the first order hypermode will always be pulled slightly from the crossover point and towards the center of the gain curve.

To quantify the above criterion, we first expand the CW small signal power gain $G(v) = 2 \cdot \text{Re}\{g_0(v)\}$ about the peak of the gain curve v_p , where $g_0(v)$ is defined in (5.48) and $v_p = 2.606$ is the corresponding resonance parameter. The expansion yields

$$G(v) = r_j [0.135 - 0.0221(v - v_p)^2] , \quad (5.52)$$

where the dimensionless current density is

$$r_j = \frac{8\pi^2 e^2}{mc^2} \left(\frac{L_w}{\gamma} \right)^3 \frac{\hat{K}^2}{\lambda_w} (J_0 - J_1)^2 \frac{I}{c(A)e} , \quad (5.53)$$

and I is the electron beam current. According to the above criterion, the resonance parameter v_c corresponding to the frequency f_c should then satisfy the following equation:

$$G(v_c) = 0.135 r_j - \left(\frac{4\pi^2 r^2 I^2}{N^2} \right) , \quad (5.54)$$

where the first order hypermode loss on the RHS is got from (5.45) with $m_h = 1$ and $\delta N = 0$.

Note that the common cavity losses γ_c and the leakage losses of the detuned hypermodes both drop out in an equivalent condition requiring that the relative eigenvalues (instead of the net gains) be the same. Solving (5.52) and (5.54) for $v = v_c$ and converting to f_c via the definition of the resonance parameter (5.31) yields

$$|f_c - f_p| = 6.73 \frac{c(r t)}{N_w \lambda N \sqrt{\Gamma_j}} . \quad (5.55)$$

By relating the frequency shift $(f_c - f_p)$ to the first order hypermode shift n_0 from (5.51),

$$|n_0| \equiv \frac{|f_c - f_p|}{\left(\frac{1}{T_e}\right)} = \frac{1}{N |\delta N_c|} \quad (5.56)$$

(in which the n_0 modes are separated by the rf frequency), and by writing the fractional detuning δN_c as the ratio of the temporal pulse displacement to the rf period,

$$\delta N_c \equiv \frac{\delta T_{\text{Mich}}^c}{T_e} \equiv \frac{-2 \cdot \delta L_{\text{Mich}}^c}{c T_e} , \quad (5.57)$$

we may finally combine (5.55), (5.56), and (5.57) to yield our final result for the secondary mirror detuning δL_{Mich}^c for which a decrease in the hypermode decay rate becomes evident:

$$|\delta L_{\text{Mich}}^c| = \frac{N_w \lambda \sqrt{\Gamma_j}}{13.5 (r t)} . \quad (5.58)$$

This result has an interesting physical interpretation. The most important consequence is that the 'critical detuning' is independent of both the rf period T_e and the number of pulses N in the cavity. Practical resonator designs will typically have beam splitter reflectances between $r^2 \sim 10\%$ and $r^2 \sim 50\%$, so that setting $r^2 = 18.4\%$ will result in no more than a 30 % error in (5.58) over that range of reflectances. This approximation gives $|\delta L_{\text{Mich}}^c| \approx 0.191 \cdot (N_w \lambda) \cdot \sqrt{\Gamma_j}$. In moderate gain devices such as the Mark III FEL, for which the small signal gain might range from 30 % to 80 %, we may approximate $\sqrt{\Gamma_j} \sim 1.90$ with, again, no more than a 30 % error over that range of gains. This second approximation gives $|\delta L_{\text{Mich}}^c| \approx 0.4 \cdot (N_w \lambda)$, which is accurate to about $\pm 50\%$ for the practical operating parameters given above. We may interpret this result as follows: in order to obtain the optimum hypermode decay, the gross overlap of the pulses in the interferometer (i.e. $2 \cdot |\delta L_{\text{Mich}}^c|$) should be accurate to within roughly one slippage length, so that the phase information between corresponding sections of successive pulses can be communicated in a single pass through the wiggler; this communication evidently occurs via the electron beam. If successive pulses are shifted by more than a slippage distance, more than one pass will be required to transmit the phase information between pulses, resulting in a decrease in the hypermode decay rates.

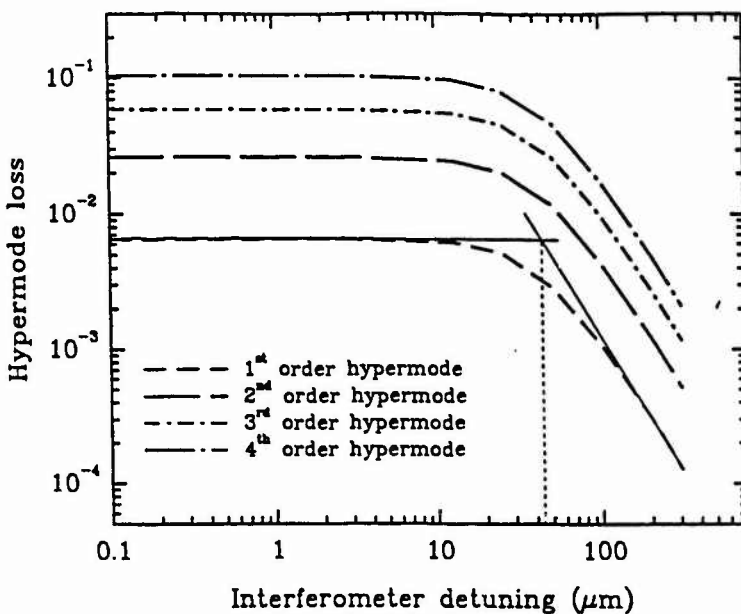


Fig. 5.12 Coupled mode simulations of hypermode loss γ_{m_h} for $N = 35$, as a function of secondary Michelson mirror detuning, calculated as the average loss of the $\pm m_h$ hypermodes.

The coupled mode simulations actually display this 'critical detuning' unambiguously. Figure 5.12 shows the relative hypermode losses $\gamma_{m_h} \equiv 1 - \Lambda_{m_h}^{\text{rel}}$ for $|m_h| = 1, 2, 3, 4$ in a Michelson resonator FEL with $N = 35$ circulating pulses and an optimum beamsplitter reflectance of $r^2 = 50\%$, where $\Lambda_{m_h}^{\text{rel}}$ are the relative eigenvalues defined in (5.50). The cavity and interferometer detunings were again adjusted in (5.46) to yield an effective desynchronism of $10 \mu\text{m}$. The log-log plot indicates a distinct transition between two asymptotic regions of essentially constant, and rapidly decreasing, losses; the decreased relative losses in the latter region lead to reduced decay rates. These asymptotes intersect at an interferometer detuning of $44 \mu\text{m}$, which compares with a detuning of $48 \mu\text{m}$ calculated directly from (5.58) and (5.53) for the parameters listed in Table 5.1 ($r_j = 4.3$); the agreement would actually be better if an appropriate filling factor were included in the calculation of r_j . Furthermore, by identifying the relative loss γ_1 of the first order hypermode with the decrease in relative gain from the second term in (5.52), and substituting for the corresponding detuning δL in a manner similar to the previous calculation, we obtain (for $\delta L > \delta L_{\text{Mich}}^c$)

$$\gamma_1 = \pi^2 (0.0221) r_j \frac{N_w^2 \lambda^2}{N^2 \delta L^2}, \quad (5.59)$$

so that the hypermode loss is proportional to the inverse square of the detuning δL . This result compares with a measured slope of -2.01 for the second asymptote on the log-log plot in Fig. 5.12.

The output coupling scheme considered in paragraph A can now be re-examined. By phase locking the optical beam in Fig. 5.9 using a secondary mirror detuning of, say, 50 to 80 μm , with a corresponding cavity detuning of $\delta L_{\text{cav}} \sim -15$ to $-30 \mu\text{m}$, we see from Fig. 5.5a that roughly 1 to 3 % of the intracavity power can be outcoupled in the form of leakage losses. Therefore, in applications to high resolution spectroscopy, outcoupling by means of leakage losses can be competitive with Brewster plate output coupling, which typically yields less than 4 % of outcoupled power per surface.

In the following chapter, I report the first operation of a Michelson resonator FEL, and provide indirect evidence for the presence of mode reduction based on numerical simulations of the leakage losses. In the resonator configuration employed in the experiment, the output coupler and beamsplitter were two sides of the same (parallel) Brewster plate. As a result, the leakage power traveled to the detector with the outcoupled power. Although practical applications of the Michelson resonator FEL in spectroscopy would normally require an isolated output beam, the concurrent detection of leakage power in the experiment actually provided the crucial diagnostic, in the absence of mode-selective spectral diagnostics on the output beam, to indirectly demonstrate the presence of phase locking.

VI. REFERENCES

- [1] G. R. Edlin, R. W. Jones, and J. F. Perkins, "Phase locked rf linac free electron laser," U. S. Patent No. 4,748,629, May 31, 1988.
- [2] D. Oepts, A. F. G. van der Meer, R. W. B. Best, P. W. van Amersfoot, and W. B. Colson, "Simulations of mode reduction with an intracavity etalon in an rf-linac based FEL," *Nucl. Instr. and Meth.*, vol. A285, pp. 204-210, 1989.
- [3] E. B. Szarmes, S. V. Benson, and J. M. J. Madey, "Mode control on short-pulse FELs using a Michelson-mirror resonator," *Nucl. Instr. and Meth.*, vol. A296, pp. 98-109, 1990.
- [4] P. Elleaume, "Microtemporal and spectral structure of storage ring free-electron lasers," *IEEE J. Quantum Electron.*, vol. QE-21, pp. 1012-1022, 1985.
- [5] E. B. Szarmes and J. M. J. Madey, "The Michelson resonator free-electron laser - Part I: Passive mode structure and mode decay," *IEEE J. Quantum Electron.*, to be published.
- [6] G. Dattoli, T. Hermans, A. Renieri, and A. Torre, "Lethargy of laser oscillations and supermodes in free-electron lasers. I.," *Phys. Rev. A*, vol. 37, pp. 4326-4333, 1988. —, "Lethargy of laser oscillations and supermodes in free-electron lasers. II. Quantitative analysis," *ibid*, vol. 37, pp. 4334-4339, 1988.
- [7] G. Dattoli, T. Hermans, L. Mezi, and A. Torre, "A review of the theory of pulse propagation in the long bunch low gain regime," *Nucl. Instr. and Meth.*, vol. A272, pp. 351-363, 1988.
- [8] See, for example, M. DiLomenico, Jr., "Small-signal analysis of internal (coupling-type) modulation of lasers," *J. Appl. Phys.*, vol. 35, pp. 2870-2876, 1965. The present study refers to a useful synopsis given in ref. [14].

- [9] G. Dattoli and A. Renieri, "The free-electron laser single-particle multimode classical theory," *Il Nuovo Cimento*, vol. 61B, pp. 153-179, 1981.
- [10] G. Dattoli, A. Marino, and A. Renieri, "A multimode small signal analysis of the single pass free electron laser," *Opt. Commun.*, vol. 35, pp. 407-412, 1980.
- [11] W. B. Colson, "Classical free electron laser theory," in *Laser Handbook, Volume 6*. Amsterdam: North Holland, 1990, ch. 5, pp. 115-194.
- [12] S. V. Benson, "Diffractive effects and noise in short pulse free-electron lasers," Ph. D. thesis, Stanford University, 1985.
- [13] A. E. Siegman, *Lasers*, Mill Valley, CA: University Science Books, 1986.
- [14] A. E. Siegman, *ibid*, section 27.5, pp. 1087-1092.
- [15] M. F. Becker, D. J. Kuizenga, and A. E. Siegman, "Harmonic mode locking of the Nd:YAG laser," *IEEE J. Quantum Electron.*, vol. QE-8, pp. 687-693, 1972.
- [16] S. V. Benson, W. S. Fann, B. A. Hooper, J. M. J. Madey, E. B. Szarmes, B. Richman, and L. Vintro, "A review of the Stanford Mark III infrared FEL program," *Nucl. Instr. and Meth.*, vol. A296, pp. 110-114, 1990.
- [17] G. W. Stewart, *Introduction to Matrix Computations*, Orlando, FL: Academic Press, 1973.
- [18] P. Elleaume and D. A. G. Deacon, "Transverse mode dynamics in a free-electron laser," *Appl. Phys. B*, vol. 33, pp. 9-16, 1984.
- [19] S. V. Benson and J. M. J. Madey, "Shot and quantum noise in free electron lasers" *Nucl. Instr. and Meth.*, vol. A235, pp. 55-60, 1985.

Chapter 6

A phase locking experiment on the Mark III free-electron laser

The broad and continuous tunability of the rf linac-driven infrared free-electron laser (FEL), coupled with its high power picosecond time structure, has greatly enhanced the research capabilities in the field of infrared spectroscopy. However, the spectral structure of the optical beam, with longitudinal modes spaced by the round trip frequency in a bandwidth determined by the Fourier transform of the short pulses, often poses a significant limitation for experiments requiring high spectral resolution. A more convenient mode structure can be obtained by using an intracavity interferometer [1]-[3] to couple successive optical pulses so that they build up from noise with a definite phase relationship. The resulting phase locked optical pulses yield a spectrum of longitudinal modes separated by the rf frequency of the linac, which modes can then be more easily isolated and filtered in applications to high resolution spectroscopy.

In this chapter, I report the first operation of an FEL using an intracavity Michelson mirror resonator [4], [5] on the Mark III FEL, and present indirect evidence for phase locked operation using a beamsplitter reflectance of only 1.4 %. Although mode-selective spectral diagnostics were not available at the time the experiment was performed, evidence for phase locking was obtained from measurements of the optical power which indicated a substantial degree of destructive interference in the output pulses at the beamsplitter. The observed power fluctuations, and the displacement of the secondary interferometer mirror over which these fluctuations were observed, are reproduced fairly accurately in both pulse propagation

simulations (Chapter 4) and coupled mode simulations (Chapter 5) using operating parameters appropriate to the experimental configuration.

II. EXPERIMENTAL DESIGN

A. Laser configuration

The Mark III FEL [6], [7] is driven by a 2.857 GHz pulsed rf linac using electrons from a synchronized microwave gun and a thermionic cathode source. Since thermionic emission fills every bucket of the rf wave, the electron micropulses are delivered to the laser at the rf frequency of 2.857 GHz; this driving frequency harmonically mode locks the 1.837 m resonator and yields 35 independently circulating optical micropulses per round trip. The linac energy was set to roughly 38.4 MeV in the present experiment and the lasing wavelength was 3.2 μm , corresponding to an rms wiggler field of 3.5 kGauss over each 2.3 cm wiggler period. The rf source was pulsed at a repetition rate of 15 Hz, and the average current was roughly 105 mA over an electron macropulse duration of 2.5 μs ; this current was inferred from an inductive toroid positioned at the exit of the linac.

The optical cavity uses metal cavity mirrors and Brewster plate output coupling of the horizontally polarized radiation. The vacuum chamber containing the upstream cavity mirror and output couplers was designed to allow four choices of Brewster plates, two of which can be placed on the beamline at the same time. In the usual configuration, a single Brewster plate is inserted into the beam, and only the reflections from one side of that plate are normally outcoupled to the user laboratory. However, one of the output couplers is positioned beside a Brewster window on the vacuum chamber, which allows the alignment of an external mirror for redirecting the secondary outcoupled reflections into the user laboratory as well.

B. Michelson mirror resonator

The Michelson mirror resonator was constructed using a 2 mm thick, uncoated zinc selenide Brewster plate placed beside the vacuum window, with one surface acting as the beamsplitter and the other surface acting as the output coupler. The optical cavity and laser diagnostics are shown in Fig. 6.1. The angle of incidence was $\theta_i = 60.8^\circ$, which was measured with a He-Ne laser co-aligned to the resonator and outcoupled through the side vacuum window. The corresponding reflectance of each surface (calculated from the Fresnel equations [8]) was 1.4 %. The radius of curvature of mirrors M1, M2, and M3 was 150 cm, with M2 positioned on a translation stage so that its distance from the Brewster plate was one half of an rf wavelength longer than the distance from M1 to the Brewster plate. As a result of this mirror placement, the linear resonator formed by M2 and M3 yielded a

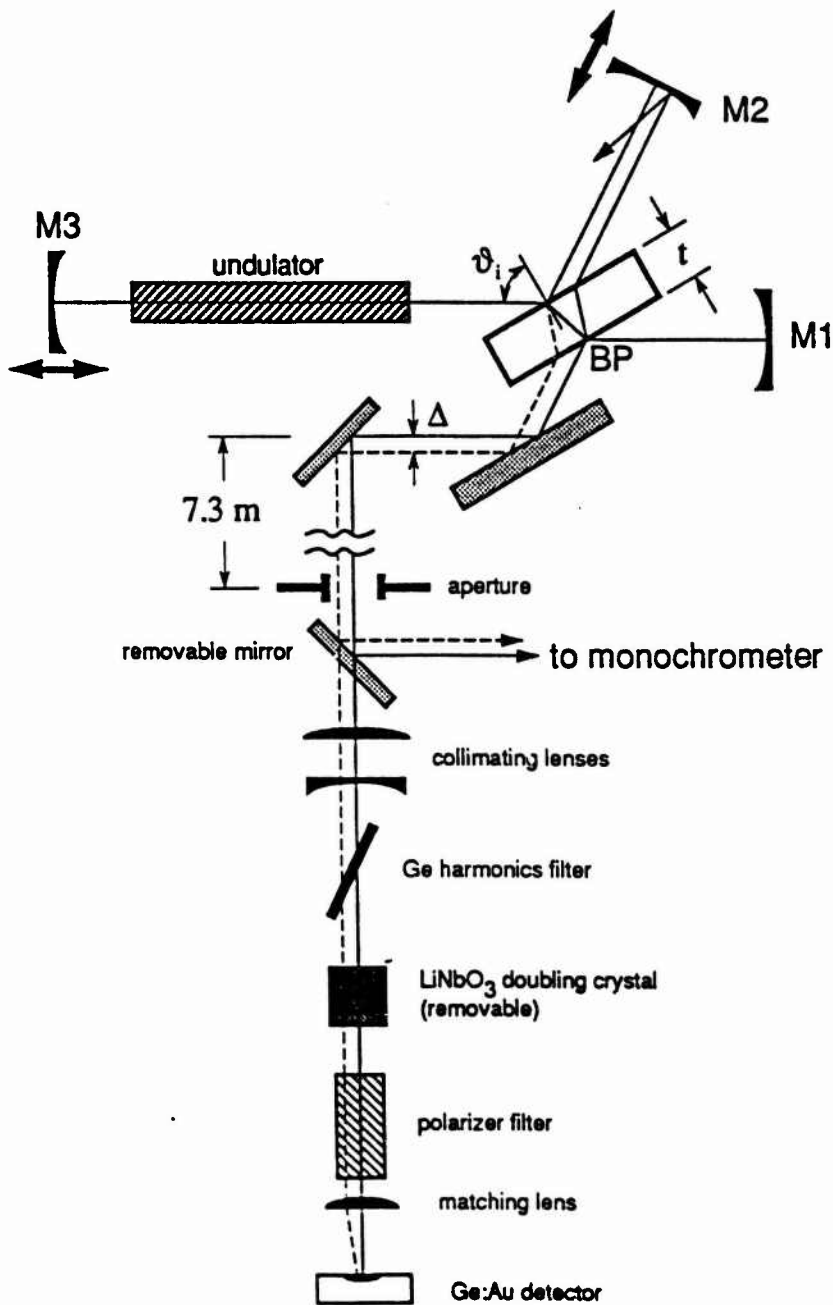


Fig. 6.1 Experimental configuration of the Michelson mirror resonator and the optical diagnostics. The round trip time from the back surface of Brewster plate BP to the secondary mirror M2 is one rf period longer than the round trip time from BP to M1. Mirrors M2 and M3 are on translation stages. The Brewster plate is an uncoated ZnSe etalon with a thickness of $t = 2$ mm and an angle of incidence of $\vartheta_i = 60.8^\circ$. The transverse deviation between the two surface reflections is $\Delta = 0.73$ mm. The leakage beam is shown as the dashed line.

slightly different Rayleigh range than the linear resonator formed by M1 and M3. However, calculations using the appropriate radii of curvature for the transverse modes at the beamsplitter indicated a negligible reduction in the Strehl ratio of the superposed beam.

The most important feature of the experiment resulted from the 5 arc second parallelism of the Brewster plate, due to which both the output and leakage beams traveled to the detector with a transverse deviation of less than $180 \mu\text{m}$ over 7.3 m. The coincident detection of leakage power was actually used to infer the presence of phase locking, as explained below. On the other hand, the 2 mm thickness yielded a transverse displacement of $\Delta = 0.73 \text{ mm}$ between the two beams. As a result, only a single secondary reflection from the external mirror could be aligned to the laser diagnostics; the other beam (shown as the skew reflection on M2 in Fig. 6.1) was displaced transversely by roughly 7 mm in the laboratory and was vignetted by an aperture placed in front of the laser diagnostics.

C. Laser diagnostics

The diagnostic apparatus consisted primarily of a monochromator to measure the wavelength and a fast gold-doped germanium detector to measure the time dependent optical power during the macropulse. A co-linear optical autocorrelator (not shown in Fig. 6.1) was also used to measure the duration of the optical micropulses.

The distance from the laser to the diagnostic table was roughly 7.3 m. The optical beam was first spatially filtered with an aperture in order to vignette the skew reflection from the secondary mirror M2. A removable mirror could then be positioned to direct the beam into a 1 m grating monochromator. Otherwise, the beam continued through a collimating telescope and a germanium Brewster plate which was used to filter out the coherent harmonics of the FEL. In order to locate the synchronous position of mirror M2, the filtered beam was first passed through a Type I phase-matched lithium niobate crystal to amplify small changes in peak intensity. A polarizer after the doubling crystal was used to filter the horizontally polarized fundamental light from the vertically polarized doubled light, and the doubled beam was then focused onto the Ge:Au detector.

III. EXPERIMENTAL PROCEDURE AND RESULTS

To bring the Michelson resonator to lasing, the secondary mirror M2 was first detuned, and the position of mirror M3 was set by scanning the cavity length until the optical macropulse through the doubling crystal showed the greatest peak power with the smallest fluctuations; this position corresponded to the stable maximum of the cavity detuning curve. The secondary mirror M2 was then aligned transversely using the co-aligned He-Ne laser, and the position of synchronism determined by translating the secondary stage until the largest power fluctuations in the doubled beam were observed on the detector. The secondary mirror was then resteered to optimize the transverse overlap, and the doubling crystal was removed in order to observe the $3.2 \mu\text{m}$ beam on the detector.

Figure 6.2 shows oscilloscope traces of the detector response displaying the envelopes of 32 successive macropulses in cases in which (a) the secondary mirror was completely detuned, and (b) the secondary mirror was longitudinally synchronized; the power fluctuations are $\pm 5\%$ and $\pm 25\%$ respectively. Note that, apart from the large intrinsic fluctuations in the synchronized case, the lower limit of the laser power in Fig. 6.2(b) is 14% smaller than the mean macropulse power from Fig. 6.2(a); in some instances, reductions as great as 27% and enhancements as large as 52% (i.e. fluctuations of $\pm 35\%$) were also observed. These power fluctuations were observed over a range of 225 μm in the position of the secondary mirror, and were rather abruptly extinguished outside of this range. Treated as an autocorrelation measurement, this tuning range would indicate a pulse width of $1.1 \pm 0.4\text{ ps}$ (the uncertainty resulting from the distorted pulse shape and the estimated degree of overlap within which any power fluctuations would be manifest.) To confirm that this tuning range was indeed due to the synchronism of mirror M2, a proper autocorrelation measurement [9] was also performed on the diagnostic table for the case in which the secondary mirror was desynchronized. The autocorrelation trace is shown in Fig. 6.3 and indicates a roughly Gaussian profile with a FWHM pulse width of $\Delta\tau = 1.2\text{ ps}$. The corresponding optical spectrum obtained on the monochromator is shown in Fig. 6.4. The time-bandwidth product for the pulses is $\Delta\tau \cdot \Delta\nu = 0.56$, which is slightly larger than the transform limited product of 0.44.

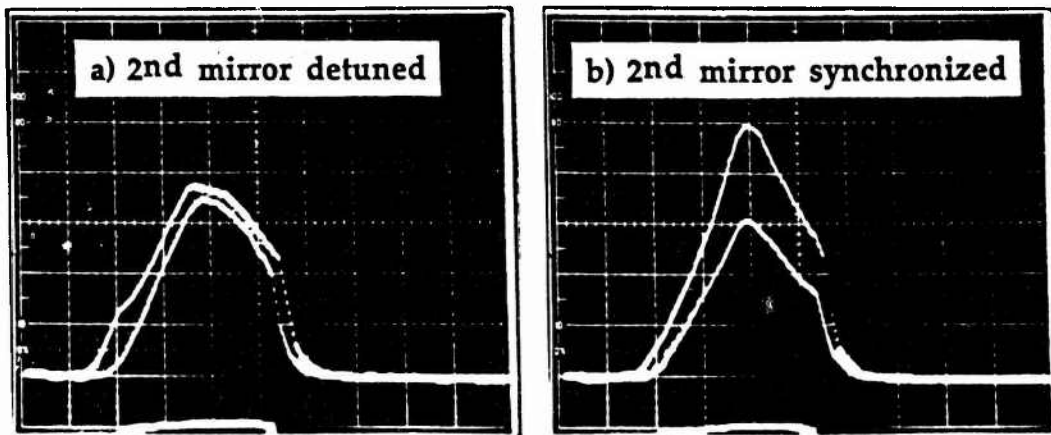


Fig. 6.2 Oscilloscope traces of the Ge:Au detector response showing the envelopes of 32 successive macropulses for a Michelson mirror resonator with $N = 35$ pulses and 1.4% coupling in which the secondary mirror was (a) completely detuned, and (b) synchronous at the position of one rf period delay. Horizontal scale is $0.5\text{ }\mu\text{s/div}$.

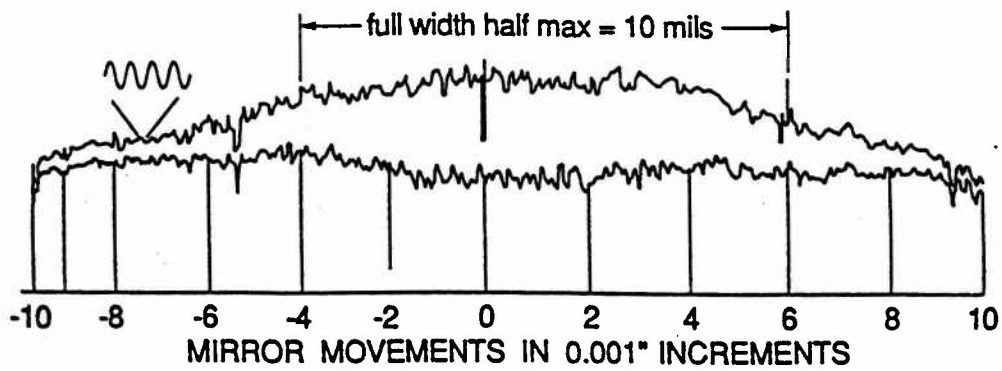


Fig. 6.3 Optical autocorrelation trace of the micropulses from the laser in which the secondary mirror was completely detuned. The $0.010''$ FWHM refers to the displacement of the autocorrelator mirror. The FWHM delay is therefore $0.020''$, which yields a FWHM pulse duration of 1.2 ps assuming a Gaussian optical pulse profile. (From [9].)

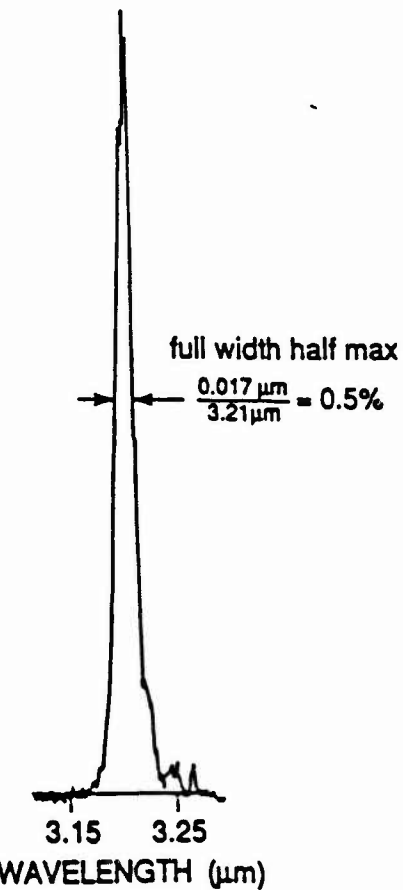


Fig. 6.4 Spectrum of the optical beam from the laser in which the secondary mirror was completely detuned, obtained using a 1 m monochromator. The time-bandwidth product of the optical pulses is 0.56, which is slightly larger than the transform limit for Gaussian pulses. (From [9].)

The most remarkable aspect of the above results is the dramatic change in the entire macropulse power resulting from only a 1.4 % beamsplitter reflectance. If mirror M2 were positioned so that the *same* optical pulses instead of successive ones were coupled at the beamsplitter, a trace of the output power (including leakage) versus mirror position would show interference fringes with an amplitude of ± 67 % for every half wavelength in the mirror position. This is not much greater than the largest fluctuations observed in the above experiment in which successive pulses were coupled, a fact which suggests strongly that the macropulses were at least partially phase locked. Nevertheless, the presence of phase locking does not explain the origin of the fluctuations; in particular, the complete destructive interference of the leakage beam due to phase locking would *always* decrease the total output power. In Section IV, we will demonstrate that such fluctuations could be caused by a mechanical jitter on the secondary mirror mount.

IV. NUMERICAL SIMULATIONS

A. *Simulation parameters*

Pulse propagation simulations of the above experiment were performed in order to determine the degree to which the optical beam would be phase locked; the computer code is described in Chapter 4. The simulations of the detuned Michelson resonator, which followed the growth of only a single pulse, assumed a total output coupling of 4.2 % (three beams aligned with the detector) and a total loss of 7.3 %. The simulations of the synchronized Michelson mirror resonator using 35 coupled pulses assumed a total output coupling of 1.4 % (one beam aligned with the detector) and a total loss of 4.6 %. In each case, the output coupling neglected the skew reflection from the secondary mirror, but the total loss included this reflection plus an extraneous mirror loss of 1.8 %. The output coupling and total losses in the detuned resonator were greater than those of the synchronized resonator by two surface reflections (2.8 %) because the second surface in the latter case acted as the beamsplitter; the leakage losses in the latter simulations appeared naturally in addition to the total losses, and were added explicitly to the outcoupled beam to compute the total output power reaching the detector.

The cavity detuning at mirror M3 was determined from a series of simulations of the detuning curve, in which eight simulations were performed at positions separated by 0.76 μm near the synchronous length. A detuning of 2.3 μm shorter than synchronous was chosen to correspond to the stable maximum of the detuning curve; the power fluctuations at that point were only ± 3 %, compared to ± 60 % at the synchronous length.

The other simulation parameters were determined from the operating configurations of the linac and FEL. The electron beam energy was 38.4 MeV and the optical wavelength

Parameter	Definition	Simulation value
<i>Optical beam parameters</i>		
λ	Resonant optical wavelength	3.2 μm
N	Number of circulating optical pulses	35
r^2	Beamsplitter reflectance	1.4 %
γ_{out}	Output coupling	4.2 % (detuned) 1.4 % (synchronized)
γ_{tot}	Total cavity losses	7.3 % (detuned) 4.6 % (synchronized)
z_R	Rayleigh range	73.08 cm
δL_{cav}	Cavity detuning (shorter than synch)	2.3 μm
P_{tot}	Number of passes (2.5 μs)	200
<i>Electron beam parameters</i>		
γ	Electron beam energy / mc^2	75.15
$\delta\gamma/\gamma$	Inhomogeneous energy spread ($1/e$)	0.5 %
τ_p	Duration of tophat electron pulse	1.6 ps
I	Peak electron current	23 A
GRF	Inhomogeneous gain reduction factor	0.8
T_e	RF period	350.1 ps
ϵ_x	Normalized horizontal emittance ($1/e$)	$8\pi \text{ mm}\cdot\text{mrad}$
ϵ_y	Normalized vertical emittance ($1/e$)	$4\pi \text{ mm}\cdot\text{mrad}$
β_x	Horizontal focussing parameter	45 cm
<i>Wiggler parameters</i>		
N_w	Number of wiggler periods	47
L_w	Wiggler length	108.1 cm
λ_w	Wiggler period	2.3 cm
\hat{K}	RMS wiggler parameter	0.756
$(J_0-J_1)^2$	Bessel function factor	0.812

Table 6.1 Parameters used in the simulations of the Mark III experiment.

- was 3.2 μm . The durations of the electron and optical pulses were assumed to be the same. Since tophat electron pulses were used in all of the simulations, the pulse duration (1.6 ps) was chosen to yield roughly the same rms pulse width as a Gaussian pulse with a FWHM duration of 1.2 ps. The electron beam current during the macropulse was roughly 105 mA, corresponding to a peak micropulse current of 23 A. However, the peak current used in the

simulations was also multiplied by an inhomogeneous gain reduction factor [10] to account for the effects of emittance and energy spread. All of the simulation parameters are listed in Table 6.1.

B. Simulation results

The degree of mode reduction resulting from a beamsplitter reflectance of 1.4 % is illustrated in Fig. 6.5, which shows the average mode spectrum of the entire macropulse for eight simulations of the synchronized resonator. The dots are the relative mode powers predicted from the eigenmode analysis of Chapter 4, weighted over the macropulse. We see that the mode reduction is substantial and can be expected to yield relatively small leakage losses. Indeed, the leakage losses calculated from eq. (4.39) of Chapter 4 are only 0.26 % after 200 passes, which is substantially smaller than the 2.8 % output coupling from the beamsplitter which would result from the superposition of pulses with uncorrelated phases.

A comparison of the simulated output powers for the detuned and synchronized resonators is shown in Fig. 6.6. We see that the total output power in the synchronized case is reduced by 42 % from the power in the detuned resonator, and the fluctuations are only $\pm 7\%$. Therefore, the degree of phase locking indicated by Fig. 6.5 can have a dramatic effect on the total outcoupled power. On the other hand, the $\pm 7\%$ fluctuations do not reproduce the fluctuations observed in the experiment. To determine whether the presence of jitter in the secondary mirror mount could cause these fluctuations, I performed a series of simulations in which the phase offset between successive pulses was continuously slewed over the macropulse. Total phase shifts of π , 2π , 4π , and 8π radians were examined using eight simulations for each value, and the largest effect was observed for a phase

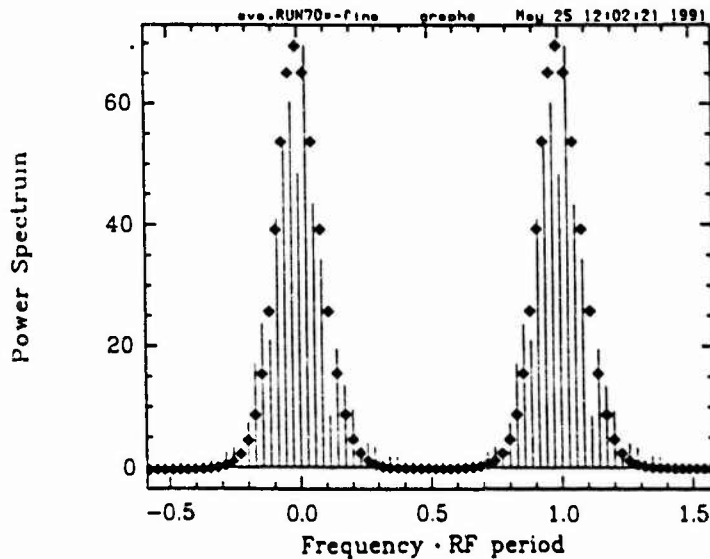


Fig. 6.5 Longitudinal mode spectrum of a perfectly tuned Michelson resonator FEL with 35 pulses and a beamsplitter reflectance of 1.4 %. The spectra for 200 passes are averaged over eight simulations. The dots are the mode powers predicted from the eigenmode analysis of Chapter 4.

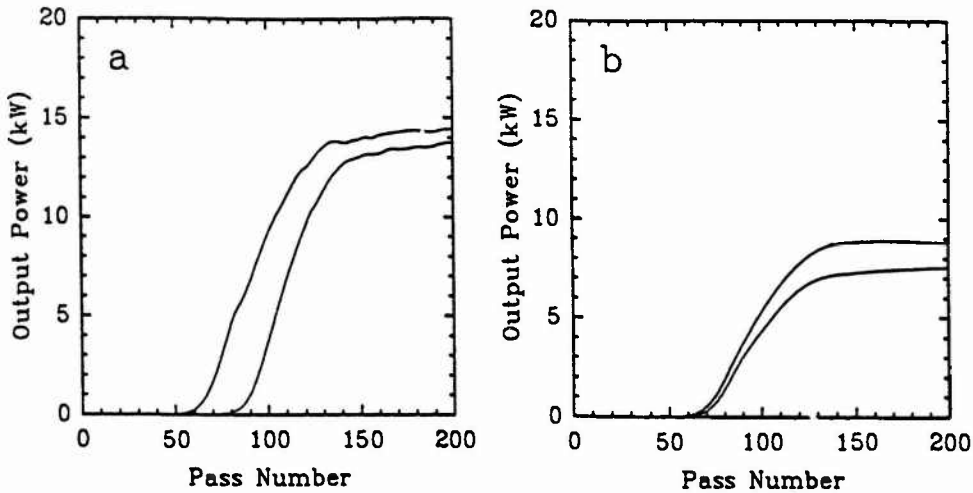


Fig. 6.6 Simulated output macropulse powers for (a) the completely detuned Michelson mirror resonator, and (b) the phase locked Michelson mirror resonator. The curves in each case show the envelopes for eight simulations.

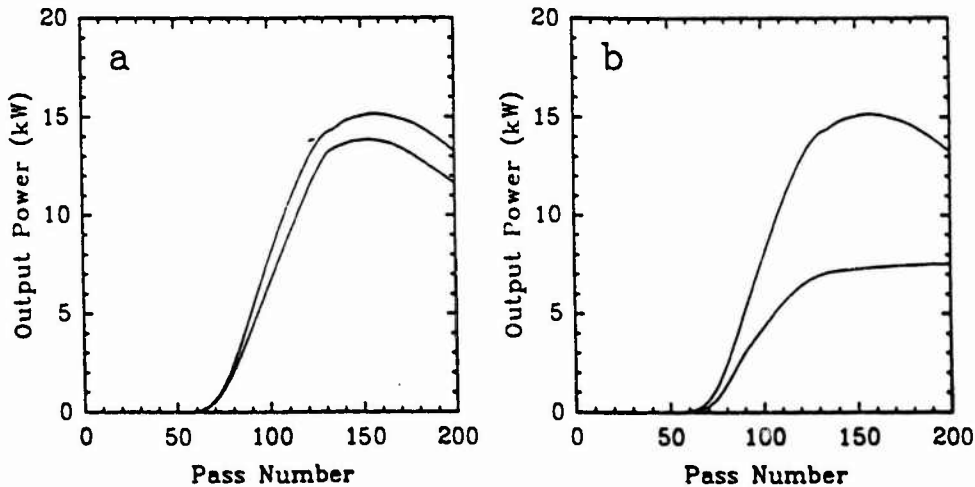


Fig. 6.7 (a) Simulated output macropulse powers for the partially phase locked Michelson mirror resonator with a total slew (during the macropulse) of 2π radians in the relative phase offset at the secondary mirror. (b) Macropulse envelopes for the partially phase locked beam from Fig. 6.7(a) and the maximally phase locked beam from Fig. 6.6(b); the fluctuations are $\pm 33\%$.

shift of 2π radians. The corresponding macropulse powers are shown in Fig. 6.7(a). We see that the total outcoupled power with jitter on the mirror mount can even be greater than the output power shown in Fig. 6.6(a) for the detuned resonator. Evidently, the phase slew acts as a kind of continuous cavity dumping, and forces the partially phase locked output pulses from destructive interference to constructive interference at the beamsplitter. The envelopes in Fig. 6.7(b) mimic the oscilloscope trace from Fig. 6.2(b) using the slewed macropulses from Fig. 6.7(a) and the stable macropulses from Fig. 6.6(b). The simulated fluctuations are $\pm 33\%$, and are consistent with the largest fluctuations observed in the experiment.

Finally, if the fluctuations observed in the experiment were indeed due to a continuous cavity dumping of the partially phase locked optical beam, then the tuning range of the secondary mirror within which these fluctuations were observed could be interpreted as the tuning range over which phase locking was induced in the macropulse. The 'critical' secondary mirror detuning was calculated in Chapter 5,

$$|\delta L_{\text{Mich}}^c| = \frac{N_w \lambda \sqrt{r_j}}{13.5 (r_t)} , \quad (6.1)$$

and yields a total detuning range of $2 \cdot |\delta L_{\text{Mich}}^c| = 360 \mu\text{m}$ for the experimental parameters ($r_j = 3.6$). Note that this range is considerably larger than the slippage distance of $150 \mu\text{m}$, because the square root of the small reflectance appears in the denominator, but it is well within a factor of two of the $225 \mu\text{m}$ range observed in the experiment. The discrepancy is most likely due to the ambiguity in using the observed power fluctuations and the decreased hypermode decay rates as indicators of the degree of phase locking. Furthermore, eq. (6.1) assumed that the optical pulses were much longer than the slippage distance and that supermode effects could be neglected. This may not be true for the 1.6 ps pulses assumed in the present experiment. Figure 6.8 shows the first order hypermode losses calculated from the coupled mode simulations for the experimental parameters in Table 6.1. The 3 dB points are roughly $100 \mu\text{m}$ on the long-cavity side and $150 \mu\text{m}$ on the short-cavity side, indicating a phase locked tuning range of $250 \mu\text{m}$ for the secondary mirror. This value is much closer to the range observed in the experiment. However, any conclusions regarding the detuning range are still ambiguous for the reasons noted above.

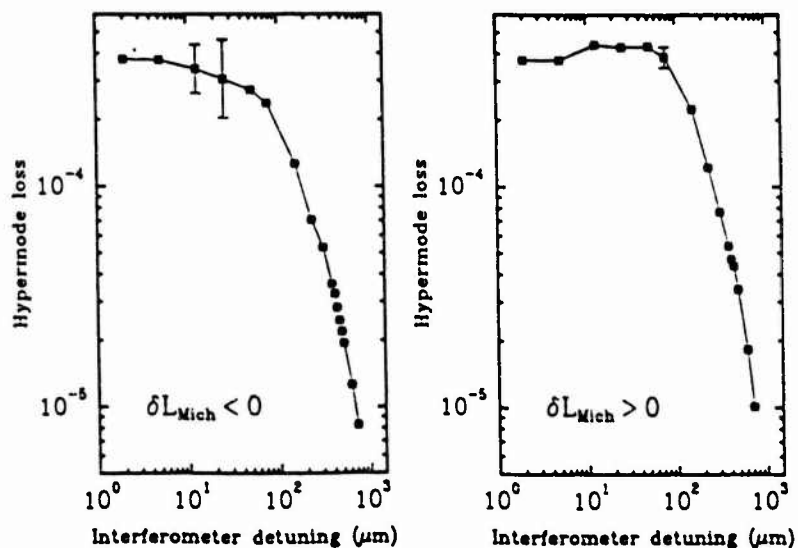


Fig. 6.8 Coupled mode simulations of the first order hypermode loss in a Michelson mirror resonator with the parameters listed in Table 6.1. (a) Mirror displacement towards the long-cavity side; (b) Mirror displacement towards the short-cavity side.

V. DISCUSSION AND CONCLUSIONS

I have described a phase locking experiment on the Mark III FEL using a Michelson mirror resonator with a beamsplitter reflectance of only 1.4 %. Measurements on the output optical beam showed substantial fluctuations (as large as $\pm 35\%$ in some instances) in the total power reaching the detector, which included the leakage power from the beamsplitter. Evidence for phase locking was inferred from a substantial reduction in power for some macropulses, which suggested the presence of destructive interference in the leakage beam. The power fluctuations were observed over a range of $225 \mu\text{m}$ in the position of the secondary mirror, which was consistent with autocorrelation measurements of the width of the output pulses.

Simulations of the above experiment showed that substantial phase locking could be induced with a 1.4 % reflectance, and that the leakage power could be almost extinguished due to destructive interference in the outcoupled beam. However, the fluctuations observed in the experiment could only be simulated by imposing a continuous slew in the relative phase offset at the secondary mirror. A phase slew of 2π radians (one optical wave) during the macropulse was sufficient to induce simulated fluctuations of $\pm 33\%$ in the outcoupled power, which was very close to the fluctuations observed in the experiment. Consequently, if the macropulses were phase locked, they were probably also subject to mechanical vibrations on the interferometer mirror. The most likely source of these fluctuations was the mechanical coupling of a turbo pump to the vacuum chamber which housed the interferometer optics. (The vibrations were later discovered to have actually unscrewed one of the small bolts on the flange of the side vacuum window.) Such vibrations could have caused a quasi-continuous cavity dumping of some of the macropulses during the phase locking process. However, the maximum output powers observed in the simulations were only slightly enhanced over the output powers from the detuned resonator, whereas the enhancements observed in the experiment were as large as 52 %. This discrepancy remains unexplained. However, it may indicate imperfections in the alignment of the infrared optical beams. Another possibility is that, if phase locking were not induced to the degree suggested by the simulations, then fluctuations could still be caused by a random walk superposition of the output pulses in the leakage beam. If we represent the N pulses in the entire intracavity macropulse train as $\exp[i\vartheta_n]$; $n = 1, \dots, N$, where the phases of the $N = 35$ circulating pulses are random but repeat identically from pass to pass, then the total output power (including leakage) is

$$\sum_{n=1}^N \left[|r e^{i\vartheta_n}|^2 + |r e^{i\vartheta_n} - r e^{i\vartheta_{n-1}}|^2 \right] = r^2 N + 2 r^2 N \left(1 \pm \frac{1}{\sqrt{2N}} \right) . \quad (6.2)$$

For $N = 35$, the rms fluctuations are $\pm 8\%$, which is considerably smaller than the fluctuations observed in the experiment. It may be possible that some of the absolute fluctuations were as large as the observed fluctuations. However, it is also clear from the theory and simulations that the phases of the optical pulses evolve considerably from pass to pass, and do not remain completely uncorrelated.

At best, the above results suggest only indirectly that phase locking was achieved in the experiment. However, the dramatic effect on the output power for a beamsplitter reflectance of only 1.4 % also suggests that phase locking should be readily achieved with an optimum reflectance of 50 %. An unambiguous demonstration of phase locking will require stabilized mirror mounts, and spectral measurements of the longitudinal mode structure of the output beam in which the leakage losses from the beamsplitter are completely isolated and filtered. Appendix B describes the design of a practical Michelson mirror resonator on the Mark III FEL, as well as spectral diagnostics which have been procured for future experiments on that laser.

VI. REFERENCES

- [1] G. R. Edlin, R. W. Jones, and J. F. Perkins, "Phase locked rf linac free electron laser," U. S. Patent No. 4,748,629, May 31, 1988.
- [2] D. Oepts, A. F. G. van der Meer, R. W. B. Best, P. W. van Amersfoot, and W. B. Colson, "Simulations of mode reduction with an intracavity etalon in an rf-linac based FEL," *Nucl. Instr. and Meth.*, vol. A285, pp. 204-210, 1989.
- [3] E. B. Szarmes, S. V. Benson, and J. M. J. Madey, "Mode control on short-pulse FELs using a Michelson-mirror resonator," *Nucl. Instr. and Meth.*, vol. A296, pp. 98-109, 1990.
- [4] E. B. Szarmes and J. M. J. Madey, "The Michelson resonator free-electron laser - Part I: Passive mode structure and mode decay," *IEEE J. Quantum Electron.*, to be published.
- [5] E. B. Szarmes and J. M. J. Madey, "The Michelson resonator free-electron laser - Part II: Supermode structure and mirror detuning effects," *IEEE J. Quantum Electron.*, to be published.
- [6] S. V. Benson, J. Schultz, B. A. Hooper, R. Crane, and J. M. J. Madey, "Status Report on the Stanford Mark III Infrared Free-Electron Laser," *Nucl. Instr. and Meth.*, vol. A272, pp. 22-28, 1987.
- [7] S. V. Benson, W. S. Fann, B. A. Hooper, J. M. J. Madey, E. B. Szarmes, B. Richman, and L. Vintro, "A review of the Stanford Mark III infrared FEL program," *Nucl. Instr. and Meth.*, vol. A296, pp. 110-114, 1990.
- [8] J. D. Jackson, *Classical Electrodynamics*, 2nd ed., New York, NY: Wiley, 1975. p. 282.
- [9] A. Cutolo, S. V. Benson, B. Hooper, J. F. Schultz, and J. M. J. Madey, "Mode characterization, autocorrelation measurements, and harmonic conversion with pico- and femtosecond pulses delivered by the Mark III free-electron laser," *Appl. Optics*, vol. 28, pp. 97-105, 1989.
- [10] D. A. G. Deacon, "Inhomogeneous broadening calculation with a single integral," *HEPL Note TN-84-2*, Stanford, CA: High Energy Physics Laboratory, Stanford University, 1984.

Chapter 7

Summary and conclusions

In this dissertation, I have reported extensive analytic and numerical investigations of the optical pulse evolution in rf linac-driven free-electron lasers in both the chirped-pulse and phase locked modes of operation. These studies were motivated in general by the tremendous potential impact that such enhancements could provide in the fields of fast-time resolved and high spectral resolution infrared spectroscopies, and in particular by the possibility of implementing both of these enhancements on the Mark III infrared FEL. The chirped-pulse mode of operation uses electron micropulses with a linear temporal energy dependence to drive the formation of broad band optical pulses with a linear temporal frequency dependence; these 'chirped' optical pulses are susceptible to pulse compression in an external dispersive delay line. The phase locked mode of operation uses an intracavity interferometer to couple successive optical pulses so that they build up from noise with a definite phase relationship; these 'phase locked' optical pulses yield well separated longitudinal modes in the output beam that can be individually filtered for applications in high resolution spectroscopy. Small signal analyses were fully developed for each of these modes of operation, which analyses were supported by numerical pulse propagation simulations whose parameters were chosen to guide the design of feasible experiments on the Mark III FEL.

The chirped-pulse FEL

The small signal regime of the chirped-pulse FEL was shown to possess completely analogous properties to the small signal tapered wiggler FEL, except that the former yields strongly chirped optical pulses whereas the latter does not. In particular, small energy

chirps merely shift the optimum resonance parameter of the small signal gain curve with no distortion in the gain function, but dimensionless energy chirps much larger than the gain bandwidth divided by the slippage distance severely distort the gain spectrum and reduce the overall gain in an analogous manner to the tapered wiggler FEL. Nevertheless, in most applications of the chirped-pulse FEL to pulse compression, substantial compression ratios can be obtained with energy chirps much smaller than this limit. For example, simulations of the Mark III FEL at 3.35 μm using relatively short electron pulses (4 ps) and modest energy chirps (+2 %) demonstrated the formation of broad band optical pulses that could be compressed from 3.4 ps to 220 fs with compressed peak powers of 30 MW.

The simulations also showed that the frequency chirp is partially affected by both the transverse mode structure of the resonator and by the onset of saturation, and that the extraction efficiency depends strongly on the energy chirp in the presence of finite cavity length detunings. The two most important consequences were that: (1) due to an intrinsic frequency chirping in the FEL, electron pulses with a positive energy chirp yielded larger frequency chirps than electron pulses with a negative energy chirp of the same magnitude; and (2) for cavity lengths shorter than the synchronous length, negatively chirped electron pulses yielded a substantially greater extraction efficiency than positively chirped pulses, although the converse was true for cavity lengths longer than the synchronous length. Negative energy chirps were originally predicted to increase the extraction efficiency at saturation due to the adiabatic deceleration of trapped electrons, and it is therefore interesting to find that enhanced efficiencies can in fact be obtained with energy chirps of *either* sign (although the energy extraction mechanism is not related to adiabatic deceleration.)

The Michelson resonator FEL

I also performed analytical and numerical investigations on the feasibility of using a Michelson mirror resonator on FELs driven by rf linacs to couple successive optical pulses in the pulse train. In such a configuration, the optical pulses will grow only if adjacent pulses maintain a definite phase relationship, and in this fashion the axial mode spacing can be increased from the round trip frequency up to the driving frequency of the rf linac. A linear eigenmode analysis was presented which predicted the time scale on which the short optical pulses become phase locked; this analysis can be used to calculate the mode losses and decay rates in practical applications of these resonators. The mode structure predicted by this analysis was also shown to be equivalent to the mode structure obtained from the passive frequency response of the Michelson mirror resonator. The latter has a wider range of application because it can be calculated for any resonator configuration (for example, the Fox-Smith interferometer) with arbitrary mirror detunings.

Pulse propagation simulations of the perfectly tuned Michelson mirror resonator, using parameters appropriate to the Mark III FEL, confirmed the corresponding increase in the axial mode spacing of the output beam on microsecond time scales. The perfectly tuned interferometer was shown to have no appreciable effect on the overall spectrum of the optical beam, but the temporal evolution of the supporting longitudinal modes was accurately predicted from the eigenmode analysis. Furthermore, the simulations also indicated that the phase locked optical beam in the perfectly tuned interferometer grows to the same saturated power level as the randomly phased beam. This latter property is particularly important for applications in nonlinear spectroscopy. Since the spectral width of the output beam is determined primarily by the duration of the short electron pulses, a decrease by a factor of N in the number of modes yields an increase by the same factor in the power per mode, where N is the number of pulses in the cavity. This can be well over an order of magnitude increase in the spectral brightness.

In order to study the effects of finite interferometer detunings, I applied conventional mode locked laser theory to the evolution of the longitudinal modes in the Michelson resonator FEL, and obtained a greatly simplified derivation of the small signal, small gain FEL coupled mode equations. These equations were solved numerically to study supermode evolution in the presence of arbitrary mirror detunings, and the results were compared with simulations of the Michelson resonator FEL using a pulse propagation code based on the Maxwell-Lorentz equations of motion. The effects of increasing the interferometer detuning included a shift and broadening of the cavity detuning curves, a narrowing of the supermode spectrum, and a decrease in the rate of hypermode decay. Practical consequences of all of these effects were discussed. A significant achievement of the coupled mode analysis was the confirmation of a simple theory describing the dependence of the hypermode decay rates on the detuning, which theory indicated for most laser configurations that the hypermode decay rates remain large as long as the relative shift between the coupled pulses in the interaction region is less than the slippage distance.

The demonstrated agreement between the pulse propagation and coupled mode simulations with regard to small signal gain, supermode structure, and hypermode decay indicated that the latter simulations are entirely appropriate for general resonator analysis. In practice, it is much simpler to implement an arbitrary mode structure in the coupled mode analysis than to implement an arbitrary pulse coupling geometry in the pulse propagation code. These analyses can easily be applied to the mode structure of resonators incorporating an intracavity etalon or Fox-Smith interferometer, and may also be appropriate for studying the supermode evolution for arbitrary slippage parameters and electron pulse shapes in conventional two-mirror resonators.

Preliminary experimental results

Finally, I described a phase locking experiment on the Mark III FEL using a Michelson mirror resonator with a beamsplitter reflectance of only 1.4 %. Evidence for phase locking was inferred from a substantial reduction in power for some of the macropulses, which suggested the presence of destructive interference in the leakage beam. Simulations of the experiment demonstrated that substantial phase locking could indeed be induced with a 1.4 % reflectance, and that the leakage power could be almost extinguished due to destructive interference in the outcoupled beam. Although substantial fluctuations in the output power were also observed in the experiment, they could be reproduced in the simulations by imposing a mechanical jitter on the interferometer mirror.

The dramatic effect on the output power for a beamsplitter reflectance of only 1.4 % suggests that phase locking should be readily achieved with an optimum reflectance of 50 %. An unambiguous demonstration of phase locking, and the application of phase locked optical beams in spectroscopy, will probably require actively stabilized mirror mounts, and will certainly require spectral diagnostics capable of resolving the individual longitudinal modes. However, the design and implementation of such apparatus should not be too technically demanding for infrared wavelengths.

Appendix A

Optical diagnostics for chirped-pulse free-electron lasers

In recent years there have been several proposals to operate rf-linac driven FELs with chirped energy electron micropulses for applications in fast time-resolved spectroscopy, in which the output optical pulses possess appreciable frequency chirps and are susceptible to pulse compression in an external dispersive delay line [1]-[3]. The physical principles governing these experiments are generally not specific to a particular wavelength, because substantial energy chirps can be achieved at a given energy simply by dephasing the electron bunches relative to the accelerating field in the accelerator. Consequently, the most practical realizations of these experiments should employ broad band optics in both the optical transport and diagnostic apparatus in order to fully exploit the inherent tunability of the FEL.

In this appendix, I describe the implementation of this experiment on the Mark III FEL for wavelengths between $2.5 \mu\text{m}$ and $4.1 \mu\text{m}$, using a broad band sapphire prism pulse compressor which has been designed and procured for applications in a user-oriented program at Duke University. Section II gives a brief tutorial review of linear pulse propagation and pulse compression, and presents some apparently original expressions for the compression of several ideal pulse shapes with linear frequency chirps. Section III reviews the relevant principles of the chirped pulse FEL, and lists the pulse parameters for the Mark III experiments on which the design of the pulse compressor (Section IV) and the autocorrelator (Section V) are based. Finally, Section VI suggests some possible extensions to other wavelength regimes in the near and far infrared.

II. PULSE PARAMETERS

A chirped optical pulse is most conveniently characterized by a chirp parameter 'b' and a pulse width parameter 'a' [4] defined by

$$\omega(t) = \omega_0 + (2b)t \quad (A.1)$$

$$\text{and} \quad a = \frac{2 \log_e 2}{\tau_p^2}, \quad (A.2)$$

where $\omega(t)$ is the time-dependent optical frequency and τ_p is the FWHM pulse width. The spectrum of an optical pulse

$$E(t) = E(t) \exp[-j(\omega_0 t + bt^2)] \quad (A.3)$$

can then be written in the general form

$$\tilde{E}(\omega) = \tilde{E}(\omega) \exp \left[+j \frac{b}{4[f(a,b) + b^2]} (\omega - \omega_0)^2 + j O(\omega - \omega_0)^3 \right] \quad (A.4)$$

where $f(a,b)$ is a form factor that depends on the pulse shape; for example, $f(a,b) = a^2$ for Gaussian pulses. The first order term in the exponent can be omitted because it affects only the centroid of the pulse, and if the frequency chirp is large and purely linear, then the higher order terms are usually negligible.

Second order phase compensation means to eliminate the $j[(\cdots)(\omega - \omega_0)^2]$ term in the spectral phase factor, and is the usual manner of compressing the pulse. This is accomplished by sending the pulse through a dispersive delay line, which has the effect of multiplying the spectrum by a phase factor of the form

$$\cdot \exp \left[+j \frac{1}{2} \frac{d^2\phi}{d\omega^2} (\omega - \omega_0)^2 + j O(\omega - \omega_0)^3 \right]. \quad (A.5)$$

The spectral width (as determined from $|\tilde{E}(\omega)|^2$) is unaltered by this propagation, but the compensated optical pulse has essentially no frequency chirp, since $b = 0$ in the absence of the second order term in (A.4). As a result, the original spectral content of the pulse is effectively transferred from the optical phase to the optical envelope, and the pulse is compressed. The coefficient of the quadratic frequency term in (A.5) which compensates the corresponding term in (A.4) can be written *phenomenologically* as

$$\frac{1}{2} \left(\frac{d^2\phi}{d\omega^2} \right)_{\text{comp}} = -\frac{1}{b \cdot K(a,b)} \quad (A.6)$$

where $K(a,b)$ is a factor that depends on the pulse shape and on the ratio of (a/b) , and has

a limiting value of $K \rightarrow 4$ as $(a/b) \rightarrow 0$. Figure A.1 displays the numerically derived values of $K(a,b)$ for several ideal pulse shapes, and Fig. A.2 displays the corresponding pulse compression ratios; in all cases, optimum compression was defined as yielding the maximum compressed peak power, not the minimum FWHM pulse duration. The curve fits appearing in those figures are given below for $|a/b| < 1$, and may be useful in the design and adjustment of phase compensators for chirped pulse experiments in which the shape and duration of the optical pulses can be inferred from autocorrelation measurements.

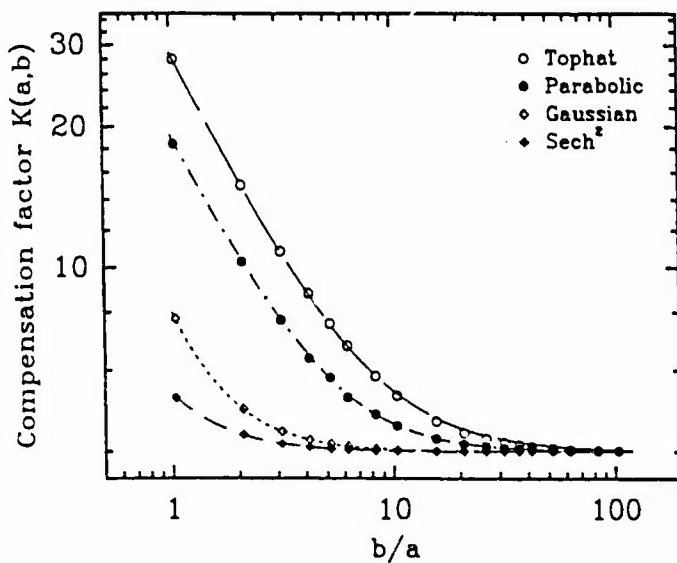


Fig. A.1 Optimum quadratic phase compensation factors $K(a,b)$ from eq. (A.6) for various ideal pulse shapes, defined as yielding the maximum compressed peak powers. The data and curve fits were obtained numerically.

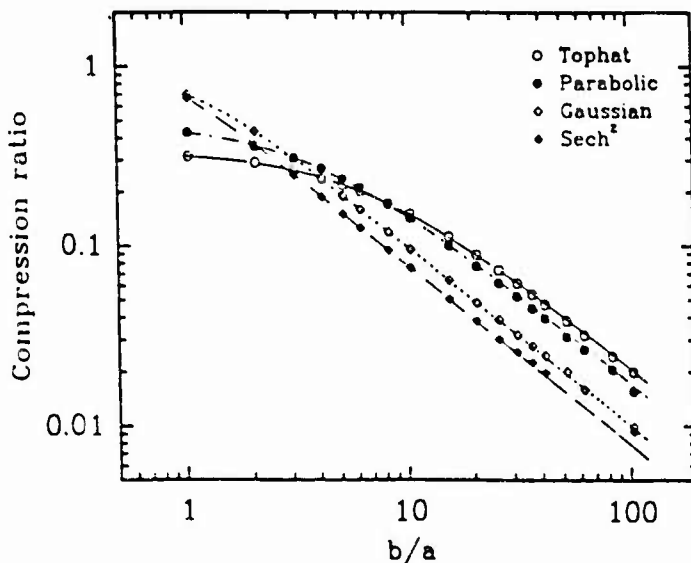


Fig. A.2 Optimum pulse compression ratios corresponding to the compensation factors in Fig. A.1.

Gaussian

$$K(a,b) = 4 \left[\left(\frac{a}{b} \right)^2 + 1 \right] ; \frac{\tau_p^{\min}}{\tau_p} = \frac{1}{\left[\left(\frac{b}{a} \right)^2 + 1 \right]^{1/2}} \quad (A.7a)$$

Sech²

$$K(a,b) = 4 \left[0.76 \left(\frac{a}{b} \right)^{2.00} + 1 \right]^{0.50} ; \frac{\tau_p^{\min}}{\tau_p} = \frac{0.784}{\left[\left(\frac{b}{a} \right)^2 + 0.311 \right]^{1/2}} \quad (A.7b)$$

Parabolic

$$K(a,b) = 4 \left[22 \left(\frac{a}{b} \right)^{1.84} + 1 \right]^{0.50} ; \frac{\tau_p^{\min}}{\tau_p} = \frac{1.74}{\left[\left(\frac{b}{a} \right)^{4/3} + 5.50 \right]^{3/4}} \quad (A.7c)$$

Tophat

$$K(a,b) = 4 \left[26 \left(\frac{a}{b} \right)^{1.60} + 1 \right]^{0.60} ; \frac{\tau_p^{\min}}{\tau_p} = \frac{2.12}{\left[\left(\frac{b}{a} \right)^{4/3} + 11.7 \right]^{3/4}} \quad (A.7d)$$

The equations for the Gaussian case are exact analytical results [4]. The only conditions assumed in the form of the remaining equations are that they depend only on the ratio of (a/b), and that they approach the limits $K(a,b) \rightarrow 4$ and $\tau_p^{\min}/\tau_p \rightarrow \text{const.} |a/b|$ as (a/b) $\rightarrow 0$; these conditions are heuristic and agree with the Gaussian case.

III. MARK III DESIGN PARAMETERS

Simulations of the optical pulse generation using chirped energy electron pulses on the Mark III FEL were previously described in Chapter 3. Those simulations were based on practical operating configurations of the Mark III linac, in which the electron pulses are compatible with the dispersion in the downstream transport line and yield chirped optical pulses with large spectral widths at saturation. For experiments near $\lambda = 3.35 \mu\text{m}$, the electron pulses in the wiggler have a duration of 4 ps and a linear energy chirp of $\delta\gamma/\gamma = +2\%$ with higher energies towards the trailing edge. The simulations assumed tophat electron pulses, since optical autocorrelation measurements on the Mark III FEL have indicated that the optical pulses at saturation are essentially tophat in shape [5]. The duration of the optical pulses ($\tau_p \sim 3.4$ ps) is slightly shorter than 4 ps due to lethargy, but the magnitude of the positive frequency chirp ($\Delta\omega/\omega \sim +4.6\%$ over 4 ps) is slightly larger than would be predicted by assuming that the resonance condition determines the lasing wavelength during the pulse; this frequency chirp is determined numerically from the simulations by fitting a least squares parabola to the optical phase over the FWHM duration of the optical pulse. The corresponding chirped pulse parameters from the simulations at $\lambda = 3.35 \mu\text{m}$ are

$$\begin{aligned}
 a &= +1.2 (10)^{23} \text{ s}^{-2} \\
 b &= +3.3 (10)^{24} \text{ s}^{-2} \\
 K(a,b) &= 4.3 \\
 \frac{1}{2} \left(\frac{d^2\phi}{d\omega^2} \right)_{\text{comp}} &= -7.0 (10)^{-26} \text{ s}^2
 \end{aligned} \tag{A.8}$$

and the compressed optical pulses have a duration of ~ 230 fs. The simulated profiles of the chirped output pulses, and the results of pulse compression, are reported in Chapter 3.

For designing experiments over a range of wavelengths, it is useful to assume that the resonance condition determines the lasing wavelength during the pulse; this will actually be a fairly good approximation if the slippage parameter is sufficiently small. The wavelength dependence of the chirp parameter b then becomes explicit:

$$b(\lambda) \cong \frac{2\pi c}{\lambda} \frac{1}{\gamma} \frac{dy}{dt}, \tag{A.9}$$

where γmc^2 is the electron energy, and if one also assumes that the duration of the optical pulses at saturation is equal to the duration of the electron pulses (appropriate for long electron pulses), then the compensation factor in (A.6) can be readily evaluated using (A.9) and (A.7).

IV. PULSE COMPRESSOR DESIGN

The two general designs for pulse compressors employ either grating pairs or Brewster angle prism pairs [6]. The latter choice is preferred in the present application because of the possibility of achieving substantial compression ratios over a wide range of wavelengths. In contrast, the diffractive geometry of a given grating system is very sensitive to wavelength, and the corresponding dispersions can be too large to yield practical compressor designs in chirped pulse FEL experiments. For example, a double pass Litrow grating system at $3.35 \mu\text{m}$, designed to compensate the pulse parameters in (A.8), would have a slant spacing of only a few millimeters.

The design of prism pulse compressors has been treated extensively in the literature [6]-[9]. A typical minimum deviation, single pass, Brewster angle prism system is shown in Fig. A.3. The second order dispersion for a corresponding *double pass* system is given by

$$\frac{1}{2} \frac{d^2\phi}{d\omega^2} = \frac{\lambda^3}{2\pi c^2} \left\{ 2 \left[\frac{d^2n}{d\lambda^2} + \left(2n - \frac{1}{n^3} \right) \left(\frac{dn}{d\lambda} \right)^2 \right] L_p \sin \beta - 4 \left(\frac{dn}{d\lambda} \right)^2 L_p \cos \beta \right\} \tag{A.10}$$

where λ is the vacuum wavelength, $n(\lambda)$ is the refractive index, and L_p and β are shown in

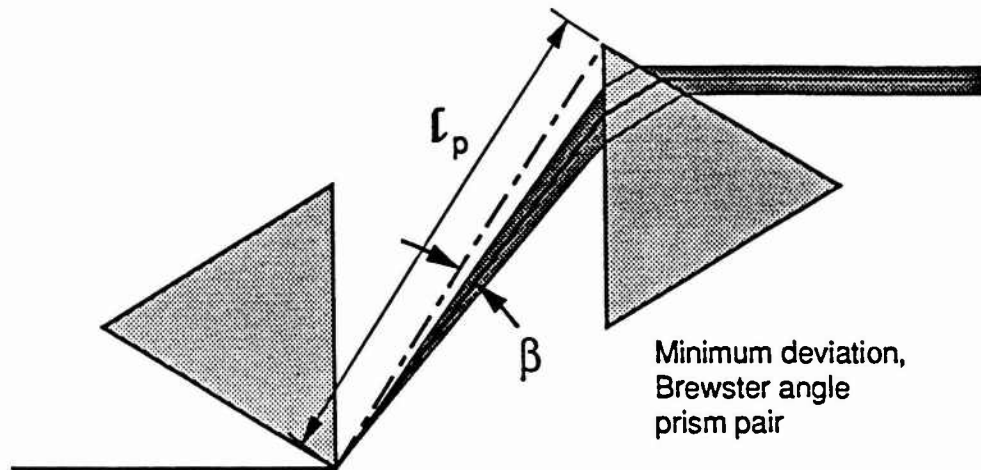


Fig. A.3 Typical prism configuration for a single pass dispersive delay line. The prisms are in the minimum deviation geometry to avoid astigmatism in the transmitted beam.

Fig. A.3. For a given set of system parameters, the LHS of (A.10) should equal the required compensating factor from (A.6).

The contributions to the dispersion arise from material dispersion and angular dispersion, the latter leading to wavelength-dependent geometrical paths through the system. In particular, material dispersion in the crystals yields the $d^2n/d\lambda^2$ term in (A.10), angular dispersion in the crystals yields the $1/n^3 \cdot (dn/d\lambda)^2$ term, and angular dispersion in air, comprising the dominant contribution in most systems, yields the two remaining terms. The angle β is usually determined by the clear aperture of the beam through the system, for example, by setting $L_p \sin \beta \gtrsim 4\omega_{beam}$, where ω_{beam} is the mode radius. If L_p is much larger than ω_{beam} , one may then set $\cos \beta \sim 1$.

The pulse compressor for the Mark III experiments consists of four minimum deviation sapphire prisms arranged as shown in Fig. A.4. The prisms are cut at Brewster's angle for $3.35 \mu m$, which yields no more than 0.03 % total reflection losses for the double pass system between $2.5 \mu m$ and $4.1 \mu m$. The optic axis of the crystal is perpendicular to the triangular faces to within 30 minutes, so that the horizontally polarized ray is ordinary. A double pass system is required in order to eliminate the presence of lateral spectral walk-off in the output beam, which can significantly increase the duration of the compressed optical pulses [10] according to

$$\frac{\tau_{comp}}{\tau_{min}} = \left[1 + \left(\frac{\tau_{init} L_p}{\tau_{min} z_R} \right) \right]^{1/2}, \quad (A.11)$$

where τ_{comp} , τ_{min} are the durations of the compressed pulses in the presence and absence of spectral walkoff, τ_{init} is the duration of the input pulse, and z_R is the Rayleigh range.

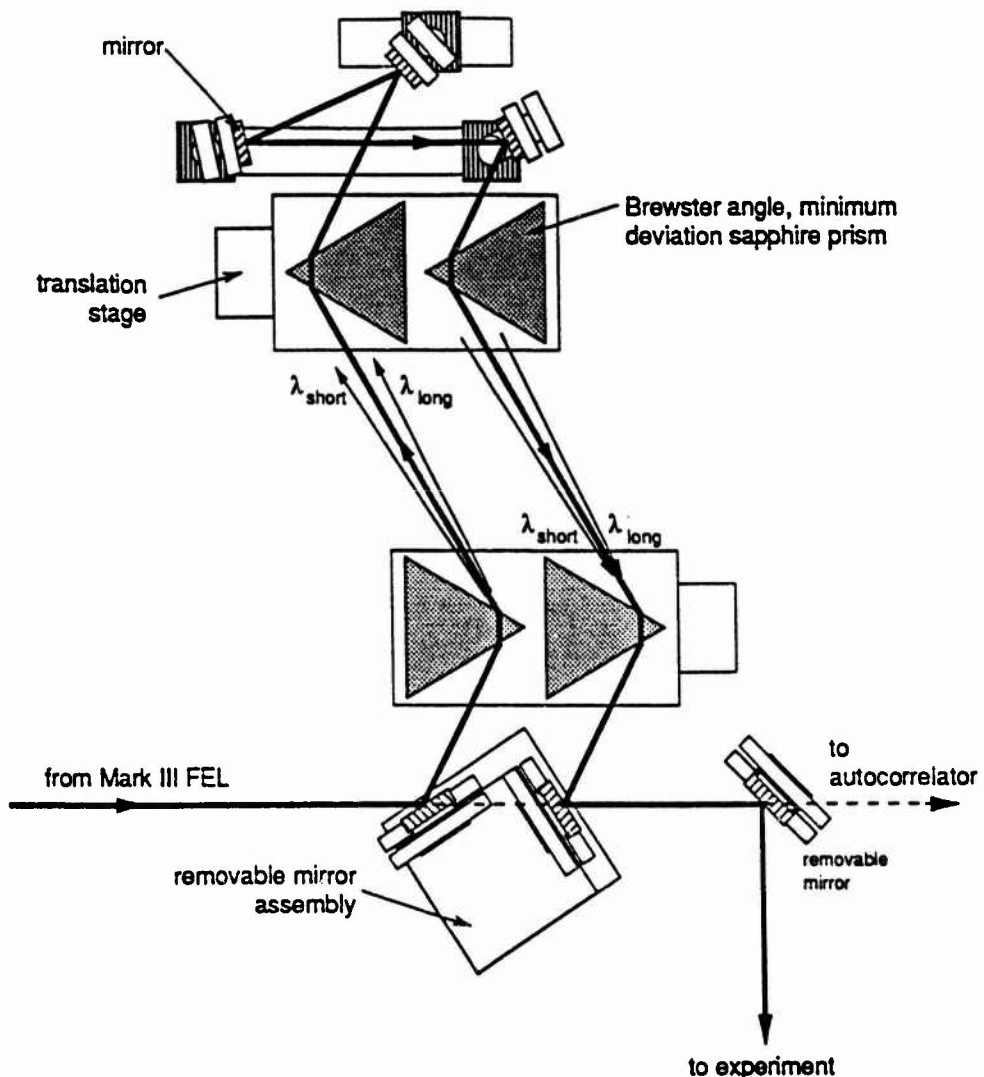


Fig. A.4 Double pass, sapphire prism dispersive delay line for the Mark III experiments between $2.5 \mu\text{m}$ and $4.1 \mu\text{m}$. The setup includes removable mirror assemblies to interchange the compressed and uncompressed pulses between the autocorrelator and the experimental sample.

For example, a single pass system designed to compensate the pulse parameters in (A.8) would compress the optical pulses to no less than 1.5 times the minimum duration that could be achieved in the absence of spectral walkoff.

The mounting of the prisms on translation stages allows the experimenter to vary the dispersion of the system by changing the path length through all four prisms without changing the position or direction of the output beam. The size of the prisms was chosen so that roughly 70 % of the required dispersion at $3.35 \mu\text{m}$ could be provided by moving the prisms in this fashion. The removable mirror assembly at the input to the system allows the quick interchange of compressed or uncompressed pulses into the autocorrelator or onto the experimental sample.

The estimated prism spacing as a function of wavelength is shown in Fig. A.5. The spacing for 3.35 μm is found by equating the prism dispersion from (A.10) with the required dispersion from (A.8), using $f_p \sin \beta \sim 5\omega_{\text{beam}}$ and $\omega_{\text{beam}} = 1.5 \text{ mm}$. The corresponding 4 m confocal parameter is much larger than the total path length of 70 cm through the system. For other wavelengths, the optical pulse widths are assumed to remain constant, and the prism spacings are found by equating the prism dispersion with the dispersion predicted from (A.6), where (A.9) and (A.7) are used to calculate $b(\lambda)$ and $K(a,b)$ (adjustments in the numerical constants appearing in (A.10) were also included to account for the deviation from Brewster's angle in the minimum deviation geometry). Although the prism spacing increases for decreasing wavelengths, the Rayleigh range increases in inverse proportion to λ , so that it should be possible to maintain a high degree of collimation with a beam whose radius need not be adjusted with wavelength. This consideration is important because the beam radius is usually limited by the clear aperture of the prism height.

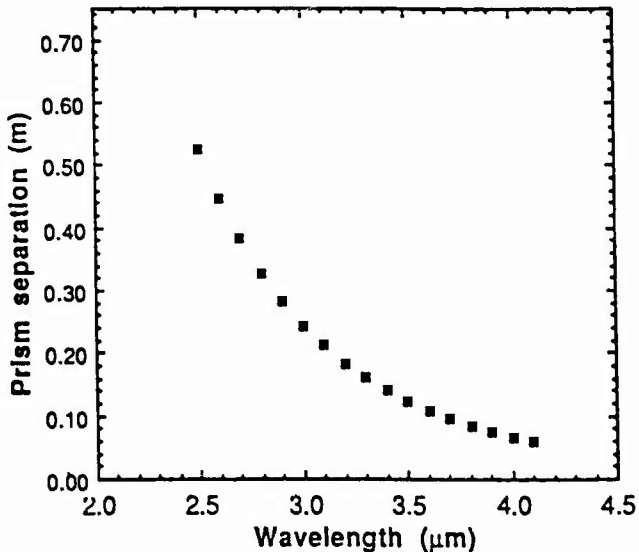


Fig. A.5 Estimated apex-to-apex prism separations for the Mark III experiments between 2.5 and 4.1 μm .

V. OPTICAL DIAGNOSTICS

The autocorrelator for the above experiments is a typical crossed beam autocorrelator [11], designed to measure pulse durations as short as 200 fs between 3.1 and 3.35 μm . The basic component arrangement is shown in Fig. A.6. The crossed beam geometry yields a background-free autocorrelation trace with no intensity fringes, and so is appropriate for digitized data acquisition. The doubling crystal is a 90° Type I phase matched silver gallium selenide (AgGaSe_2) wafer with a thickness of $l_c = 450 \mu\text{m}$; this is the coherence length for a 200 fs optical pulse which yields a phase matching factor of

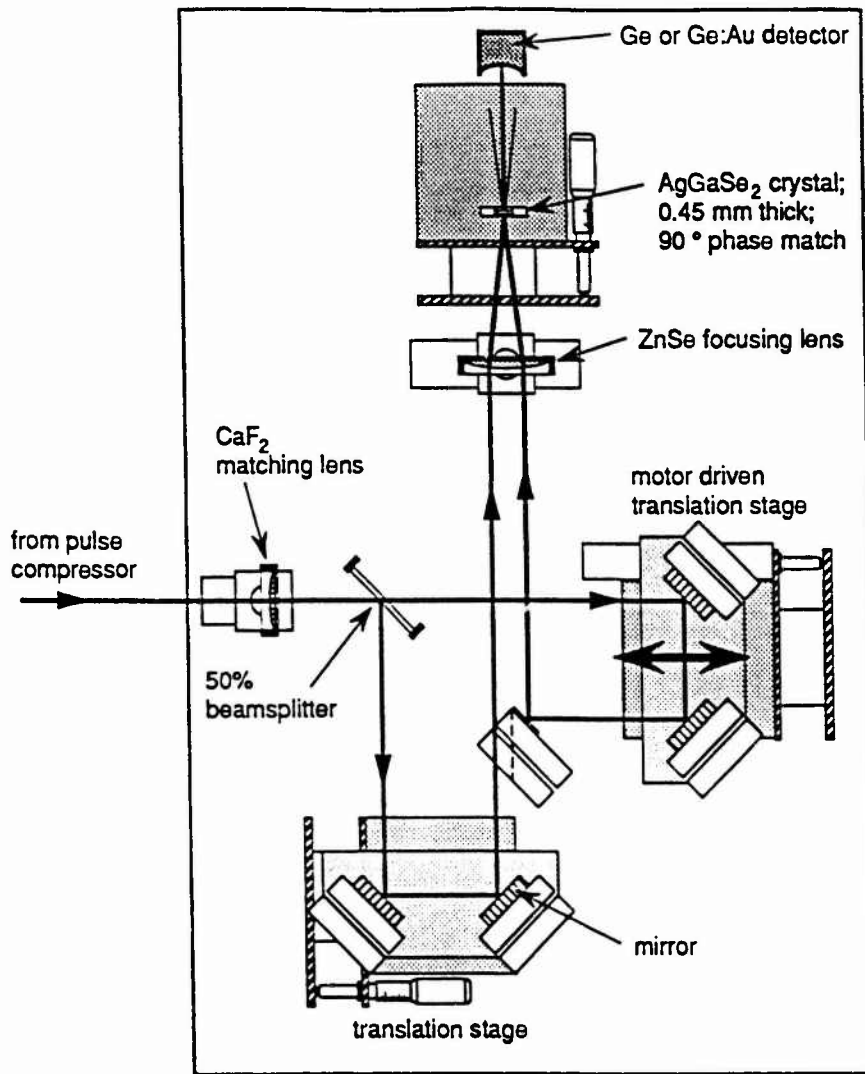


Fig. A.6 Layout of the autocorrelator for measuring pulse durations as short as 200 fs.

$$\frac{\sin^2(\Delta k \cdot l_c / 2)}{(\Delta k \cdot l_c / 2)^2} \geq 0.5 \quad (\text{A.12})$$

for all frequencies within the FWHM bandwidth. Here, $\Delta k = 2 k_1(\omega_1) \cos(\alpha/2) - k_2(\omega_2)$ is the phase mismatch between the fundamental (ω_1) and second harmonic (ω_2) waves, and α is the internal crossed beam angle. By moving the lower translation stage in Fig. A.6, this internal angle can be changed from 3.5° (9.2° external) at $3.1 \mu\text{m}$ to 7.5° (19.7° external) at $3.35 \mu\text{m}$ without altering the path length. For wavelengths less than $3.1 \mu\text{m}$ or greater than $3.35 \mu\text{m}$, one can use $\theta^{\text{Type I}} < 90^\circ$ phase matched LiNbO₃ crystals or AgGaSe₂ crystals respectively.

The focussing geometry is chosen to accept the 1.5 mm radius beam directly from

the pulse compressor and focus it down to a radius of 190 μm at the crystal surface (note that the waists of the focussed beams are located in front of the crossover point). This focussing geometry is of critical importance for the measurement of short optical pulses, because if the beams are too wide the pulse duration will be grossly overestimated. For marginally wide beams, the overestimate can be calculated exactly (assuming Gaussian temporal pulse profiles [12]) from

$$\tau_{\text{meas}}^2 = \tau_{\text{pulse}}^2 + \frac{\log 2}{2} \frac{\alpha^2 \omega_{\text{beam}}^2}{v_{\text{group}}^2} \quad (\text{A.13})$$

where τ are fundamental FWHM pulse durations, and v_{group} is the group velocity of the fundamental pulses in the crystal. Note that group velocity dispersion in the crystal has a negligible effect on the fundamental pulse duration. For $\tau_{\text{pulse}} = 200$ fs, the above autocorrelator with a cross beam angle of 3.5° will yield an overestimate of $\tau_{\text{meas}} = 209$ fs for the fundamental pulse duration.

VI. EXPERIMENTS AT OTHER WAVELENGTHS

As previously noted, chirped pulse FEL experiments can in principle be performed on rf linac-driven systems at any wavelength. At present, several such systems are designed to deliver wavelengths throughout the near and far infrared [13]-[16]. As suggested by the experimental design described above, prism systems should provide the greatest wavelength flexibility in FEL pulse compression experiments. Figure A.7 shows the dispersions

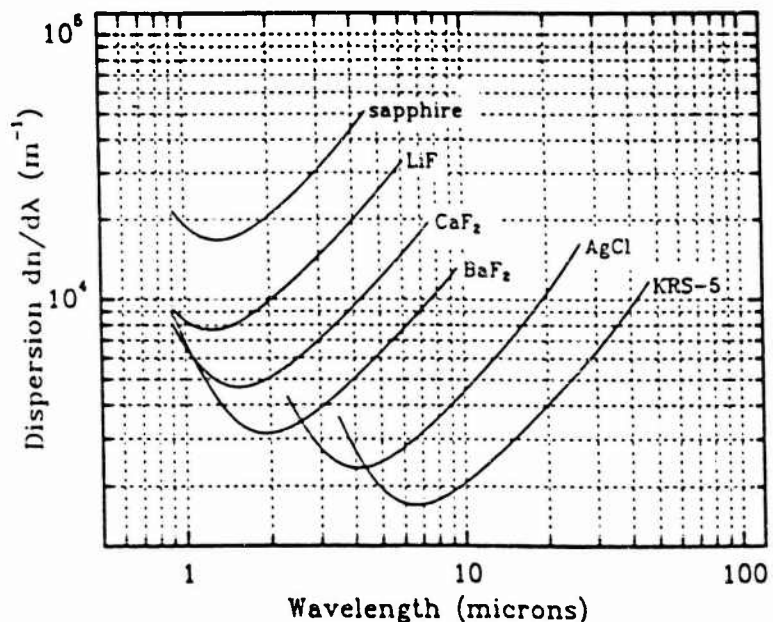


Fig. A.7 Dispersion of several low- or non-hygroscopic infrared materials over their range of transparency; all of these materials also transmit at 633 nm, and may be suitable as prism delay lines for chirped-pulse FEL experiments in the near and far infrared.

$|dn/d\lambda|$ of several infrared materials over their range of transparency, which were calculated from the published Sellmeier equations [17]. These materials also transmit at 632 nm, so that alignment is possible using a He-Ne laser. For a given material, the most useful wavelength range is the one in which the dispersion increases with wavelength. However, materials which transmit at longer wavelengths generally have lower dispersions. This is not a serious problem in the design of long-wavelength pulse compressors, because the dominant contribution to the prism dispersion comes from the last term in (A.10), i.e.

$$\frac{1}{2} \frac{d^2\phi}{d\omega^2} \approx -\frac{\lambda^3}{2\pi c^2} 4 \left(\frac{dn}{d\lambda}\right)^2 L_p . \quad (\text{A.14})$$

Therefore, the reduction in dispersion due to decreased $(dn/d\lambda)^2$ is compensated by the presence of the λ^3 factor. Even for electron pulse lengths or energy chirps which do not change greatly with wavelength, the required dispersion from (A.6) and (A.9) is proportional only to λ , so that the prism spacing L_p is roughly proportional to $1/\lambda^2$. Therefore, broad band pulse compressors for experiments at other wavelengths can most likely be designed within convenient dimensions on a laboratory bench.

VII. REFERENCES

- [1] G. T. Moore, "The Chirped-Pulse Free Electron Laser," *Nucl. Instr. and Meth.*, vol. A272, pp 302-310, 1988.
- [2] G. T. Moore, "Frequency Chirping of the Free-Electron Laser," *Phys. Rev. Lett.*, vol. 60, pp 1825-1827, 1988.
- [3] E. B. Szarmes, S. V. Benson, and J. M. J. Madey, "Pulse compression on the Mark III FEL using energy chirping," *Nucl. Instr. and Meth.*, vol. A296, pp. 755-761, 1990.
- [4] A. E. Siegman, *Lasers*, Mill Valley, CA: University Science Books, 1986. Chapter 9.
- [5] B. A. Richman, J. M. J. Madey, and E. Szarmes, "First Observation of Spiking in the Time Domain in a Free-Electron Laser," *Phys. Rev. Lett.*, vol. 63, pp. 1682-1684, 1989.
- [6] R. L. Fork, C. H. Brito Cruz, P. C. Becker, and C. V. Shank, "Compression of optical pulses to six femtoseconds by using cubic phase compensation," *Opt. Lett.*, vol. 12, pp. 483-485, 1987.
- [7] O. E. Martinez, J. P. Gordon, and R. L. Fork, "Negative group-velocity dispersion using refraction," *J. Opt. Soc. Am. A*, vol. 1, pp. 1003-1006, 1984.
- [8] R. L. Fork, O. E. Martinez, and J. P. Gordon, "Negative dispersion using pairs of prisms," *Opt. Lett.*, vol. 9, pp. 150-152, 1984.
- [9] J. D. Kafka and T. Baer, "Prism-pair dispersive delay lines in optical pulse compression," *Opt. Lett.*, vol. 12, pp. 401-403, 1987.
- [10] O. E. Martinez, "Grating and prism compressors in the case of finite beam size," *J. Opt. Soc. Am. B*, vol. 3, pp. 929-934, 1986.
- [11] S. L. Shapiro, ed., *Ultrashort Light Pulses*, 2nd ed., Berlin, FRG: Springer-Verlag, 1984.
- [12] J. Janszky, G. Corradi, and R. N. Gyuzalian, "On a possibility of analysing the temporal characteristics of short light pulses," *Opt. Commun.*, vol. 23, pp. 293-298, 1977.
- [13] C. Brau, "The Vanderbilt University Free-Electron Laser Center," presented at the Thirteenth

- International Free-Electron Laser Conference, Santa Fe, NM, 1991.
- [14] A. F. G. van der Meer *et al*, "The FELIX Project - Status Report October 1990," FOM-Instituut Voor Plasmaphysica *Rijnhuizen Report* 90-199, 1990; P. W. van Amersfoort *et al*, "Update on FELIX," *Nucl. Instr. and Meth.*, vol. A304, pp. 163-167, 1991.
 - [15] M. Castellano *et al*, "Status report of the IR FEL project on the superconducting linac LISA at LNF-Frascati," *Nucl. Instr. and Meth.*, vol. A304, pp. 204-207, 1991.
 - [16] A. H. Lumpkin *et al*, "First direct observation of FEL lasing from $\lambda = 20$ to $45 \mu\text{m}$," *Nucl. Instr. and Meth.*, vol. A296, pp. 181-185, 1990.
 - [17] W. G. Driscoll, ed., *Handbook of Optics*, New York, NY: McGraw-Hill, 1978.

Appendix B

Spectral diagnostics for phase locked free-electron lasers

The practical design of a Michelson resonator free-electron laser [1], [2] requires the outcoupled optical beam to be separated from the leakage beam at the beamsplitter, and subsequent applications in high resolution spectroscopy require sensitive spectral diagnostics to measure the longitudinal mode structure, tune the laser line, and monitor any drifts in frequency. This appendix describes the practical design of a Michelson mirror resonator on the Mark III FEL [3], as well as mode-selective spectral diagnostics which have been procured for experiments in high resolution spectroscopy near $3 \mu\text{m}$.

II. RESONATOR DESIGN

As noted in Chapter 6, the Mark III optical cavity uses Brewster plate output coupling for the horizontally polarized radiation. The vacuum chamber containing the upstream cavity mirror and output couplers was designed to allow four choices of Brewster plates, two of which can be placed on the beamline at the same time. In the usual configuration, a single Brewster plate is inserted into the beam, and only the reflections from one side of that plate are normally outcoupled to the user laboratory. However, one of the output couplers is positioned beside a Brewster window on the vacuum chamber, which allows the alignment of an external mirror for redirecting the secondary outcoupled reflections into the user laboratory as well.

The design of the intracavity Michelson interferometer represents a trivial extension to the above arrangement, and is shown in Fig. B.1. In the proposed configuration, two

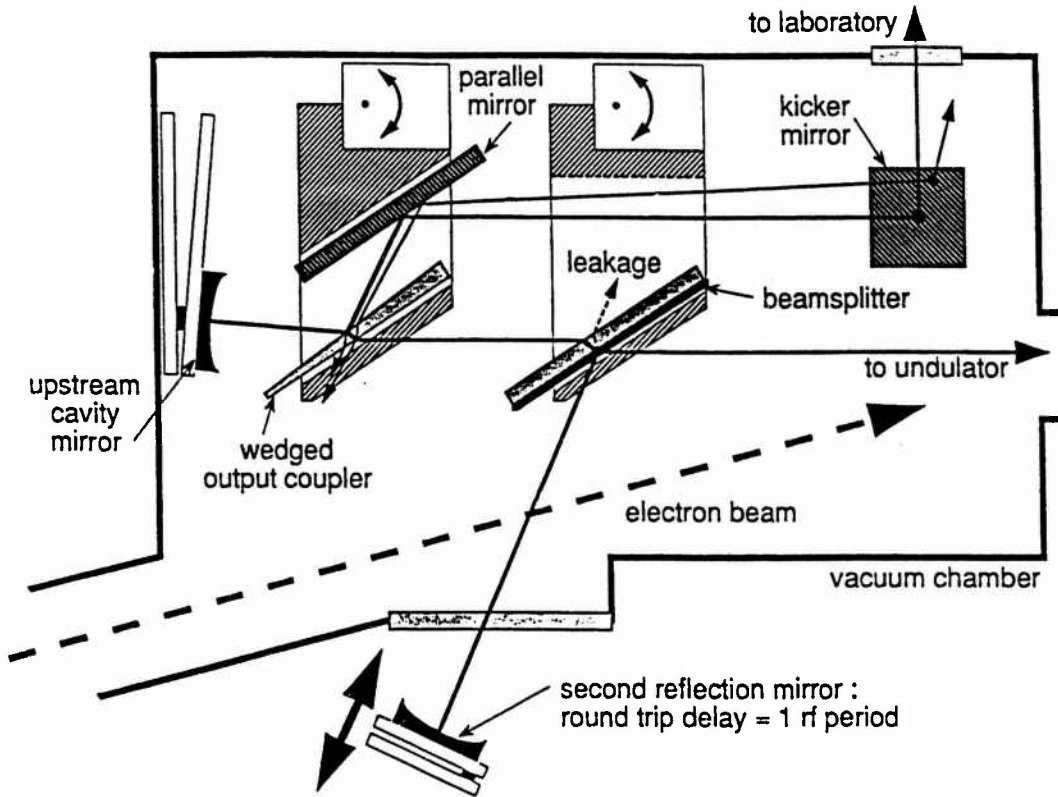


Fig. B.1 The design of the Michelson mirror resonator for the phase locking experiments on the Mark III FEL, showing the position of the beamsplitter, output coupler, and interferometer mirrors.

Brewster plates are inserted into the beamline, but one of them is a beamsplitter that reflects the secondary reflection to an interferometer mirror outside of the vacuum window. Two different beamsplitters have been procured for these experiments. The first one consists of an Al_2O_3 monolayer on a TiO_2 monolayer on a calcium fluoride substrate, yielding a reflectance of 8.5 % to 13 % for wavelengths between $2.5 \mu\text{m}$ and $3.7 \mu\text{m}$. The second beamsplitter consists of several alternating Al_2O_3 and TiO_2 monolayers on calcium fluoride, yielding a reflectance of 40 % to 50 % for wavelengths between $2.6 \mu\text{m}$ and $3.2 \mu\text{m}$. These coating materials were chosen for their potentially high damage thresholds [4]-[7]. The output coupler located between the beamsplitter and the upstream cavity mirror is a wedged calcium fluoride Brewster plate, aligned so that only a single surface reflection is outcoupled to the diagnostic apparatus.

The secondary external cavity mirror is mounted on a translation stage to facilitate the location of the synchronous mirror position. The procedure is as follows. For each of the 10 % and 50 % beamsplitters, an identical uncoated Brewster plate is first inserted onto the beamline, along with a parallel mirror to reflect the outcoupled beams to the laboratory. The synchronous position is located by using one side of this uncoated plate as the output

coupler, and the other side of the same plate as the beamsplitter. With an unsynchronized external mirror, the total outcoupled power reaching the detector will consist of three surface reflections (neglecting the skewed reflection from the external mirror.) However, when the mirror is scanned through the synchronous position, two of these reflections will interfere destructively due to partial phase locking in the optical beam, yielding as much as a 60 % decrease in the detected power. After locating the synchronous mirror position in this manner, the coated beamsplitter (without a parallel mirror) is reinserted onto the beamline in place of the uncoated plate, and outcoupling is recovered from the wedged output coupler.

The location of the output coupler within one of the interferometer arms slightly affects the phase locking properties of the resonator. For the configuration shown in Fig. B.1, the passive frequency response of the resonator can be calculated following the procedure outlined in Chapter 4, Section III, and the resonator losses can then be extracted. The results of the calculation are as follows.

Let the outcoupled losses from all four surfaces of the Brewster plate equal δ_{plate} , so that the round trip power transmission is $[1 - \delta_{\text{plate}}]$. If the reflectance of the beamsplitter is r^2 , then the cavity losses δ_{cav} due to output coupling are

$$\delta_{\text{cav}} = \delta_{\text{plate}}(1 - r^2) , \quad (\text{B.1})$$

and the leakage losses at the beamsplitter, which are finite even for a perfectly phase locked beam, are (to lowest order in δ_{plate})

$$\delta_{\text{leak}} = \frac{1}{4} r^2 t^2 \delta_{\text{plate}}^2 . \quad (\text{B.2})$$

The optimum beamsplitter reflectance yielding the maximum hypermode decay rate is

$$r_{\text{opt}}^2 = \frac{1}{2} \left(1 - \frac{\delta_{\text{plate}}}{4} \right) , \quad (\text{B.3})$$

and the corresponding decay rate for the first order hypermode with N circulating pulses is

$$|\gamma_1|^2 = \frac{1 + \cos\left(\frac{2\pi}{N}\right)}{2} , \quad (\text{B.4})$$

which is *independent* of δ_{plate} . i.e. the first order hypermode falls to a power of $|\gamma_1|^{2p}$ times the power in the lowest order hypermode after p passes. These results suggest a way to reduce the optimum beamsplitter reflectance for the resonator. For example, in a sufficiently high gain FEL with a total loss of $\delta_{\text{cav}} \approx 16 \%$, the losses through the Brewster plate could be as high as $\delta_{\text{plate}} \approx 30 \%$. Then the optimum reflectance would be reduced from $r^2 = 50 \%$ to $r^2 = 46 \%$, the leakage losses would be only $\delta_{\text{leak}} \approx 0.6 \%$, and the power in the first order hypermode would fall to 9 % of the power in the dominant mode after 300 passes (less than 4.0 μs in the Mark III FEL).

III. SPECTRAL DIAGNOSTICS

I have designed and procured a spectral diagnostics capable of detecting the axial modes in both the phase locked and randomly phased optical beams for wavelengths near 3 μm . The setup is shown in Fig. B.2. In order to unambiguously detect a single longitudinal mode in a device such as etalon, the optical beam must first be filtered so that only a single mode is incident; otherwise, any unfiltered modes will be aliased into the spectral window of the etalon [8]. Consequently, the FEL optical beam is first filtered with a 1 m grating monochrometer with a resolution of approximately 20 GHz. The filtered beam is then passed through a planar etalon prefilter with a free spectral range wider than the resolution of the monochrometer, but with an axial mode bandwidth of just under 3 GHz. This secondary filtering yields an optical beam with a total bandwidth of roughly 3 GHz, containing 35 FEL axial modes for the randomly phased optical beam, and a single FEL axial for the perfectly phase locked optical beam. Because the coating reflectance for the planar etalons varies slightly with wavelength, the substrates were designed to have slightly different thicknesses, so that the proper axial mode bandwidth could be chosen within a

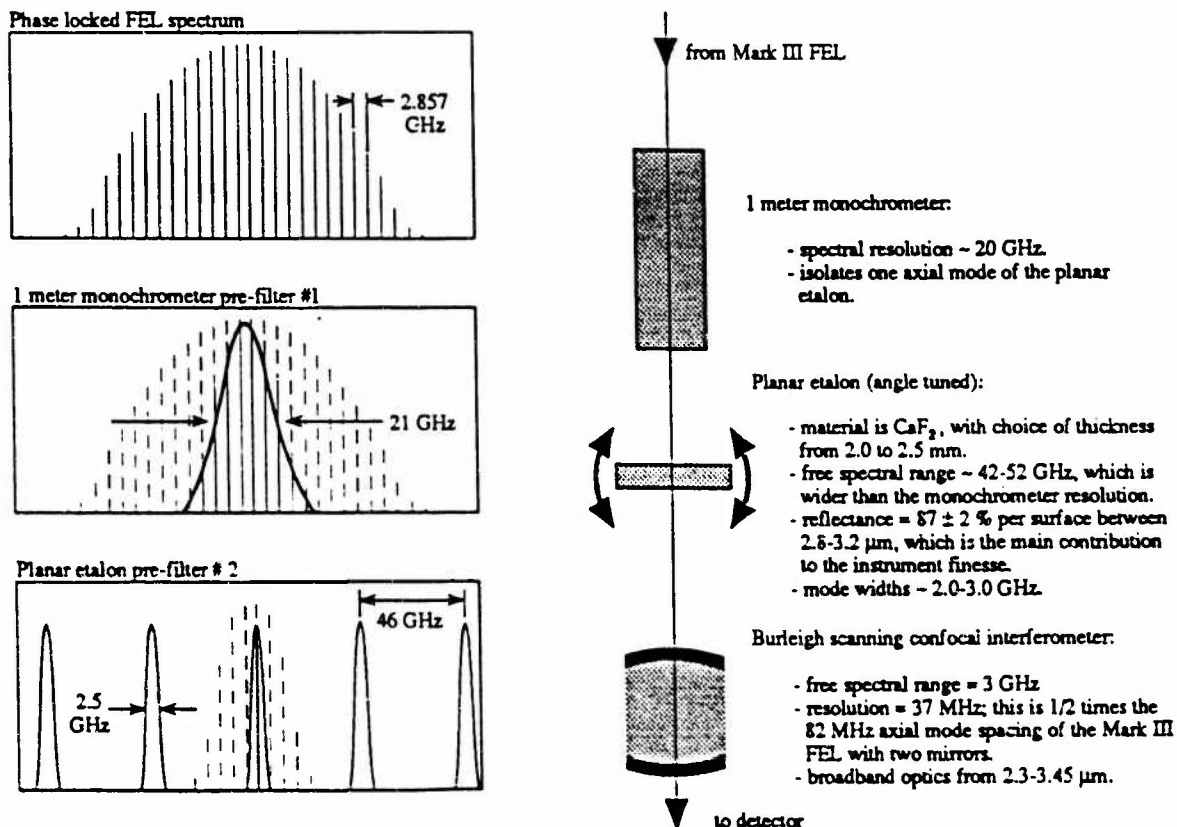


Fig. B.2 Spectral diagnostics for filtering and resolving the individual FEL axial modes in the phase locked optical beam from the Mark III FEL.

wide wavelength range; the final design is appropriate for wavelengths between 2.8 μm and 3.2 μm .

The individual FEL axial modes within the 3 GHz bandwidth of the prefiltered beam are detected with a commercial scanning confocal interferometer from Burleigh, with a free spectral range of 3 GHz by design. This particular interferometer has a resolution of 37 MHz, capable of differentiating axial modes spaced by the FEL round trip frequency of 82 MHz, and can be used for wavelengths between 2.3 μm and 3.45 μm . By scanning the frequency of the confocal etalon through the filtered FEL beam, the longitudinal mode structure and the degree of hypermode decay can then be monitored.

IV. REFERENCES

- [1] E. B. Szarmes and J. M. J. Madey, "The Michelson resonator free-electron laser - Part I: Passive mode structure and mode decay," *IEEE J. Quantum Electron.*, to be published.
- [2] E. B. Szarmes and J. M. J. Madey, "The Michelson resonator free-electron laser - Part II: Supermode structure and mirror detuning effects," *IEEE J. Quantum Electron.*, to be published.
- [3] S. V. Benson, W. S. Fann, B. A. Hooper, J. M. J. Madey, E. B. Szarmes, B. Richman, and L. Vintro, "A review of the Stanford Mark III infrared FEL program," *Nucl. Instr. and Meth.*, vol. A296, pp. 110-114, 1990.
- [4] B. E. Newnam and L. G. DeShazer, "Study of Laser-Irradiated Thin Films," *Laser Induced Damage In Optical Materials: 1972*, Boulder, CO: NBS Special Publication 372, pp. 123-134, 1972.
- [5] R. R. Austin, R. C. Michaud, A. H. Guenther, J. M. Putman, and R. Harniman, "Influence of Structural Effects on Laser Damage Thresholds of Discrete and Inhomogeneous Thin Films and Multilayers," *ibid*, pp. 135-164, 1972.
- [6] B. E. Newnam and D. H. Gill, "Spectral Dependence of Damage Resistance of Refractory Oxide Optical Coatings," *Laser Induced Damage In Optical Materials: 1976*, Boulder, CO: National Bureau of Standards, pp. 292-300, 1976.
- [7] J. O. Porteus, T. M. Donovan, J. L. Jernigan, and W. N. Faith, "Multithreshold Evaluation of 100-nsec Pulsed Laser Damage to Coating Materials at 2.7- and 3.8- μm Wavelengths," *Laser Induced Damage In Optical Materials: 1978*, Boulder, CO: NBS Special Publication 541, pp. 202-211, 1978.
- [8] A. E. Siegman, *Lasers*, Mill Valley, CA: University Science Books, 1986.